

UNIVERSITY OF POTSDAM

INSTITUTE FOR PHYSICS AND ASTRONOMY  
DOCTORAL THESIS

---

**Probing the ultrafast dynamics of  
2-Thiouracil with soft x-rays**

---

*Author:*  
Fabiano Lever

*Supervisor:*  
Markus Gühr

November 2021

Unless otherwise indicated, this work is licensed under a Creative Commons License Attribution – ShareAlike 4.0 International.

This does not apply to quoted content and works based on other permissions.

To view a copy of this licence visit:

<https://creativecommons.org/licenses/by-sa/4.0>

Published online on the

Publication Server of the University of Potsdam:

<https://doi.org/10.25932/publishup-55523>

<https://nbn-resolving.org/urn:nbn:de:kobv:517-opus4-555230>



# Contents

<b>Abstract</b>	<b>5</b>
<b>Acknowledgements</b>	<b>7</b>
<b>Introduction</b>	<b>9</b>
<b>List of my contributions</b>	<b>13</b>
<b>1 Elements of molecular and ultrafast physics</b>	<b>15</b>
1.1 Molecules and Born-Oppenheimer Approximation . . . . .	15
1.1.1 Molecular Hamiltonian . . . . .	15
1.1.2 Nuclear dynamics in the Born-Oppenheimer Approximation . . . . .	17
1.1.3 When BOA breaks down: ultrafast dynamics . . . . .	19
1.2 Thionucleobases . . . . .	23
1.2.1 Nucleobases in DNA . . . . .	23
1.2.2 Thionucleobases . . . . .	24
1.2.3 UV-induced ultrafast dynamics in thionucleobases . . . . .	26
1.3 Light-matter interactions . . . . .	29
1.3.1 Light in quantum mechanics . . . . .	29
1.3.2 X-ray Spectroscopy . . . . .	32
1.3.3 Auger spectroscopy . . . . .	37
1.4 UV pump/X-ray probe spectroscopy . . . . .	39
<b>2 Experimental Setup</b>	<b>43</b>
2.1 Free Electron Laser . . . . .	43
2.1.1 Principles of FEL operation . . . . .	43
2.1.2 The FLASH FEL . . . . .	46
2.1.3 FLASH2 Beamlines and photon diagnostic . . . . .	49
2.1.4 Pump-probe optical laser at FL24 . . . . .	50
2.2 URSA-PQ . . . . .	52
2.2.1 Vacuum apparatus . . . . .	52
2.2.2 Sample delivery oven and diagnostic paddle . . . . .	53
2.2.3 eTOF spectrometer . . . . .	55
<b>3 Published Research</b>	<b>59</b>
3.1 URSA-PQ: A Mobile and Flexible Pump-Probe Instrument for Gas Phase Samples at the FLASH Free Electron Laser . . . . .	60
3.2 Core-Level Spectroscopy of 2-Thiouracil at the Sulfur $L_1$ and $L_{2,3}$ Edges Utilizing a SASE Free-Electron Laser . . . . .	74
3.3 Following excited-state chemical shifts in molecular ultrafast x-ray photoelectron spectroscopy . . . . .	86

3.4	Ultrafast dynamics of 2-thiouracil investigated by time-resolved Auger spectroscopy . . . . .	95
<b>A</b>	<b>Experimental Control and Online Data Analysis</b>	<b>103</b>
A.1	Safety, monitoring and control system . . . . .	103
A.2	Measurement and Online Data Analysis . . . . .	106
<b>B</b>	<b>Data analysis</b>	<b>109</b>
B.1	Data preprocessing and data fusion . . . . .	109
B.2	GPU accelerated computing . . . . .	110
	<b>Bibliography</b>	<b>113</b>



# Abstract

Understanding the changes that follow UV-excitation in thionucleobases is of great importance for the study of light-induced DNA lesions and, in a broader context, for their applications in medicine and biochemistry. Their ultrafast photophysical reactions can alter the chemical structure of DNA - leading to damages to the genetic code - as proven by the increased skin cancer risk observed for patients treated with thiouracil for its immunosuppressant properties.

In this thesis, I present four research papers that result from an investigation of the ultrafast dynamics of 2-thiouracil by means of ultrafast x-ray probing combined with electron spectroscopy. A molecular jet in the gas phase is excited with a uv pulse and then ionized with x-ray radiation from a Free Electron Laser. The kinetic energy of the emitted electrons is measured in a magnetic bottle spectrometer. The spectra of the measured photo and Auger electrons are used to derive a picture of the changes in the geometrical and electronic configurations. The results allow us to look at the dynamical processes from a new perspective, thanks to the element- and site- sensitivity of x-rays.

The custom-built URSA-PQ apparatus used in the experiment is described. It has been commissioned and used at the FL24 beamline of the FLASH2 FEL, showing an electron kinetic energy resolution of  $\Delta E/E \sim 40$  and a pump-probe timing resolution of 190 *fs*. X-ray only photoelectron and Auger spectra of 2-thiouracil are extracted from the data and used as reference. Photoelectrons following the formation a  $2p$  core hole are identified, as well as resonant and non-resonant Auger electrons. At the  $L_1$  edge, Coster-Kronig decay is observed from the  $2s$  core hole.

The UV-induced changes in the  $2p$  photoline allow the study the electronic-state dynamics. With the use of an Excited-State Chemical Shift (ESCS) model, we observe a ultrafast ground-state relaxation within 250 *fs*. Furthermore, an oscillation with a 250 *fs* period is observed in the  $2p$  binding energy, showing a coherent population exchange between electronic states. Auger electrons from the  $2p$  core hole are analyzed and used to deduce a ultrafast  $C-S$  bond expansion on a sub 100 *fs* scale. A simple Coulomb-model, coupled to quantum chemical calculations, can be used to infer the geometrical changes in the molecular structure.





# Acknowledgements

The research that I present in this thesis would not have been possible without the help that many people gave me in these years.

My first thank you goes to Dr. Markus Gühr. Not only for the invaluable guidance he provided as a scientific mentor, but also for being a friend and a source of inspiration. You have helped me make the decision to transition from theory into experiments. In hindsight, that was one of the best choices of my life.

I am grateful to all past and current colleagues with which I shared these years, for the many hours of discussions and for the suggestions they offered. A particular thank goes to Dr. Jan Metje and Dr. Matthew Robinson, as well as to my closest collaborator Dennis Mayer, for their friendship and the jovial times spent together.

To my best friend and life partner Fucsia, for being there with me throughout my adult life and for supporting me during these years in Potsdam: thank you, from the bottom of my heart.

A special thanks to all of my friends and university colleagues of the Æquipe group. We started together in the very first day of university, and I am happy that after all this time and distance, we are still united and continue sharing our passions.

I also want to thank all of the new friends I made in Berlin, you have made the years of my doctorate much more meaningful.

I thank my mother and sister for their encouragement and assistance in all the aspects of life. To my dad: thank you for inspiring me. I know you'd be proud



# Introduction

Deoxyribonucleic acid, or DNA, is the blueprint of life. It contains the information used by cells to produce the structures needed for their functioning by encoding the arrangement of amino acids in proteins [1].

The information is represented as a sequence of nucleobases (Adenine, Cytosine, Thymine and Guanine) forming a code for the amino acid sequences that constitute proteins. DNA is formed by a double-helix of two strands of nucleobases, each strand consisting of a dextrose-phosphate backbone linking the nucleobases in sequence. The two strands are bound together by hydrogen bonds between pairs of nucleobases, with Adenine binding to Cytosine and Thymine to Guanine [2, 3].

Mutations and damage to the DNA molecule break the integrity of the genetic information. Although in rare occasions these mutations are beneficial to the carrier (after all, this is the process that drives evolution), a large fraction of these mutations have unfavorable effects such as cancer [4] or cell death. Highly energetic albeit non ionizing radiation such as UV light can induce chemical changes in DNA [5,6], where the electronic excitation caused by the absorption of UV light induces the rearrangement of chemical bonds, leading to mutations.

A prominent example of such UV induced damages is the cross linking of neighboring pyrimidines (cytosine, thymine and uracil) by the formation of Cyclobutane Pyrimidine Dimers (CPD) [7–9]. In humans, skin tissue takes the blunt of UV irradiation from sunlight, and thus CPD formation is the most common source of skin cancers [10,11].

Active repair mechanisms for this kind of lesions are used by the cell [8] to reduce the incidence of mutations, but a first barrier that reduces the rate of photodamage is built into the pyrimidine basis themselves. A hint for this mechanism was first observed by Daniels and Hauswirth [12] in 1971, with the measure of the low quantum yield for UV induced fluorescence in pyrimidines. Further research showed that the effect is caused by ultrafast electronic relaxation back to the ground state, converting the excitation energy from electronic energy into heat and suppressing fluorescence [13–16], as the initially excited fluorescent state is no longer active. Such fast relaxation allows the molecule to spend little time in the active excited state that can lead to the formation of CPD, suppressing the rate of formation for UV induced DNA lesions [17–19].

This defense mechanism is inhibited in thionucleobases, a class of molecules derived from canonical nucleobases by substituting one or more oxygen atoms with the chemically

similar sulfur [20]. They show a high UV-induced yield of the long-lived, chemically active triplet state, leading to much higher rates of lesion formation [21, 22]. Thionucleobases can function as substitutes for their canonical counterparts in nucleic acids [23], have been suggested as components of primordial RNA molecules [24, 25]. They are actively used in medicine as immunosuppressants [26], and are of interest in biochemistry for their cross-linking capabilities [27].

Substituting oxygen atoms with the much heavier sulfur leads to changes in the photophysics [28]. Firstly, a shift of the UV absorption from the UVC to the UVA region is seen [29, 30], leading to a higher likelihood of photoexcitation due to the higher abundance of UVA in the sun irradiation. Second, UV-excited thionucleobases produce the aforementioned long-lived triplet states, leading to cross linking [21, 22] and to the formation of reactive singlet oxygen [31, 32].

These changes negatively affect the ability of nucleic acid containing thionucleobases to resist UV-induced photodamage, as shown by the increased skin cancer risk for patients treated with these molecules for immunosuppression [33]. On the other hand, the high reactivity of the triplet state could open another route to targeted photoinduced cancer therapy [34, 35].

Ultrafast transitions such as the one observed in pyrimidines proceed through phase-space configurations that do not allow the use of the Born-Oppenheimer Approximation (BOA), one of the most useful tools in molecular physics [36]. The BOA allows for separate treatment of the electronic and nuclear degrees of freedom of a molecule, significantly simplifying the study of the molecular dynamics. However, non-radiative ultrafast transitions require explicit modeling of the energy interplay between the electronic and nuclear motion. This complicates the theoretical study of the molecular dynamics [37, 38], as well as introducing challenges in the experimental investigation of such phenomena [13, 14, 16, 39].

The strong differences in triplet state yield observed between canonical and thionucleobases must be due to different electronic relaxation pathways following UV excitation. We chose 2-thiouracil (2TU) as a sample to study such molecular dynamics. The absence of tautomerization [40] and the amount of information already available on 2TU makes it a natural choice for further study. It has been the focus of many recent experimental investigations, both in solution and gas phase [30, 41, 42], as well as theoretical studies with different computational methods [43–46]. From the available studies, a sketch of the reaction pathway that follows UV absorption can be constructed. Light excites the molecule to the  $S_2$  state, with  $^1\pi\pi^*$  electronic character: the molecule then undergoes an ultrafast transition, on a time scale of 60–80 fs, to the  $^1n\pi^*$   $S_1$  state. The  $S_1$  state acts as a doorway to the triplet states via intersystem crossing, with a time constant of about 500 fs.

In this work, the ultrafast dynamic of 2TU is investigated by the use of gas phase UV-pump, x-ray probe electron spectroscopy [47]. In our case, a UV ‘pump’ pulse is used to excite 2TU to the  $S_2$  state. After a controllable delay, an x-ray ‘probe’ pulse is used to ionize core orbitals in the target molecule, and the kinetic energy of the resulting

photo and Auger-Meitner electrons is measured. Repeating this investigation for a range of pump-probe delays, we can reconstruct the dynamics that follows UV excitation from the recorded kinetic energy electron spectra.

The use of a gas phase target allows direct comparison of the obtained results to *ab initio* quantum simulations, allowing experiments to be used as a benchmark for the theoretical calculations. It also enables charged-particle methods for probing, such as electron spectroscopy [48]. Moreover, gas phase experiments have enhanced sensitivity to quantum coherence effects, a kind of measurement that is not feasible in the liquid phase due to water-induced decoherence.

Using x-rays as probe pulse allows for a different kind of investigation when compared to other setups where photoionization is carried out by UV or visible light. Due to their high energies, x-rays can target localized core orbitals on the sample, as opposed to the spread-out valence orbitals, and can therefore be used for site-specific studies. Photoelectron experiments focusing on valence electrons are affected by both electronic and nuclear dynamics, complicating the interpretation of the results. The use of x-rays enables the study of the dynamics from a different point of view, with higher sensitivity to local electronic structure changes.

This local sensitivity derives from the difference in the electron emission spectra of each element present in the sample. Each element in the sample can be identified by the characteristic spectrum of the emitted electrons, and since the electronic binding energies of an atom depend also on its chemical environment, this technique gives site-selective information [49].

The development of coherent, high-brilliance FEL sources enabled this new type of investigations. Ultrafast x-ray spectroscopy has been initially developed on molecular metal centers at the K-edges in the hard x-ray [50–52] and L-edges in the soft x-ray region [53, 54]. More recently, studies at the soft x-ray edges of oxygen, nitrogen and carbon have employed this technique on purely organic molecules [55, 56].

By observing the variations in the photoelectron spectra on an ultrafast time scale, it is possible to follow changes in the electron distribution during reactions [57]. Results in thymine have tracked ultrafast relaxation from the UV excited  $^1\pi\pi^*$  to  $^1n\pi^*$  state [58]. Moreover, a CO bond expansion has been inferred from the changes in the observed Auger-Meitner electrons [59].

The results contained in this thesis have the objective of investigating the ultrafast dynamics of 2-thiouracil. The papers presented explore the nuclear and electronic changes that follow UV-excitation, using data from photoelectron and Auger emission from the sulfur L-edge.

Chapter 1 introduces concepts of molecular and ultrafast physics, and provides the foundations for the following discussion. Chapter 2 describes the experimental setup and the details of its operation. The results are exposed in chapter 3, through four research papers. A x-ray only static study concentrates on the x-ray electron spectra of sulfur in

2TU; while x-ray data on sulfur is readily available, this is the first time (to my knowledge) such data is made available for 2TU. Two dynamical studies are presented, focusing on the nuclear and electronic dynamics respectively. The electronic dynamics is investigated by following changes to the binding energy, sensing the chemical environment [60]. The nuclear geometry changes are followed by studying Auger electrons, on the basis that their energy spectrum depends on the spatial distribution of the charge of neighboring atomic cores. An additional paper describing the construction and commissioning of the experimental apparatus is also presented. The two appendices focus on the experimental control and data analysis techniques that I developed and used to obtain the results shown.

# List of my contributions

The results presented in this thesis arise from the collaboration of many different people, as is often the case for this kind of investigations at free-electron-laser facilities. I contributed throughout the planning and realization of the experiment in which the data presented was collected.

I assisted in the physical assembly of the apparatus and of its many ancillary systems. I designed and implemented all the software used to monitor, control and integrate the experiment with the DESY infrastructure; moreover, I designed and implemented the online data filtering and visualization routines used during the data collection phase. An overview of such systems is given in appendix A.

I actively participated during the commissioning of the apparatus and during the actual data collection, with particular focus on the management of the measurement control systems and online data analysis.

After the experiment, I designed and implemented the data sorting and filtering routines (described in appendix B), and contributed in the data analysis and interpretation of the results. I participated in the writing of all manuscripts, and I took leadership in writing papers ‘Core-level spectroscopy of 2-thiouracil at the sulfur  $L_1$  and  $L_{2,3}$  edges utilizing a SASE free-electron-lase’ and ‘Ultrafast dynamics of 2-thiouracil investigated by time-resolved Auger spectroscopy’





# Chapter 1

## Elements of molecular and ultrafast physics

The goal of this chapter is to provide the reader with the elements of molecular and ultrafast physics needed to understand the research papers contained in chapter 3. An overview of molecular physics and of the Born-Oppenheimer Approximation is given in section 1.1. Section 1.2 introduces the biological and physical properties of nucleobases and analyzes their ultrafast behaviour. Section 1.3 concentrates on light-matter interactions, focusing on the UV and x-ray parts of the electromagnetic spectrum. Finally, section 1.4 shows how ultrashort light pulses can be used in a pump-probe setup to create ‘molecular movies’ of ultrafast phenomena. This technique can be used to shed light on the ultrafast dynamics of thionucleobases.

### 1.1 Molecules and Born-Oppenheimer Approximation

Describing the structure and behaviour of molecules can shed light on a variety chemical and biological processes, and is therefore one of the most important tasks in molecular physics. Except for the simple case of the hydrogen atom, with one electron and one proton only, describing more complex atomic and molecular systems requires the introduction of many-body interactions. Therefore, approximations have to be used to model molecules. The Born-Oppenheimer Approximation (BOA) is a most useful tool in the study of such systems, allowing separate treatment of the electronic and nuclear degrees of freedom. However, most ultrafast molecular transitions proceed through violation of the BOA, with radiationless transitions dissipating energy without the emission of light. This section will introduce the basic techniques used to model this type of quantum systems and their limitations.

#### 1.1.1 Molecular Hamiltonian

The first step for the construction of a quantum mechanical model for a molecule is the description of the degrees of freedom (DOF) available to the system, and their different

contributions to the overall energy. Treating the atomic nuclei as point particles, we identify the nuclear and electronic coordinates and their relative momenta as the DOF. Since the system is translation invariant, only relative coordinates are needed.

As an example, we will treat the case of a diatomic molecule composed of two atoms  $A$  and  $B$ , with nuclear masses  $M_A$  and  $M_B$  and atomic numbers  $Z_A$  and  $Z_B$  respectively. A full treatment for the general case can be found in [61]. Letting  $\mathbf{R}_A = (x_A, y_A, z_A)$  be the position vector for  $A$  and similarly for  $\mathbf{R}_B$ , the kinetic energy of the two nuclei is then described as:

$$\hat{T}_N = -\frac{\nabla_{\mathbf{R}_A}^2}{2M_A} - \frac{\nabla_{\mathbf{R}_B}^2}{2M_B} = -\frac{\nabla_{\mathbf{R}}^2}{2\mu} \quad (1.1)$$

Where  $\mathbf{R} = \mathbf{R}_A - \mathbf{R}_B$  is the relative coordinate and  $\mu = \left(\frac{1}{M_A} + \frac{1}{M_B}\right)^{-1}$  is the reduced mass.  $\nabla = \left(\frac{\partial}{\partial x}, \frac{\partial}{\partial y}, \frac{\partial}{\partial z}\right)$  is the gradient vector.

The electronic component to the kinetic energy can similarly be written as:

$$\hat{T}_{el} = -\sum_{i=1}^N \frac{\nabla_{\mathbf{r}_i}^2}{2m_e} \quad (1.2)$$

Where  $i$  iterates over electrons, up to a total of  $N$ . Regarding electrostatic potential energy, we have three types of interactions: nucleus-nucleus, electron-electron and nucleus-electron. Respectively:

$$\begin{aligned} \hat{V}_{NN} &= \frac{1}{4\pi\epsilon_0} \frac{Z_A Z_B}{|\mathbf{R}|}; & \hat{V}_{ee} &= \frac{1}{4\pi\epsilon_0} \sum_{i,j=1, i<j}^N \frac{1}{|\mathbf{r}_i - \mathbf{r}_j|}; \\ \hat{V}_{Ne} &= -\frac{1}{4\pi\epsilon_0} \left( \sum_{i=1}^N \frac{Z_A}{|\mathbf{R}_A - \mathbf{r}_i|} + \sum_{i=1}^N \frac{Z_B}{|\mathbf{R}_B - \mathbf{r}_i|} \right) \end{aligned} \quad (1.3)$$

Using atomic units, where  $m_e = 1$  and  $\frac{1}{4\pi\epsilon_0} = 1$ , we can now write the full Hamiltonian by combining together equations 1.1, 1.2 and 1.3:

$$\hat{H} = -\frac{\nabla_{\mathbf{R}}^2}{2\mu} - \sum_{i=1}^N \frac{\nabla_{\mathbf{r}_i}^2}{2} - \sum_{i=1}^N \frac{Z_A}{|\mathbf{R}_A - \mathbf{r}_i|} - \sum_{i=1}^N \frac{Z_B}{|\mathbf{R}_B - \mathbf{r}_i|} + \frac{Z_A Z_B}{|\mathbf{R}|} + \sum_{i,j=1, i<j}^N \frac{1}{|\mathbf{r}_i - \mathbf{r}_j|} \quad (1.4)$$

Solving Eq. 1.4 provides many challenges to both analytic and numerical approaches. A multitude of methods and approximations have been proposed, the most notable is perhaps the Born-Oppenheimer Approximation (BOA), first introduced in 1927 by M. Born and J. R. Oppenheimer [36].

### 1.1.2 Nuclear dynamics in the Born-Oppenheimer Approximation

The idea at the core of the BOA is to decouple the motion of the nuclei from the one of the electrons, with the former being virtually motionless on the time scales of electronic motion. This is justified by the large mass difference between electrons and nuclei, giving very different inertias to the two subsystems while the forces acting on them are the same (coulomb interactions).

Continuing the derivation of the previous section, we can divide the Hamiltonian in Eq. 1.4 in two components, isolating the nuclear kinetic energy from the rest:

$$\hat{H} = \hat{T}_N + \hat{H}_{el}; \quad \hat{H}_{el} = \hat{T}_{el} + \hat{V}_{NN} + \hat{V}_{ee} + \hat{V}_{Ne} \quad (1.5)$$

Let  $\varphi_i(\mathbf{R}, \mathbf{r})$  be a complete and orthonormal set of eigenvectors for  $\hat{H}_{el}$  with eigenvalues  $\mathcal{V}_k$ . Note that  $\hat{H}_{el}(\mathbf{R}, \mathbf{r})$  depends only parametrically on  $\mathbf{R}$ , since it does not contain any differential term in  $\mathbf{R}$ . The same will hold for the eigenvalues  $\mathcal{V}_k(\mathbf{R})$ .

Without loss of generality, we can write all solutions to  $\hat{H}$  as:

$$\Psi(\mathbf{R}, \mathbf{r}) = \sum_i \Phi_i(\mathbf{R}) \varphi_i(\mathbf{R}, \mathbf{r}) \quad (1.6)$$

with:

$$\hat{H}\Psi(\mathbf{R}, \mathbf{r}) = E\Psi(\mathbf{R}, \mathbf{r}) \quad (1.7)$$

Multiplying both sides of Eq. 1.7 by  $\varphi_k^\dagger(\mathbf{R}, \mathbf{r})$  and integrating over  $\mathbf{r}$ , we get:

$$\langle \varphi_k^\dagger(\mathbf{R}, \mathbf{r}) | \hat{T}_N + \hat{H}_{el} | \sum_i \Phi_i(\mathbf{R}) \varphi_i(\mathbf{R}, \mathbf{r}) \rangle_{\mathbf{r}} = \langle \varphi_k^\dagger(\mathbf{R}, \mathbf{r}) | E | \sum_i \Phi_i(\mathbf{R}) \varphi_i(\mathbf{R}, \mathbf{r}) \rangle_{\mathbf{r}} \quad (1.8)$$

The  $\varphi_k$  are eigenvectors of  $\hat{H}_{el}$ , and  $\langle \varphi_i(\mathbf{R}, \mathbf{r}) | \varphi_k(\mathbf{R}, \mathbf{r}) \rangle_{\mathbf{r}} = \delta_{ik}$ , therefore:

$$\sum_i \langle \varphi_k^\dagger(\mathbf{R}, \mathbf{r}) | \hat{T}_N | \Phi_i(\mathbf{R}) \varphi_i(\mathbf{R}, \mathbf{r}) \rangle_{\mathbf{r}} + \mathcal{V}_k(\mathbf{R}) \Phi_k(\mathbf{R}) = E \Phi_k(\mathbf{R}) \quad (1.9)$$

Let us first calculate explicitly the term:

$$\begin{aligned} \hat{T}_N | \Phi_i(\mathbf{R}) \varphi_i(\mathbf{R}, \mathbf{r}) \rangle &= -\frac{1}{2\mu} | \nabla_{\mathbf{R}}^2 [ \Phi_i(\mathbf{R}) \varphi_i(\mathbf{R}, \mathbf{r}) ] \rangle \\ &= -\frac{1}{2\mu} [ | \Phi_i(\mathbf{R}) \nabla_{\mathbf{R}}^2 \varphi_i(\mathbf{R}, \mathbf{r}) \rangle + | \nabla_{\mathbf{R}} \varphi_i(\mathbf{R}, \mathbf{r}) \nabla_{\mathbf{R}} \Phi_i(\mathbf{R}) \rangle + | \varphi_i(\mathbf{R}, \mathbf{r}) \nabla_{\mathbf{R}}^2 \Phi_i(\mathbf{R}) \rangle ] \\ &= -\frac{1}{2\mu} [ | \Phi_i(\mathbf{R}) \nabla_{\mathbf{R}}^2 \varphi_i(\mathbf{R}, \mathbf{r}) \rangle + | \nabla_{\mathbf{R}} \varphi_i(\mathbf{R}, \mathbf{r}) \nabla_{\mathbf{R}} \Phi_i(\mathbf{R}) \rangle ] + | \varphi_i(\mathbf{R}, \mathbf{r}) \rangle \hat{T}_N \Phi_i(\mathbf{R}) \end{aligned} \quad (1.10)$$

Combining equations 1.9 and 1.10, we arrive at a set of coupled eigenvalues equations for the nuclear wavefunctions  $\Phi_i(\mathbf{R})$ :

$$\left[ \hat{\mathcal{H}}_k + \hat{T}_N + \mathcal{V}_k(\mathbf{R}) \right] \Phi_k(\mathbf{R}) = E \Phi_k(\mathbf{R}) \quad (1.11)$$

Where the coupling operator  $\hat{\mathcal{H}}_k$  is given by:

$$\hat{\mathcal{H}}_k = -\frac{1}{2\mu} \sum_i [\langle \varphi_k(\mathbf{R}, \mathbf{r}) | \nabla_{\mathbf{R}}^2 | \varphi_i(\mathbf{R}, \mathbf{r}) \rangle_{\mathbf{r}} + \langle \varphi_k(\mathbf{R}, \mathbf{r}) | \nabla_{\mathbf{R}} | \varphi_i(\mathbf{R}, \mathbf{r}) \rangle_{\mathbf{r}} \nabla_{\mathbf{R}}] \quad (1.12)$$

The Born-Oppenheimer Approximation consists in neglecting the coupling  $\hat{\mathcal{H}}_k$ . In this case, Eq. 1.11 reduces to a set of decoupled equations for nuclear motion, one for each electronic state:

$$\left[ \hat{T}_N + \mathcal{V}_k(\mathbf{R}) \right] \Phi_k(\mathbf{R}) = E \Phi_k(\mathbf{R}) \quad (1.13)$$

The absence of the coupling term given in Eq. 1.12, that involves the nuclear gradient operator acting on the electronic part of the wavefunction, means that the electronic wavefunction is considered to be instantaneously adapting to nuclear motion, without memory of past nuclear positions.

Therefore, the electronic energies  $\mathcal{V}_k(\mathbf{R})$  act as external potentials, and are usually referred to as Born-Oppenheimer Potential Energy Surfaces (PES), since they define the energetic landscape for nuclear motion.

In most cases, the approximation is justified. Since  $\frac{1}{2\mu}$  is a small number<sup>1</sup>, the terms  $\hat{\mathcal{H}}_k$  are small and can indeed be safely neglected. However, when the energies of different electronic states are close to degeneracy, the first term in Eq. 1.12 diverges. This fact can be made explicit by calculating the coupling operator element:

$$\langle \varphi_k | \nabla_{\mathbf{R}}^2 | \varphi_i \rangle_{\mathbf{r}} = \frac{\langle \varphi_k | [\nabla_{\mathbf{R}}^2, H_{el}] | \varphi_i \rangle_{\mathbf{r}}}{\mathcal{V}_k(\mathbf{R}) - \mathcal{V}_i(\mathbf{R})} \quad (1.14)$$

Therefore, for nuclear configurations that correspond to degenerate (or close to degenerate) electronic energies, the BOA breaks down. In such configurations, the nuclear motion cannot be decoupled from the electronic dynamics, and the full coupled equations must be used.

Figure 1.1 a) shows an example of PES for various electronic states in a diatomic molecule. In this case, the surfaces are one dimensional since there is only one internuclear coordinate; for larger molecules, the PES become a multidimensional manifold.

---

<sup>1</sup>We remind the reader that we are using atomic units where  $m_e = 1$ . In usual unit, this term would be proportional to the ratio of  $m_e$  to  $\mu$

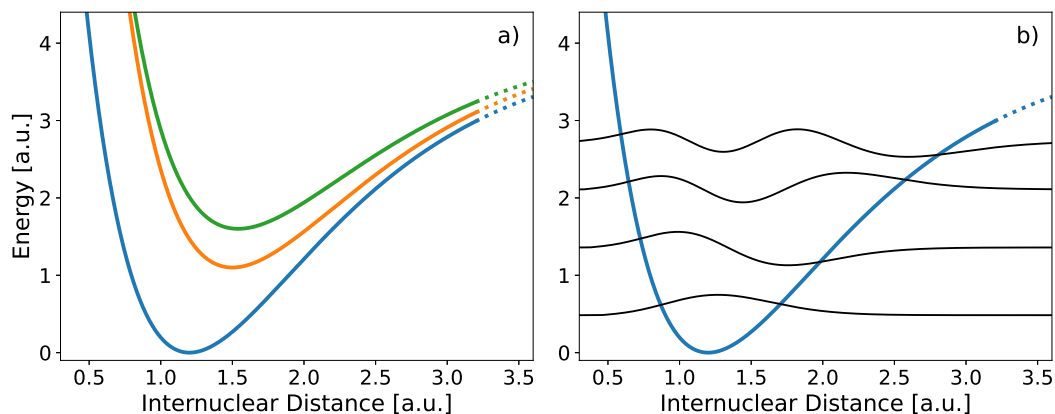


**Figure 1.1:** a) Potential Energy Surfaces (PES)  $\mathcal{V}_k(\mathbf{R})$  for various electronic levels in a diatomic molecule. b) Eigenfunctions  $\Phi_k(\mathbf{R})$  of one of the shown PES.

In Fig. 1.1 b) the eigenstates of one of the PES are shown. Since the PES act as potentials for nuclear motion, vibrational excitations can be described as a population of one or more of the so-obtained vibronic levels. When a coherent superposition is constructed (*e.g.* through excitation with an ultrafast laser pulse), the excited population evolves as a wavepacket oscillating in the potential well. Due to the anharmonicity of the potential, dispersion and revival phenomena are observed [62].

### 1.1.3 When BOA breaks down: ultrafast dynamics

The previous section introduced the BOA and its uses for modeling molecular dynamics. However, Eq. 1.14 shows how in some configurations this approximation breaks down, giving rise to interesting phenomena where the electronic and nuclear degrees of freedom are coupled and able to exchange energy. This happens when the potential energy surfaces of neighboring electronic states become degenerate and/or cross.

Section 1.1.2 shows the derivation of the BOA for a diatomic molecule. In this case, the PES of states with the same spin symmetry cannot cross due to the Von Neumann non-crossing rule [63]. For larger molecules, this constraint is lifted, and the multi-dimensional landscape defined by the PES can include crossing.

An example of such configurations is shown in Fig 1.2, where the PES corresponding to two different electronic states cross each other. In the crossing region, the energy states are close to degeneracy and the nuclear and electronic motion are coupled. Such a region is referred to as a Conical Intersection (CI) [37, 64]. Some other configurations, called Avoided Crossings, lead to manifolds that never reach degeneracy due to symmetry constraints, but are still in violation of the BOA assumptions [63, 65, 66].

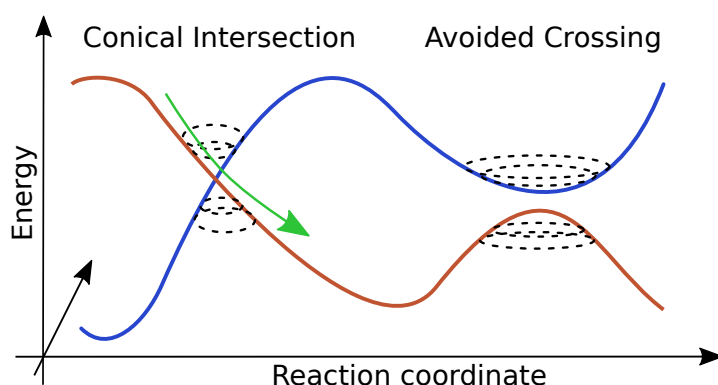


**Figure 1.2:** Example of Conical Intersection and Avoided Crossing. The horizontal plane represents the multi-dimensional configuration space of the molecule, while the vertical axis shows the electronic energy for each configuration. The two potential energy surfaces, drawn in blue and red, undergo a conical intersection (left side) and an avoided crossing (right side) when viewed along a molecular coordinate. The green arrow shows a potential pathway for a molecular transition through the CI.

These configurations allow the molecule to transfer population between electronic states non-radiatively, *i.e.* without emitting photons. Transitions usually happen on an ultrafast timescale when compared to the radiative lifetime of electronic states [67,68], and give rise to many interesting molecular phenomena.

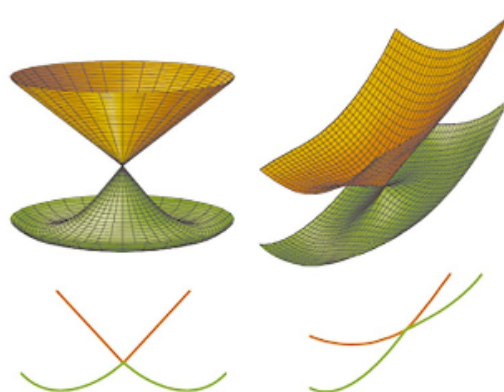


**Figure 1.3:** Example of branching spaces in conical intersections for two different topologies. In this view of the multi-dimensional landscape, the electronic states are degenerate only in a single point. The two main patterns for CI, Peaked (left) and Sloped (right) are shown. Image used with permission from [69].

It can be shown that for a given CI, the energy degeneracy occupies a  $N - 2$  dimensional space, where  $N$  is the number of atomic degrees of freedom [38]. The remaining 2-dimensional space in which the degeneracy is lifted (with the exception of a single point) is called the branching space, and can be thought as the reaction-coordinate space for the non radiative transition. Figure 1.3 shows examples of such spaces, where the PES degeneracy is lifted except for a single point. Along the remaining  $N - 2$  dimensions the degeneracy is preserved, and the conical intersection appears as a seam between the PES. Such space is named the seam space.

The probability of a transition is affected by the topology of the branching space [70]. Figure 1.3 shows the main classes of patterns: peaked (P) or sloped (S) intersections, highlighting how the shape of the PES can guide the wavepacket in the vicinity of the CI. In the case of sloped intersections, transitions from the lower to the upper surface are also conceivable, provided the wavepacket approaches the intersection from the downhill direction.

Moreover, the dynamical properties of the wavepacket as it approaches the CI play a role in the transition probability (Landau-Zener formula) [71, 72]. Since the Rabi oscillation frequency between coupled states depends on the energy gap, the velocity at which the two energies converge affects the relative phases of the wavepacket components that cross the barrier at different energy gaps. This phase interplay creates a dependency of the overall transition probability on the speed at which the system approaches the intersection.

The branching space can be determined from the energy structure of the intersecting electronic states, and is spanned by the so-called  $\mathbf{h}$  and  $\mathbf{g}$  vectors, respectively the energy difference and non-adiabatic coupling vector [73].

$$\begin{aligned} \mathbf{g} &= \frac{1}{2} \left( \langle \Psi_1(\mathbf{R}, \mathbf{r}) | \nabla \hat{H}_{el} | \Psi_1(\mathbf{R}, \mathbf{r}) \rangle - \langle \Psi_2(\mathbf{R}, \mathbf{r}) | \nabla \hat{H}_{el} | \Psi_2(\mathbf{R}, \mathbf{r}) \rangle \right) \\ \mathbf{h} &= \langle \Psi_1(\mathbf{R}, \mathbf{r}) | \nabla \hat{H}_{el} | \Psi_2(\mathbf{R}, \mathbf{r}) \rangle \end{aligned} \quad (1.15)$$

As an example of such degrees of freedom, Fig. 1.4 shows the  $\mathbf{h}$  and  $\mathbf{g}$  vectors for the  $S_2/S_1$  conical intersection in thymine. See section 1.2 for a more detailed discussion of such ultrafast transitions in nucleobases.

Fig 1.5 shows a representation of such non-radiative transitions in a energy diagram. They are usually classified as Internal Conversion (IC) or Inter System Crossing (ISC) depending whether the transition happens between states with the same (for IC) or different (for ISC) molecular spin.

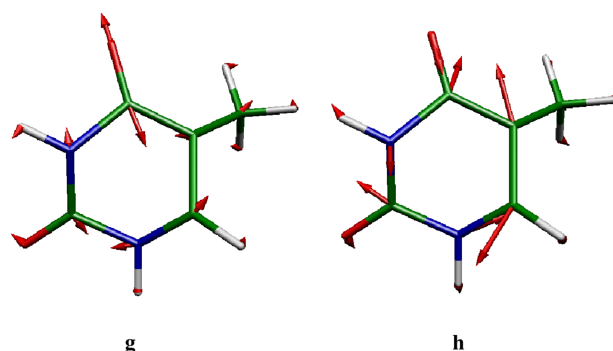


**Figure 1.4:** Basis vectors for the branching space of the  $S_2/S_1$  conical intersection in thymine. The red arrows indicate the direction and magnitude of the displacement of each atom in the molecule along the given coordinate. Reprinted with permission from [74]. Copyright 2009 American Chemical Society.

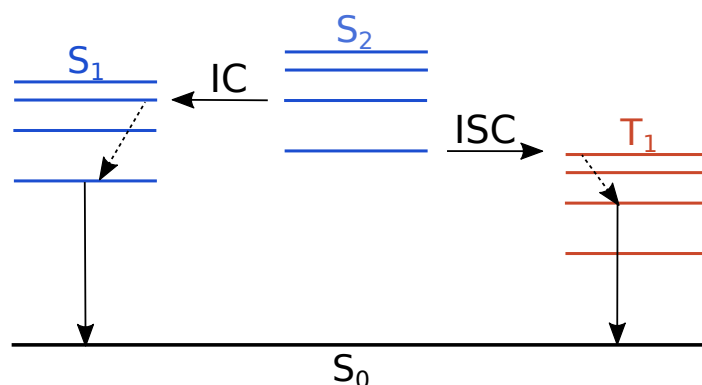


**Figure 1.5:** Comparison between Internal Conversion (IC) and Inter System Crossing (ISC). Excited singlet states are drawn in blue, triplet states in red. IC moves population between states with the same spin multiplicity, while in ISC the molecular spin state is changed. Other possible transitions are shown, with dashed lines representing vibronic relaxation and solid vertical lines corresponding to radiative transitions.

Since ISC is formally forbidden in non-relativistic quantum mechanics (as spin-orbit coupling is a relativistic effect), selection rules favour transitions between states with the same spin multiplicity. As a consequence, IC usually happens on much faster time frames than ISC [75,76]. However, when an ISC transition involves a change in molecular orbital type, the rate of ISC is significantly increased (a fact known as El-Sayed rule) [77] and can be so high to compete with IC transitions [78,79].



## 1.2 Thionucleobases

The photophysics of nucleobases is of particular importance in the understanding of photoinduced DNA lesions such as CPD. This section will introduce canonical and noncanonical nucleobases and their ultrafast UV-induced dynamics.

### 1.2.1 Nucleobases in DNA

The DNA (Deoxyribonucleic Acid) double-helix, discovered in 1953 by Watson and Crick [2] on the basis of Rosalind Franklin's 'photo 51' [80], is perhaps the most iconic molecular structure in history. This structure, as shown in Fig 1.6 (right) consists of two long strands of nucleotides joined together.

Each nucleotide is formed by a phosphate group, a deoxyribose sugar, and one of the four nucleobases: adenine, cytosine, guanine and thymine [81] (respectively: A, C, G and T). In RNA, thymine is substituted by uracil (U). The sugar and phosphate groups alternate forming a backbone that links together the nucleotides in each strand. Hydrogen bonds among pairs of nucleobases link together the two DNA strands, and together with base-stacking interactions between neighboring nucleobases contribute in giving DNA its double-helix structure [82]. This structure is shown in Fig 1.6 (left).

Nucleobases are heterocyclic aromatic compounds, derived from purine and pyrimidine. The purine-derived nucleobases are adenosine and guanine, while thymine and cytosine are pyrimidine derivatives. In DNA, each base pair consists of a purine-derived nucleobase bonded to a pyrimidine-derived one. The different bonding patterns of each base-pair (two vs three hydrogen bonds) ensures that adenine bonds only to thymine and guanine only to cytosine. [85]. As result of this complementarity, each strand contains the full genetic information, allowing for the construction of the full DNA molecule based on one strand only [81].

One of the functional roles of DNA is to store the information needed for protein production in the cell [1, 81]. Triplets of base-pairs, known as codons, are used to encode the sequence of aminoacids in a polypeptide chain, with each codon corresponding to one aminoacid. After transcription from DNA into RNA [86], ribosomes read the genetic information and assemble proteins by bonding aminoacids in sequence. Once produced, the protein folds into a functional three-dimensional structure. Errors in this process can result in non-functional proteins, causing diseases or leading to cell death [87–90].

In nucleic acids, the cross linking of nucleobases can lead to lesions to the genome such as the formation of cyclo pyrimidine dimers (CPD) or the so-called 6-4 dimers [6–9]. Since skin tissue receives most of the UV irradiation from the sun, the formation of CPD is the leading cause of skin cancer in humans [10, 11].

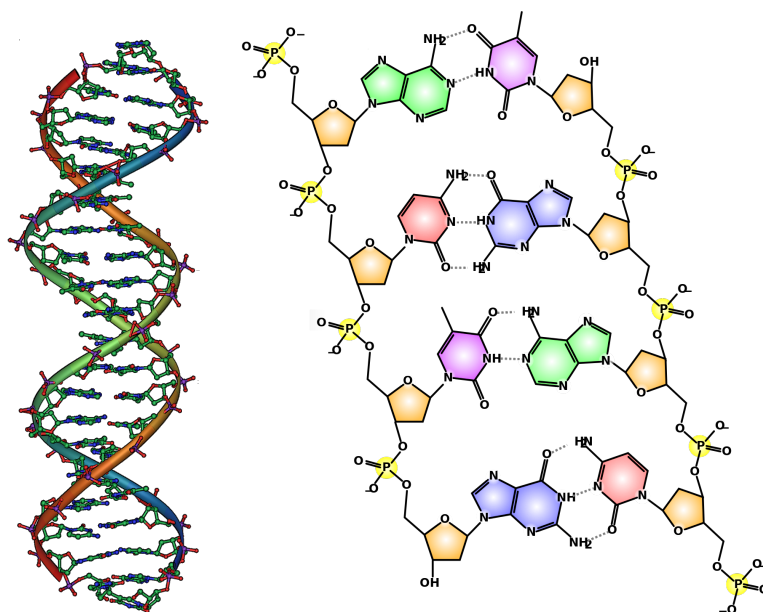


**Figure 1.6:** Left: Double helix arrangement of the nucleotides strands to form DNA. Image used under Creative Commons License from [83]. Right: Structure of nucleotides and hydrogen bonding patterns between nucleobases. Orange: deoxyribose, green: adenine, purple: thymine, blue: guanine, red: cytosine. Image used under Creative Commons License from [84].

## 1.2.2 Thionucleobases

In addition to the aforementioned nucleobases, other nucleobases are found in DNA and RNA performing a variety of roles, from encoding epigenetic information to regulating gene expression [20,91]. They are known as non-canonical nucleobases, and are found in both DNA and RNA [92,93]. The first non-canonical nucleobase to be discovered was 5-methyl-cytosine [94], obtained from cytosine by the addition of a methyl group in position 5.

Thionucleobases are a class of nucleobase analogues obtained by substituting one or more oxygen atoms with sulfur, as shown in Fig 1.7 for 2-thiouracil (2TU). The chemical similarities between oxygen and sulfur allow for thionucleobases to have similar chemistry to their canonical counterparts, maintaining function when used as substitutes in nucleic acids [23]. They are of interest in medicine for their use as immunosuppressants [26] and in cancer therapy [29,34], and are used in biochemistry for their high cross linking ability, especially towards pyrimidines such as thymine [23,27].

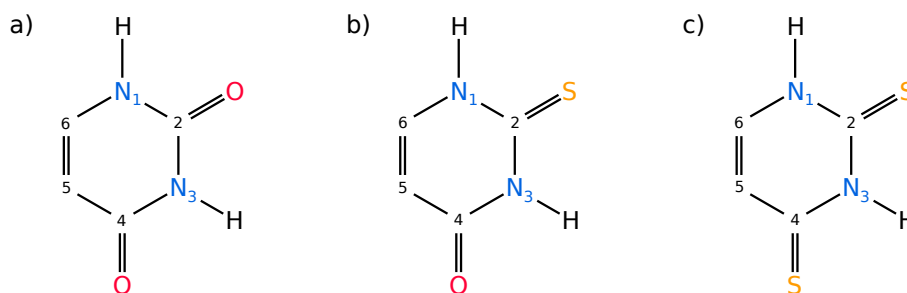


**Figure 1.7:** Chemical structure of Uracil (a), 2-Thiouracil (b) and 2,4-Thiouracil (c). One or both of the oxygen atoms is substituted with a sulfur atom.

The presence of sulfur shifts the UV absorption spectra towards lower photon energies, from the UVC into the UVA region [29, 30], as shown in Fig. 1.8. The relatively higher abundance of UVA radiation in earth's atmosphere, together with the increased tissue penetration depth of UVA radiation, makes thiated nucleobases more susceptible to photoinduced damage than their canonical counterparts.

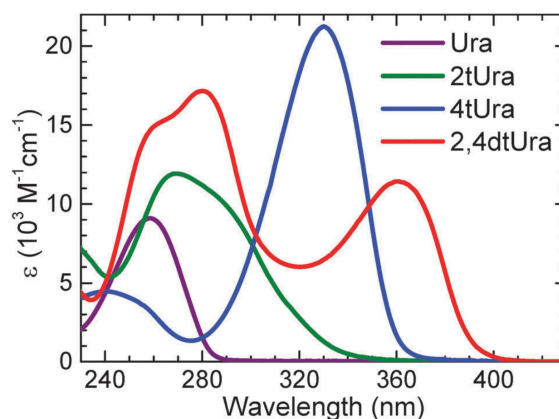


**Figure 1.8:** Molar absorptivity of canonical uracil (purple) and of thiated uracils (green, blue, red), in aqueous phosphate-buffered saline solution. A general shift of the absorption spectrum towards longer wavelengths is observed for the sulfur substituted compounds. Image used with permission from [30].

This shift in absorption is accompanied by a notable shift in the photophysics: thionucleobases have a remarkably high yield for UV-induced triplet state generation. The long lived triplet state can react with neighboring oxygen molecules leading to highly reactive triplet oxygen. Moreover, the reactive triplet state catalyzes cross-linking reactions, with the thio base bonding to neighboring nucleobases or to amino acids, creating lesions in the genome [29].

### 1.2.3 UV-induced ultrafast dynamics in thionucleobases

The high triplet state yield of thiated nucleobases is in contrast with the processes occurring in canonical nucleobases following UV excitation, where ultrafast relaxation to the ground state limits the time spent in active excited states [13–16], contributing to the protection of DNA from UV-induced lesions. [17–19]. The discrepancy between thiated and canonical nucleobases is caused by the different ultrafast dynamics brought on by the changes in the molecular potential energy surfaces caused by the oxygen-sulfur substitution [28]. Moreover, the classically-forbidden singlet to triplet transition is enhanced by the presence of the heavier sulfur, since it features a stronger relativistic spin-orbit coupling (a phenomenon known as the heavy-atom effect) [95].

In order to characterize the light-induced ultrafast processes in nucleobases, it is necessary to study the changes in electronic configuration brought on by UV excitation. For thionucleobases, UV absorption generally excites the so-called  $S_2$  state, from which the population quickly transfer to the lower lying  $S_1$  through a conical intersection [28]. The subsequent population transfer to the triplet manifold happens through a variety of channels, with differences between each particular species. The complex topology of the PES makes the study of such processes extremely challenging, both from a theoretical and an experimental point of view. Occasionally, contrasting results make the interpretation of the dynamics a difficult task. In 4-thiouracil, a transient absorption study measures a ISC lifetime to the triplet manifold of  $225 fs$  [96]. However, another gas phase photoelectron investigation from the same year infers a time constant for the same transition of several picoseconds [97]. This discrepancy is unlikely to be solvent effect, as similar comparisons between gas and condensed phases for 2-thiouracil studies agree quite well [42]. The use of x-rays to probe such system may open a new avenue for giving insights on such complex phenomena.

We now concentrate on the case of 2-thiouracil (2TU). S. Mai *et al* [44] have calculated various molecular orbitals for 2TU, shown in Fig 1.9, that can be used as a reference for understanding excited state electronic configurations.

The initial UV excitation populates states with  $^1\pi_S\pi_2^*$  and  $^1\pi_S\pi_6^*$  character [44], usually referred to as  $S_2$  states [98,99], although it is worth noting that there is not yet a consensus on the energy ordering of the Frank-Condon states [44,95,100]. They describe excitations from the  $\pi_S$  orbital, localized on the sulfur atom, to the  $\pi_6^*$  and  $\pi_2^*$  orbitals respectively, localized on  $C_6$  and  $C_2$ . In the case of 2TU, the relative contribution of these two states to the total absorption is still object of debate [44].

The lowest singlet excited state, the  $^1n_S\pi_2^*$   $S_1$ , denotes excitation from the  $n_S$  orbital to the  $\pi_2^*$  orbital. In the relaxation dynamics following UV excitation, this state is thought to act as a doorway for the long lived triplet states via inter system crossing (ISC) [41].

A possible relaxation pathway, obtained with nonadiabatic dynamics simulations at the CASPT2 level [45] is shown in Fig 1.10. They predict the majority of the population to excite the  $^1\pi_S\pi_6^*$  state, undergoing IC to the  $^1n_S\pi^*$  within  $59 fs$ , with the remaining population flowing through the  $^1\pi_S\pi_2^*/^1n_S\pi^*$  CI. Interestingly, an oscillation in the popu-

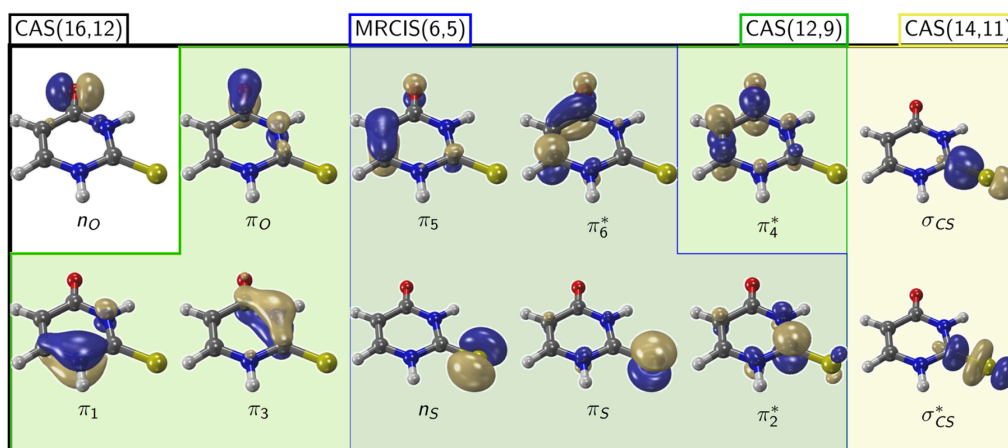


**Figure 1.9:** Molecular orbitals for 2-thiouracil, numerically calculated at different levels of theory (as indicated by the colored backgrounds). Image used under Creative Commons License from [44].

lation interplay between the  $S_1$  and  $T_1$  states can be seen for times  $> 200\text{ fs}$ . The electronic state transitions are accompanied by geometrical changes, most notably an elongation of the  $C_2 - S$  bond (detailed data of such elongation from [45] is shown in the paper of section 3.4).

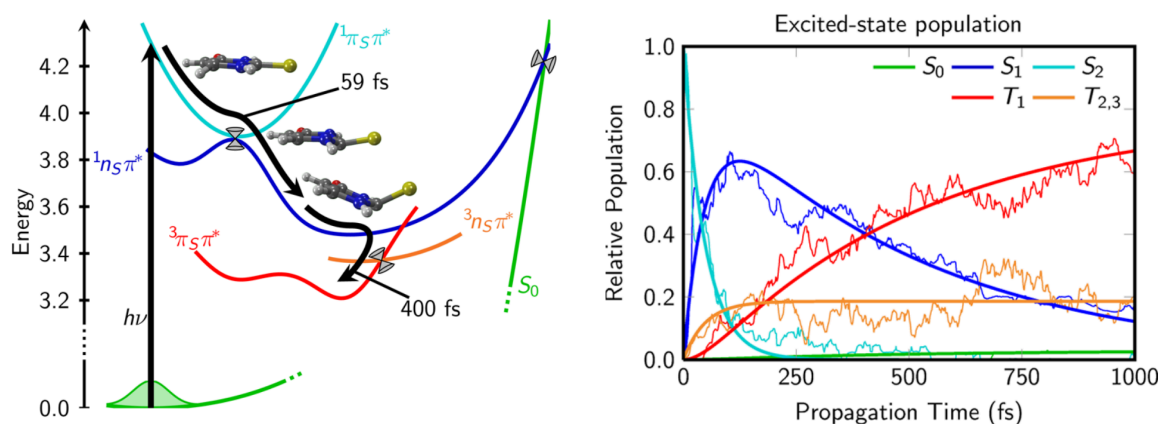


**Figure 1.10:** Simulated relaxation dynamics of 2-TU. After photoexcitation, population flows from the  $\pi\pi^*$  to the  $n\pi^*$  state through the  $S_2/S_1$  canonical intersection. The triplet state is subsequently populated via ISC from the  $n\pi^*$ . Left: proposed relaxation pathway. Right: excited state population interplay after UV excitation. Image used under Creative Commons License from [45].

A later study from the same group, using surface-hopping ADC(2) simulations, predicts a similar de-excitation pathway. However, a longer  $250\text{ fs}$  time constant for the

$S_2/S_1$  transition is observed, as well a larger population transfer through the  $^1\pi_S\pi_2^*$  state, leading to a pyramidization of the sulfur atom out of the molecular plane.

Different experimental studies have investigated the ultrafast dynamics with different methods. Pollum *et al.* [101], in a UV transient-absorption study (TRAS), measure a sub-200 fs transition from the  $S_2$  to the  $S_1$  state, that then transfers population to the triplet  $T_1$  state with near unity yield. A time-resolved photoelectron spectroscopy (TRPES) study from Mai *et al.* [43] measured a time constant for the  $S_2 \rightarrow S_1$  transition of 45 fs, and observed inter system crossing to the triplet manifold on a 500 fs time scale (shown in Fig 1.11).

A joint TRPES-TRAS study from Sánchez-Rodríguez *et al.* [42] compares gas and condensed phase data and systematically studies the effect of pump wavelength, showing an inverse dependency of the singlet-triplet transition time constant on UV excitation energy. In gas phase, this effect is attributed to excess excitation energy helping the wavepacket overcoming a barrier to access the ISC seam.

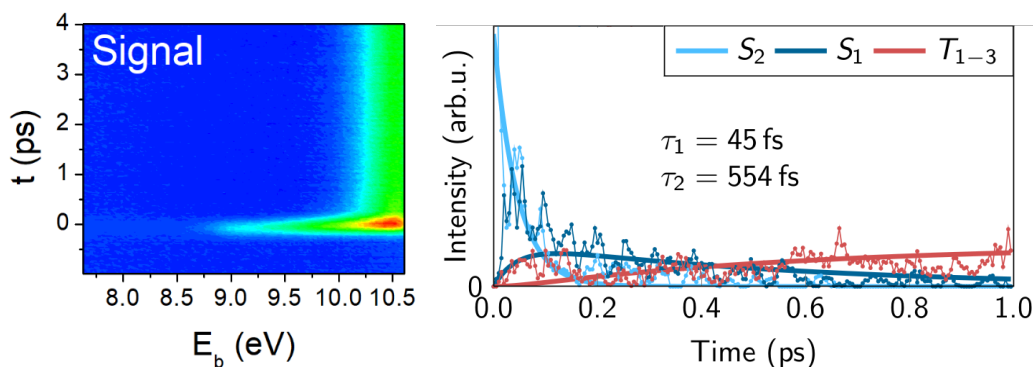


**Figure 1.11:** Left: Time-Resolved photoelectron spectra of 2-thiouracil, 293 nm excitation and 194 nm one-photon ionization. Right: Integrated TR-PES signal divided in its  $S_2$ ,  $S_1$  and triplet state component. A ultrafast (45 fs) transition from  $S_2$  to  $S_1$  is observed immediately after photoexcitation, with subsequent  $S_1 \rightarrow T_{1-3}$  ISC on a 554 fs time scale. Image modified under Creative Commons from [43].

A sketch of the potential energy surfaces along the relaxation coordinate for canonical and thiated nucleobases is shown in Fig 1.12. The locations and relative slopes of the conical intersections along the reaction coordinate can illustrate the observed difference in triplet state yield. For thiated nucleobases, the  $\pi\pi^*$  to  $n\pi^*$  transition happens through the  $S_2/S_1$  conical intersection on a sub 100 fs scale. In their canonical counterparts, this transition is believed to happen on a longer timescale, and has to compete with population converting to the ground state  $S_0$  through the  $S_2/S_0$  conical intersection [41].

These differences in the relaxation pathways provide evidence for the different rates of triplet generation observed between canonical and sulfur-substituted nucleobases.

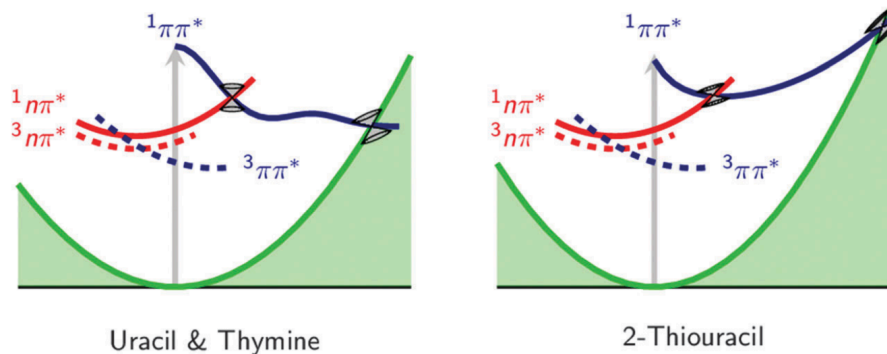


**Figure 1.12:** Comparison between the potential energy surfaces involved in the the UV-induced dynamics between canonical and thiated nucleobases. For the case of 2TU, nearly all the population flows from the  $\pi\pi^*$  to the  $n\pi^*$  state. For uracil and thymine, this process competes with ultrafast internal conversion to the ground state. Image used with permission from [41].

### 1.3 Light-matter interactions

Modeling the exchange of energy between matter and the electromagnetic field is an extremely important task for the understanding of many physical phenomena. Our study of 2TU involves both UV and x-ray light, coupling respectively to the valence and core electrons of molecules. We will therefore introduce two different models to describe such interactions.

#### 1.3.1 Light in quantum mechanics

Unlike the case of strong-field phenomena, the absorption/emission of single photons by a molecule, such as the case of UV excitation, requires a quantum mechanical description of light-matter interactions. Therefore, a quantum model of the electromagnetic field has to be constructed. As this is a fairly complex topic, we will only show parts of the derivation, with the intent of providing the reader with an intuition for the steps and approximations taken. We refer to [102] for the full derivation.

The starting point for the quantization of electrodynamics is the formulation of the electric and magnetic fields  $\mathbf{E}$  and  $\mathbf{B}$  in terms of the vector and scalar potentials  $\mathbf{A}$  and  $\varphi$ . The fields can be determined from the potentials as:

$$\mathbf{B} = \nabla \times \mathbf{A}; \quad \mathbf{E} = -\nabla\varphi - \frac{\partial}{\partial t}\mathbf{A} \quad (1.16)$$

The potentials  $\mathbf{A}$  and  $\varphi$  have an extra degree of freedom, so that  $\mathbf{E}$  and  $\mathbf{B}$  remain unchanged under a *gauge transformation*:  $\mathbf{A} \rightarrow \mathbf{A} - \nabla f$  and  $\varphi \rightarrow \varphi + \frac{\partial}{\partial t}f$ , where  $f$  is an

arbitrary function of position  $\mathbf{r}$  and time  $t$ . We chose  $f$  so that  $\nabla \cdot \mathbf{A} = 0$ , this is known as the Coulomb gauge.

In this gauge, the field equations read:

$$-\nabla^2 \mathbf{A} + \frac{1}{c^2} \frac{\partial}{\partial t} \nabla \varphi + \frac{1}{c^2} \frac{\partial^2}{\partial t^2} \mathbf{A} = \mu_0 \mathbf{j}; \quad -\nabla^2 \varphi = \frac{\rho}{\epsilon_0} \quad (1.17)$$

where  $\mathbf{j}$  and  $\rho$  are the current and charge densities respectively. In free space ( $\mathbf{j} = 0$  and  $\rho = 0$ ), the electric field is purely transverse (that is,  $\nabla \cdot \mathbf{E} = 0$ ) and the energy of the EM field is:

$$E_{EM} = \frac{1}{8\pi} \int d\mathbf{r} (\mathbf{E}^2 + \mathbf{B}^2) = \frac{1}{8\pi} \int d\mathbf{r} \left( \alpha^2 \left[ \frac{\partial \mathbf{A}}{\partial t} \right]^2 + [\nabla \times \mathbf{A}]^2 \right) \quad (1.18)$$

In this gauge, only the vector potential  $\mathbf{A}$  is quantized, corresponding to the transverse component of the electromagnetic field. Electrostatic interactions (described by the longitudinal component) are modeled by the  $\varphi$  potential, and are not quantized.

By expanding  $\mathbf{A}$  as a sum of plane waves in a box of volume  $V$  (called the quantization cavity),  $E_{EM}$  can be expressed as a sum of contributions from uncoupled harmonic oscillators, one for each cavity mode  $\mathbf{k}$ . These oscillators can be quantized as usual. We can therefore write the Hamiltonian for the free (transverse) field as:

$$\hat{H}_{EM} = \sum_{\mathbf{k}} \omega_{\mathbf{k}} \hat{a}_{\mathbf{k}}^\dagger \hat{a}_{\mathbf{k}} \quad (1.19)$$

Where  $\hat{a}_{\mathbf{k}}^\dagger$  and  $\hat{a}_{\mathbf{k}}$  are the photon creation and destruction operators for mode  $\mathbf{k}$ . The quantized  $\hat{\mathbf{A}}$  operator becomes:

$$\hat{\mathbf{A}}(\mathbf{r}, t) = \sqrt{\frac{\hbar}{2\epsilon_0 V \omega_{\mathbf{k}}}} \left[ \hat{a}_{\mathbf{k}} e^{-i\omega_{\mathbf{k}} t + i\mathbf{k} \cdot \mathbf{r}} + \hat{a}_{\mathbf{k}}^\dagger e^{i\omega_{\mathbf{k}} t - i\mathbf{k} \cdot \mathbf{r}} \right] \quad (1.20)$$

Under *minimal coupling*<sup>2</sup>, the Hamiltonian for a system of charged particles reads:

$$\hat{H} = \sum_{i=1}^N \frac{1}{2m_i} \left[ \nabla_{\mathbf{r}_i} + \alpha q_i \hat{\mathbf{A}}(\mathbf{r}_i) \right]^2 + \sum_{i=1}^N q_i \varphi(\mathbf{r}_i) + \sum_{\mathbf{k}} \omega_{\mathbf{k}} \hat{a}_{\mathbf{k}}^\dagger \hat{a}_{\mathbf{k}} \quad (1.21)$$

where the scalar potential  $\varphi$  is not quantized and takes the usual form:

$$\varphi(\mathbf{r}_i) = \sum_{j=1}^N \frac{q_j}{|\mathbf{r}_i - \mathbf{r}_j|} \quad (1.22)$$

The last term of Eq.1.21 is the free field Hamiltonian  $\hat{H}_{EM}$ . The second term corresponds to the electrostatic coulomb energy, while the first term contains a mix of the

---

<sup>2</sup>The term minimal coupling refers to a Lagrangian where the coupling terms involve only the charge distribution and not higher multipole moments. Together with the Euler-Lagrange Equations, it produces the Lorentz force law



particles kinetic energy and their couplings to the electromagnetic field. A unitary transformation [102, 103] allows us to rewrite it in a form where the coupling is explicit:

$$\hat{H} = \sum_{i=1}^N \frac{1}{2m_i} \nabla_{\mathbf{r}_i}^2 + \sum_{i=1}^N q_i \varphi(\mathbf{r}_i) + \sum_{\mathbf{k}} \omega_k \hat{a}_{\mathbf{k}}^\dagger \hat{a}_{\mathbf{k}} + \sum_i \mathbf{P}(\mathbf{r}_i) \cdot \hat{\mathbf{E}}_T(\mathbf{r}_i) \quad (1.23)$$

where  $\hat{\mathbf{P}}(\mathbf{r}) = \sum_i q_i \hat{\mathbf{r}} \delta(\mathbf{r} - \mathbf{r}_i)$  is the polarization vector arising from the charges, and  $\hat{\mathbf{E}}_T$  is the transverse component of the electric field operator (derived from  $\hat{\mathbf{A}}$ ).

In the context of molecular physics, the coupling term  $\sum_i \hat{\mathbf{P}}(\mathbf{r}_i) \cdot \hat{\mathbf{E}}_T(\mathbf{r}_i)$  is approximated by expanding the polarization vector as a Taylor series, and taking into account the dipole term only. This is justified if the wavelength of the radiation is larger than the size of the molecular system. Such approximation is known as the dipole approximation, and the last term of Eq.1.23 becomes:

$$\hat{H}_{int} = \hat{\mathbf{D}} \cdot \hat{\mathbf{E}}_T(0) \quad (1.24)$$

where the dipole operator  $\hat{\mathbf{D}}$  is the first term in the multipole expansion of the polarization.

In the context of light-induced molecular transitions, we can now use the dipole approximation to calculate the transition rate between molecular eigenstates. Let  $\langle g_k | = \langle \varphi_g \Phi_{gk} |$  and  $\langle f_l | = \langle \varphi_f \Phi_{fl} |$  be two eigenstates of the molecular Hamiltonian, where we used the Born-Oppenheimer approximation to write them as product states of their electronic ( $\varphi$ ) and nuclear ( $\Phi$ ) wavefunctions.  $g$  and  $f$  label the electronic state, while  $k$  and  $l$  label the vibronic eigenstates for each of the electronic configurations.

Using Fermi's golden rule, we have that the transition probability is proportional to:

$$p \propto |\langle g_k | \hat{H}_{int} | f_l \rangle|^2 = |\langle \varphi_g \Phi_{gk} | \hat{H}_{int} | \varphi_f \Phi_{fl} \rangle|^2 \quad (1.25)$$

By dividing the dipole operator  $\hat{\mathbf{D}} = \hat{\mathbf{D}}_n + \hat{\mathbf{D}}_{el}$  in its nuclear and electronic contributions, we can rewrite Eq.1.25 as: (note that  $\hat{\mathbf{E}}_T(0)$  is constant and can be factored out):

$$p \propto |\langle \varphi_g \Phi_{gk} | \hat{\mathbf{D}}_n + \hat{\mathbf{D}}_{el} | \varphi_f \Phi_{fl} \rangle|^2 = |\langle \Phi_{gk} | \hat{\mathbf{D}}_n | \Phi_{fl} \rangle \langle \varphi_g | \varphi_f \rangle + \langle \Phi_{gk} | \Phi_{fl} \rangle \langle \varphi_g | \hat{\mathbf{D}}_{el} | \varphi_f \rangle|^2 \quad (1.26)$$

The first term vanishes due to the orthonormality of the electronic wavefunctions. In the second term, we have assumed that the electronic dipole term  $\langle \varphi_g | \hat{\mathbf{D}}_{el} | \varphi_f \rangle$  does not depend on the nuclear coordinates and can be factored out (in the BOA, the electronic wavefunctions do have a parametric dependence on the nuclear coordinates). This is known as the Condon approximation.

Equation 1.26 tell us that for transitions between two different electronic levels, the vibronic component of the state is excited according to the factors  $\mathcal{F}_{kl}^{gf} = \langle \Phi_{gk} | \Phi_{fl} \rangle$  (known as the Frank-Condon factors) between the vibronic levels.

That is: the vibronic state  $|\nu\rangle$  resulting from a molecular transition is constructed by projecting the initial state  $|\Phi_{gk}\rangle$  on the space spanned by the set of final state eigenfunctions (Eq.1.27). Figure 1.13 shows a sketch of this process, where the ground state wavepacket is excited 'vertically' onto the PES defined by the final electronic state.

$$|\nu\rangle = \sum_l |\Phi_{fl}\rangle \langle \Phi_{fl} | \Phi_{gk}\rangle = \sum_l |\Phi_{fl}\rangle \mathcal{F}_{kl}^{gf} \quad (1.27)$$

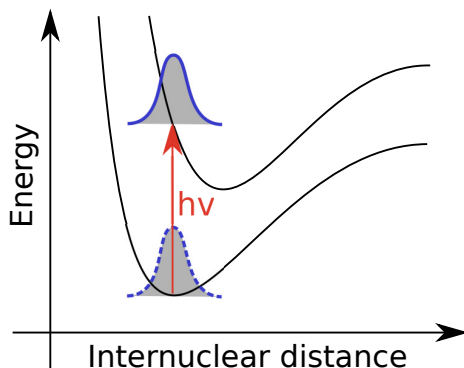


**Figure 1.13:** Diagram of a molecular transition between two different electronic states. The nuclear component of the wavefunction (depicted as a nuclear wavepacket) is ‘vertically’ excited to the final state PES. The nuclear dynamics that follows photoexcitation depends on the initial state wavepacket and on the shape of the final state PES.

The Dipole and Condon approximation presented above are particularly useful in the context of infrared and optical transitions, where the photon wavelength is significantly longer than the size of the atoms. Representations such as Fig. 1.13 provide a powerful intuitive tool for modeling such transitions.

In a classical picture, transitions between two electronic levels are allowed only if the nuclear position and momentum are conserved. In Fig. 1.13, the transition from the ground state leads to the inner turning point of the excited state; that is, the nuclear wavefunction (and therefore its position and momentum) is unchanged during the electronic transition.

### 1.3.2 X-ray Spectroscopy

The x-ray band of the electromagnetic spectrum is usually considered to cover photon energies ranging from  $\sim 100$  eV to  $\sim 100$  KeV. Such a broad energy range corresponds to a broad spectrum of phenomena. This section will focus on some of the effects that soft x-ray (energies up to  $\sim 1$  KeV) induce in atoms and molecules.

The interaction of soft x-ray photons with molecules produce remarkably different effects from the phenomena induced by optical and UV radiation. The higher energy of the photons allow interactions with atomic core orbitals, making soft x-rays an ideal probe to study localized changes in molecular structures.

The short wavelengths of x-ray radiation are only slightly larger than the interatomic distances in molecules, and the dipole approximation introduced in subsection 1.3.1 is not longer fully justified.

In the mathematical description, we do not transform Eq. 1.21 in the multipolar form given in Eq. 1.23. For the phenomena introduced in this section, only the  $\mathbf{p} \cdot \mathbf{A}$  component in the expansion of the first term in equation Eq. 1.21 is considered as part of the interaction Hamiltonian  $\hat{H}_{int}$ . The remaining  $\mathbf{A}^2$  term describes one-photon scattering processes, and is therefore ignored in the context of absorption spectroscopy. For a formal derivation of the theoretical framework used to describe such interactions, see [104].

In Near Edge X-ray Absorption Fine Structure (NEXAFS) spectroscopy, the overall absorption of the probe is measured as a function of x-ray wavelength, producing a spectrum. Fig 1.14 shows an example for *OCS* at the sulfur L-edge (that is, for photon energies in the region of the sulfur  $2p$  binding energy) [105].

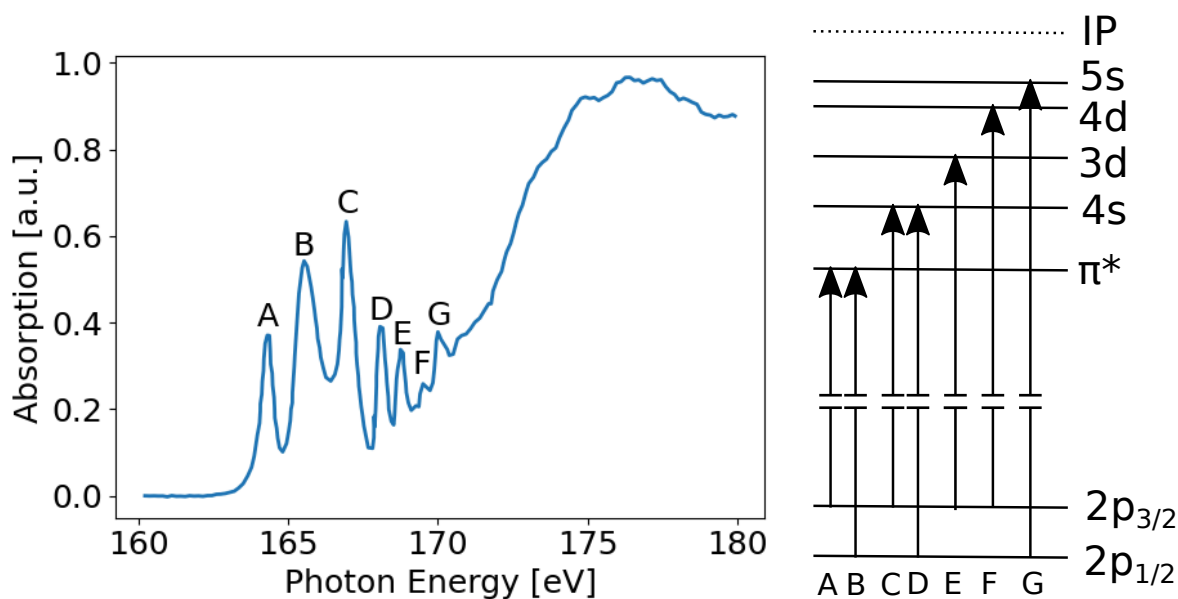


**Figure 1.14:** Left: NEXAFS spectrum of *OCS* at the sulfur l-edge. The  $2p$  edge at  $171\text{eV}$  is preceded by pre-edge resonance peaks, due to the absorption of light to unoccupied valance orbitals. Right: energy diagram highlighting the transitions responsible for the NEXAFS resonances. Data source: [105].

Broad absorption is seen for energies above the photoionization threshold of  $\sim 171\text{ eV}$ , where the molecule is left in a cationic state corresponding to a vacancy in the  $2p$  core orbital. Pre-edge features appearing at around  $\sim 164\text{ eV}$  are also visible. These peaks correspond to excitation of a  $2p$  core electron to one of the unoccupied valance orbitals, and are therefore not caused by photoionization. Their relative intensities are dictated by the difference in their corresponding excitation matrix element  $\int \Psi^*(\mathbf{r})\hat{H}_{int}\Psi(\mathbf{r})\text{d}\mathbf{r}$ , where  $\Psi^*$  and  $\Psi$  are the final (excited) and initial wavefunctions respectively. The lifetime of the core-hole state left behind after the excitation determines the observed linewidth, according to the well-known time-energy uncertainty relation. The  $\sim 1\text{ eV}$  spin-orbit

splitting of the  $2p$  orbital is visible between lines  $A - B$  and  $C - D$ .

In the context of molecular dynamics, this technique can be used to probe the electronic configuration of a molecule. The appearance/disappearance of a particular absorption line can be used to infer the lack/presence of an electron in the corresponding valence orbital [58].

The paper attached in section 3.2 shows NEXAFS spectra for 2TU at both sulfur L-edges. Pre-edge features are not resolved, due to the the broad bandwidth of the x-ray radiation used to excite the sample.

Since x-ray radiation has sufficient energy to ionize the molecule from one of its atoms core orbitals, so-called core-hole vacancies can be created. The resulting electron is ejected with a kinetic energy corresponding to the difference between the photon's energy and the orbital binding energy, so that  $E_{kin} = h\nu - \text{B.E.}$  as in the photoelectric effect. An electron spectrometer can be used to measure the kinetic energy of such ejected electrons and obtain information on the state of the molecule.

First order perturbation theory can be used to estimate the transition rate of the photoionization process. According to Fermi's golden rule, we have:

$$\Gamma_{FI} = 2\pi\delta(E_F - E_I)|\langle F|\hat{H}_{int}|I\rangle|^2 \quad (1.28)$$

Where,  $F$  and  $I$  are the initial and final states for the atom-electric field system,  $E_F$  and  $E_I$  their energies.

Since different atomic species have vastly different binding energies for their core electrons, this technique offers element specific sensitivity when applied to molecules. *E.g.*, Figure 1.15 shows the photoelectron spectrum of 2TU, where the emission lines from multiple elements are visible. For sulfur  $2p$  electrons two peaks are visible, as their binding energy is modulated by spin-orbit coupling, splitting the emission in two separate lines [40].

Moreover, the chemical environment of atoms (neighboring atoms and chemical bonds) influences electron binding energies, and therefore electron spectroscopy will also give site selective information: *e.g.* it will be able to distinguish two different carbon atoms in a molecule, based on the different bonds they form with the rest of the molecule. For this reason, this technique is known as Electron Spectroscopy for Chemical Analysis (ESCA) [49], as it relies on the observation of the so-called chemical shifts to obtain structural information on molecules. The most emblematic example of this phenomenon is given by ethyl trifluoroacetate, where the  $1s$  binding energies for the four carbon atoms show a spread over 8 eV [106, 107].

For the case of 2TU, Fig. 1.15 shows how carbon  $1s$  emission is affected by the chemical environment. The lowest binding energy of 290.8 eV is found for  $C_5$  (we refer to Fig. 1.7 b) for atom numbering ), as this carbon is entirely bound to other carbon atoms. Carbons 4 and 2 have a significantly higher binding energy (294.1 eV), due to

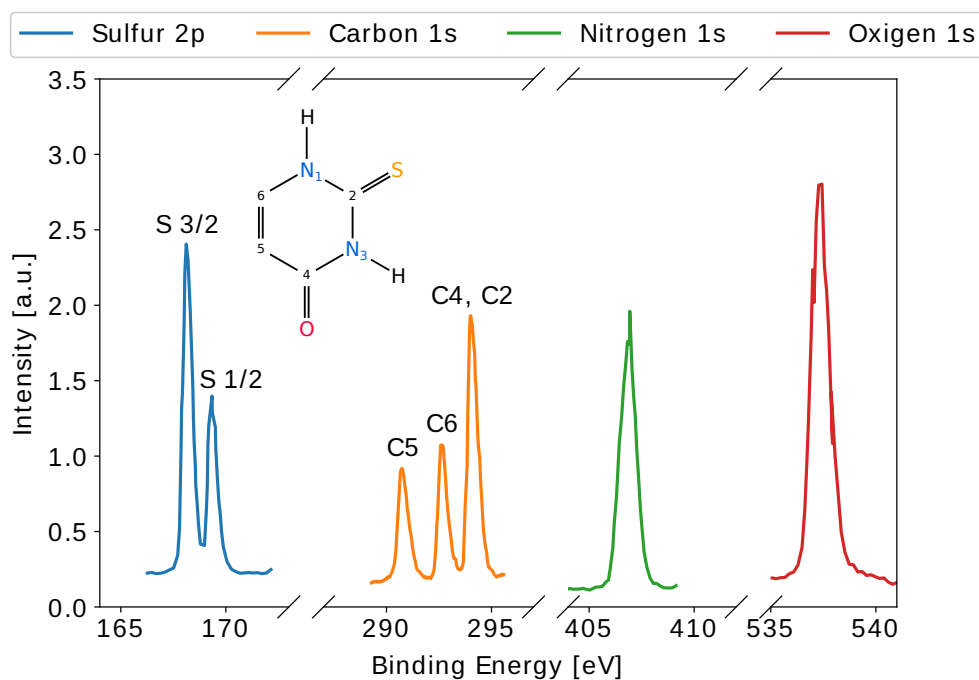


**Figure 1.15:** X-ray photoelectron spectrum of 2TU. Peaks from  $O\ 1s$ ,  $C\ 1s$ ,  $N\ 1s$  and  $S\ 2p$  are visible, with each element characterized by a specific binding energy. In the case of sulfur, two lines are visible, corresponding to the spin-orbit split components of the  $2p_{1/2}$  and  $2p_{3/2}$  states. For carbon, different peaks originating from different carbon atoms in the molecule are identified, showing how the chemical environment affects the binding energy of the  $1s$  orbital. Inset: 2TU structure. Data source: [40].

being bound to the more electronegative oxygen and nitrogen, leading to a shift of the electronic density away from the carbon. The chemical environment of  $C_6$  is in between this two cases, as reflected by its binding energy of  $292.7\ eV$ .

The spin-orbit splitting of the sulfur  $2p$  orbital is also visible in the XPS spectrum, as highlighted by the two peaks at  $168.2\ eV$  and  $169.4\ eV$ . As for the case of NEXAFS spectroscopy, the lifetime of the core-hole state generating the photoelectrons influences the linewidth in the observed spectrum.

The sensitivity of X-ray Photoelectron Spectroscopy (XPS) to the chemical environment of an atom makes it a prime tool for probing changes in the electronic and nuclear configurations of molecules, as the electron binding energy will be directly influenced by such changes. XPS is therefore well suited for the study of ultrafast phenomena, such as the ultrafast dynamics of nucleobases discussed in subsection 1.2.3 [57].

Accompanying the main emission line of a certain core orbital, another ‘satellite’ emis-

sion line can in some cases be observed at lower kinetic energies [108–110]. Since the valence configuration of the neutral atom is not necessarily maintained in the ion, one of the valence electrons might be promoted to an unoccupied orbital during the photoionization process, if one thinks about this in an orbital picture. This additional excitation removes some of the energy available to the ejected electron, lowering its kinetic energy [111]. The relative intensities of main and satellite photolines depend on the overlap between the valence and cationic state wavefunctions. Since the two states have different number of electrons, the overlap calculation takes the form of a Dyson orbital [112].

Fig 1.16 shows the sulfur  $2p$  photoline (spin-orbit splitting is not resolved) with the adjacent electron correlation satellite. With a photon energy of  $272\text{ eV}$ , we observe a peak in the electron signal corresponding to a kinetic energy of  $102.6\text{ eV}$ , preceded with a satellite peak at  $96.4\text{ eV}$ .

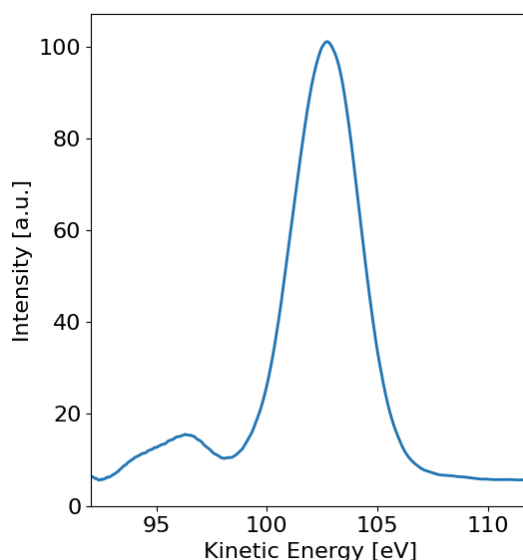


**Figure 1.16:** Sulfur  $2p$  photoline and satellite for 2TU, measured in the URSA-PQ spectrometer. Satellite photoemission is seen with a lower kinetic energy than the main photoline, due to the energy lost to the shake-up process in the valence orbitals.

In order to construct intuitive models for the satellite lines, two approaches are possible: the so-called single and multielectron pictures (see Fig. 1.17). In the single electron picture, a simple ladder of energy levels is used to represent the molecular orbitals, with electrons filling the available levels.

In the multielectron picture, a full set of energy eigenstates is calculated for every nuclear configuration. In the context of the BOA, this process can be repeated for different positions of the atomic nuclei, and PES for the nuclear motion can be built for every electronic eigenstate. This allows for predictions that take the nuclear geometry into

account, and that can be used to follow dynamical processes in the molecule.

Figure 1.17 compares the two models in the case of photoionization, exemplifying the processes underlying the emission of both the main and satellite photolines.

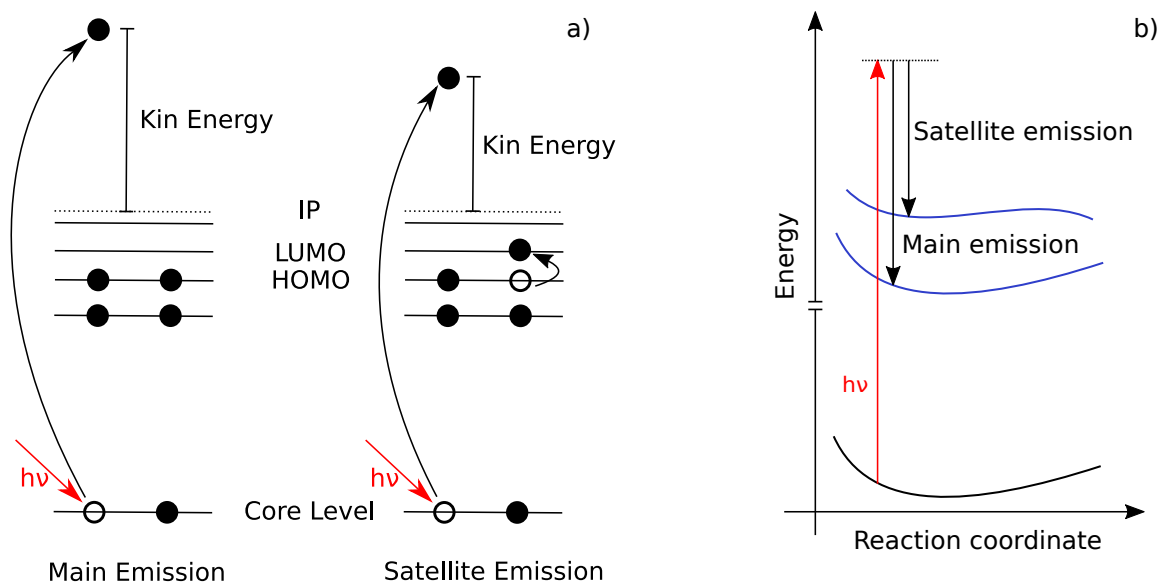


**Figure 1.17:** a) Photoionization in the single electron picture. The photon ejects an electron from a core level and the excess energy is released as kinetic energy. In the case of satellite emission, another valence electron is promoted in the process. b) Photoionization in the multielectron picture. PES for ground state (black) and core-ionized states (blue) vs nuclear geometry. The main and satellite emission energies can be calculated as the difference between the photon energy and the different core excited states.

### 1.3.3 Auger spectroscopy

Following photoionization, the atom is left with one of the core orbitals unoccupied. Such states are unstable, and in most cases the atom undergoes a de-excitation cascade that leaves it in a dicationic state, with two electrons missing from its valence orbitals. Electrons decay from higher laying states into the hole left by the missing core electron, releasing energy that is used to eject another electron from the valence shells. The kinetic energy of the outgoing electron is therefore given as  $K_e = \Delta_E - B.E.$ , where  $\Delta_E$  is the energy gap of the decay and  $B.E.$  is the binding energy of the ejected electron.

This class of phenomena is known as Auger decay (first observed independently by Pierre Auger and Lisa Meitner [113–115]) when the transition happens between levels with different main quantum number *e.g.*  $3d \rightarrow 2p$ , and Coster–Kronig decays [116] for transition between levels with the same main quantum number *e.g.*  $2p \rightarrow 2s$ .

The transition rate for such decays can be derived considering the Coulomb interaction between the electrons [117, 118]. To first order, the matrix element reads:

$$\Gamma = \frac{2\pi}{\hbar} \int d^3\mathbf{k} |\langle \Psi_{\mathbf{k}} | \sum_{i \neq j} \frac{e^2}{r_{ij}} | \Phi \rangle|^2 \quad (1.29)$$

Where  $|\Phi\rangle$  is the initial core-hole state, and  $|\Psi_{\mathbf{k}}\rangle$  is the final state with a new electronic configuration and an outgoing Auger electron of momentum  $\mathbf{k}$ .

Since Coster-Kronig involves a decay between states with large wave function overlap, it is generally much faster than Auger, a fact that is reflected in the much broader spectral bandwidth of Coster-Kronig decay. Fig 1.19 sketches these type of decays in the single electron picture.

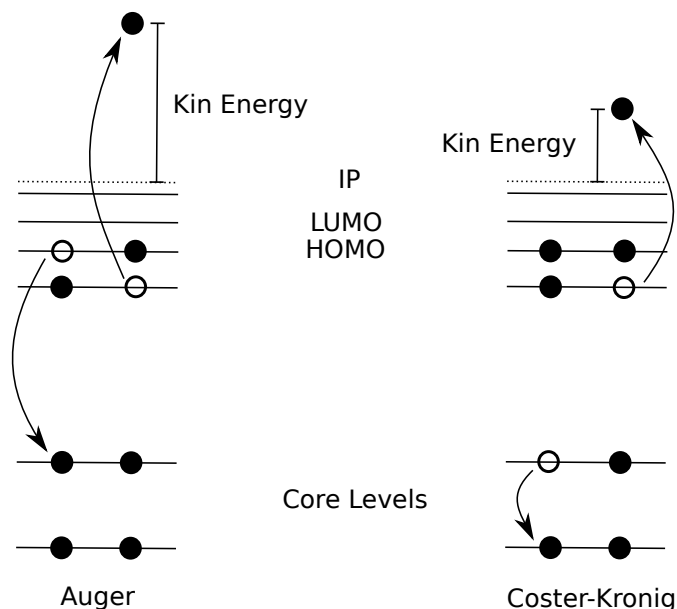


**Figure 1.18:** Comparison between Auger and Coster-Kronig decays in the single electron picture. Auger processes involve a valence electron decaying to fill a core hole. For the Coster-Kronig case, the decay happens between core levels with the same main quantum number.

In the multielectron picture, we can model the Auger kinetic energy as the gap between core-hole and dicationic states. For the case of sulfur in 2TU, the lowest dicationic state has a binding energy of about 24 eV, as shown in Fig.1.19 left. In combination with the aforementioned 168 eV binding energy for the 2p we expect the highest Auger feature to have a kinetic energy of circa 144 eV. More energetic dicationic states (not shown in Fig.1.19), contribute to the overall Auger emission in the lower kinetic energy part.

Fig.1.19 right shows the measured sulfur Auger spectrum in 2TU, spanning the energy range 110 – 145 eV. Such a broad spectrum is caused by the high density of dicationic



state that contribute to the overall emission. Such high density is to be expected in molecules with a relatively large number of atoms. As an example of this phenomenon we can point to the UV-induced fragmentation of thymine. The smaller fragments have a lower dicationic state density than the parent molecule, and as a consequence, the Auger spectrum becomes increasingly structured as the fragment separate [119].

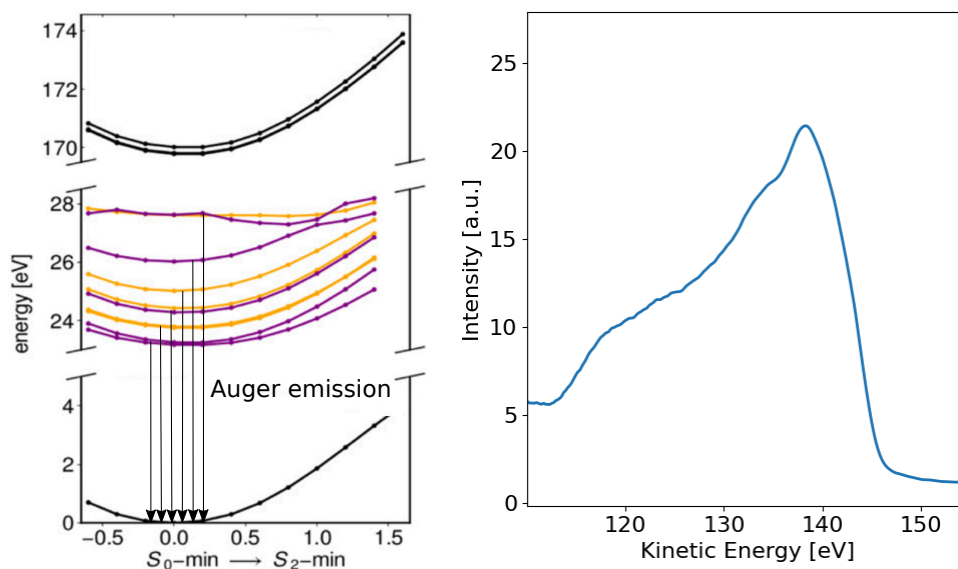


**Figure 1.19:** Left: Calculated potential energy surfaces for 2TU, along the  $S_1 \rightarrow S_2$  reaction coordinate, for neutral (bottom), core-ionized (top) and dicationic (middle) states. Only the 9 lowest laying dicationic states are shown. Image Source: David Picconi, private communication. Right: Measured Auger spectrum of 2TU.

## 1.4 UV pump/X-ray probe spectroscopy

In order to experimentally study ultrafast phenomena, a similarly ultrafast technique has to be used. Pump-probe spectroscopy is a powerful tool able to follow such dynamical phenomena. The Zewail group pioneered this technique with femtosecond studies on *ICN* [120–123], *NaI* [124–126] and *I<sub>2</sub>* [127], for a review of the topic, see [128].

Two short pulses are employed: a pump pulse excites the sample to the desired state, starting the process under scrutiny. After a controllable time delay  $\Delta T$ , during which the sample undergoes dynamical changes, a probe pulse is used to ‘read’ the new state of the system. By repeating the experiment with different delays between the two pulses, we can record the response of the sample to the probe pulse at all time delays. A ‘movie’ of the dynamics can then be constructed by interpreting the response to the probe pulse

together with other known properties of the sample.

The results presented in this thesis use a UV-pump, x-ray probe setup to follow the dynamics of 2-TU. Different x-ray probing methods are possible, such as transient absorption, photoemission, Auger decay, or photoions detection [55, 56, 58, 59, 129, 130]. Fig. 1.20 sketches the measurement scheme in the single electron picture. A ultrafast UV laser is used to excite the molecule to the  $S_2$  state, launching the molecular dynamics discussed in section 1.2.3. The molecule undergoes Internal Conversion (IC) and Inter System Crossing (ISC), changing its electronic configuration and nuclear geometry in the process.

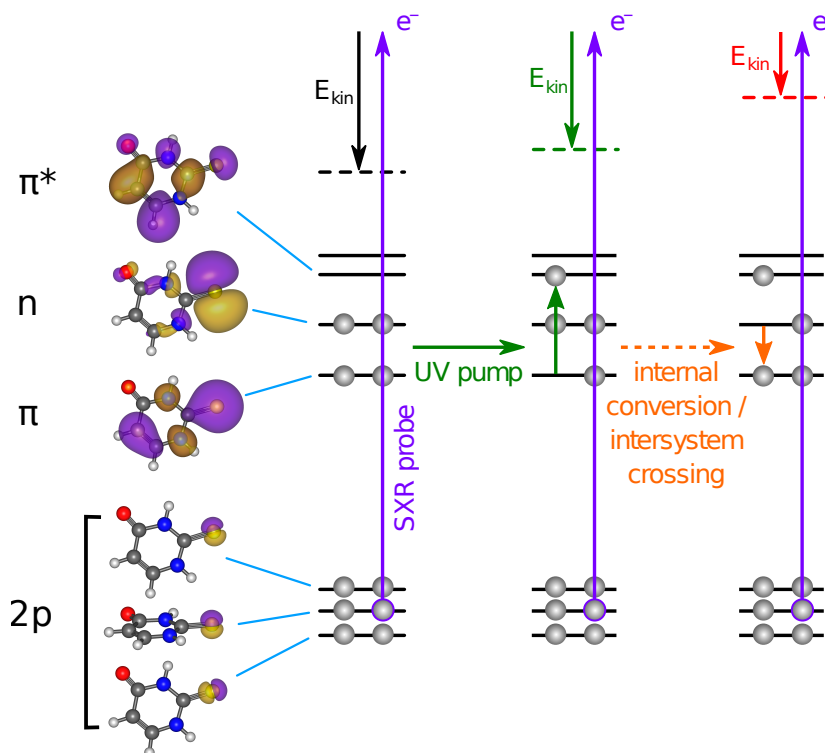


**Figure 1.20:** Single-electron picture of the pump-probe photoionization scheme for 2TU. Changes in the valence structure affect the ionization energy (dashed lines), allowing core-level photoelectron spectroscopy to probe the ultrafast relaxation dynamics. Image Source: David Picconi, private communication.

A soft x-ray (SXR) pulse from a Free Electron Laser (FEL) is used to probe the system via photoemission. The electrons emitted by the molecule after the SXR excitation are measured in a magnetic bottle time of flight spectrometer, in order to obtain information on their kinetic energy. By following changes in the electron spectrum as a function of UV-SXR delay, we are able to study the ultrafast relaxation discussed in subsection 1.2.3 from a novel point of view.

In analogy with the concept of chemical shift presented in section 1.3.2, we can model such changes with the introduction of an Excited State Chemical Shift (ESCS). The observation of a shift in the photoline energy can be used as a marker for the presence of an excited state. The paper attached in section 3.3 develops this concept and shows how the magnitude of the shift can be directly linked to the local charge present on the atom. This allows a computationally efficient interpretation of time-resolved XPS spectra as a way to image the charge transfer dynamics during ultrafast processes.

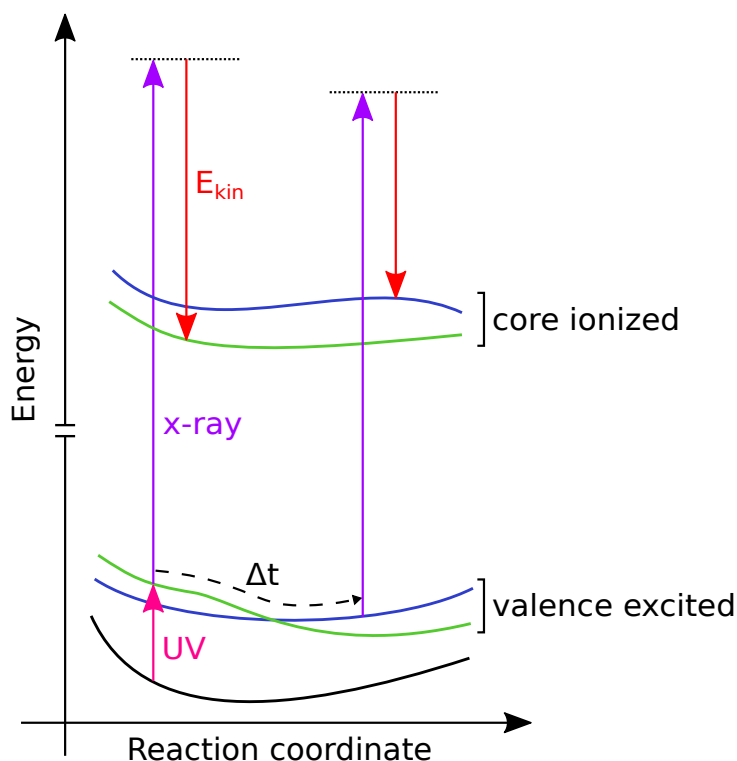


**Figure 1.21:** Photoelectron kinetic energy  $E_{kin}$  dependence on pump-probe delay  $\Delta t$ . The molecule is excited by the UV to a valence orbital, where it undergoes nuclear dynamics and IC/ISC. The x-ray probe pulse ionizes the molecule into a core-ionized state, with the excess energy released as kinetic energy of the photoelectron.

Both photo and Auger electrons are detected and studied, as they provide information on the process from two different point of views. The photoelectron spectrum shows a high dependence on the electronic dynamics, being particularly sensitive to changes in the local distribution of electronic charge. Fig 1.21 shows how the measured observable (electron kinetic energy) changes as the molecule undergoes electronic transitions in the multielectron picture.

Auger electrons are emitted due to the decay of the core-hole into a dicationic state. In general, such states display a repulsive character with a strong dependence of the binding

energy on the nuclear separation, according to coulomb repulsion:  $E \propto 1/r$ . This is due to the positive nucleic charges being exposed by the missing electrons, pushing the nuclei apart.

This feature makes Auger electrons particularly suited to study changes in the geometric configuration, as their kinetic energy directly depends on the dicationic state potentials. Intuitively, a bond length increase leads to a decrease in the amount of potential energy stored in the bond. This energy is made available to the outgoing electron once the molecule transitions from the core-hole to the dicationic state.

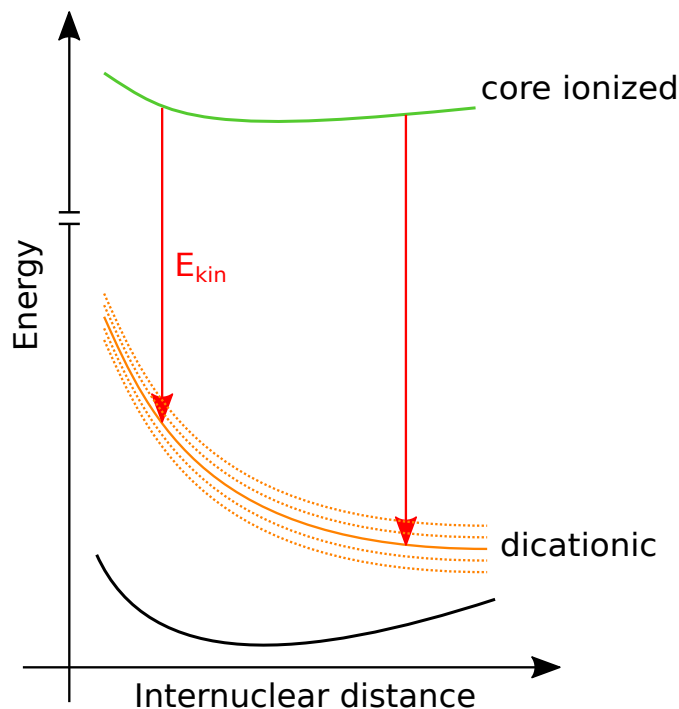


**Figure 1.22:** Auger electron kinetic energy as a function of nuclear internuclear distance. Auger electron kinetic energy corresponds to the energy gap between the core-ionized state in the dicationic manifold. The repulsive character of dicationic states on internuclear distance makes Auger electrons particularly well-suited for following geometrical changes in an ultrafast reaction.

For the case of 2TU, changes in the  $C - S$  bond length are followed as the molecule relaxes after UV excitation (see the paper in section 3.4). Since the Auger decays happens on much faster timescales than the nuclear dynamics, we can use Auger electrons to capture snapshots of the geometric changes throughout the relaxation process. After the UV pulse, the nuclear wavepacket travels along the valence excited PESs, and the subsequent x-ray induced Auger decay probes the system in different geometric configurations.

# Chapter 2

## Experimental Setup

This chapter provides an introduction to the experimental techniques used to obtain the data on which the papers of chapter 3 are based. Section 2.1 introduces the principles of operations of Free Electron Lasers, with a particular focus on the FLASH FEL. Section 2.2 provides an overview of some of the features of the URSA-PQ measurement apparatus.

### 2.1 Free Electron Laser

Free Electron Lasers (FEL) are sources of high-brilliance, ultrashort x-ray pulses. Initially used in the IR domain, they have been developed for x-ray generation in the early 2000s, with the first user facilities becoming available in the late 2000s [131, 132]. They improve on previous synchrotron sources by coherently amplifying radiation through spontaneous emission, not unlike the amplification process of an optical laser. The high brilliance<sup>1</sup> that can be obtained in this way makes FELs the ideal light source for probing gas phase targets. This section will provide a basic overview of FELs functioning principles, focusing on the specific case of the FLASH (Free electron LASer in Hamburg) FEL.

#### 2.1.1 Principles of FEL operation

A Free Electron Laser consists in a electron source, an electron accelerator and a undulator. Figure 2.1 shows a typical FEL layout. An ultrashort optical laser pulse hits a metal target, extracting an electron bunch via the photoelectric effect. These electrons are then accelerated through the use of RF (Radio Frequency) cavities, where an oscillating electric field is synchronized to the passage of the electrons in order to increase their kinetic energy. As a last step, the electrons fly through an undulator. This is a linear arrangement of magnets with consecutively alternating polarity. The undulator magnetic field causes oscillations in the electrons trajectory. These accelerated trajectories cause the emission of radiation, through the same mechanism underlying *bremsstrahlung* [131, 133]. After the

---

<sup>1</sup>The *Brilliance*  $b = N/(t \cdot d \cdot A \cdot \Delta E)$  is a measure of an x-ray source quality. It takes into account the number of generated photons  $N$  per unit of time  $t$ , angular divergence  $d$ , beam cross-section  $A$  and spectral range  $\Delta E$ .

undulator, the electron bunch is dumped and the generated x-ray radiation is delivered to the experimental station.

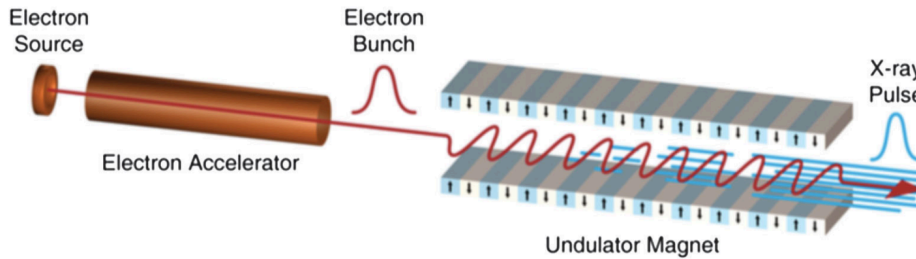


**Figure 2.1:** Example of a Free Electron Laser (FEL) layout. The red line highlights the path of the electrons through the apparatus. In the undulator, coherent buildup of x-ray radiation occurs, depicted as blue lines. Image used with permission from [133].

At first glance, it might appear that there is not much difference between a synchrotron source and a FEL. After all, in both cases the radiation is generated by the *bremsstrahlung* of relativistic electrons traveling through oscillating magnetic fields. However, making this analogy would be akin to claiming that there is not much difference between a light emitting diode (LED) and a diode laser. Synchrotrons produce incoherent radiation that scales linearly<sup>2</sup> with respect to the number of electrons per bunch  $N_e$ . In contrast, FELs are able to create pulses of coherent radiation through amplified spontaneous emission, with a brilliance scaling (in ideal conditions) as  $N_e^2$ .

This is due to the ability of FELs to induce Self Amplified Spontaneous Emission, or *SASE*, by exploiting the so-called electron microbunching instability of the electrons-radiation-undulator system [134]. The initial process is similar to a synchrotron: incoherent radiation is produced from the motion of the electrons in the undulator. The electric field of this radiation is parallel to the transverse velocity of the oscillating electrons. Depending on the position within the bunch, the undulations of the electrons will be in phase (red shaded regions of Fig. 2.2) or out of phase (blue shaded regions of Fig. 2.2) with the electric field of the emitted radiation. Therefore, the interaction of the electrons with their own emitted field produces modulations in the electron energy across the bunch, on the scale of the radiation wavelength  $\lambda_r$ . The electrons oscillating in phase gain energy, conversely, the ones oscillating out of phase lose energy.

<sup>2</sup>In second-generation synchrotron sources, the intensity scales linearly in both electron number and undulator length. Third-generation synchrotron sources allow for quadratic scaling with respect to undulator length, with each electron in the bunch emitting in phase with respect to its own field

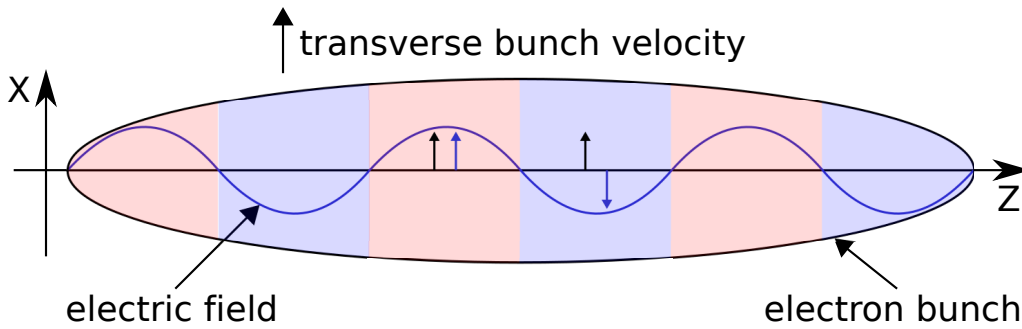


**Figure 2.2:** Interaction between the electron bunch and the generated electric field. The  $Z$  axis is the undulator longitudinal direction, along which the electron bunch travels. The oscillation induced by the undulator occurs in the transverse  $X$  axis. Depending on the position within the bunch, the transverse oscillation of the electrons will be in phase (red shaded region) or out of phase (blue shaded region) with the electric field. This introduces energy modulations within the bunch, with electrons in the red region gaining energy and electron in blue regions losing energy.

As shown in Fig 2.3, electrons with different energy travel along different paths in the undulator, due to the different bending radius: higher energy electrons have shorter paths. The path length difference produces bunching of the electron on the scale  $\lambda_r$ , with the electrons moving towards the nodes of the electric field, which are stable with respect to the energy modulation.

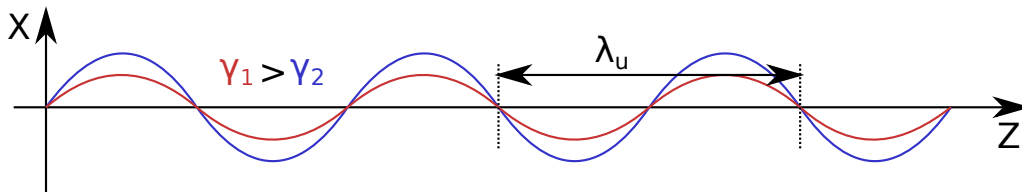


**Figure 2.3:** Trajectory of electrons in a undulator, oscillating around the propagation direction with a wavelength equal to the step of the undulator magnets,  $\lambda_u$ . More energetic electrons (represented by a higher relativistic  $\gamma$  factor) have a smaller bending radius and therefore travel a shorter path in the undulator, moving them forward in the bunch with respect to less energetic electrons.

Since electrons clustered within a wavelength  $\lambda_r$  emit in phase, the bunching leads to more intensity, producing more modulation and more bunching. This produces an exponential increase in the intensity of the emitted radiation: the phenomenon known as SASE [133]. Figure 2.4 shows the exponential increase in radiation power as the electrons travel through the undulator, as well as the increase in electron bunching.

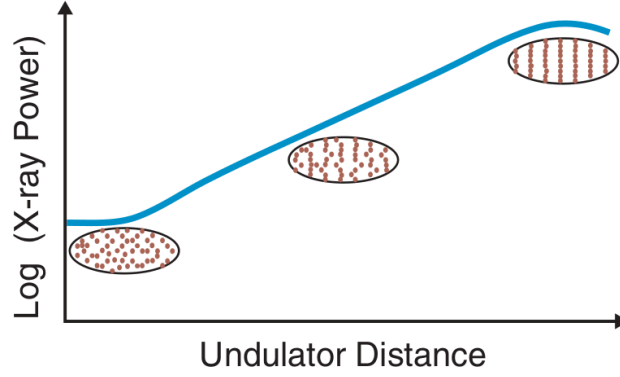


**Figure 2.4:** Exponential growth of the radiation power along the undulator length. The electron bunch structure is shown, with electron microbunching increasing as the beam propagates in the undulator. Image used with permission from [135].

In order for SASE to be possible, the system has to satisfy several conditions on the undulator length and electron beam quality [136] that make the use of linear accelerators (as opposed to storage rings) a necessity.

The wavelength of the SASE radiation depends on the accelerator/undulator parameters as follows:

$$\lambda_r = \frac{\lambda_u}{2\gamma^2} \left( 1 + \frac{K^2}{2} \right); \quad K = \frac{eB_0\lambda_u}{2\pi m_e c} \quad (2.1)$$

The dimensionless  $K$  parameter is known as *undulator strength*, where  $\lambda_u$  is the step of the undulator magnets and  $B_0$  is the applied magnetic fields.  $\lambda_u$  is usually a few *cm* and the field  $B_0$  as large as 1 *T*, so that  $K \sim 1$ .

Notice that  $\lambda_r$  is scaled by a factor of  $\frac{1}{\gamma^2}$  with respect to  $\lambda_u$ , where  $\gamma = \left[ 1 - \frac{v^2}{c^2} \right]^{-\frac{1}{2}}$  is the relativistic gamma factor. From the point of view of the electrons, the spacing of the undulator magnets appears length contracted by a factor of  $\gamma$ ; furthermore, the radiation emitted in the electron bunch frame is Doppler shifted by another  $\gamma$  factor to the lab frame, giving the overall  $\frac{1}{\gamma^2}$  scaling.

### 2.1.2 The FLASH FEL

The Free electron LAsEr in Hamburg, or FLASH, is one of the few user-accessible FELs in operation around the world. It began routine operations in 2005, and produces radiation covering the soft x-ray range, from  $\sim 20$  to  $\sim 300$  *eV* [137, 138]. Figure 2.5 shows the layout of the facility. The electron gun and linear accelerator are connected to two different sets of undulators, FLASH1 and FLASH2, so that two FELs can be operated simultaneously by the same electron accelerator [139].



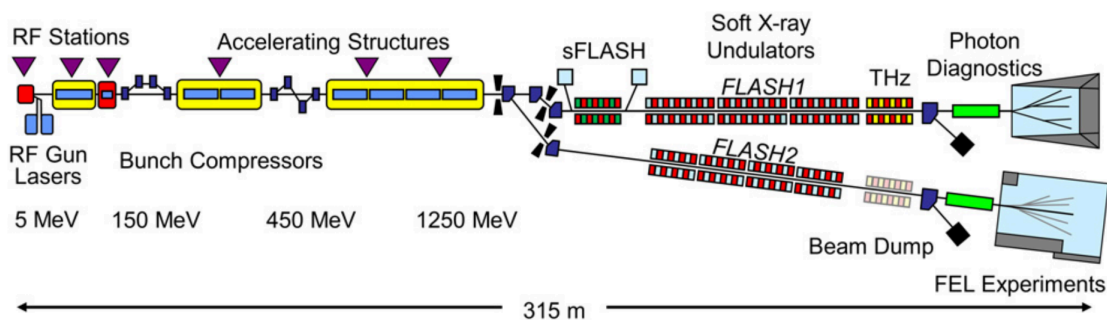


**Figure 2.5:** Layout of the FLASH facility at DESY in Hamburg, Germany. Two FELs, FLASH1 and FLASH2 are operated with the same electron accelerator. Two distinct lasers are used to produce the electron bunches for the two FELs. The electrons are then accelerated in stages; bunch compressors are used between each stage to pack together electron with different kinetic energies and reduce the temporal length of the packet. The electrons are routed to either FLASH1 or FLASH2, where the undulators generate the x-ray radiation. The electrons are then dumped, while the x-ray are delivered to users in one of the ends stations. Photon diagnostic station are inserted along the photon beam-line, to provide information on the status and quality of the generated radiation. Image used under Creative Commons License from [139].

The FLASH1 FEL was the first to become operational, with FLASH2 being built later on as an expansion. FLASH1 uses fixed gap undulator, meaning that the distance between the two opposing sets of magnets is constant. In this case, the  $K$  parameter of the undulator is fixed, and the photon energy is controlled by changing the electron kinetic energy and therefore the relativistic  $\gamma$  factor in Eq 2.1.

In the case of FLASH2, variable gap undulators are used. Actuators control the distance between the two sets of magnets, changing the magnetic field strength  $B_0$  and therefore the  $K$  parameter. This allows FLASH2 to tune the photon energy without requiring changes to the electron accelerator, allowing the two FELs to operate independently. Figure 2.6 shows the relationship between wavelength and undulator gap for different electron energies.

The electron accelerator delivers trains of electron bunches with a repetition rate of 10  $Hz$ . Each train consists of multiple bunches, with a spacing that can be varied between 5 – 25  $\mu s$ . Figure 2.7 shows the bunch pattern generated by the accelerator, delivering electron bunches to both FLASH1 and FLASH2.

The data presented in this thesis has been obtained at FLASH2, with a 4.6  $nm$  wavelength and a 5  $\mu s$  bunch spacing. A total of 50 electron bunches per train were used, giving a total rate of 500 x-ray pulses per second.

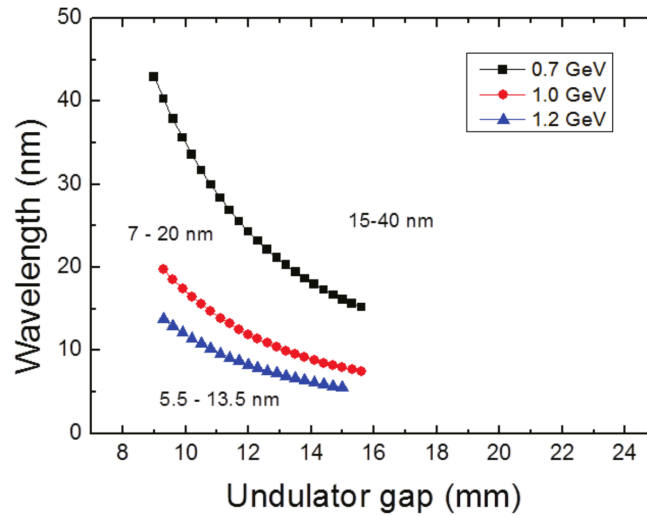


**Figure 2.6:** Photon wavelength vs undulator gap for FLASH2. Lower electron energies produce longer wavelengths. By varying the undulator gap, a wide range of wavelengths can be generated from a single accelerator setting. Image used with permission from [140].

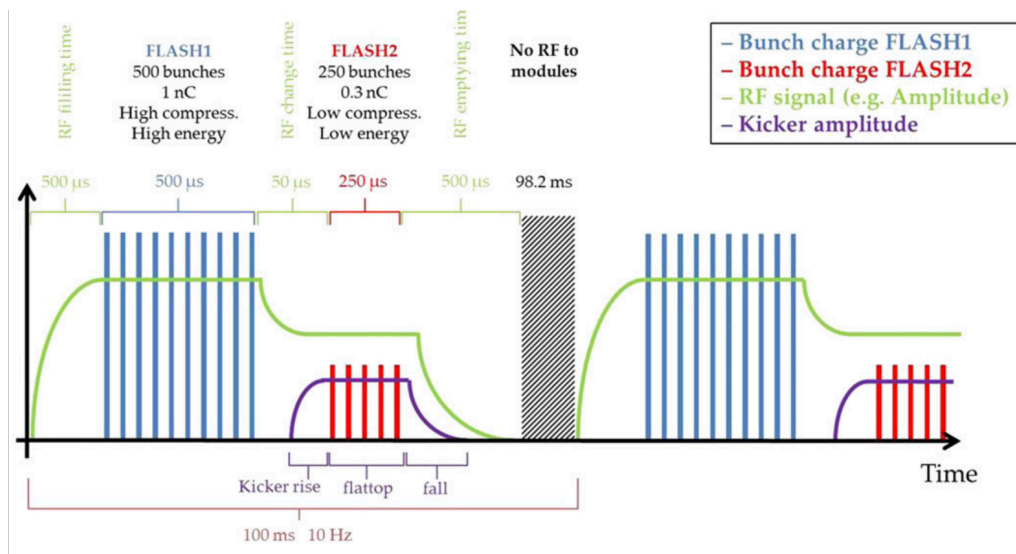


**Figure 2.7:** Bunch train structure at FLASH. A  $800 \mu\text{s}$  RF (radio frequency) pulse is available to accelerate electrons, repeating at  $10 \text{ Hz}$ . Within this window, both FLASH1 and FLASH2 bunch trains are generated, with a  $50 \mu\text{s}$  pause between them to allow for the switch in RF frequency. For each macropulse, up to 250 electron bunches can be injected in FLASH2. Image used under Creative Commons License from [139].

### 2.1.3 FLASH2 Beamlines and photon diagnostic

The FLASH2 experimental hall is subdivided in multiple beamlines, where the x-ray light can be routed to different experimental end stations. The layout is shown in Fig 2.8. Currently, beamlines FL22, FL24 and FL26 are operational, with the last two being available for user access [140].

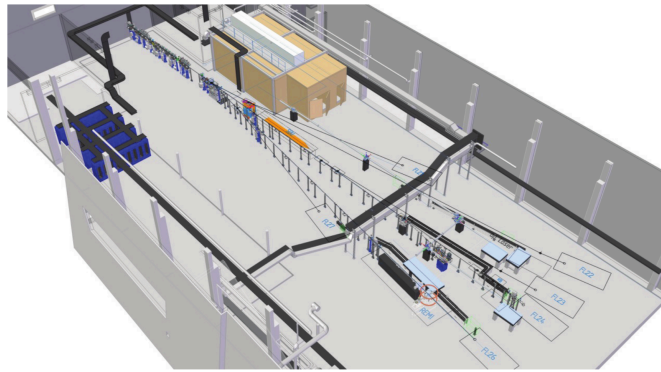


**Figure 2.8:** Layout for the planned beamlines at FLASH2. Currently only FL22, FL24 and FL26 are operational. Image used with permission from [140].

Before the beam reaches the experimental hall, a 20 m long gas attenuator is inserted in the beamline to allow fine control on the x-ray flux reaching the experiment [?, 141]. A differentially-pumped section of the beamline allows the insertion of controlled quantities of gas in the path of the photons, in order to attenuate the beam intensity by absorbing some of the radiation with the gas target. To cover the available range of wavelengths, different gas targets with different absorption cross sections are available:  $Xe$ ,  $N_2$ ,  $Kr$  and  $Ar$ . By controlling the pressure of the target gas, different attenuation levels can be obtained, allowing for fine-tuning of the photon flux reaching the experimental end station [141].

A non-invasive Online PhotoIonization Spectrometer (OPIS), shown in Fig 2.9, is also present, in order to measure the wavelength of the produced radiation [142, 143] without affecting the beam downstream of the spectrometer. A dilute reference gas target is inserted in the beamline, and the kinetic energy of the emitted photoelectron is measured, allowing for estimation of the photon energy.

A bunch arrival monitor is installed on the FLASH electron beamline, measuring the arrival time of each electron bunch [144, 145]. This data allows to estimate the arrival time of the x-ray pulse, and therefore to increase the resolution of pump-probe experiments that depend on the x-ray timing (see subsection 2.1.4 for a description of the synchronous laser system).

The results presented in this thesis have been obtained at the end station FL24, where focusing Kirkpatrick-Baez (KB) optics [146, 147] and an optical pump-probe laser are

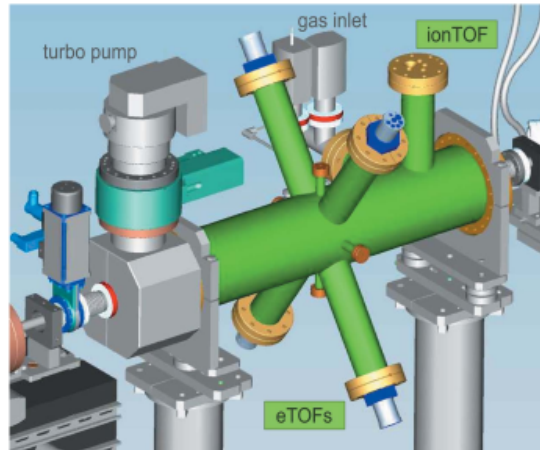


**Figure 2.9:** Schematics of the OPIS instrument. Four photoelectron spectrometers (eTOF) surround the beamline, where a dilute gas target is inserted in a differentially-pumped section. The four spectrometers measure the time of flight of emitted electrons. From this data, the horizontal and vertical location of the beam can be inferred, together with the electron kinetic energy. Image used under Creative Commons License from [142].

integrated in the beamline [148]. KB optics, shown in Fig 2.10, allow for controlled focusing of the x-ray beam, by utilizing two bendable mirrors in sequence, with each mirror focusing the light along one axis (horizontal and vertical). The focal length can be controlled by bending the mirrors, changing their curvature [149].

#### 2.1.4 Pump-probe optical laser at FL24

A ultrafast  $< 100$  fs infrared laser is present at FLASH2 [148], with a wavelength tunable in the range  $700 - 900$  nm. It is synchronized to the FEL with a timing jitter  $< 5$  fs, and a controllable delay stage allows for its usage in pump-probe experiments [151]. The laser is distributed to beamlines FL24 and FL26, where Modular Optical Delivery stations (MOD) can be set up for beam diagnostic and incoupling in the x-ray beamline.

For the data presented in this thesis, a triple harmonic generation setup was used to bring the wavelength from the IR into the UV range, at  $266$  nm, with a UV pulse duration of  $\sim 80$  fs. As showing in Fig 2.11, the UV pump light was coupled to the x-ray probe via a holey mirror.

After the THG (Third Harmonic Generation) setup, a motorized waveplate and polarizer combination was used to control the UV pulse energy reaching the sample. Figure 2.12 shows the measured relation between waveplate angle and pulse energy.

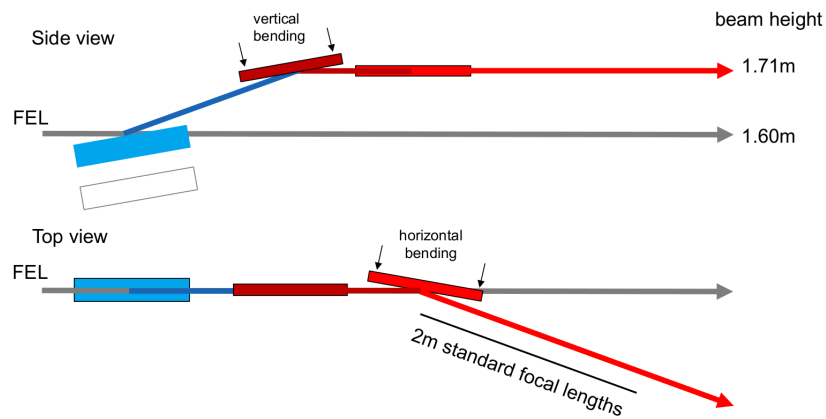


**Figure 2.10:** Schematics of Kirkpatrick-Baez (KB) focusing optics at beamline FL24. A pre-mirror (blue) deviates the beam upward before the KB mirrors, in order to keep the output beam horizontal. The two bendable mirrors (red) are used to adjust the focal length of the beam along the horizontal and vertical axes. Image used with permission from [150].

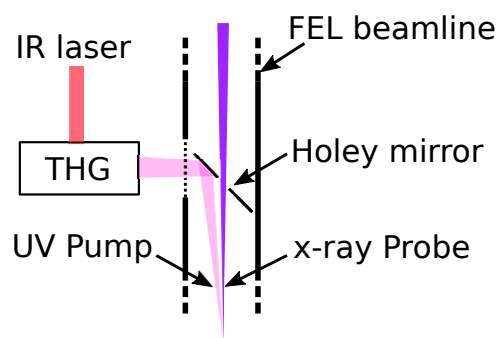


**Figure 2.11:** Generation of UV from IR laser and incoupling of the pump beam into the FL24 beamline. The UV pulse is generated from the IR laser in a THG setup is situated in the FL24 MOD. The UV beam is then incoupled in the vacuum beamline and spatially overlapped to the x-ray beam through a holey mirror.

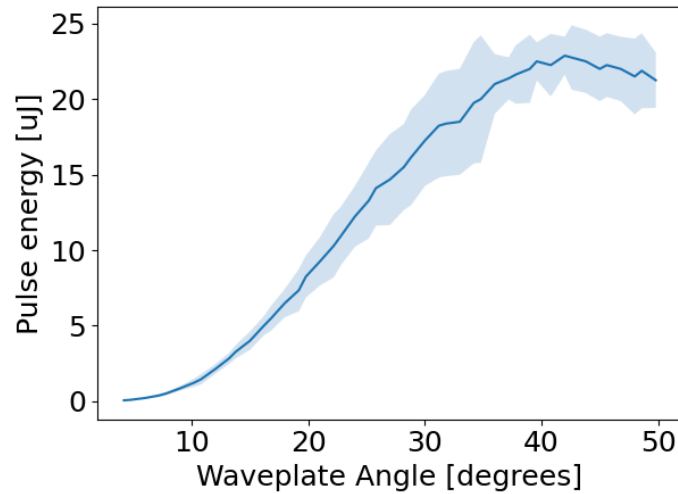


**Figure 2.12:** Relationship between waveplate angle and UV laser pulse energy, as measured at the focal point. Shaded area represents the shot-to-shot standard deviation.

## 2.2 URSA-PQ

The URSA-PQ (German for ‘Ultraschnelle Röntgenspektroskopie zur Abfrage der Photoenergiekonversion an Quantensystemen’, Engl. ‘ultrafast x-ray spectroscopy for probing photoenergy conversion in quantum systems’) chamber was developed in the Experimental Quantum Physics group at the University of Potsdam. It’s equipped with a magnetic bottle electron spectrometer (MBES) and a capillary oven for sample delivery.

The results on the ultrafast dynamics of 2TU contained in this thesis are based on data obtained with the URSA-PQ chamber in march 2019 at the beamline FL24 at FLASH2. This section will introduce the principles of operation of the various components and systems, in order to provide a foundation for the technical description of the apparatus given in the paper attached in section 3.1. Subsection 2.2.1 will give an overview of the chamber layout, while subsection 2.2.2 and 2.2.3 will describe the operation of the sample delivery oven and of the magnetic bottle spectrometer.

### 2.2.1 Vacuum apparatus

The experimental setup consists in a portable vacuum chamber that can be connected to the beamline, shown in Fig. 2.13. The sample is introduced from the top via a capillary oven [152], and exits the capillary as a gas jet a few *mm* above the interaction region. The oven is mounted on a three-axis motorized manipulator, in order to allow fine tuning of the oven positioning. A diagnostic paddle with a ultrafast diode and a YAG screen is mounted over the oven and can be inserted in the interaction region using the manipulator.

The generated photoelectrons are detected in a Magnetic Bottle Electron Spectrometer (MBES) [153] via a Multi Channel Plate (MCP) detector. The spectrometer is oriented horizontally, at  $90^\circ$  from both the sample delivery oven and the incoming x-ray beam.

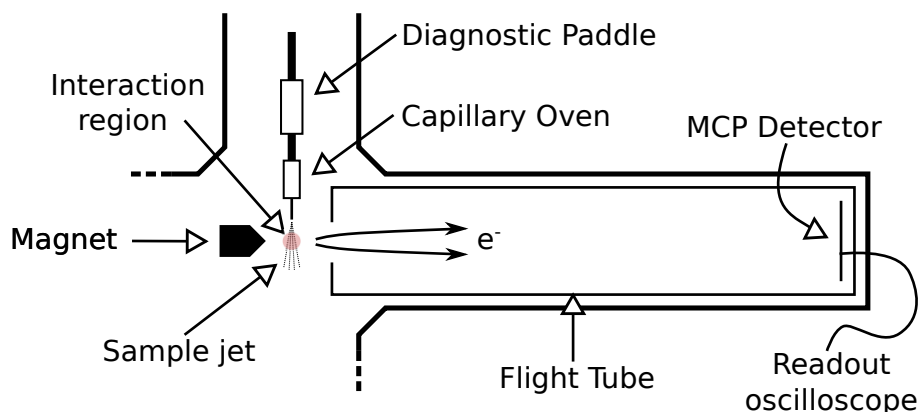


**Figure 2.13:** Schematics of the URSA-PQ apparatus. A vacuum vessel contains the magnetic bottle spectrometer and the sample delivery oven. The oven is mounted on a rod together with a diagnostic paddle, and the entire unit can be translated in all three dimensions via a motorized stage. A permanent magnet and a  $\mu$ -metal flight tube form the electron spectrometer.

### 2.2.2 Sample delivery oven and diagnostic paddle

At room temperature, 2-thiouracil is a white powder with very low vapour pressure [154]. In order to create a dense molecular jet that can be used as a target, the sample needs to be evaporated and collimated. A purpose-built oven, shown in Fig. 2.14 was used for this task. A similar oven design was used in [152]. It consists of three sections: a main body, a capillary tube and a screw-on cap.

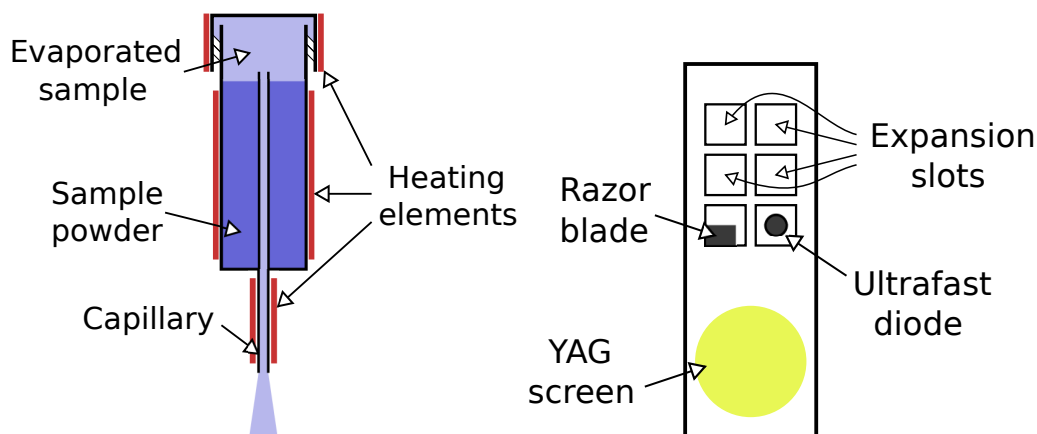


**Figure 2.14:** (Left) Sample delivery oven. The solid sample powder (dark blue) is heated and evaporates, filling the volume of the body (light blue). It then flows down the capillary and leaves the oven as a gas jet. (Right) Diagnostic paddle. Six  $1\text{ cm} \times 1\text{ cm}$  slots are available for instruments, two of which are currently used for an ultrafast diode and a razor blade (for beam shape profiling). Below, a 1-inch fluorescent YAG screen is mounted. The paddle can be lowered via a motorized manipulator mount, and the various instruments can be brought into the beam.

The cap can be removed to allow for pre-filling the oven, the oven is then mated to the diagnostic paddle on the manipulator rod and inserted in the apparatus. To provide the heat for sample evaporation, three cylindrical heating elements are mounted around each section, together with thermocouples for temperature monitoring. The evaporated sample fills the internal volume of the body and travels down the capillary. This creates a gas jet that exits the capillary a few  $mm$  above the interaction region.

Each heating element is individually controlled by a PID (Proportional Integral Derivative) filter, allowing an easy operation of the oven. The oven tip is kept at a higher temperature to avoid a build up of condensed sample that could block the capillary.

Typical operating temperatures are  $150^\circ\text{C}$  ( $423^\circ\text{K}$ ) for body and cap, and  $170^\circ\text{C}$  ( $443^\circ\text{K}$ ) for the capillary tip. A similarly designed oven, using [152] thymine at  $175^\circ\text{C}$  ( $448^\circ\text{K}$ ) showed a jet divergence of  $40^\circ$  with an estimated molecular density of  $1.7 \cdot 10^{13}\text{ cm}^{-3}$ . We expect our design to have similar characteristics.

At the operating temperatures of our oven 2TU maintains its chemical structure, with no evidence of tautomerization<sup>3</sup> up to a temperature of  $163^\circ\text{C}$  ( $435^\circ\text{K}$ ) [40].

Fig. 2.15 shows the vapour pressure curve of 2TU compared to other chemical compounds.

<sup>3</sup>isomerization due to relocation of one or more hydrogen atoms



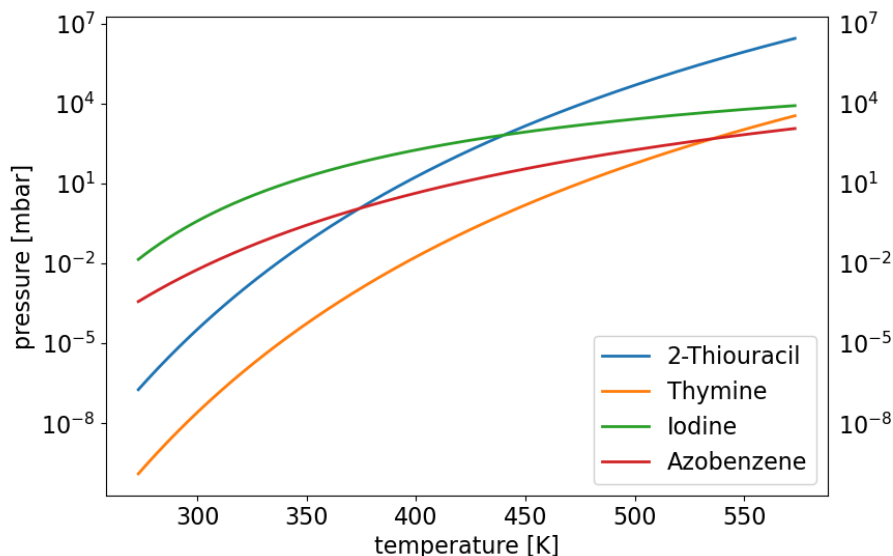


**Figure 2.15:** Vapour pressure curve of 2TU compared to other reference compounds. Data sources: [154–156].

A diagnostic paddle (Fig 2.14) is mounted above the oven, and can be inserted into the beam to aid with spatial and temporal optimization of the pump and probe beams. A fluorescent YAG screen (viewed through a telescope camera) can be used to ensure spatial overlap of the UV and x-ray beams; an ultrafast photodiode can be used to measure the time of arrival of the two pulses, in order to optimize their temporal overlap.

### 2.2.3 eTOF spectrometer

After the x-ray pulse interacts with the gas jet, electrons are ejected from the molecular sample. The eTOF (electron Time Of Flight) spectrometer measures the kinetic energy of the emitted electrons by measuring the time taken by the electrons to travel through a tube of known length. The electrons enter the flight tube through an opening near the interaction region, on the other side of the tube a Micro Channel Plate (MCP) detector [157] measures their arrival. The time delay between the x-ray pulse and the electron detection can be used to calculate the speed of the emitted electron, and therefore their kinetic energy.

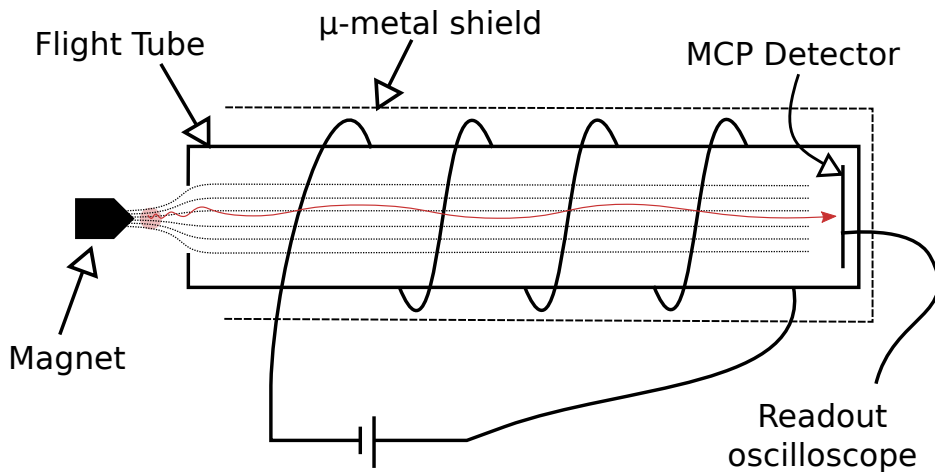


**Figure 2.16:** Schematics of a magnetic bottle electron spectrometer. The electrons are emitted in the interaction region (red dot) and are guided by the magnetic field (dotted lines) into the flight tube. The red line represent the electron's trajectory. A MCP detector is used to measure their arrival time. The magnetic bottle field is generated by a solenoid in conjunction with a permanent magnet, and is shielded from external fields by a  $\mu$ -metal tube. A retardation potential can be applied to the flight tube to increase the energy resolution.

In order to improve the collection efficiency of such a spectrometer, a magnetic field can be used to guide the electrons into the flight tube. A magnetic bottle [153] allows a collection angle up to  $4\pi$ , allowing the detection of electrons that would otherwise fly off without entering the flight tube. The high magnetic field in the vicinity of the permanent magnet acts as a magnetic mirror and pushes the electrons towards the flight tube entrance. In the flight tube, the electrons follow a spiral trajectory around the magnetic field lines, and are guided by the magnetic field towards the MCP detector.

Figure 2.16 shows a schematics of the spectrometer with the magnetic filed lines and electron trajectory overlaid.

The presence of the magnetic bottle decreases the resolution of the spectrometer, since electrons with the same kinetic energy that are emitted in different direction will have slightly different time of flight due to the different paths traveled. However, the high angular collection efficiency given by Magnetic Bottle Electron Spectrometers (MBES) makes them the ideal choice for use with dilute gas targets.

In order to increase the time resolution of the spectrometer, an electric potential can be applied to the flight tube. This potential, called retardation voltage, fights against the motion of the electrons and slows them down. *E.g.* a retardation voltage of 20 V would lower the kinetic energy of incoming electrons by 20 eV, increasing their total time of flight and allowing for a more precise estimate of their kinetic energy (see Fig 2.17). Electron with a kinetic energy lower than the retardation potential are repelled out of the

flight tube and cannot be measured.

To calibrate the spectrometer, a time-of-flight to kinetic energy function has to be chosen. This function is obtained by numerically inverting the kinetic energy to time-of-flight relation shown in Eq. 2.2.

$$t(E) = \sqrt{\frac{m_e}{2e}} \left[ \frac{l_1}{\sqrt{E}} + \frac{l_2}{\sqrt{E - V_{ret}}} + \frac{l_3}{\sqrt{E + V_{mcp}}} \right] \quad (2.2)$$

This equation is built from three terms, with each term corresponding to one of three phases in the electrons path along the flight tube. Between the interaction region and the mouth of the flight tube, the electrons do not feel any retardation voltage.  $l_1$  is therefore the distance between the interaction region and the beginning of the flight tube. For the entire length of the flight tube  $l_2$ , the electrons encounter the retardation potential  $V_{ret}$ . The final term in Eq. 2.2 models the last few  $mm$  of the electrons flight, where they are accelerated toward the MCP detector by the voltage applied to its front face  $V_{mcp}$ .

The calibrated conversion function can be seen plotted in Fig 2.17. Each retardation setting provides a different energy range over which the spectrometer is most sensitive.

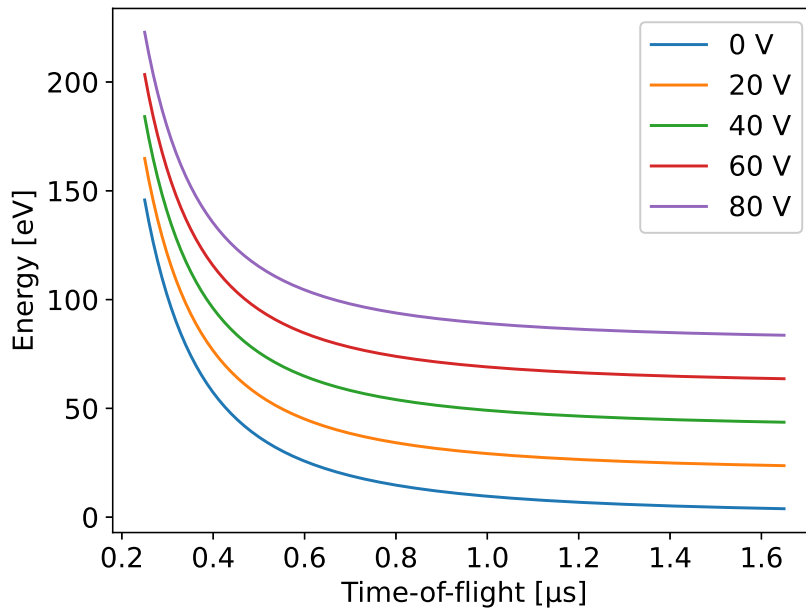


**Figure 2.17:** Time-of-flight to eV conversion function, plotted for different values of the retardation voltage. Depending on the energy range of the observed electrons, the different retardation settings allow for optimal energy resolution in the chosen range (small values for the slope of the conversion function lead to high energy resolutions). As the retardation increases, some parts of the electron spectra are cut out, as their energy falls below the asymptote.



# Chapter 3

## Published Research

Attached to this chapter are four research papers that resulted from the experimental investigations described in this thesis.

Article

# URSA-PQ: A Mobile and Flexible Pump-Probe Instrument for Gas Phase Samples at the FLASH Free Electron Laser

Jan Metje <sup>1</sup>, Fabiano Lever <sup>1</sup> , Dennis Mayer <sup>1</sup> , Richard James Squibb <sup>2</sup>, Matthew S. Robinson <sup>1</sup>, Mario Niebuhr <sup>1</sup>, Raimund Feifel <sup>2</sup>, Stefan Düsterer <sup>3</sup> and Markus Gühr <sup>1,\*</sup>

<sup>1</sup> Institut für Physik und Astronomie, Universität Potsdam, 14476 Potsdam, Germany; jan.metje@uni-potsdam.de (J.M.); fabiano.lever@uni-potsdam.de (F.L.); dennis.mayer@uni-potsdam.de (D.M.); mattrobinson@uni-potsdam.de (M.S.R.); mniebuhr@uni-potsdam.de (M.N.)

<sup>2</sup> Department of Physics, University of Gothenburg, SE-412 96 Gothenburg, Sweden; richard.squibb@physics.gu.se (R.J.S.); raimund.feifel@physics.gu.se (R.F.)

<sup>3</sup> Deutsches Elektronen Synchrotron (DESY), 22607 Hamburg, Germany; stefan.duesterer@desy.de

\* Correspondence: mguehr@uni-potsdam.de

Received: 18 October 2020; Accepted: 4 November 2020; Published: 6 November 2020



**Abstract:** We present a highly flexible and portable instrument to perform pump-probe spectroscopy with an optical and an X-ray pulse in the gas phase. The so-called URSA-PQ (German for ‘Ultraschnelle Röntgenspektroskopie zur Abfrage der Photoenergiekonversion an Quantensystemen’, Engl. ‘ultrafast X-ray spectroscopy for probing photoenergy conversion in quantum systems’) instrument is equipped with a magnetic bottle electron spectrometer (MBES) and tools to characterize the spatial and temporal overlap of optical and X-ray laser pulses. Its adherence to the CAMP instrument dimensions allows for a wide range of sample sources as well as other spectrometers to be included in the setup. We present the main design and technical features of the instrument. The MBES performance was evaluated using Kr M<sub>4,5</sub>NN Auger lines using backfilled Kr gas, with an energy resolution  $\Delta E/E \cong 1/40$  in the integrating operative mode. The time resolution of the setup at FLASH 2 FL 24 has been characterized with the help of an experiment on 2-thiouracil that is inserted via the instruments’ capillary oven. We find a time resolution of 190 fs using the molecular 2p photoline shift and attribute this to different origins in the UV-pump—the X-ray probe setup.

**Keywords:** X-ray probe; molecular dynamics; gas phase electron spectroscopy

## 1. Introduction

Photoexcited molecules channel the energy of light into different energetic degrees of freedom, such as vibrational energy, charge transfer and rearrangement of chemical bonds. This process is fast and complex, and often happens in a way that cannot be described within the framework of the Born-Oppenheimer approximation (BOA) [1–4]. In fact, many relevant photoinduced molecular changes, such as retinal isomerization in vision [5], bacterial light harvesting, as well as nucleobase photoprotection [6–9] happen on an ultrafast timescale as non-BOA processes. In order to better understand the molecular dynamics, a close comparison of simulations and experiments is extremely fruitful. Using small and isolated chromophores is advantageous for quantitative comparisons of experiments to simulations, the latter can be performed using the highest level of electronic structure methods under these constraints. Moreover, in the gas phase, experiments can use rather powerful spectroscopic methods for charged particles including highly differential coincidence experiments [10,11]. In addition, quantum manipulation such as molecular nonadiabatic, field-free

alignment [12,13] and quantum state-selection [14] to prepare specific molecular target states are possible in the gas phase.

X-ray probing of molecular dynamics offers substantial new opportunities complementary to well-established optical pump-probe methods. The X-ray-matter-interaction is element selective due to large differences of the inner shell binding energies between different elements and has been demonstrated to be site selective [15]. We have used these advantages in past time resolved UV pump—X-ray probe studies, to investigate the dynamics of isolated nucleobases. The molecular internal conversion from and to  $n\pi^*$  states leads to a strong pre-edge feature in the X-ray absorption spectrum of the element at which the  $n$  lone-pair orbital is localized [16]. Since both the core-level as well as the lone pair level of one particular atom are having a large overlap, the dipole matrix element and thus the absorption cross section is larger than cross sections involving delocalized molecular orbitals. The method is therefore ideally suited for detection of any  $n\pi^*$  states via the spectroscopy at the corresponding heteroatom [17]. Changes in the bond distance manifest themselves as shifts in the Auger kinetic energy of one of the atoms in this bond [18]. This is due to the strongly repulsive, Coulomb-repulsion shape of the final, dicationic states in the Auger decay. In addition, time-resolved Auger probing can also be used to detect the dissociation into a neutral and charged fragment in a time resolved way [19].

In this work, we describe the design and first tests of a new user instrument at the free-electron laser (FEL) facility FLASH (Free Electron Laser in Hamburg), called URSA-PQ (German for 'Ultraschnelle Röntgenspektroskopie zur Abfrage der Photoenergiekonversion an Quantensystemen', Engl. 'ultrafast X-ray spectroscopy for probing photoenergy conversion in quantum systems'), for pump-probe experiments primarily on gas-phase targets.

The new instrument is equipped with a 'magnetic bottle' electron spectrometer (MBES) [20], a molecular source, as well as several tools for finding the spatial and temporal overlap of the optical and X-ray laser pulses. The MBES is characterized by a high solid angle collection, ideal for dilute targets. In addition, it is able to measure a large range of kinetic energies, and the resolution at a particular range can be optimized by an electrostatic retardation system. We, furthermore, equipped the present system with a capillary resistively heated oven source for the evaporation of condensed molecular samples [21]. This system works well for fairly small molecules like nucleobases, which can reach an appreciable vapor pressure around  $10^{-4}$  mbar, as for the example of thymine [22], without undergoing pyrolysis or tautomerization. The capillary confines the molecular sample to a beam of small divergence fitted to a narrowly defined interaction region. Tools for spatial and temporal overlap include a cerium doped YAG (Yttrium Aluminium Garnet) screen viewed with magnifying optics as well as diodes for coarse timing, allowing a temporal synchronization of optical and X-ray pulses within about 100 ps.

We present a system that includes all these parts and in addition has a high degree of flexibility. Due to adherence to the flange and distance dimensions set by the so-called CAMP chamber [23], multiple, already existing molecular sources and spectrometers can be integrated with the setup described in this paper.

In what follows, the instrument design and measurement procedures will be described. We will then focus on the energy calibration of the MBES as well as the time resolution in our optical-pump X-ray-probe measurements by using the example of 2-thiouracil.

## 2. Materials and Methods

### 2.1. Overview and Vacuum System

Figure 1 shows an overview of the URSA-PQ instrument and its functionalities. In the current version, the sample is introduced by either backfilling the vacuum vessel or using a capillary oven. In this paper, the former is used to characterize the MBES, and the latter is used with 2-thiouracil to evaluate the time resolution. The interaction region is defined by the crossing point of the optical

and X-ray beams overlapping with the region of highest sensitivity of the MBES. Molecules in the interaction region are excited by an optical laser pulse, in this case a 266 nm UV pulse, and subsequently probed by an X-ray pulse. Optical and X-ray pulses are focused by separate mirrors and combined inside the beamline by a mirror having a hole for X-ray transmission. The UV beam is set on side or top of the hole to avoid power losses. The tunable X-rays can induce a resonant core-to-valence excitation and/or non-resonant ionization. The resulting photo- and Auger electrons are then efficiently guided by the MBES's magnetic field arrangement along a flight tube of 1.7 m length to a micro-channel-plate (MCP) detector. The time-of-flight of the electrons is measured and converted to electron kinetic energy. The apparatus is designed in a modular way that also allows upgrades at later times, the usage of different measurement devices from the FLASH environment and other types of sample delivery systems. The desired high flexibility is achieved by designing the central vacuum vessel as a customized six-way cross (see Figure 2), following the most critical dimensions of the permanent CAMP instrument situated at FLASH 1.

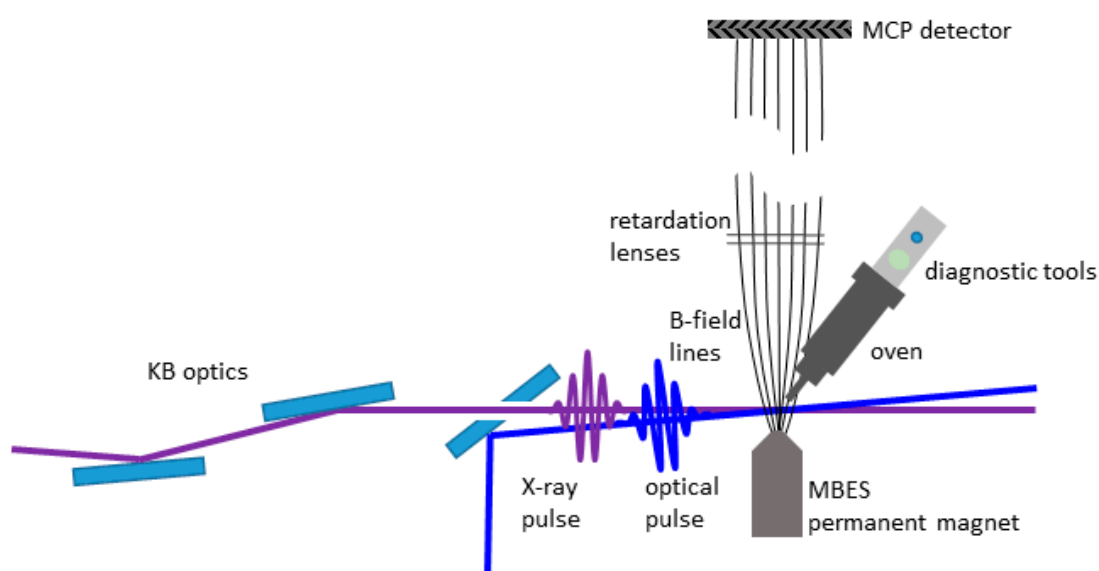


**Figure 1.** Diagrammatic representation of the URSA-PQ (German for ‘Ultraschnelle Röntgenspektroskopie zur Abfrage der Photoenergiekonversion an Quantensystemen’, Engl. ‘ultrafast X-ray spectroscopy for probing photoenergy conversion in quantum systems’) instrument with its functionalities. The molecular sample is evaporated and guided into the interaction region by a capillary oven. An optical laser pulse excites the sample before a delayed X-ray pulse from the FLASH FEL, focused by a Kirkpatrick-Baez (KB) mirror set, probes the excited molecular ensemble. Photo- and Auger-electrons created by the light-matter interaction are guided by the magnetic field of the magnetic bottle electron spectrometer (MBES) towards a detector. The diagnostic tools for spatial and time-overlap can be driven into the interaction region.

An overview of the instrument is shown in Figure 2. A central cross serves as the light-matter interaction chamber. A manipulator is mounted vertically ( $z$ -direction), holding the capillary oven molecular source and diagnostics tools on top of that source. Either one two of the devices (oven or diagnostics tools) can be brought into the center and thus the interaction region of the instrument. Shown in the positive  $y$ -direction is the MBES spectrometer flight tube with the MCP detector at the end. The manipulator holding a permanent magnet in the negative  $y$ -direction provides the up to 1 Tesla strong B-field of the MBES. The optical and X-ray beams travel in the  $x$ -direction, entering by the center flange, through the interaction region in the center of the cross to the center flange at the end.



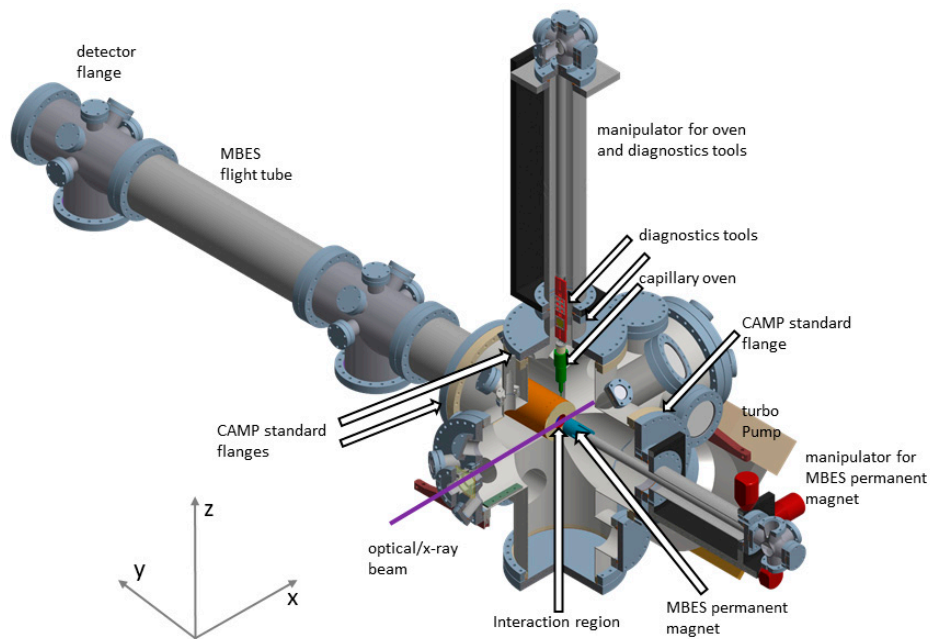


**Figure 2.** Design-drawing of the URSA-PQ (German for ‘Ultraschnelle Röntgenspektroskopie zur Abfrage der Photoenergiekonversion an Quantensystemen’, Engl. ‘ultrafast X-ray spectroscopy for probing photoenergy conversion in quantum systems’) instrument. The central body contains flanges that adhere to the standard defined by the CAMP-chamber in size as well as distance to the interaction region (marked). The capillary oven and diagnostic tools are mounted on a manipulator allowing for insertion of either device into the beam. The permanent magnet of the magnetic bottle electron spectrometer (MBES) sits on another manipulator to optimally overlap the region of highest sensitivity of the MBES with the interaction region of the optical and X-ray pulses. The 1.7 m long flight tube connects the main body to the detector flange housing the microchannel plate electron detector.

The central cross of the instrument has three flanges (top in z-direction and left, right in  $\pm y$  direction) that adhere to the CAMP instrument dimensions concerning flange size (DN 250 CF) and distance of flanges from the interaction region. For the front port where the FEL enters, the chamber is kept at short distance to the interaction region (280 mm) to support short focal lengths of the beamline. Breadboards are welded to the bottom of this port and the rear port to allow the incorporation of in-vacuum equipment such as incoupling optics and diagnosis tools. The floor facing port ( $-z$  direction) can be used for a  $\text{LN}_2$  cold trap (not shown here). A 1300 l/s turbomolecular pump is attached to a flange facing 45 degrees downwards. A variety of smaller flanges (DN40 to DN100) face the chamber center at the diagonals, or are located at the sides of the cross’s arms. Notably, three DN40 flanges at the entrance arm may be used for baffles. The vacuum apparatus is mounted on a movable frame (not shown here) that allows height and level adjustment by means of four legs. To simplify the alignment of the chamber axis to the FEL beam, the frame is equipped with a motorized x-y-stage and a manual rotation stage with the vertical axis below the connection to the beamline. In this way, the frame can be easily aligned to the path of the FEL beam. The motors of the frame, and the capillary oven magnet manipulators are controlled by a programmable logic controller (PLC).

## 2.2. Integration at the FLASH FL 24 Beamline

For the results presented here, the URSA-PQ chamber was integrated at FL 24 at FLASH 2 in Deutsches Elektronen Synchrotron (DESY), Hamburg, Germany. The beamline is equipped with bendable Kirkpatrick–Baez (KB) optics [24]. The distance from the KB optics to the interaction region in our experiment is 2.1 m.

The focus position of the X-rays can be manipulated within the chamber by using the KB degrees of freedom. We chose to have the focus beyond the interaction region, as we did want to maximize the number of X-ray photons on target without introducing X-ray nonlinearities. At about 90 cm in front of the interaction region, after the KB optics, the UV beam is coupled in by a 45 degree high reflectivity plane mirror for 266 nm wavelength. This mirror has a central hole for the X-ray beam to pass through. The optical beam is reflected from a position below the center hole, and steered up so that the two beams cross in the interaction region of the MBES.

The control and monitoring of the setup's hardware, such as motor position, oven temperature and chamber pressure is handled by an industrial PLC system working in tandem with a UNIX server. All safety and/or time-sensitive tasks, such as vacuum valves control or high voltage interlocks, are managed by the PLC in a closed loop in order to ensure real-time responsiveness. The UNIX server offers a server-client interface that allows multiple operators to monitor and control the system status from different terminals through the use of a purpose-built graphical user interface that connects to the server through a Python API (application program interface).

Integration with the DESY DOOCS (distributed object oriented control system) framework is seamlessly handled by the UNIX server. Experiment parameters such as chamber pressure and MCP voltages are constantly pushed to DOOCS for storage, allowing for later correlation of the chamber parameters with the experimental data. Moreover, the raw experimental data is retrieved from DOOCS and processed in real time. The data is sliced into single-shot traces, separating UV-pumped from non-pumped shots and averaged over a controllable time window. It is then made available to users for visualization (through a purpose built utility) or online analysis (through the python API). A real time calibrated time-of-flight to electron kinetic energy conversion of the measured traces is also provided through the API. After the experiment, all recorded data are available to the user group for offline analysis as hdf5 data files through the standard DESY channels.

### 2.3. Diagnostics and Oven

We have implemented a diagnostic paddle that is located on top of the oven on the same manipulator (see Figure 2), allowing for precise positioning inside the interaction region of the MBES spectrometer. The diagnostic paddle hosts a number of tools used for spatial as well as temporal characterization.

The spatial diagnostics serve to spatially overlap the UV and X-ray beams in the interaction region, as well as estimating the beam size. We use a 0.2 mm thick, 25 mm diameter YAG screen, possessing a matte, sandblasted surface. The screen is externally viewed through a vacuum window with the aid of a long working distance lens.

For timing diagnostics, we use a fast AXUV-type diode on a subminiature version A (SMA) connector that is not directly illuminated, but by a highly-attenuated beam created using solid filters which are moved in and out. The beam hits the mounting rim of the diode and only scattered light hits the active area in our case. We illuminate it separately with the optical and X-ray pulses. These signals are viewed on a 13 GHz bandwidth oscilloscope. The X-ray induced trace is saved as reference on the scope and the delay of the optical pulse is manipulated by a delay stage such that the rising edges of the two signals overlap. This strategy allows us to temporally overlap the optical and X-ray pulses with a sub 100 ps accuracy. Temporal overlap on the femtosecond scale is achieved using photo or Auger electrons of atoms or molecules shown later in this paper.

We use a resistively-heated capillary oven that we developed some years ago and successfully used before as a sample source at the linac coherent light source (LCLS) [16,18,21,25,26] as well as with high harmonic vacuum ultraviolet sources [27,28]. The oven consists of a body, a cap that is screwed on after filling the main body with a solid molecular sample, and a capillary tip. All components are made from aluminum. The three parts are separately heated using thin-film sheet heaters. The temperatures of the three sections are monitored using thermocouples and we control the heating current using a proportional-integral-derivative PID feedback circuit implemented on the control

computer. The sample density has been once tested with the nucleobase thymine and can reach up to  $10^{12}$  molecules/cm<sup>3</sup> [21]. The capillary reduces the angular width of the beam compared to usual effusive sources and we have measured the full width at half maximum (FWHM) of 10 degrees when operating in the  $10^{11}$  molecules/cm<sup>3</sup> density regime [21].

#### 2.4. Magnetic Bottle Electron Spectrometer

The magnetic bottle time-of-flight electron spectrometer (MBES) has a high collection efficiency, covering up to the full  $4\pi$  solid angle [26]. Thus, a large number of electrons can be efficiently detected, which is especially important in experiments with dilute samples. The magnetic bottle spectrometer is characterized by a strong and inhomogeneous magnetic field of about 1 Tesla at the interaction region, which joins onto a much weaker ( $\sim 1$  mT), homogeneous magnetic field created by a solenoid around the flight tube. Electrons ejected in the interaction region into any direction are thus confined into the flight tube. The time-of-flight (TOF) of the electrons from the interaction region to detection is determined and subsequently transformed into kinetic energy.

Our specific design is illustrated in Figure 3. A vacuum tube with DN160 flanges houses the flight tube, which is protected from external magnetic fields by a  $\mu$ -metal shield. Wound onto the flight tube, a solenoid is generating the weak homogeneous field along the electron flight path. The coil has 1450 windings and is fed by a current of 400 mA producing a magnetic field of around 0.4 mT. Winding the coil directly on the flight tube has the advantage that the solenoid can be brought close to the interaction region. In addition, the design allows that the whole instrument can be taken out of the main chamber by unbolting a single DN 250 flange at the central cross. Close to the interaction region, right at the entrance of the flight tube, a stack of electrostatic lenses can be used to retard/repel the electrons. A permanent magnet with a soft iron pole tip generates the strong, inhomogeneous field in the interaction region. The space available at the beamline is used efficiently to maximize the instruments resolution, resulting in an optimal flight tube length of 1.7 m.

The transition from the inhomogeneous to homogeneous field occurs over a short distance of about 10 cm. The lens stack is placed inside the front of the flight tube, at the beginning of the homogeneous part of the magnetic field. At this point, the momentum in direction of the center axis of the flight tube is approximately equal for electrons of equal kinetic energy.

The permanent magnet of the instrument is mounted in a temperature-controlled holder on a manipulator. By this construction, the magnet can be brought close to the interaction region as well as retracted if other equipment is brought into the interaction region, such as a diode or a Ce-YAG screen. Elevated temperatures of 60 °C generally prevent sample building up on the magnet tip and introducing electrostatic inconsistencies.

The detector assembly (purchased from Roentdek Handels GmbH) consists of a grid, followed by a chevron MCP stack with an 80 mm diameter and an anode. The grid is held at the potential of the flight tube (i.e., the retardation potential). The electrons are then accelerated towards the front MCP by a +300 V potential change over 3 mm. Subsequently, the electrons are multiplied by the MCP arrangement using a potential on the MCP backside of 1950 V. The anode, used for picking up the signal is held at 2300 V. The signal is picked up by a high-pass filter and sent to a 12 bit analog-digital converter, which we use at a sample rate of 2Gs. A single electron pulse has a width of 10 ns. The data we present in this paper has been accumulated in the integration mode, i.e., all individual TOF traces have been added. Alternatively, for lower electron yield, individual electron hits can be identified by using a (software) constant fraction discriminator and then added individually to a TOF array.

We transform spectra taken in the TOF domain to the kinetic energy domain by the following procedure. The distance from the interaction region to the detector is divided into three parts. The electric potential in these parts is treated as a step function and the lengths are taken from the CAD drawing of the spectrometer but refined in the calibration by fitting to Auger electron features. In the first part, the electrons are traveling with their original kinetic energy for a distance of 90 mm from the interaction region to the flight tube entrance. In the second part through the flight tube, which is

1694 mm long, their kinetic energy is reduced by the retardation voltage. We fit these distances based on observed electron spectra in the calibration procedure shown below. In the 3-mm-long final part from the flight tube to the detector, their kinetic energy is increased by 300 V.

After axis transformation from TOF to kinetic energy, the signal strength is multiplied by a Jacobian function which corrects for the non-linear mapping of bins from the TOF domain and the kinetic energy domain.

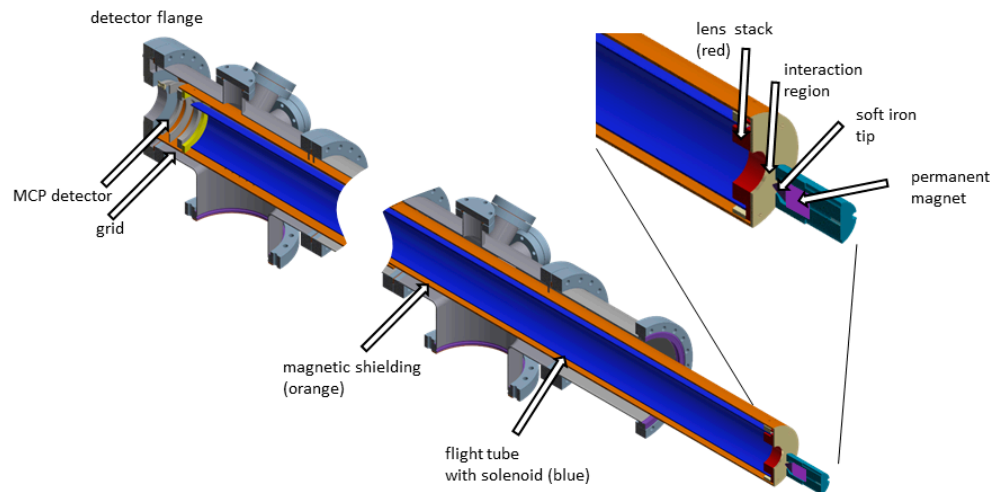


**Figure 3.** Cut-down scheme of the magnetic bottle time of flight spectrometer, with the magnified area around the interaction region. The interaction region is defined by the overlap of the optical and X-ray pulse with the region of highest sensitivity of the MBES. The magnetic field in the interaction region is dominated by the permanent magnet having a tapered soft-iron pole piece on top. The strong, inhomogeneous magnetic field drops quickly to a weak, homogeneous solenoid field surrounding the flight tube, thus guiding the electrons from the interaction region towards the detector. A  $\mu$ -metal tube (orange) around the flight-tube and solenoid assembly (blue) shields the long flight region from external magnetic fields. At the entrance of the flight tube, an electrostatic lens stack can be used to retard the electrons to optimally utilize the energy resolution at a mean kinetic energy of choice. The micro-channel-plate (MCP) detector assembly contains a grid at the front to accelerate electrons towards the first plate. The grid and lens stack are equipotential so that the electrons travel through the flight tube with constant velocity.

### 3. Results and Discussion

#### 3.1. MBES Energy Resolution

The spectrometer has been calibrated with the Kr  $M_{4,5}$  NN Auger lines, appearing in the kinetic energy range shown in Figure 4. The background pressure in the interaction region was  $2 \times 10^{-7}$  mbar before filling in Kr, although much lower pressures in the  $10^{-9}$  mbar range have been reached by pumping for longer times and baking. We backfilled the chamber with Kr gas at a pressure of  $5.5 \times 10^{-7}$  mbar for calibration purposes.

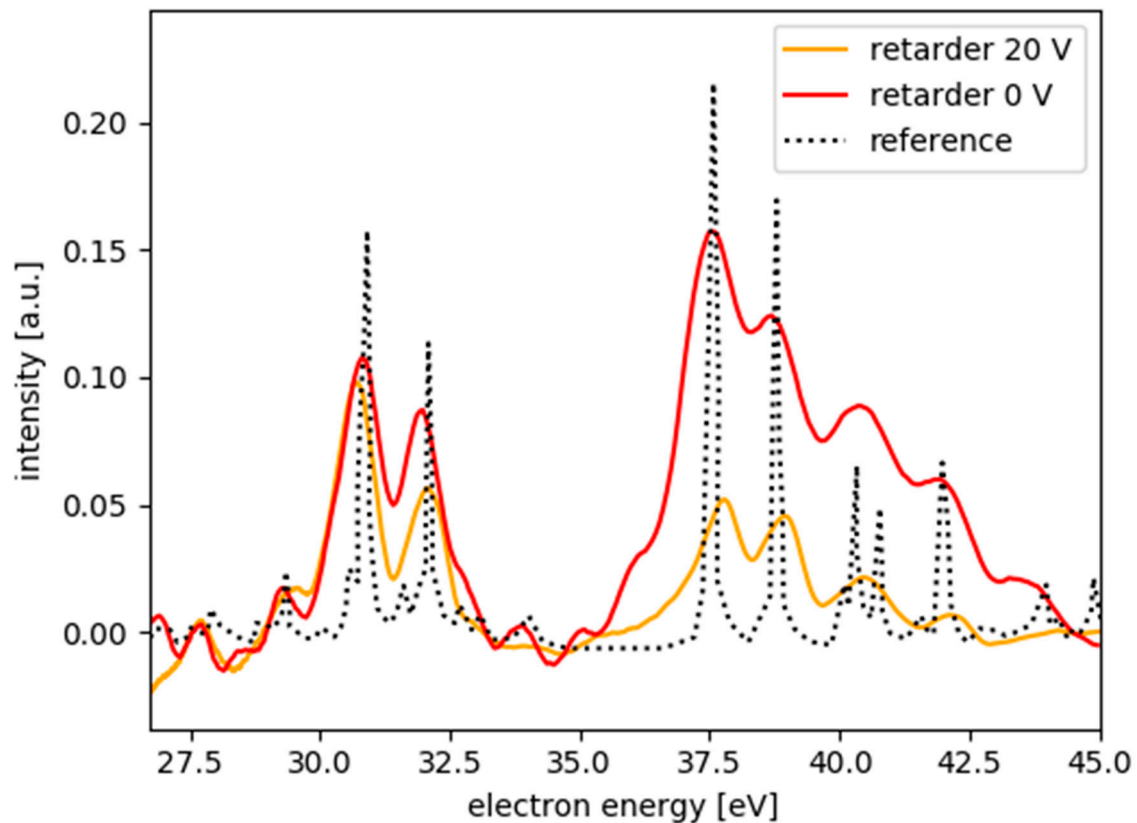


**Figure 4.** Krypton  $M_{4,5}NN$  Auger spectra recorded with the URSA-PQ instrument using 270 eV photons (red spectrum using a retardation of 0 V, orange spectrum using a retardation of 20 V). The spectra are recorded with a back-filled interaction chamber and converted from time-of-flight (TOF) to kinetic energy. The black spectrum from Reference [29] serves as a reference.

We chose an FEL photon energy of 270 eV; the spectral jitter was on the order of 2% as observed by an inline diagnostic instrument at the beamline [30]. The nonresonant Auger lines however are not affected by the spectral jitter of the light source. The permanent magnet of the spectrometer was moved close to the interaction region and scanned vertically to and horizontally along the FEL beam to optimize the position for highest electron signal. A halo of scattered light around the laser focus prohibited distances of the magnet tip to laser focus to be smaller than 4 mm. Even a small amount of scattered light produced many more photoelectrons from the solid magnet tip than from the gas in the real focus because of the orders of magnitude lower density of our gas compared to solid matter.

The Auger spectra used for calibration are shown in Figure 4. The red line is recorded using a retardation potential of 0 V. The black reference spectrum is obtained from Werme et al. [29]. One can clearly identify the two different groups of Kr  $M_{4,5}NN$  Auger lines in our spectra. In the higher energy group, we identify the two lines at 37.7 and 38.7 eV as two separate lines. This results in an energy resolution without retardation of  $\Delta E/E \cong 1/40$ . The kinetic energy spectrum with 20 V retardation voltage (orange) shows deeper modulation indicating higher energy resolution, as the kinetic energy decreased.

We now discuss the resolution-limiting factors in the calibration measurements. We note a large background in the kinetic energy range between 35 and 37.5 eV. This results from a saturation of the detector due to a large amount of electron counts per X-ray pulse. In the TOF-spectrum, the group of Auger electrons between 37 and 42.5 eV hit the detector at early times and thereby produces a long lasting background of several nanoseconds. By the time the next group between 30 and 32 eV hits the detector, this signal has decayed. This memory effect in the detector certainly degrades the resolution as background accumulates in a group of Auger lines. This issue can be easily solved by reducing

the FEL pulse energy or the Kr pressure; in the following experimental runs for 2-thiouracil, we had adjusted pressure as well as FEL pulse energy accordingly.

A single electron pulse coupled out at the detector-anode has a width of 10 ns and is completely symmetric, i.e., the rising edge is not shorter than the falling edge. As mentioned above, we used the system in 'integration-mode' by adding up individual traces from the detector. The 10 ns pulse width in TOF corresponds to 0.5 eV of energy resolution in the kinetic energy range around 20 eV. The experimental energy resolution of 1/40 corresponds to a 10 ns time-interval at a TOF of 300 ns (kinetic energy of 101 eV).

A possibility to improve the time resolution would be the reduction of the number of electrons hitting the detector. This would reduce the detector saturation and therefore accumulated background in the different groups. Another important advantage would be the possibility to identify individual electrons hitting the detector. This will allow for edge detection, for instance via a constant fraction discriminator. In this case, the resolution is fundamentally limited by the sample interval of the analog-to-digital converter (ADC), which is 500 ps in our case. In analogy to the resolution limit of 10 ns, the 500 ps would correspond to an energy resolution of 0.03 eV in the energy range of 20 eV. However, there is also the turn-around time of the electrons emitted initially away from the detector, which will also limit the resolution [20].

### 3.2. Temporal Resolution

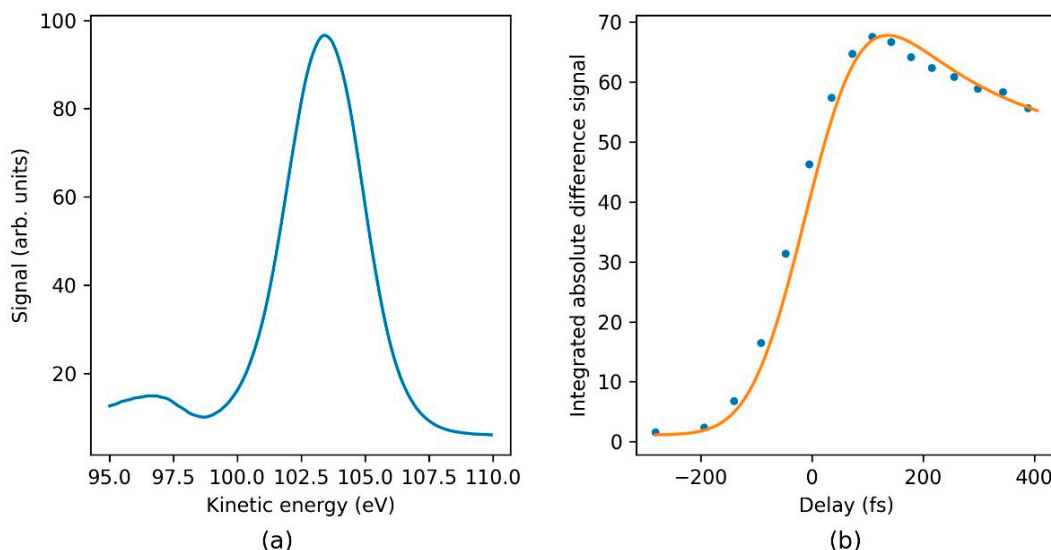
We now investigate the temporal resolution in the optical pump—these are X-ray probe experiments. As mentioned above, we initially determined the coarse temporal overlap by monitoring a fast-diode response, induced by UV and X-ray pulses, on an oscilloscope. The setup had an accuracy in the sub-100 ps domain. As 100 ps resolution is not sufficient for the experiments, more accurate information on the temporal overlap, as well as the temporal resolution achievable by this setup, we performed measurements of photoelectron signals of molecules using the URSA instrument. We used the molecule 2-thiouracil ( $C_4H_4N_2OS$ ), as this has been the molecule of interest for our first beamtime utilizing this instrument. Thionucleobases are interesting as they show an efficient relaxation to long-lasting triplet states after UV excitation, thereby showing different behavior compared to canonical nucleobases, which relax relatively quickly to the ground state [31].

Figure 5a shows a core level photoelectron spectrum of 2-thiouracil illuminated by X-ray photons of 272 eV mean-photon-energy. The pulses have less than 1% mean-photon-energy-jitter and a relative bandwidth of 1–1.5%. Shown in this particular part of the spectrum is the 2p-photoline of sulfur at 103.5 eV kinetic energy. This line should be spin-orbit split resulting in the  $j = 3/2$  and  $1/2$  components with an energy spacing of 1.2 eV [32], however already the photon energy resolution is not sufficient to resolve that splitting. The small shoulder visible on the lower kinetic energy side at 95–97 eV is a satellite structure that accompanies the main 2p photoline (as, for instance, previously documented for sulfur on surfaces [33]).

Upon UV excitation, the main photoline shifts towards lower kinetic energies, due to the molecular dynamics setting in immediately. The molecular origin for this observation will be discussed in detail in a separate paper. Here, we use this feature to determine the temporal overlap with sub-ps precision, and the overall time resolution of the experiment itself. We take here the difference spectrum (not shown), calculate its absolute value  $|UV_{on} - UV_{off}|$  as a measure for the UV induced change in the spectrum. This observable as a function of relative delay between UV-pump and X-ray-probe pulse is shown by the blue dots in Figure 5b, together with a theoretical fit shown by the orange line. The fit function includes a Gaussian describing the time-resolution, convoluted with two exponential decays (see for instance Equation (3) in Reference [34]). The second exponential decay is longer than 100 ps and has limited influence on the data in the delay window shown. The faster exponential decay of  $(230 \pm 30)$  fs describes some molecular dynamics. Most interesting in the context here is the Gaussian time-resolution function. We actually determined the relative time-overlap by the maximum of this

Gaussian, which can be done with a sub-10 fs accuracy. The Gaussian time resolution when correcting data using the beam arrival monitor [35] has a FWHM of  $\sigma_{TR} = (190 \pm 10)$  fs.

There are different contributions to the origin of the time-resolution known in the literature which sum up geometrically to the final time resolution  $\sigma_{TR} = \sqrt{\sigma_{UVL}^2 + \sigma_{FEL}^2 + \sigma_{FELtrain}^2 + \sigma_{UVLtrain}^2 + \sigma_{FEL-UVLjitter}^2}$ , where  $\sigma_{UVL}$  is the UV pulse length,  $\sigma_{FEL}$  the X-ray pulse length,  $\sigma_{FELtrain}$  the intra-train jitter of the X-ray pulses within the macro-bunch,  $\sigma_{UVLtrain}$  the intra-train jitter of the UV pulses within the macrobunch and  $\sigma_{FEL-UVLjitter}$  the relative timing jitter of X-ray and UV laser pulses [36]. The UV pulse duration has been determined to be  $\sigma_{UVL} = 80$  fs by a frequency resolved optical gating (FROG) measurement [37]. Subtracting the UV pulse duration geometrically yields 170 fs Gaussian FWHM total for all other components. The other components have been estimated with  $\sigma_{FELtrain} = \sigma_{UVLtrain} = 30\text{--}40$  fs and  $\sigma_{FEL-UVLjitter} = 70$  fs [38,39]. Subtracting all these components out delivers a remaining X-ray pulse duration in the experiment in the region of about 150 fs. Taking all these components into account results in a remaining X-ray pulse duration in the experiment on the order of 150 fs. However, we would expect a sub-100 fs X-ray pulse duration for this bunch charge. The discrepancy could possibly be attributed to a higher jitter compared to past experiments and longer term drifts.



**Figure 5.** (a) Experimental photoelectron spectrum showing the sulfur-2p photoline of 2-thiouracil taken with a photon energy of  $\sim 270$  eV. (b) Increase of the absolute value in the difference signal  $|(UV_{on} - UV_{off})|$  as a function of pump-probe delay (blue dots) and fit by the model explained in the text (orange line).

#### 4. Conclusions

We presented the new URSA-PQ instrument which is now available for general users at the FLASH FEL facility. We described its major design features and its flexibility because of its adherence to CAMP instrument dimensions. The instrument is already equipped with a molecular source and a magnetic bottle spectrometer, allowing for ultrafast X-ray probe studies of photoexcited molecular dynamics. We demonstrated the current spectral resolution of the MBES of 1/40 using the  $M_{4,5}NN$  Auger decay of Kr in the range of 30–45 eV electron energy. This can be improved further by treating electron signals digitally using a combination of an edge finder and time-to-digital conversion. We investigated the time-resolution in conjunction with the FLASH 2 pump-probe laser delivering 266 nm pulses at FL 24. For that purpose, we used a UV-induced shift of the sulfur 2p photoelectron line of the molecules 2-thiouracil. We find a temporal resolution of 190 fs using photoelectron features from UV excited 2-thiouracil.

**Author Contributions:** Instrument design, J.M. and M.G.; MBES design, J.M. with help of R.J.S. and R.F.; realization of the instrument: J.M., D.M., F.L., M.N., M.S.R., S.D., M.G.; instrument software, F.L. with help of J.M., performing experiments, all authors; analyzing data, F.L., D.M. with help of M.G.; writing paper: J.M., F.L., D.M. and M.G.; comments and suggestions on the paper drafts, all authors. All authors have read and agreed to the published version of the manuscript.

**Funding:** The URSA-PQ instrument and the position of J.M. was funded by the German Federal Ministry for Education and Research (BMBF) under ‘Verbundforschungsprojekt 05K16IP1’. The Potsdam Research Group is funded by a Lichtenberg Professorship of the Volkswagen-Stiftung. We acknowledge DFG funding via grant GU 1478/1-1. We acknowledge DESY (Hamburg, Germany), a member of the Helmholtz Association HGF, for the provision of experimental facilities. Part of this research was carried out at FLASH2. R.F. and R.J.S. received funding from the Swedish Research Council and the Knut and Alice Wallenberg Foundation, Sweden. We acknowledge the support of the Deutsche Forschungsgemeinschaft and Open Access Publishing Fund of University of Potsdam.

**Acknowledgments:** We acknowledge S. Alisauskas, F. Calegari, B. Manschwetus, M. Kuhlmann, T. Mazza, A. Trabattoni, M. Wallner and T. J. A. Wolf for participating in the experiments on thiouracil.

**Conflicts of Interest:** The authors declare no conflict of interest. The funders had no role in the design of the study; in the collection, analyses, or interpretation of data; in the writing of the manuscript, or in the decision to publish the results.

## References

1. Yarkony, D. Diaboloical conical intersections. *Rev. Mod. Phys.* **1996**, *68*, 985–1013. [[CrossRef](#)]
2. Levine, B.G.; Martínez, T.J. Isomerization through Conical Intersections. *Annu. Rev. Phys. Chem.* **2007**, *58*, 613–634. [[CrossRef](#)] [[PubMed](#)]
3. Matsika, S.; Krause, P. Nonadiabatic Events and Conical Intersections. *Annu. Rev. Phys. Chem.* **2011**, *62*, 621–643. [[CrossRef](#)] [[PubMed](#)]
4. Domcke, W.; Yarkony, D.R.; Köppel, H. *Conical Intersections Electronic Structure, Dynamics and Spectroscopy*; World Scientific Publishing Company: Singapore, 2011; ISBN 978-981-4313-45-2.
5. Polli, D.; Altoè, P.; Weingart, O.; Spillane, K.M.; Manzoni, C.; Brida, D.; Tomasello, G.; Orlandi, G.; Kukura, P.; Mathies, R.A.; et al. Conical intersection dynamics of the primary photoisomerization event in vision. *Nature* **2010**, *467*, 440–443. [[CrossRef](#)] [[PubMed](#)]
6. Crespo-Hernández, C.E.; Cohen, B.; Hare, P.M.; Kohler, B. Ultrafast Excited-State Dynamics in Nucleic Acids. *Chem. Rev.* **2004**, *104*, 1977–2020. [[CrossRef](#)]
7. Middleton, C.T.; de La Harpe, K.; Su, C.; Law, Y.K.; Crespo-Hernández, C.E.; Kohler, B. DNA Excited-State Dynamics: From Single Bases to the Double Helix. *Annu. Rev. Phys. Chem.* **2009**, *60*, 217–239. [[CrossRef](#)]
8. Schreier, W.J.; Gilch, P.; Zinth, W. Early Events of DNA Photodamage. *Annu. Rev. Phys. Chem.* **2015**, *66*, 497–519. [[CrossRef](#)] [[PubMed](#)]
9. Improta, R.; Santoro, F.; Blancafort, L. Quantum Mechanical Studies on the Photophysics and the Photochemistry of Nucleic Acids and Nucleobases. *Chem. Rev.* **2016**, *116*, 3540–3593. [[CrossRef](#)]
10. Dörner, R.; Mergel, V.; Jagutzki, O.; Spielberger, L.; Ullrich, J.; Moshhammer, R.; Schmidt-Böcking, H. Cold Target Recoil Ion Momentum Spectroscopy: A “momentum microscope” to view atomic collision dynamics. *Phys. Rep.* **2000**, *330*, 95–192. [[CrossRef](#)]
11. Ullrich, J.; Moshhammer, R.; Dorn, A.; Dörner, R.; Schmidt, L.P.H.; Schmidt-Böcking, H. Recoil-ion and electron momentum spectroscopy: Reaction-microscopes. *Rep. Prog. Phys.* **2003**, *66*, 1463–1545. [[CrossRef](#)]
12. Stapelfeldt, H.; Seideman, T. Colloquium: Aligning molecules with strong laser pulses. *Rev. Mod. Phys.* **2003**, *75*, 543. [[CrossRef](#)]
13. McFarland, B.K.; Farrell, J.P.; Bucksbaum, P.H.; Gühr, M. High Harmonic Generation from Multiple Orbitals in N<sub>2</sub>. *Science* **2008**, *322*, 1232. [[CrossRef](#)]
14. Filsinger, F.; Meijer, G.; Stapelfeldt, H.; Chapman, H.N.; Kuepper, J. State- and conformer-selected beams of aligned and oriented molecules for ultrafast diffraction studies. *Phys. Chem. Chem. Phys.* **2011**, *13*, 2076–2087. [[CrossRef](#)]
15. Siegbahn, K. *ESCA Applied to Free Molecules*; North-Holland Pub. Co.: Amsterdam, The Netherlands, 1969; ISBN 0-7204-0160-7.



16. Wolf, T.J.A.; Myhre, R.H.; Cryan, J.P.; Coriani, S.; Squibb, R.J.; Battistoni, A.; Berrah, N.; Bostedt, C.; Bucksbaum, P.; Coslovich, G.; et al. Probing ultrafast  $\pi\pi^*/n\pi^*$  internal conversion in organic chromophores via K-edge resonant absorption. *Nat. Commun.* **2017**, *8*, 29. [[CrossRef](#)]
17. Ehlert, C.; Gühr, M.; Saalfrank, P. An efficient first principles method for molecular pump-probe NEXAFS spectra: Application to thymine and azobenzene. *J. Chem. Phys.* **2018**, *149*, 144112. [[CrossRef](#)]
18. McFarland, B.K.; Farrell, J.P.; Miyabe, S.; Tarantelli, F.; Aguilar, A.; Berrah, N.; Bostedt, C.; Bozek, J.D.; Bucksbaum, P.H.; Castagna, J.C.; et al. Ultrafast X-ray Auger probing of photoexcited molecular dynamics. *Nat. Commun.* **2014**, *5*, 4235. [[CrossRef](#)]
19. Wolf, T.; Holzmeier, F.; Wagner, I.; Berrah, N.; Bostedt, C.; Bozek, J.; Bucksbaum, P.; Coffee, R.; Cryan, J.; Farrell, J.; et al. Observing Femtosecond Fragmentation Using Ultrafast X-ray-Induced Auger Spectra. *Appl. Sci.* **2017**, *7*, 681. [[CrossRef](#)]
20. Kruit, P.; Read, F.H. Magnetic field paralleliser for  $2\pi$  electron-spectrometer and electron-image magnifier. *J. Phys. E Sci. Instrum.* **1983**, *16*, 313–324. [[CrossRef](#)]
21. McFarland, B.K.; Berrah, N.; Bostedt, C.; Bozek, J.; Bucksbaum, P.H.; Castagna, J.C.; Coffee, R.N.; Cryan, J.P.; Fang, L.; Farrell, J.P.; et al. Experimental strategies for optical pump – soft x-ray probe experiments at the LCLS. *J. Phys. Conf. Ser.* **2014**, *488*, 012015. [[CrossRef](#)]
22. Ferro, D.; Bencivenni, L.; Teghil, R.; Mastromarino, R. Vapour pressures and sublimation enthalpies of thymine and cytosine. *Thermochim. Acta* **1980**, *42*, 75–83. [[CrossRef](#)]
23. Strueder, L.; Epp, S.; Rolles, D.; Hartmann, R.; Holl, P.; Lutz, G.; Soltau, H.; Eckart, R.; Reich, C.; Heinzinger, K.; et al. Large-format, high-speed, X-ray pnCCDs combined with electron and ion imaging spectrometers in a multipurpose chamber for experiments at 4th generation light sources. *Nucl. Instrum. Methods Phys. Res. Sect. A-Accel. Spectrom. Detect. Assoc. Equip.* **2010**, *614*, 483–496. [[CrossRef](#)]
24. Raimondi, L.; Manfreda, M.; Mahne, N.; Cocco, D.; Capotondi, F.; Pedersoli, E.; Kiskinova, M.; Zangrando, M. Kirkpatrick–Baez active optics system at FERMI: System performance analysis. *J. Synchrotron Rad.* **2019**, *26*, 1462–1472. [[CrossRef](#)]
25. Zhaunerchyk, V.; Kamińska, M.; Mucke, M.; Squibb, R.J.; Eland, J.H.D.; Piancastelli, M.N.; Frasiniski, L.J.; Grilj, J.; Koch, M.; McFarland, B.K.; et al. Disentangling formation of multiple-core holes in aminophenol molecules exposed to bright X-FEL radiation. *J. Phys. B At. Mol. Opt. Phys.* **2015**, *48*, 244003. [[CrossRef](#)]
26. Sanchez-Gonzalez, A.; Barillot, T.R.; Squibb, R.J.; Kolorenč, P.; Agaker, M.; Averbukh, V.; Bearpark, M.J.; Bostedt, C.; Bozek, J.D.; Bruce, S.; et al. Auger electron and photoabsorption spectra of glycine in the vicinity of the oxygen K-edge measured with an X-FEL. *J. Phys. B At. Mol. Opt. Phys.* **2015**, *48*, 234004. [[CrossRef](#)]
27. Koch, M.; Wolf, T.J.A.; Gühr, M. Understanding the modulation mechanism in resonance-enhanced multiphoton probing of molecular dynamics. *Phys. Rev. A* **2015**, *91*. [[CrossRef](#)]
28. Wolf, T.J.A.; Parrish, R.M.; Myhre, R.H.; Martínez, T.J.; Koch, H.; Gühr, M. Observation of Ultrafast Intersystem Crossing in Thymine by Extreme Ultraviolet Time-Resolved Photoelectron Spectroscopy. *J. Phys. Chem. A* **2019**, *123*, 6897–6903. [[CrossRef](#)] [[PubMed](#)]
29. Werme, L.O.; Bergmark, T.; Siegbahn, K. The High Resolution  $L_{2,3}$  MM and  $M_{4,5}$  NN Auger Spectra from Krypton and  $M_{4,5}$  NN and  $N_{4,5}$  OO Auger Spectra from Xenon. *Phys. Scr.* **1972**, *6*, 141–150. [[CrossRef](#)]
30. Braune, M.; Buck, J.; Kuhlmann, M.; Grunewald, S.; Düsterer, S.; Viehhaus, J.; Tiedtke, K. Non-invasive online wavelength measurements at FLASH2 and present benchmark. *J. Synchrotron Rad.* **2018**, *25*, 3–15. [[CrossRef](#)]
31. Arslançan, S.; Martínez-Fernández, L.; Corral, I. Photophysics and Photochemistry of Canonical Nucleobases' Thioanalogs: From Quantum Mechanical Studies to Time Resolved Experiments. *Molecules* **2017**, *22*, 998. [[CrossRef](#)]
32. Giuliano, B.M.; Feyer, V.; Prince, K.C.; Coreno, M.; Evangelisti, L.; Melandri, S.; Caminati, W. Tautomerism in 4-Hydroxypyrimidine, S-Methyl-2-thiouracil, and 2-Thiouracil. *J. Phys. Chem. A* **2010**, *114*, 12725–12730. [[CrossRef](#)]
33. Föhlisch, A.; Feulner, P.; Hennies, F.; Fink, A.; Menzel, D.; Sanchez-Portal, D.; Echenique, P.M.; Wurth, W. Direct observation of electron dynamics in the attosecond domain. *Nature* **2005**, *436*, 373–376. [[CrossRef](#)] [[PubMed](#)]
34. Beckwith, J.S.; Rumble, C.A.; Vauthey, E. Data analysis in transient electronic spectroscopy—An experimentalist's view. *Int. Rev. Phys. Chem.* **2020**, *39*, 135–216. [[CrossRef](#)]

35. Savelyev, E.; Boll, R.; Bomme, C.; Schirmel, N.; Redlin, H.; Erk, B.; Düsterer, S.; Müller, E.; Höppner, H.; Toleikis, S.; et al. Jitter-correction for IR/UV-XUV pump-probe experiments at the FLASH free-electron laser. *New J. Phys.* **2017**, *19*, 043009. [[CrossRef](#)]
36. Dziarzhytski, S.; Biednov, M.; Dicke, B.; Wang, A.; Miedema, P.S.; Engel, R.Y.; Schunck, J.O.; Redlin, H.; Weigelt, H.; Siewert, F.; et al. The TRIXS end-station for femtosecond time-resolved resonant inelastic x-ray scattering experiments at the soft x-ray free-electron laser FLASH. *Struct. Dyn.* **2020**, *7*, 054301. [[CrossRef](#)] [[PubMed](#)]
37. Trebino, R. *Frequency-Resolved Optical Gating: The Measurement of Ultrashort Laser Pulses*; Springer Science & Business Media: New York, NY, USA, 2000; ISBN 978-1-4613-5432-1.
38. Schulz, S.; Grguraš, I.; Behrens, C.; Bromberger, H.; Costello, J.T.; Czwalińska, M.K.; Felber, M.; Hoffmann, M.C.; Ilchen, M.; Liu, H.Y.; et al. Femtosecond all-optical synchronization of an X-ray free-electron laser. *Nat. Commun.* **2015**, *6*, 5938. [[CrossRef](#)]
39. Schulz, S.; Czwalińska, M.K.; Felber, M.; Predki, P.; Schefer, S.; Schlarb, H.; Wegner, U. Femtosecond-precision synchronization of the pump-probe optical laser for user experiments at flash. In Proceedings of the Advances in X-ray Free-Electron Lasers ii: Instrumentation, Prague, Czech Republic, 17–19 April 2013; Tschentscher, T., Tiedtke, K., Eds.; SPIE-Int Soc Optical Engineering: Bellingham, WA, USA, 2013; Volume 8778.





**Publisher's Note:** MDPI stays neutral with regard to jurisdictional claims in published maps and institutional affiliations.



© 2020 by the authors. Licensee MDPI, Basel, Switzerland. This article is an open access article distributed under the terms and conditions of the Creative Commons Attribution (CC BY) license (<http://creativecommons.org/licenses/by/4.0/>).

## Article

# Core-Level Spectroscopy of 2-Thiouracil at the Sulfur L<sub>1</sub>- and L<sub>2,3</sub>-Edges Utilizing a SASE Free-Electron Laser

Fabiano Lever<sup>1</sup>, Dennis Mayer<sup>1</sup> , Jan Metje<sup>1</sup>, Skirmantas Alisauskas<sup>2</sup>, Francesca Calegari<sup>3,4,5</sup>, Stefan Düsterer<sup>2</sup>, Raimund Feifel<sup>6</sup>, Mario Niebuhr<sup>1</sup> , Bastian Manschwetus<sup>2</sup>, Marion Kuhlmann<sup>2</sup>, Tommaso Mazza<sup>7</sup>, Matthew Scott Robinson<sup>1,2,3,4</sup>, Richard J. Squibb<sup>6</sup>, Andrea Trabattoni<sup>3</sup> , Måns Wallner<sup>6</sup>, Thomas J. A. Wolf<sup>8</sup>  and Markus Gühr<sup>1,\*</sup>

- <sup>1</sup> Institut für Physik und Astronomie, Universität Potsdam, 14476 Potsdam, Germany; fabiano.lever@uni-potsdam.de (F.L.); dmayer@uni-potsdam.de (D.M.); metje.jan@gmail.com (J.M.); mniebuhr@uni-potsdam.de (M.N.); matthew.robinson@desy.de (M.S.R.)
- <sup>2</sup> Deutsches Elektronen Synchrotron (DESY), 22607 Hamburg, Germany; skirmantas.alisauskas@desy.de (S.A.); stefan.duesterer@desy.de (S.D.); bastian.manschwetus@desy.de (B.M.); marion.kuhlmann@desy.de (M.K.)
- <sup>3</sup> Center for Free-Electron Laser Science (CFEL), Deutsches Elektronen Synchrotron (DESY), Notkestraße 85, 22607 Hamburg, Germany; francesca.calegari@desy.de (F.C.); andrea.trabattoni@desy.de (A.T.)
- <sup>4</sup> The Hamburg Centre for Ultrafast Imaging, Universität Hamburg, 22761 Hamburg, Germany
- <sup>5</sup> Institut für Experimentalphysik, Universität Hamburg, 22761 Hamburg, Germany
- <sup>6</sup> Department of Physics, Gothenburg University, SE-41296 Gothenburg, Sweden; raimund.feifel@physics.gu.se (R.F.); richard.squibb@physics.gu.se (R.J.S.); mans.wallner@physics.gu.se (M.W.)
- <sup>7</sup> European XFEL, 22869 Schenefeld, Germany; tommaso.mazza@xfel.eu
- <sup>8</sup> Stanford PULSE Institute, SLAC National Accelerator Laboratory, Menlo Park, CA 94025, USA; thomas.wolf@stanford.edu
- \* Correspondence: mguehr@uni-potsdam.de



**Citation:** Lever, F.; Mayer, D.; Metje, J.; Alisauskas, S.; Calegari, F.; Düsterer, S.; Feifel, R.; Niebuhr, M.; Manschwetus, B.; Kuhlmann, M.; et al. Core-Level Spectroscopy of 2-Thiouracil at the Sulfur L<sub>1</sub>- and L<sub>2,3</sub>-Edges Utilizing a SASE Free-Electron Laser. *Molecules* **2021**, *26*, 6469. <https://doi.org/10.3390/molecules26216469>

Academic Editor: R. Daniel Little

Received: 6 October 2021

Accepted: 22 October 2021

Published: 26 October 2021

**Publisher's Note:** MDPI stays neutral with regard to jurisdictional claims in published maps and institutional affiliations.



**Copyright:** © 2021 by the authors. Licensee MDPI, Basel, Switzerland. This article is an open access article distributed under the terms and conditions of the Creative Commons Attribution (CC BY) license (<https://creativecommons.org/licenses/by/4.0/>).

**Abstract:** In this paper, we report X-ray absorption and core-level electron spectra of the nucleobase derivative 2-thiouracil at the sulfur L<sub>1</sub>- and L<sub>2,3</sub>-edges. We used soft X-rays from the free-electron laser FLASH2 for the excitation of isolated molecules and dispersed the outgoing electrons with a magnetic bottle spectrometer. We identified photoelectrons from the 2p core orbital, accompanied by an electron correlation satellite, as well as resonant and non-resonant Coster–Kronig and Auger–Meitner emission at the L<sub>1</sub>- and L<sub>2,3</sub>-edges, respectively. We used the electron yield to construct X-ray absorption spectra at the two edges. The experimental data obtained are put in the context of the literature currently available on sulfur core-level and 2-thiouracil spectroscopy.

**Keywords:** X-ray; photoelectron; sulfur; thiouracil; nucleobases; Coster–Kronig; Auger–Meitner; NEXAFS; FLASH

## 1. Introduction

Recent years have seen increasing interest in the study of sulfur-substituted nucleobases, known as thionucleobases, for applications in medicine and biochemistry [1,2]. They differ from their canonical counterparts in their response to UV radiation. The substitution of an oxygen atom with the much heavier sulfur atom significantly changes the potential energy landscape, affecting how the molecules interact with light. The absorption spectrum is shifted from UVC into the UVA range, and the resulting excitation produces long-lived triplet states [3–8]. Their reactive triplet state makes thionucleobases useful as cross-linking agents [9,10], as well as candidates for photoinduced cancer treatment [11,12].

Ultrafast radiationless transitions are crucial in funneling the molecular population from the initially excited <sup>1</sup>ππ\* states into the long-lived <sup>3</sup>ππ\* states. The details of these dynamics have been the topic of theoretical and experimental efforts (see Ref. [8] and the references therein). The particular thionucleobase 2-thiouracil (2-tUra) is among the most studied systems. Its static potential energy landscape properties indicate the existence

of several conical intersection (CI) seams [13]. Dynamical simulations predict how an initially UV-excited population traverses the CI regions to end up in the lowest  $^3\pi\pi^*$  state. Experiments using UV pump and visible-ultraviolet probe pulses in solvents [4,14] and in the gas phase [14–16] confirm the ultrafast nature of the molecular transitions. The combination of dynamics predictions with experimental transient spectra present a powerful approach to deduce molecular dynamics. These combined studies suggested ultrafast sub-picosecond transitions from the  $^1\pi\pi^*$  to a  $^1n\pi^*$  ‘doorway’ state, from which the lower-lying triplet states are accessed [14,16].

Using ultrafast X-ray pulses to probe molecular dynamics via core-electron excitations provides insight into the molecular dynamics, a process which is complementary to the well-established probe methods that utilize valence electron transitions [17]. X-rays provide an element-sensitive probe as the core-level electron binding energies differ strongly among elements. The tight binding afforded also makes this method highly spatially selective. This particular advantage has been used to examine the  $^1n\pi^*$  channel via UV-pump X-ray probe studies on thymine [18,19]. For 2-tUra, we used the sulfur L-edges to probe the local dynamics at the C-S bond using time-resolved Auger–Meitner spectroscopy [20]. In addition, we could attribute electronic states using the excited-state chemical shift (ESCS) resulting from the local charge at the sulfur atom probed in time-resolved X-ray photoelectron studies [21].

In this paper, we present a static X-ray spectroscopic study of 2-tUra performed at the sulfur L-edge. Our work includes near-edge absorption fine structure (NEXAFS) spectra at the  $L_1$ - and  $L_{2,3}$ -edges, as well as photoelectron spectra involving the 2s and 2p core-holes. We furthermore investigate the Auger–Meitner spectra induced by sulfur 2p vacancies and the Coster–Kronig decay of the sulfur 2s core-hole as a function of X-ray energy.

## 2. Results

We first investigated the photon-energy range of the sulfur  $L_{2,3}$ -edge creating a sulfur 2p core hole through either resonant transitions to core-valence excited states or non-resonant promotion of the core electron into the continuum. The FEL photon energy  $h\nu$  was scanned over the ionization edge region from  $h\nu = 155$  to 175 eV, with 0.75 eV steps in randomized order; the averaged FEL bandwidth was about 4 eV. For each photon energy setting, a full electron spectrum of 2-tUra was recorded. The electron time-of-flight spectra were converted to the kinetic energy scale by taking the Jacobian correction in the binning process into account. The results are shown in Figure 1a, with electron spectral intensity shown in the form of grayscale false-color code as a function of electron kinetic energy and photon energy.

The 2D spectrum shows two qualitatively different groups of features. First, we discerned a group of maxima that did not change their kinetic energy as the photon energy was varied. We refer to these as ‘non-dispersing’ lines or bands. The strongest is a broad line at 140 eV with a width of  $\sim 9$  eV, which appears from photon energies of 167 eV and higher. This component is accompanied by a weaker one at  $E_{\text{kin}} = 130$  eV and a smaller background towards lower kinetic energies.

The second group of features are ‘dispersing’, meaning they change their kinetic energy with  $h\nu$ . In the photon energy range of 155–163 eV, we observed several such lines which changed  $E_{\text{kin}}$  linearly with  $h\nu$  in the kinetic energy range above 120 eV. The highest kinetic energy lines also continued to be visible for larger photon energies up to 175 eV. A further dispersing line starting at  $E_{\text{kin}} = 48$  eV at  $h\nu = 155$  eV also linearly changed its kinetic energy with  $h\nu$ . This line is not part of the molecule and we discuss it further in the discussion below. An additional transition region was visible around  $h\nu = 165$  to 167 eV, where dispersive features convert into non-dispersive bands. In this region, a line with ‘negative’ dispersion seems to change from high to lower kinetic energies around  $E_{\text{kin}} = 140$  eV. We integrated the full two-dimensional spectrum over the kinetic energy range and present it as a function of photon energy in Figure 1b. The NEXAFS spectrum obtained in this way

shows a decreasing electron yield (absorption) from the lowest  $h\nu$  to about 165 eV, where the absorption rises. This rise occurs over a photon energy interval of  $\sim 2$  eV.

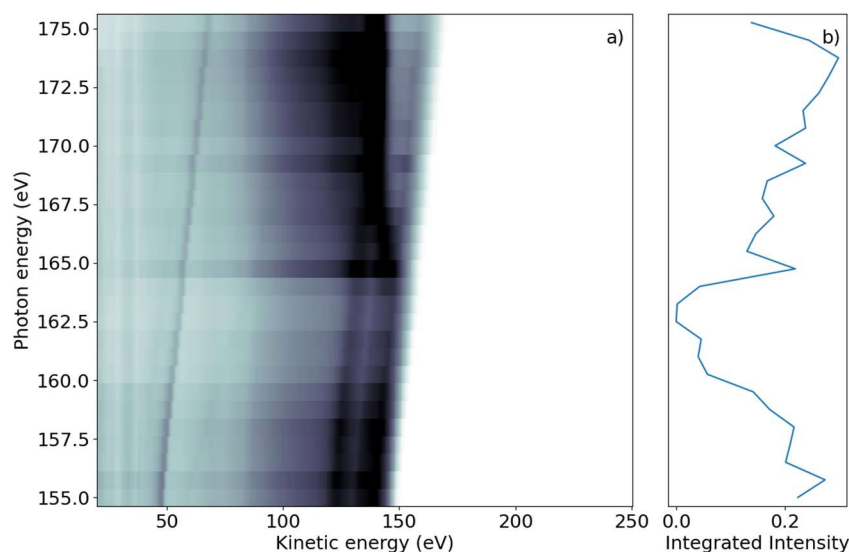


**Figure 1.** (a) Photon energy vs. electron kinetic energy for the 2-tUra sulfur 2p edge. The valence emission can be discerned as dispersing diagonal lines. Resonant and non-resonant Auger–Meitner emission splits off from the valence signal when the photon energy reaches the 2p binding energy. (b) NEXAFS spectrum obtained by integrating the electron emission intensity over the whole kinetic energy range. The 2p edge marks an increase in emitted signal, with some spectral features visible as peaks in the NEXAFS.

We subsequently demonstrate the energy range around the sulfur  $L_1$ -edge, which creates features connected to a sulfur 2s core-hole. We scanned the photon energy in the range of 206 to 240 eV, with 1 eV steps. Figure 2a shows a false-color 2D spectrum of electron yield as a function of kinetic energy and photon energy. Similar to the  $L_{2,3}$  spectrum, we again identified dispersing and non-dispersing lines. The most prominent dispersing feature changes  $E_{kin}$  linearly with  $h\nu$  from  $E_{kin} = 38.5$  eV to 75 eV over the full range shown in Figure 2a. The line is accompanied by a weaker dispersing line shifted by 6 eV towards lower kinetic energy. In addition, weaker dispersing features from valence ionization are visible for kinetic energies over 150 eV and up to 200 eV for the lowest photon energy.

In the lower kinetic energy range, we observed a non-dispersing broad line centered around  $E_{kin} = 42.5$  eV. At higher kinetic energies, we observed a non-dispersing band around  $E_{kin} = 140$  eV with a tail towards lower energies. Analogous to the  $L_{2,3}$ -edge, we generated a NEXAFS spectrum from the integrated electron yield, shown in Figure 2b. In addition to the decrease in intensity from lower to higher photon energies, an absorption increase starting at  $h\nu = 222$  eV with a maximum at  $h\nu = 227$  eV was observed.

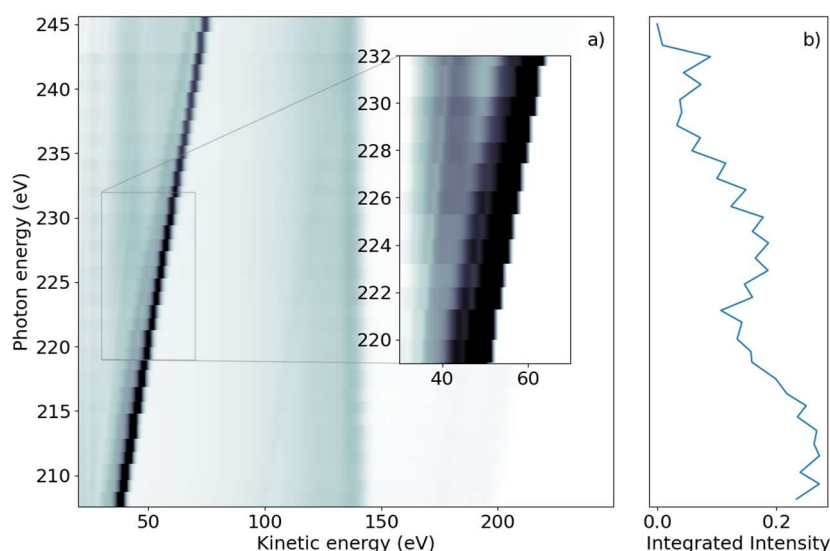


**Figure 2.** (a) Photon energy vs. kinetic energy for the 2-tUra sulfur 2s edge, with the photon energy varying from 208 eV to 245 eV. The bright diagonal feature is the dispersing 2p photoelectron line. A satellite photoelectron line is visible to the left of the main feature. Non-resonant 2p Auger–Meitner electron emission can be seen in the 100 eV to 150 eV range. Coster–Kronig electrons from the 2p  $\rightarrow$  2s decay are visible at 40 eV for photon energies above 220 eV. The dispersing dip overlapping the Coster–Kronig feature visible in the inset is an artifact of the readout electronics. (b) NEXAFS spectrum obtained by integrating the emission intensity over the whole kinetic energy range.

### 3. Discussion

We first discuss the spectra at the sulfur  $L_{2,3}$ -edge. According to calculations [22], the ionization potential of sulfur is given as 162.5 eV and 163.6 eV for the two spin-orbit split components  $2p_{3/2}$  and  $2p_{1/2}$ , respectively. Photoelectron measurements of 2-tUra found the ionization potential values to be 168.17 eV and 169.37 eV for the spin-orbit split components [23]. The photon energy window from  $h\nu = 155$  eV to 176 eV in Figure 1 thus spans from well below to above the ionization potential.

At the lowest photon energies, the spectrum must be dominated by valence emission, and we can clearly identify dispersing features with a high energy edge around 150 eV kinetic energy. We thus compare the electron spectrum to the He-lamp induced valence photoemission spectrum taken over a range of only 10 eV (from 8 to 18 eV binding energy) [24]. Figure 3 shows a photoelectron spectrum taken at FLASH2 at  $h\nu = 155.75$  eV (blue line). The inset of Figure 3 compares a small region of that spectrum with the photoelectron spectrum obtained using the He (I) line at  $h\nu = 21.2$  eV. While the He spectrum shows rich detail attributed to photoemission from different valence orbitals [24], our spectrum at FLASH2 is only weakly modulated as a function of  $E_{kin}$ . The ionization potential overlaps with the measured ionization potential of 8.8 eV [24]. The poor modulation of the FLASH2 valence photoelectron spectrum in Figures 1 and 3 is a combined effect of the photon energy bandwidth of 4 eV and the reduced resolution of the magnetic bottle spectrometer at these comparatively high kinetic energies. The magnetic bottle was operated at retardation of only 5 eV; taking the measured 1/40 resolution [25], we arrive at a feature width of about 4 eV at  $E_{kin} = 150$  eV. The valence features disperse with a slope of one in  $h\nu$  per eV in  $E_{kin}$  throughout the whole measurement range, confirming the use of fundamental undulator radiation.

A second dispersive feature, starting at  $E_{kin} = 47.9$  eV, has a binding energy of 108 eV (see also Figure 2). The slope, equal to the slope of the valence lines, indicates its origin from photoemission with the fundamental of the undulator. We suggest that this line stems from the Al tip of the oven, sitting at a distance of a few mm from the interaction region but still being hit by some halo of the X-ray beam. The 2s line of Al is nominally expected

to be around 120 eV, but due to patch charges at the oxidized tip, this line might be shifted by a few eV towards its apparent binding energy of 108 eV.

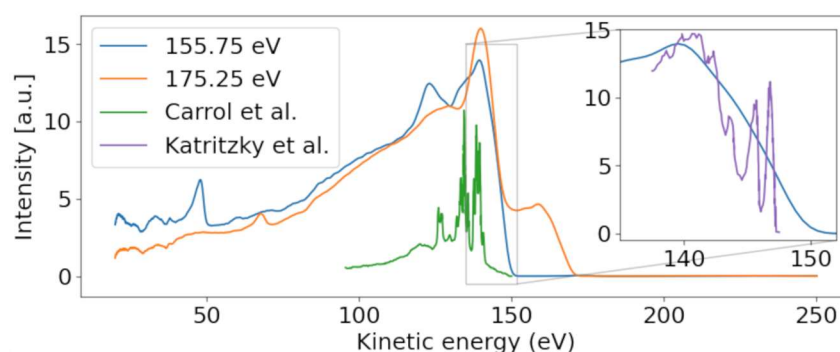


**Figure 3.** Photoelectron spectra for photon energies above (175.25 eV) and below (157.25 eV) the sulfur 2p binding energy. A dispersive behavior of the valence band is visible, moving from ~140 to ~160 eV with increasing photon energy. Our valence spectrum at  $h\nu = 155.75$  eV is compared with a He-lamp-induced valence photoelectron spectrum (purple) from Ref. [24] in the inset, which is scaled in kinetic energy according to the difference of photon energies used in the experiments. Conversely, the Auger–Meitner feature is only present for the higher photon energy. The Auger–Meitner data are compared with the sulfur Auger–Meitner spectrum of OCS (green) from Ref. [26].

We now concentrate on the non-dispersive features. At the limit of the highest photon energy in Figure 1, we observe a non-dispersive band peaking at 140 eV, shown in the orange line in Figure 3. As the photon energy of 175.25 eV is above the ionization limit for the sulfur 2p electrons, we assume that these features belong to non-resonant Auger–Meitner (NAM) decay of 2-tUra. An Auger–Meitner spectrum of the molecule is not available; we therefore compare the features with a sulfur L-MM Auger–Meitner spectrum of OCS (green line Figure 3) from Ref. [26]. The OCS reference shows four dominant groups of lines, which are attributed to different bands of dicationic final states in Ref. [26]. Generally, we observe less resolved features than in the OCS reference. On the one hand, this is due to the reduced resolution of our magnetic bottle spectrometer. On the other hand, larger species such as 2-tUra tend to not show resolved features on the eV scale. This argument can be made in analogy to thymine and its fragment isocyanic acid (HNCO). While the Auger–Meitner spectrum of the latter shows details on an eV scale in analogy to OCS, thymine only exhibits broad bands about 10 eV wide [27]. This effect is due to the increased density of final dicationic states in NAM decay for growing molecular size. The different bands at 140 and 130 eV correspond to broadened bands in the OCS spectrum. We do not know the exact electronic configuration of the valence dicationic states after Auger decay of the sulfur core-hole. However, the sulfur atom has two valence orbitals that must be strongly involved in the sulfur core hole decay: a strongly bound 3s and a shallow bound 3p valence orbital. A decay involving strongly bound valence orbitals in dicationic states leads to less kinetic energy of the Auger electron. Therefore, a very coarse interpretation can attribute the different band ‘humps’ at 140, 130, and 105 eV to dicationic decays with two valence holes dominated by sulfur  $3p^{-2}$ ,  $3p^{-1}3s^{-1}$ , and  $3s^{-2}$  configurations, respectively. The hole-character refers to the sulfur atomic orbital contained in the molecular orbitals.

The NEXAFS spectrum in Figure 1b shows an intensity decrease from lower  $h\nu$  up to about 164 eV, where the integrated electron yield in the spectrum increases. This is about 4 eV below the first sulfur 2p binding energy and thus in the region of core-to-valence resonances from 2p core levels to unoccupied valence levels. The valence state in the transition needs to fulfill symmetry requirements, meaning it needs to contain either atomic sulfur s or d orbitals. As we do not observe any fine structure because of the comparatively large bandwidth, we have not pursued any calculations of the unoccupied valence electronic states. The lowest unoccupied states of 2-tUra, the so-called  $\pi^*$  resonances, are dominated

by sulfur atomic character. As in every NEXAFS spectrum, a dense series of Rydberg states with many different atomic contributions spans from the lowest resonances up to the ionization limit. There is currently no NEXAFS reference data available for 2-tUra. We thus compare our data to NEXAFS spectra of OCS and CS<sub>2</sub> at the sulfur L<sub>2,3</sub>-edge [28], as well as on dimethyl disulfide at the sulfur L<sub>2,3</sub>- and also L<sub>1</sub>-edges [29]. In CS<sub>2</sub> as well as OCS, the first resonances are described by 2p<sub>3/2</sub> and 2p<sub>1/2</sub> to π\* transitions, located around 163–164 eV and 164–165 eV for CS<sub>2</sub> and OCS, respectively. Higher resonances are attributed to Rydberg-transitions with 4s and 3d sulfur character. Above the ionization limit, the spectra of CS<sub>2</sub> and OCS show a broad shape resonance.

The kinetic energy-resolved region of the core-valence resonances shows so-called resonant Auger–Meitner processes. The resonant Auger–Meitner (RAM) decay [30] has been studied in several molecules, from diatomic to quadratomic [31,32]. Part of our group has studied RAM decay in the nucleobase thymine, where it has been used to infer molecular excited state dynamics [33]. In RAM decay, the initial core-excited neutral state decays into a cationic state, in contrast to decay to dicationic states, as is the case for core-ionized states in a NAM process. We clearly see the effect of the final state in the transition of the RAM to the NAM decay of 2-tUra. At the 1s-π\* resonance, the most prominent feature in the RAM sits at 146 eV, which then transforms into the NAM feature at 140 eV kinetic energy. The shift results from a more attractive dicationic potential for the outgoing Auger–Meitner electron in NAM as compared with the cationic potential in RAM. The transition region of RAM to NAM in thymine shows a very similar shift, appearing as dispersion in the wrong direction, i.e., the kinetic energy decreases as the photon energy increases (see Figure 2 in Ref. [33]). The spectrum in Figure 1 does not possess sufficient kinetic energy resolution to distinguish participator (final states are identical to outer valence ionized final states) and spectator decay (final states possess an excited valence electron corresponding to inner valence ionized final states), in contrast to Ref. [33].

We now discuss features at the L<sub>1</sub>-edge, which implies a sulfur 2s hole being created upon X-ray interaction. Unlike the L<sub>2,3</sub>-edges, only one core-hole state is created here due to the absence of spin-orbit coupling. According to calculations, the binding energy of the sulfur 2s-ionized state is 230 eV [22]. The photon energy window in Figure 2, therefore, contains the sulfur L<sub>1</sub>-edge.

For the discussion, we first concentrate on the most prominent feature in Figure 2: the dispersive line presented more prominently in the inset. Figure 4 presents some lineouts of kinetic energy spectra at specific photon energies. We find a kinetic energy of 39.8 eV at the photon energy of 209.35 eV, corresponding to a binding energy of 169.5 eV. The linewidth is about 4 eV, masking any splitting below that width. We thus conclude that the dispersive feature must be the sulfur 2p photoelectron line at the binding energies of 168.17 eV and 169.37 eV for the 2p<sub>3/2</sub> and 2p<sub>1/2</sub> spin-orbit split components, respectively [23]. The experimentally found dispersion fits to ionization by the first order of undulator radiation from FLASH2.

Parallel to the main photoelectron line, a correlation satellite line [34] appears 5 eV below in kinetic energy, most clearly visible in the hν = 240 eV spectrum (orange line in Figure 4) at a kinetic energy of 68 eV. In an orbital picture, the structure corresponds to a shake-up process from an occupied to an unoccupied valence orbital induced by the sulfur 2p photoionization. Thus, the photoelectron has the energy of the main line reduced by the energy to accomplish that shake-up. Satellite structures of the sulfur 2p photoelectron line have also been documented for comparatively small molecules such as SF<sub>6</sub> [35] or sulfur atoms on a metal surface [36]. For the latter, a similar shift is observed.



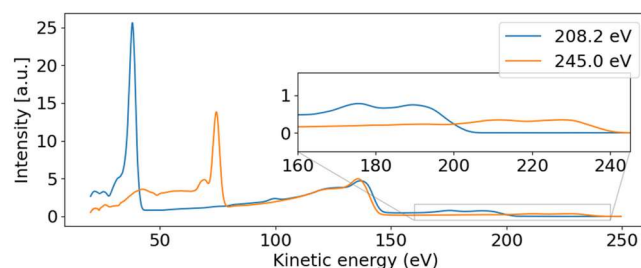


**Figure 4.** Photoelectron spectra for photon energies above ( $\sim 245$  eV) and below ( $\sim 208$  eV) the 2s binding energy. The dispersive behavior of the 2p photoelectron line is visible, moving from 39.8 to 74.4 eV with increasing photon energy. The 2p non-resonant Auger–Meitner band from 100 eV to 144 eV remains stable and is independent of the photon energy. The dispersive valence features are visible in the inset.

The non-dispersive part is composed of the sulfur 2p NAM decay in the 100 to 150 eV kinetic energy range. For photon energies above the 2s binding energy, we also see a non-dispersive feature with a kinetic energy of about 40 eV. We attribute this second feature to the Coster–Kronig spectrum of the 2s hole, which is dominated by one broad peak at 42.5 eV kinetic energy, visible in the orange line of Figure 4. Photon energies above the 2s binding energy are able to create a 2s core hole, which is rapidly filled by a 2p electron in the form of Coster–Kronig decay, ejecting a valence electron in the process. The observed kinetic energy is therefore given by the 2s–2p energy gap, minus the valence binding energy, and is independent of the photon energy that produced the 2s core hole. To our knowledge, there are no S 2s Coster–Kronig spectra documented for molecules. We thus compare the spectra to those of sulfur atoms on surfaces from Ref. [36], showing two bands at 40 and 50 eV kinetic energy, which falls energetically within our observed broad band. Those bands are attributed to  $2s^{-1}$  Coster–Kronig decays with a  $2p^{-1} 3s^{-1}$  and  $2p^{-1} 3p^{-1}$  final state accompanied by a charge transfer from the sulfur atom into the substrate.

The 2p induced NAM decay is visible in both the blue and orange lines of Figure 4, where a slight shift in the peak position is observed. At low photon energies, the 2p decay is induced by 2p photoelectron emission. For the higher photon energies, however, the 2p NAM decay can be induced by both 2p and 2s photoelectron emission. In case of 2s ionization, the 2s Coster–Kronig decay will create a valence hole and 2p-core hole; the latter will then decay via NAM channels. We suggest that the Auger spectra of NAM and Coster–Kronig induced NAM are different because of the additional valence hole. Thus, the shift is caused by photon energy-dependent changes in the relative intensities of the NAM decay channels originating from either 2s or 2p ionization.

For the  $L_1$ -NEXAFS spectrum, we observed the peak of the absorption feature as being between  $h\nu = 225$  and 230 eV. The ‘generic’ binding energy of the 2s electron of 230 eV likely needs to be shifted upwards in the molecule by a few eV in analogy to the 2p electron. Thus, we end up with  $2s-\pi^*$  transitions at the maximum of the NEXAFS spectrum. Again, because of a lack of molecular NEXAFS spectra, we point to Ref. [36] for comparison, where the maximum of the  $2s-3p_z$  absorption was observed at 225 eV.

The relatively large bandwidth of the X-rays—of up to 2%—limits the energy resolution in NEXAFS and resonant Auger–Meitner and photoelectron spectroscopy. Nevertheless, we were able to discern features that are attributed to core–valence resonances and core-level electron binding energies. The non-resonant Auger–Meitner and Coster–Kronig features are independent of the initial photon energy and bandwidth. Their shape is therefore governed by the resolution of the electron spectrometer and the number of electronic states accessible by Auger–Meitner and Coster–Kronig decay in large molecules.

#### 4. Materials and Methods

The data were obtained at the FL24 beamline of the FLASH2 free-electron laser (FEL) [37,38] as part of a more extensive investigation of the dynamics following UV excita-

tion [20,21]. An instrument containing sample injection and a magnetic bottle-type electron spectrometer (URSA-PQ, German: Ultraschnelle Röntgenspektroskopie zur Abfrage der Photoenergiekonversion in Quantensystemen, English: Ultrafast X-ray spectroscopy for probing photoenergy conversion in quantum systems)—designed and built by the group at University of Potsdam—was connected to the beamline [25].

At the FLASH FEL, the X-rays are produced by self-amplified spontaneous emission (SASE), and we used photon energies at the FLASH2 branch in the range of 150 eV to 250 eV tuned by variable gap undulators. Rare-gas photoelectron spectrometers built in the beamline, the OPIS (Online PhotoIonization Spectrometer) [39], were used to determine the wavelength and spectrum of the emitted light; for the machine settings used in this study, the average bandwidth (including jitter) was found to be 4 eV. This kind of spectrometer does not provide shot-to-shot resolved data. We instead averaged the OPIS spectra for a complete run with minutes of data to determine the average photon energy value for each photon energy bin. The different step sizes for the two energy scans (1 eV and 0.75 eV) were chosen to allow for efficient use of experimental time; a finer step size of about 4 eV effective bandwidth would not improve the data. We scanned with a slightly larger step size at the  $L_{1}$ -edge, as we expected wider features at the  $L_{1}$ -edge compared with the  $L_{2,3}$ -edge.

The FEL delivers the radiation in trains of pulses with a repetition rate of 10 Hz [40]. Each train consists of 50 pulses at 200 kHz internal repetition rate, with an estimated pulse duration of 150 fs [25]. Pulse energy scans were carried out to avoid X-ray saturation of the obtained electron spectra. During the data collection, the average pulse energy used was 5  $\mu$ J. The X-rays are focused by means of Kirkpatrick–Baez (KB) mirrors to a spot of  $\sim 100$   $\mu$ m size, located in the interaction region of our magnetic bottle electron spectrometer (MBES) [41]. The X-rays are linearly polarized parallel to the axis of the spectrometer.

Figure 5 presents a sketch of the URSA-PQ apparatus. The use of an MBES allows for high collection efficiency. A permanent magnet with a soft iron pole produces a high magnetic field in the interaction region, which adiabatically changes into a homogeneous solenoid field that guides the confined electrons through an almost 2 m long flight tube [41]. The emitted electrons are detected by a multi-channel plate (MCP) assembly at the end of the flight tube. Their kinetic energy can then be obtained from the time-of-flight measurements. A time-of-flight spectrum was recorded for each pulse of the FEL, and the results were subsequently averaged. An electrostatic lens was used to apply a retardation potential to the electrons as they enter the flight tube, slowing them down and thus increasing the time-of-flight resolution. Calibration of the spectrometer was carried out using Kr-MNN Auger–Meitner electrons [25]. Using the calibration data together with a geometric model of the flight tube, a time-of-flight to kinetic energy conversion function was developed. This function was then adapted to enable the conversion of data acquired under different retardation settings. Specifically, we used recorded krypton spectra to construct a model of the spectrometer and extrapolated it to other retardation settings/energy ranges. The resolution ( $E/\Delta E$ ) was found to be around 40 under the chosen settings [25]. For each X-ray pulse, FLASH provides a shot-to-shot measurement of the pulse energy (photon number) through the use of gas-monitor detectors (GMD). We used these data to normalize our electron spectra.

The 2-tUra sample (acquired from Sigma-Aldrich (St. Louis, MO, USA) and used without further processing) was delivered by a capillary oven [42] heated to 150°C and located near the tip of the permanent magnet of the spectrometer. At this oven temperature, the only tautomer is the oxo-form [23], as noted in a comparison of gas-phase 2-tUra experiments [15,23].

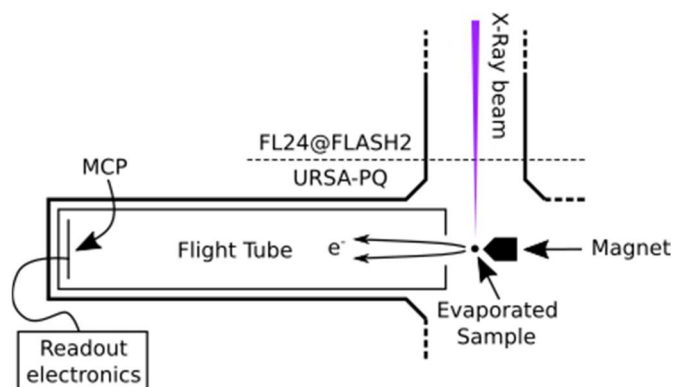


**Figure 5.** Sketch of the experimental setup. The soft X-rays from FLASH2 are focused into the interaction region of the magnetic bottle spectrometer, where the sample is provided by means of a capillary oven (located above the spectrometer, out of plane of the diagram). The emitted photoelectrons enter the flight tube and are detected by an MCP detector.

## 5. Conclusions

Here, we present the results of an X-ray sulfur core-level investigation of 2-thiouracil. The data obtained—primarily covering previously unobserved energy ranges—provide novel information about this molecule which is complementary to the currently available literature.

The valence and 2p photoelectron features present a dispersive character, with the electron kinetic energy linearly following the changes in photon energy. However, the Auger–Meitner and Coster–Kronig decay channels are associated with constant kinetic energies and do not show dispersion.

The previously measured value for the sulfur 2p binding energy in 2-tUra of 168 eV [23] is consistent with our observations for both the 2p photoelectron line kinetic energy and the onset of the 2p Auger–Meitner features. Moreover, our NEXAFS spectra show a similar position of the sulfur-2p edge as the already available ion-yield NEXAFS spectra of related sulfur-containing compounds [28], although with a significantly lower resolution in the finer details of our spectrum. This is due to the large bandwidth of the FEL radiation used, acting to broaden the observed features. The future use of a monochromator would help to increase the energy resolution, as in [19]. It increases the shot-to-shot fluctuations when used with SASE sources, but this can be corrected for on a single-shot basis.

To our knowledge, this work is the first available NEXAFS spectrum of 2-tUra at the sulfur 2p and 2s edges.

The observed 2p Auger–Meitner spectrum does not present any fine structure or discernable lines. In other cases, such as OCS, pronounced features in the sulfur Auger–Meitner spectra were observed [26]. We attribute the lack of fine structure to the relatively high number of atoms forming 2-tUra, leading to a high density of dicationic states and thus leading to spectral congestion [27].

Resonant and non-resonant Auger–Meitner emissions can be distinguished by their kinetic energy, with resonant electrons showing a shift of about 10 eV toward higher kinetic energies. Similar shifts are observed in other molecules [32], and are attributed to the spectating electron affecting the energy landscape in which the decay takes place.

At the sulfur L<sub>1</sub>-edge, we observe the dispersive 2p photoline as well as a broad non-dispersing Coster–Kronig band at around 40 eV. Comparisons to a core level spectroscopy study of sulfur atoms on a metal surface confirm our interpretation of the features in the absence of comparable molecular data for this spectral region.

**Author Contributions:** Data collection: all authors. Data analysis: F.L. and D.M. with the help of M.G. Instrument design/construction: J.M., F.L., D.M. and M.G. with the help of S.D., M.N., M.S.R., R.F. and R.J.S. Paper text: F.L. and M.G. Comments and suggestions on the paper drafts: all authors. All authors have read and agreed to the published version of the manuscript.

**Funding:** We acknowledge the Volkswagen foundation for a Lichtenberg Professorship. We thank the BMBF for URSA-PQ apparatus funding and for funding J.M. and F.L. via Verbundforschungsprojekt 05K16IP1 and 05K19IP1. Furthermore, we acknowledge DFG funding via grant GU 1478/1-1. T.J.A.W was supported by the US Department of Energy, Office of Science, Basic Energy Sciences, Chemical Sciences, Geosciences, and Biosciences Division. F.C. acknowledges support from the European Research Council under ERC-2014-StG STARLIGHT (grant agreement No. 637756). R.F. acknowledges funding from the Swedish Research Council and the Knut and Alice Wallenberg Foundation, Sweden. T.M. acknowledges the support by the SFB 925, Project A3 of the University of Hamburg.

**Institutional Review Board Statement:** Not applicable.

**Informed Consent Statement:** Not applicable.

**Data Availability Statement:** Data is available upon request.

**Acknowledgments:** We acknowledge DESY (Hamburg, Germany), a member of the Helmholtz Association HGF, for the provision of experimental facilities. Part of this research was carried out at FLASH2.

**Conflicts of Interest:** The authors declare no conflict of interest.












**Sample Availability:** Samples of the compounds are available from Sigma-Aldrich.

## References

1. Swann, P.F.; Waters, T.R.; Moulton, D.C.; Xu, Y.-Z.; Zheng, Q.; Edwards, M.; Mace, R. Role of Postreplicative DNA Mismatch Repair in the Cytotoxic Action of Thioguanine. *Science* **1996**, *273*, 1109–1111. [[CrossRef](#)] [[PubMed](#)]
2. Kramer, K.; Sachsenberg, T.; Beckmann, B.M.; Qamar, S.; Boon, K.-L.; Hentze, M.W.; Kohlbacher, O.; Urlaub, H. Photo-Cross-Linking and High-Resolution Mass Spectrometry for Assignment of RNA-Binding Sites in RNA-Binding Proteins. *Nat. Methods* **2014**, *11*, 1064–1070. [[CrossRef](#)]
3. Ashwood, B.; Pollum, M.; Crespo-Hernández, C.E. Photochemical and Photodynamical Properties of Sulfur-Substituted Nucleic Acid Bases. *Photochem. Photobiol.* **2019**, *95*, 33–58. [[CrossRef](#)] [[PubMed](#)]
4. Pollum, M.; Jockusch, S.; Crespo-Hernández, C.E. Increase in the Photoreactivity of Uracil Derivatives by Doubling Thionation. *Phys. Chem. Chem. Phys.* **2015**, *17*, 27851–27861. [[CrossRef](#)]
5. Matsika, S. Modified Nucleobases. In *Photoinduced Phenomena in Nucleic Acids I*; Barbatti, M., Borin, A.C., Ullrich, S., Eds.; Springer International Publishing: Cham, Switzerland, 2014; Volume 355, pp. 209–243. ISBN 978-3-319-13370-13376.
6. Bai, S.; Barbatti, M. Spatial Factors for Triplet Fusion Reaction of Singlet Oxygen Photosensitization. *J. Phys. Chem. Lett.* **2017**, *8*, 5456–5460. [[CrossRef](#)]
7. Bai, S.; Barbatti, M. On the Decay of the Triplet State of Thionucleobases. *Phys. Chem. Chem. Phys.* **2017**, *19*, 12674–12682. [[CrossRef](#)]
8. Arslançan, S.; Martínez-Fernández, L.; Corral, I. Photophysics and Photochemistry of Canonical Nucleobases' Thioanalogs: From Quantum Mechanical Studies to Time Resolved Experiments. *Molecules* **2017**, *22*, 998. [[CrossRef](#)]
9. Brem, R.; Daehn, I.; Karran, P. Efficient DNA Interstrand Crosslinking by 6-Thioguanine and UVA Radiation. *DNA Repair* **2011**, *10*, 869–876. [[CrossRef](#)]
10. Zhang, X.; Jeffs, G.; Ren, X.; O'Donovan, P.; Montaner, B.; Perrett, C.M.; Karran, P.; Xu, Y.-Z. Novel DNA Lesions Generated by the Interaction between Therapeutic Thiopurines and UVA Light. *DNA Repair* **2007**, *6*, 344–354. [[CrossRef](#)] [[PubMed](#)]
11. Massey, A.; Xu, Y.-Z.; Karran, P. Photoactivation of DNA Thiobases as a Potential Novel Therapeutic Option. *Curr. Biol.* **2001**, *11*, 1142–1146. [[CrossRef](#)]
12. Reelfs, O.; Karran, P.; Young, A.R. 4-Thiothymidine Sensitization of DNA to UVA Offers Potential for a Novel Photochemotherapy. *Photochem. Photobiol. Sci.* **2012**, *11*, 148–154. [[CrossRef](#)] [[PubMed](#)]
13. Mai, S.; Marquetand, P.; González, L. A Static Picture of the Relaxation and Intersystem Crossing Mechanisms of Photoexcited 2-Thiouracil. *J. Phys. Chem. A* **2015**, *119*, 9524–9533. [[CrossRef](#)]
14. Sánchez-Rodríguez, J.A.; Mohamadzade, A.; Mai, S.; Ashwood, B.; Pollum, M.; Marquetand, P.; González, L.; Crespo-Hernández, C.E.; Ullrich, S. 2-Thiouracil Intersystem Crossing Photodynamics Studied by Wavelength-Dependent Photoelectron and Transient Absorption Spectroscopies. *Phys. Chem. Chem. Phys.* **2017**, *19*, 19756–19766. [[CrossRef](#)] [[PubMed](#)]
15. Mohamadzade, A.; Bai, S.; Barbatti, M.; Ullrich, S. Intersystem Crossing Dynamics in Singly Substituted Thiouracil Studied by Time-Resolved Photoelectron Spectroscopy: Micro-Environmental Effects Due to Sulfur Position. *Chem. Phys.* **2018**, *515*, 572–579. [[CrossRef](#)]
16. Mai, S.; Mohamadzade, A.; Marquetand, P.; González, L.; Ullrich, S. Simulated and Experimental Time-Resolved Photoelectron Spectra of the Intersystem Crossing Dynamics in 2-Thiouracil. *Molecules* **2018**, *23*, 2836. [[CrossRef](#)]
17. Stolow, A.; Bragg, A.E.; Neumark, D.M. Femtosecond Time-Resolved Photoelectron Spectroscopy. *Chem. Rev.* **2004**, *104*, 1719–1758. [[CrossRef](#)]

18. McFarland, B.K.; Farrell, J.P.; Miyabe, S.; Tarantelli, F.; Aguilar, A.; Berrah, N.; Bostedt, C.; Bozek, J.D.; Bucksbaum, P.H.; Castagna, J.C.; et al. Ultrafast X-Ray Auger Probing of Photoexcited Molecular Dynamics. *Nat. Commun.* **2014**, *5*, 4235. [[CrossRef](#)]
19. Wolf, T.J.A.; Myhre, R.H.; Cryan, J.P.; Coriani, S.; Squibb, R.J.; Battistoni, A.; Berrah, N.; Bostedt, C.; Bucksbaum, P.; Coslovich, G.; et al. Probing Ultrafast  $\Pi\pi^*/N\pi^*$  Internal Conversion in Organic Chromophores via K-Edge Resonant Absorption. *Nat. Commun.* **2017**, *8*, 29. [[CrossRef](#)] [[PubMed](#)]
20. Lever, F.; Mayer, D.; Picconi, D.; Metje, J.; Alisauskas, S.; Calegari, F.; Düsterer, S.; Ehlert, C.; Feifel, R.; Niebuhr, M.; et al. Ultrafast Dynamics of 2-Thiouracil Investigated by Time-Resolved Auger Spectroscopy. *J. Phys. B At. Mol. Opt. Phys.* **2020**, *54*, 014002. [[CrossRef](#)]
21. Mayer, D.; Lever, F.; Picconi, D.; Metje, J.; Alisauskas, S.; Calegari, F.; Düsterer, S.; Ehlert, C.; Feifel, R.; Niebuhr, M.; et al. Following UV-Induced Electronic Dynamics of Thiouracil by Ultrafast x-Ray Photoelectron Spectroscopy. Available online: <https://arxiv.org/abs/2102.13431> (accessed on 25 September 2021).
22. Thompson, A.; Vaughan, D. *X-RAY Data Booklet*; Center for X-ray Optics and Advanced Light Source Lawrence, Berkeley National Laboratory: Berkeley, CA, USA, 2009.
23. Giuliano, B.M.; Feyer, V.; Prince, K.C.; Coreno, M.; Evangelisti, L.; Melandri, S.; Caminati, W. Tautomerism in 4-Hydroxypyrimidine, S-Methyl-2-Thiouracil, and 2-Thiouracil. *J. Phys. Chem. A* **2010**, *114*, 12725–12730. [[CrossRef](#)] [[PubMed](#)]
24. Katritzky, A.R.; Szafran, M.; Pfister-Guillouzo, G. The Tautomeric Equilibria of Thio Analogues of Nucleic Acid Bases. Part 3. Ultraviolet Photoelectron Spectra of 2-Thiouracil and Its Methyl Derivatives. *J. Chem. Soc.* **1990**, *6*, 871–876. [[CrossRef](#)]
25. Metje, J.; Lever, F.; Mayer, D.; Squibb, R.J.; Robinson, M.S.; Niebuhr, M.; Feifel, R.; Düsterer, S.; Gühr, M. URSA-PQ: A Mobile and Flexible Pump-Probe Instrument for Gas Phase Samples at the FLASH Free Electron Laser. *Appl. Sci.* **2020**, *10*, 7882. [[CrossRef](#)]
26. Carroll, T.X.; Ji, D.; Thomas, T.D. Carbon and Oxygen K $\alpha$  and Sulfur L $\alpha$  Auger Spectra of OCS. *J. Electron. Spectrosc. Relat. Phenom.* **1990**, *51*, 471–486. [[CrossRef](#)]
27. Wolf, T.; Holzmeier, F.; Wagner, I.; Berrah, N.; Bostedt, C.; Bozek, J.; Bucksbaum, P.; Coffee, R.; Cryan, J.; Farrell, J.; et al. Observing Femtosecond Fragmentation Using Ultrafast X-ray-Induced Auger Spectra. *Appl. Sci.* **2017**, *7*, 681. [[CrossRef](#)]
28. Ankerhold, U.; Esser, B.; von Busch, F. Ionization and Fragmentation of OCS and CS $_2$  after Photoexcitation around the Sulfur 2p Edge. *Chem. Phys.* **1997**, *220*, 393–407. [[CrossRef](#)]
29. Schnorr, K.; Bhattacharjee, A.; Oosterbaan, K.J.; Delcey, M.G.; Yang, Z.; Xue, T.; Attar, A.R.; Chatterley, A.S.; Head-Gordon, M.; Leone, S.R.; et al. Tracing the 267 nm-Induced Radical Formation in Dimethyl Disulfide Using Time-Resolved X-Ray Absorption Spectroscopy. *J. Phys. Chem. Lett.* **2019**, *10*, 1382–1387. [[CrossRef](#)] [[PubMed](#)]
30. Armen, G.B.; Aksela, H.; Åberg, T.; Aksela, S. The Resonant Auger Effect. *J. Phys. B At. Mol. Opt. Phys.* **2000**, *33*, R49–R92. [[CrossRef](#)]
31. Feifel, R.; Piancastelli, M.N. Core-Level Spectroscopy and Dynamics of Free Molecules. *J. Electron. Spectrosc. Relat. Phenom.* **2011**, *183*, 10–28. [[CrossRef](#)]
32. Holzmeier, F.; Wolf, T.J.A.; Gienger, C.; Wagner, I.; Bozek, J.; Nandi, S.; Nicolas, C.; Fischer, I.; Gühr, M.; Fink, R.F. Normal and Resonant Auger Spectroscopy of Isocyanic Acid, HNCO. *J. Chem. Phys.* **2018**, *149*, 034308. [[CrossRef](#)] [[PubMed](#)]
33. Wolf, T.J.A.; Paul, A.C.; Folkestad, S.D.; Myhre, R.H.; Cryan, J.P.; Berrah, N.; Bucksbaum, P.H.; Coriani, S.; Coslovich, G.; Feifel, R.; et al. Transient Resonant Auger–Meitner Spectra of Photoexcited Thymine. *Faraday Discuss.* **2021**, 228. [[CrossRef](#)] [[PubMed](#)]
34. Svensson, S.; Eriksson, B.; Mårtensson, N.; Wendin, G.; Gelius, U. Electron Shake-up and Correlation Satellites and Continuum Shake-off Distributions in X-Ray Photoelectron Spectra of the Rare Gas Atoms. *J. Electron. Spectrosc. Relat. Phenom.* **1988**, *47*, 327–384. [[CrossRef](#)]
35. Declava, P.; Fronzoni, G.; Kivimäki, A.; Álvarez Ruiz, J.; Svensson, S. Shake-up Transitions in S 2p, S 2s and F 1s Photoionization of the SF $_6$  Molecule. *J. Phys. B At. Mol. Opt. Phys.* **2009**, *42*, 055102. [[CrossRef](#)]
36. Föhlich, A.; Feulner, P.; Hennies, F.; Fink, A.; Menzel, D.; Sanchez-Portal, D.; Echenique, P.M.; Wurth, W. Direct Observation of Electron Dynamics in the Attosecond Domain. *Nature* **2005**, *436*, 373–376. [[CrossRef](#)] [[PubMed](#)]
37. Faatz, B.; Baboi, N.; Ayvazyan, V.; Balandin, V.; Decking, W.; Duesterer, S.; Eckoldt, H.-J.; Feldhaus, J.; Golubeva, N.; Honkavaara, K.; et al. FLASH II: Perspectives and Challenges. *Nucl. Instrum. METHODS Phys. Res. Sect.-Accel. Spectrometers Detect. Assoc. Equip.* **2011**, 635, S2–S5. [[CrossRef](#)]
38. Kuhlmann, M.; Ploenjes, E. FLASH2 Phontodiagnosics and Beamline Concepts. In *Advances in X-ray Free-Electron Lasers II: Instrumentation*; Tschentscher, T., Tiedtke, K., Eds.; SPIE-International Society of Optical Engineering: Bellingham, WA, USA, 2013; Volume 8778.
39. Braune, M.; Buck, J.; Kuhlmann, M.; Grunewald, S.; Düsterer, S.; Viefhaus, J.; Tiedtke, K. Non-Invasive Online Wavelength Measurements at FLASH2 and Present Benchmark. *J. Synchrotron Radiat.* **2018**, *25*, 3–15. [[CrossRef](#)]
40. Faatz, B.; Plönjes, E.; Ackermann, S.; Agababyan, A.; Asgekar, V.; Ayvazyan, V.; Baark, S.; Baboi, N.; Balandin, V.; Von Bargen, N.; et al. Simultaneous Operation of Two Soft X-Ray Free-Electron Lasers Driven by One Linear Accelerator. *New J. Phys.* **2016**, *18*, 062002. [[CrossRef](#)]
41. Kruit, P.; Read, F.H. Magnetic Field Paralleliser for 2 $\pi$  Electron-Spectrometer and Electron-Image Magnifier. *J. Phys. [E]* **1983**, *16*, 313–324. [[CrossRef](#)]
42. McFarland, B.K.; Berrah, N.; Bostedt, C.; Bozek, J.; Bucksbaum, P.H.; Castagna, J.C.; Coffee, R.N.; Cryan, J.P.; Fang, L.; Farrell, J.P.; et al. Experimental Strategies for Optical Pump–Soft x-Ray Probe Experiments at the LCLS. *J. Phys. Conf. Ser.* **2014**, *488*, 012015. [[CrossRef](#)]

# Following excited-state chemical shifts in molecular ultrafast x-ray photoelectron spectroscopy

D. Mayer <sup>1,11</sup>, F. Lever <sup>1,11</sup>, D. Picconi <sup>2✉</sup>, J. Metje<sup>1</sup>, S. Alisauskas <sup>3</sup>, F. Calegari <sup>4,5,6</sup>, S. Düsterer <sup>3</sup>, C. Ehlert <sup>7</sup>, R. Feifel<sup>8</sup>, M. Niebuhr <sup>1</sup>, B. Manschwetus <sup>3</sup>, M. Kuhlmann<sup>3</sup>, T. Mazza<sup>9</sup>, M. S. Robinson<sup>1,4,5</sup>, R. J. Squibb<sup>8</sup>, A. Trabattoni <sup>4</sup>, M. Wallner<sup>8</sup>, P. Saalfrank<sup>2</sup>, T. J. A. Wolf <sup>10</sup> & M. Gühr<sup>1✉</sup>

The conversion of photon energy into other energetic forms in molecules is accompanied by charge moving on ultrafast timescales. We directly observe the charge motion at a specific site in an electronically excited molecule using time-resolved x-ray photoelectron spectroscopy (TR-XPS). We extend the concept of static chemical shift from conventional XPS by the excited-state chemical shift (ESCS), which is connected to the charge in the framework of a potential model. This allows us to invert TR-XPS spectra to the dynamic charge at a specific atom. We demonstrate the power of TR-XPS by using sulphur 2*p*-core-electron-emission probing to study the UV-excited dynamics of 2-thiouracil. The method allows us to discover that a major part of the population relaxes to the molecular ground state within 220–250 fs. In addition, a 250-fs oscillation, visible in the kinetic energy of the TR-XPS, reveals a coherent exchange of population among electronic states.

<sup>1</sup>Institut für Physik und Astronomie, Universität Potsdam, 14476 Potsdam, Germany. <sup>2</sup>Institut für Chemie, Universität Potsdam, 14476 Potsdam, Germany. <sup>3</sup>Deutsches Elektronen Synchrotron (DESY), 22607 Hamburg, Germany. <sup>4</sup>Center for Free-Electron Laser Science (CFEL), Deutsches Elektronen Synchrotron (DESY), 22607 Hamburg, Germany. <sup>5</sup>The Hamburg Centre for Ultrafast Imaging, Universität Hamburg, 22761 Hamburg, Germany. <sup>6</sup>Institut für Experimentalphysik, Universität Hamburg, 22761 Hamburg, Germany. <sup>7</sup>Heidelberg Institute for Theoretical Studies, HITS gGmbH, 69118 Heidelberg, Germany. <sup>8</sup>Department of Physics, University of Gothenburg, SE-41296 Gothenburg, Sweden. <sup>9</sup>European XFEL, 22869 Schenefeld, Germany. <sup>10</sup>Stanford PULSE Institute, SLAC National Accelerator Laboratory, Menlo Park, CA 94025, USA. <sup>11</sup>These authors contributed equally: D. Mayer, F. Lever. ✉email: [david.picconi@uni-potsdam.de](mailto:david.picconi@uni-potsdam.de); [mguehr@uni-potsdam.de](mailto:mguehr@uni-potsdam.de)

Light-induced charge flow in molecules forms the basis to convert photon energy into other energetic forms. The excitation of valence electrons by light triggers a change in charge density that eventually couples to nuclear motion. The complex interplay of nuclear and electronic degrees of freedom in the electronically excited states continues to move charge on an ultrafast time-scale by nonadiabatic couplings<sup>1</sup>. This in turn gives rise to phenomena like photoisomerization<sup>2</sup> and proton-coupled electron transfer<sup>3</sup> with rich applications in light-harvesting and photocatalysis<sup>4</sup>. Finding a way to image the charge flow in electronically excited systems, including organic molecules, on its natural timescale and with atomic precision would provide new ground for understanding molecular photophysics and excited-state (ES) reactivity.

X-ray photoelectron spectroscopy (XPS) is a proven tool to obtain information about local charge with atomic specificity in electronic ground states<sup>5</sup>. The tight localisation of core orbitals makes the method site selective. The ionisation potential (IP) measures the difference between neutral state and core-ionised state at a particular atom in a molecule. The so-called chemical shift (CS) of the IP reflects the charge at, and in close vicinity of, the probed atom. Within the potential approximation, the CS can be directly converted into local charge<sup>6</sup>.

In this paper we generalise the CS concept known from conventional, static XPS to electronically excited states, introducing the excited-state chemical shift (ESCS, not to be confused with the ESCS in nuclear magnetic resonance). We test this on the thionucleobase 2-thiouracil (2-tUra), which is photoexcited to a  $\pi\pi^*$  state by an ultraviolet (UV) light pulse (Fig. 1). The S 2*p* photoionization with a soft x-ray pulse, of photon energy  $h\nu$ ,

leads to a photoelectron with kinetic energy  $E_{\text{kin}} = h\nu - E_{\text{bind}}$ . The molecular UV photoexcitation changes the local charge density at the probed atom (Fig. 1b bottom), which leads to a specific ESCS. We find a direct relation between the ESCS and the local charge at the probe site in analogy to the potential model for the CS in static XPS<sup>6</sup>. This allows one to circumvent complex calculations of IPs, while allowing for an interpretation based on chemical intuition. We show that the largest effect on the ESCS is due to electronic relaxation, especially if the local charge at the probed atom is grossly changed in the process. A smaller, but non-negligible effect, stems from geometry changes, which can also alter local charge at the probed atom.

Our studies extend existing theoretical<sup>7–10</sup> and experimental<sup>11–13</sup> time-resolved (TR)-XPS by the demonstration of direct local charge recovery from ESCS. The x-ray typical element- and site-specific responses<sup>14,15</sup> are also accomplished using the now well-established TR x-ray absorption spectroscopy (TR-XAS) method. In the soft x-ray range, TR-XAS has the capability to monitor electronic and nuclear dynamics<sup>16–18</sup>, which has been demonstrated in ring-opening reactions<sup>19</sup>, dissociation<sup>20</sup>, intersystem-crossing<sup>21</sup>, ionisation<sup>22</sup> as well as the interplay between  $\pi\pi^*$  and  $n\pi^*$  valence electronic states<sup>23,24</sup>. Hard x-ray absorption and emission spectroscopy is highly sensitive to charge and spin states, however, only on metal atoms within molecules<sup>25,26</sup>. The novel TR-XPS extends this characteristic to lighter atoms and has the advantage that a fixed x-ray wavelength can be used to address several elements and sites. In addition, the use for molecules in thick solvent jets can also be accomplished by employing harder x-rays for increased penetration depth of the radiation as well as escape depth of the photoelectrons for light-element XPS.

We demonstrate the opportunities provided by TR-XPS on electronically excited states of a thionucleobase. Photoexcited thionucleobases are interesting because of efficient relaxation into long-lived triplet states (see Ref. 27,28 and references therein) triggering applications as photoinduced cross-linkers<sup>29,30</sup> and photoinduced cancer therapy<sup>28</sup>. Among those, 2-tUra is one of the most-studied cases on an ultrafast scale<sup>27</sup>, both experimentally, using transient absorption<sup>31</sup> and photoelectron spectroscopy<sup>31–33</sup>, and theoretically in static calculations<sup>34</sup> and surface hopping trajectory simulations<sup>35,36</sup>. The latter predict coherent population exchange among electronic states. The model emerging from joint experimental-theoretical investigations includes ultrafast internal conversion from the photoexcited  $S_2$   $\pi\pi^*$  state into the  $S_1$   $n\pi^*$  state, followed by a sub-picosecond intersystem crossing<sup>32</sup>. Relaxation from the triplet states to the ground state has previously been observed with a time constant of several ten picoseconds<sup>32</sup> while also indirect evidence for an ultrafast direct ground-state (GS) relaxation from the photoexcited state has been reported<sup>37</sup>.

In this work, we show that TR-XPS on electronically excited states allows us to identify the relaxation paths of 2-tUra by direct analysis of the ESCS and in addition comparisons to the calculated binding energy of different states and geometries. Most interestingly, we identify a ground state relaxation and the predicted coherent electronic population oscillation modulating the sulphur 2*p* binding energy periodically.

## Results

**Difference spectra.** Figure 2a shows a photoelectron spectrum of 2-tUra obtained at the FLASH2 free-electron laser (FEL)<sup>38</sup> using a nominal photon energy of 272 eV and an average bandwidth of 1–2%. The electron spectra are taken with a magnetic-bottle electron spectrometer (MBES). We identify the sulphur 2*p*-photoelectron line (blue) at a kinetic energy of 103.5 eV in agreement with the literature<sup>39</sup>. The width of about 4 eV does prevent us from distinguishing the spin-orbit splitting<sup>39,40</sup>. The photoelectron line is accompanied by shake-up satellites at around 91 and

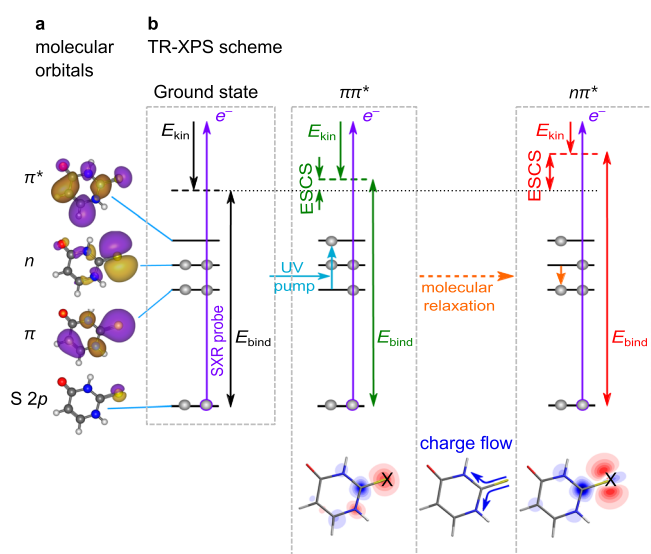


**Fig. 1 Schematic picture of TR-XPS and ESCS in 2-thiouracil in a molecular orbital representation.** **a** Molecular valence ( $\pi$ ,  $n$ ,  $\pi^*$ ) orbitals and a core (sulphur 2*p*) orbital. **b** Probe of the S 2*p* core level with a binding energy  $E_{\text{bind}}$  by means of a soft x-ray (SXR) light pulse, leading to a photoelectron with a kinetic energy,  $E_{\text{kin}}$ . A UV pump pulse (cyan arrow) excites the 2-thiouracil from its electronic ground state ( $S_0$ ) to a  $\pi\pi^*$  state ( $S_2$ ) which then relaxes further, for instance into the  $S_1$  ( $n\pi^*$ ) state shown here. The difference in  $E_{\text{bind}}$  with respect to the ground state is the excited-state chemical shift ( $\text{ESCS} = E_{\text{bind}}^{\text{excited state}} - E_{\text{bind}}^{\text{ground state}}$ ). The molecular structures in the lower part of the panel represent the difference in charge density between the ground state and the respective excited states (red: decreased electron density, blue: increased electron density). Increase in positive charge at the sulphur site (marked with X) increases  $E_{\text{bind}}$  and the ESCS.

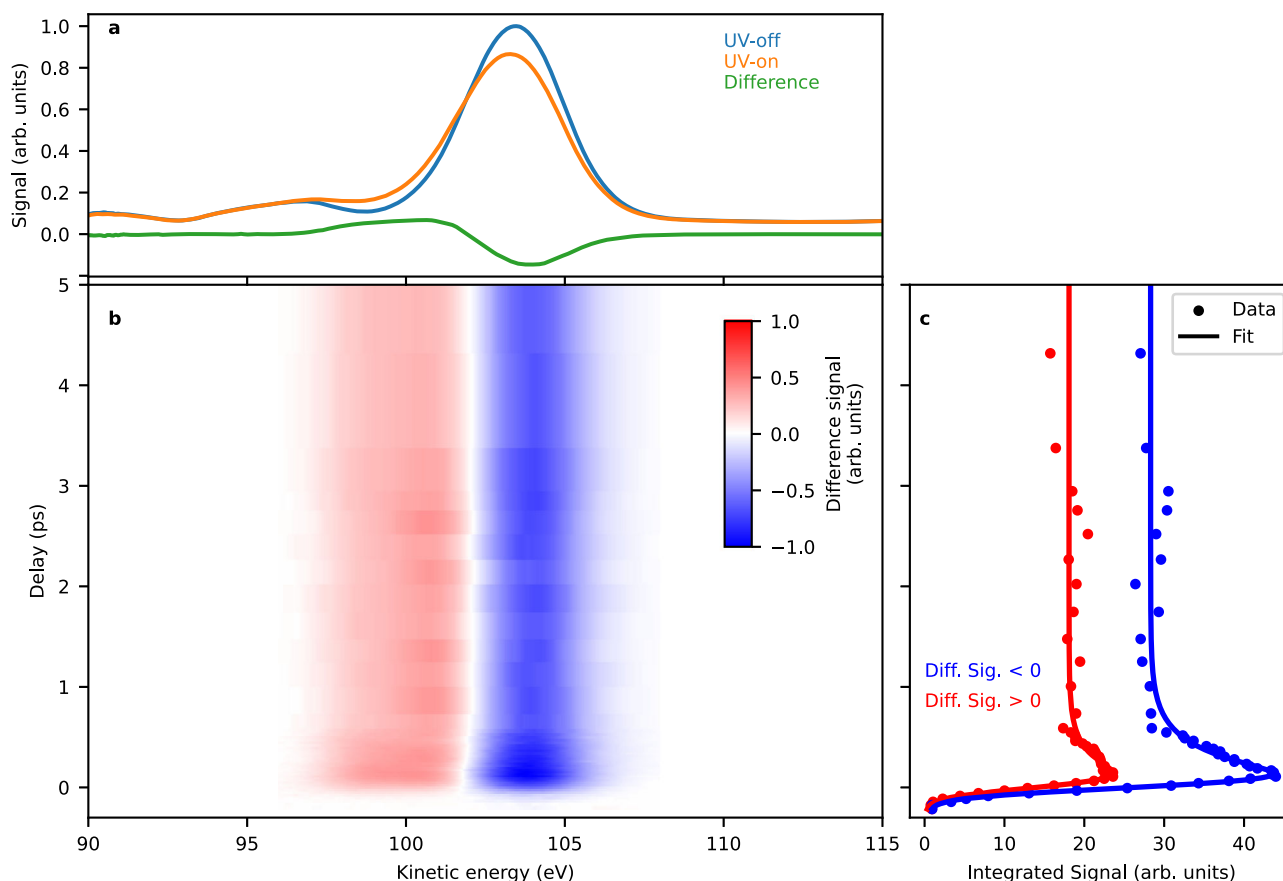


**Fig. 2 Experimental time-resolved XPS spectra of 2-thiouracil.** **a** UV-on (orange) and UV-off (blue) photoelectron spectra as well as the difference spectrum (green) between UV-on and UV-off at a delay of 200 fs. **b** False-colour plot of time-dependent difference XPS with red indicating UV-induced increase of the photoelectron spectrum and blue a UV-induced decrease. **c** Integrated signal of the positive (red) and negative (blue) parts of the difference spectra (dots) and fit to the data (solid line). Source data are provided as Source Data file.

96 eV<sup>41</sup>. Upon UV excitation (“UV-on”, orange line), the  $2p$ -photoelectron line shifts towards lower kinetic energies. The difference spectrum (“UV-on” - “UV-off”, green line at a delay of 200 fs) is equal to the difference between GS and ES spectra times the fraction,  $f$ , of excited molecules ( $f \cdot (\text{ES-GS})$ ). Part of the main photoelectron line is shifted into the region of the upper shake-up satellite, but the main part of the satellite line at 96 eV and the satellite at 91 eV remains unaffected. Figure 2b shows a time-dependent false-colour plot of the difference spectra. Temporal overlap has been determined by analysing the integrated absolute difference signal. The integrated signal under the positive/negative lobe in the difference spectrum is given in Fig. 2c.

The difference feature keeps its characteristic lineshape over the timescale of our measurement shown in Fig. 2b, indicating a persistent kinetic energy shift to smaller values over the whole range. The difference-amplitude changes significantly during the first picosecond. We use an exponential model function convoluted with a Gaussian time-uncertainty function of 190 ( $\pm 10$ ) fs FWHM (see Supplementary Discussion 1). We observe an exponential decay of 250 ( $\pm 20$ ) fs to 75% of the maximal signal for the negative part and 220 ( $\pm 40$ ) fs to 65% of the maximal signal for the positive part. The positive amplitude is always smaller than the negative amplitude. Systematic investigations of the difference spectra for various experimental settings exhibit the influence of so-called cyclotron resonances on the relative amplitudes in the MBES (see Supplementary Discussion 2). We therefore abstain from interpreting further the relative strength of the positive and negative features.

**Spectral oscillations at small delays.** Figure 3a shows a magnified part of the difference spectrum in Fig. 2b. To enhance the visibility of the spectral dynamics, we normalised each delay-slice on the area of the positive lobe. Despite the spectral width of about 4 eV, we identify oscillatory features in the positive part of the difference spectrum within the first  $\sim 600$  fs. From zero delay to 150 fs, the spectrum shifts to lower kinetic energies and the peak of the spectrum widens. The shifts are most clearly visible in the spectral region from 99 to 101 eV. In the ground state, the shake-up peak at 96 eV has some spectral wing in this region. However, we do not observe a UV-induced change on the shake-up peak in its main part and lower energy wing. We thus assume that the main spectral effects in the 99–101 eV range are solely due to the UV-altered main photoelectron line.

After reaching minimal kinetic energies at 150 fs, the spectrum shifts towards higher kinetic energies by about 0.5 eV and the peak narrows reaching its extreme in the range between 200 and 300 fs. Subsequently, the spectrum shifts and widens again to reach its other extreme at 400 fs. For larger delays, the spectrum shifts again to higher kinetic energies. Further oscillations are not observed, however, for reasons of scarce experimental time, the delay steps are too coarse to follow additional oscillations (for more details see Supplementary Discussion 3). The negative lobe does not show systematic trends in this region and is therefore not shown in Fig. 3.

**Difference spectra simulations.** We will interpret the experimental results, casting them in the context of the rich literature



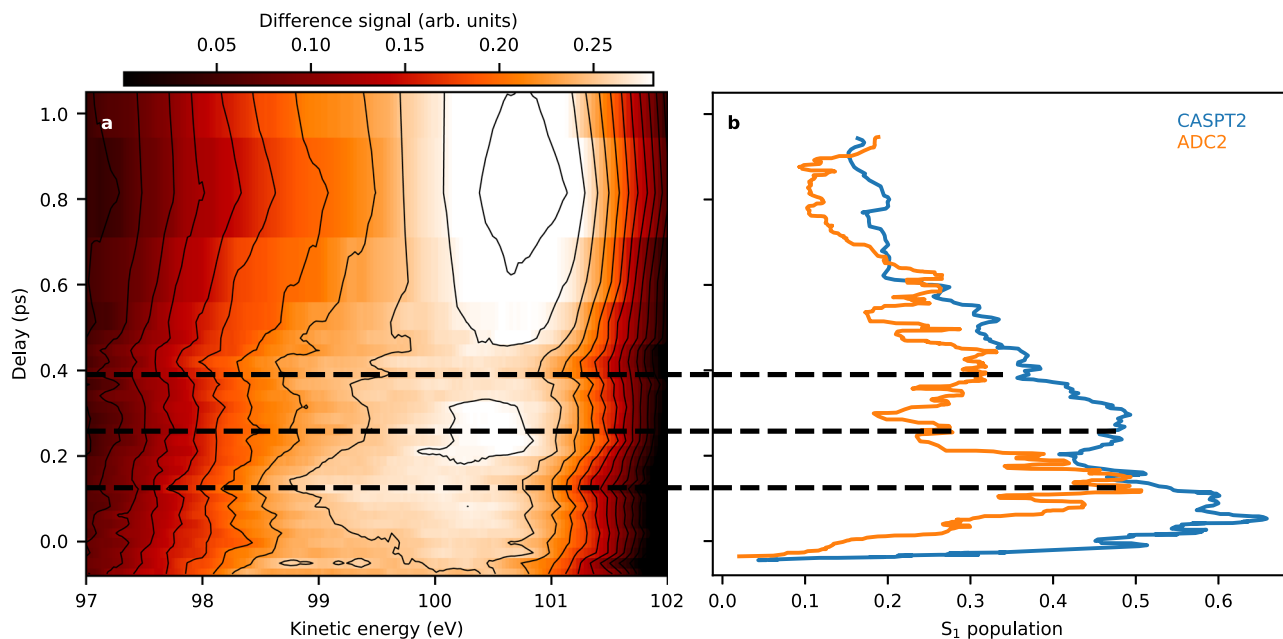


**Fig. 3 Experimental shifts and theoretical predictions on state population.** **a** False-colour contour plot of the positive lobe in Fig. 2b, normalised on the time-dependent area under the lobe. An oscillatory dynamic in the lineshape and position is visible for the first ~600 fs. At 150 fs and 400 fs delay, the spectrum is shifted to lower kinetic energy, while it is shifted to higher kinetic energies in between and afterwards. **b** Comparison of the oscillation dynamics with trajectory simulations. The population of the  $S_1$  ( $n\pi^*$ ) state, obtained from CASPT2 calculations of Ref. 35 (blue line) and ADC(2) calculations of Ref. 36 (orange line) are plotted. The dashed lines highlight the extrema of the oscillation observed in the experiment. The theoretical simulations do not include finite time-resolution and we shifted them by 50 fs to smaller delays to induce a transient rise of the signal around zero delay. The experimental 250 fs oscillation features have their counterparts in the simulated  $S_1$  population, indicating the observation of a population exchange between the  $S_1$  state and other electronic states. Source Data (for a) are provided as Source Data file.

on this molecule. Conclusions will also be drawn based on non-relativistic quantum chemical coupled-cluster calculations of the ground, valence-excited and core-ionised states of 2-tUra.

Previous calculations in the gas phase<sup>34</sup> or in the presence of water solvent molecules<sup>42</sup> identified global, non-planar minima, as well as nearly planar minima, which can be potentially visited by the photoinduced wave packet.

Along the same lines, we optimised the geometry of the lowest valence singlet ( $S_0$ ,  $S_1$ ,  $S_2$ ) and triplet ( $T_1$ ,  $T_2$ ,  $T_3$ ) states with and without the constraint of planarity. Since the  $S_0$  minimum is nearly planar, the excited state (unstable) planar minima are likely to play a role in the short time dynamics and are marked with an asterisk in Figs. 4 and 5. Fully-optimised, stable non-planar minima could be found for the  $S_1$ ,  $S_2$  and  $T_1$  states. The computational details are given in the Methods section and more extended in Supplementary Discussion 4. For all the geometries considered in this work the states  $S_1$ ,  $S_2$ ,  $T_1$ ,  $T_2$  and  $T_3$  have  $n\pi^*$ ,  $\pi\pi^*$ ,  $\pi\pi^*$ ,  $n\pi^*$  and  $\pi\pi^*$  character, respectively.

For each optimised geometry and each valence state we calculated the binding energy of the electrons in the three  $2p$  core orbitals of the S atom. We estimated the ionisation cross sections as proportional to the norm of the associated Dyson orbitals and used this data to simulate pump-probe photoelectron spectra at different geometries. The stick spectrum (shown in the Supplementary Discussion 5) was convoluted with a Gaussian of a FWHM of 3.5 eV, to match the width of the experimental bands.

## Discussion

We first discuss the experimental data without reference to the XPS simulations. The difference spectra of Fig. 2, with their shift towards lower kinetic energies, indicate an increased  $E_{\text{bind}}$  of the

UV excited states. The classical static XPS connects the  $E_{\text{bind}}$  of a particular element on a particular site within a molecule to the total charge at the probed atom, which is related to the electronegativity of the nearest neighbour atoms<sup>5</sup>. This connection is known as a ‘chemical shift’. Accordingly, we anticipate that the CS can be generalised to a dynamic context as an ESCS in form of the difference of excited and ground state binding energy. The long-lasting shift of the kinetic energy would then indicate that the net effect of the photoexcitation is charge redistribution away from the sulphur atom (see Fig. 1). The electronic states inducing the strongest charge changes at the sulphur heteroatom are the  $n\pi^*$  states. This is because the  $n$  (lone-pair orbital) is strongly localised at the sulphur heteroatom (see Fig. 1b) and in the  $n\pi^*$  states  $n$  is singly occupied with respect to double occupation in the electronic ground state. Overall, this will lead to a strong ESCS to higher binding energies. The  $^1n\pi^*$  state is generally considered a doorway state, leading from the UV excited  $^1\pi\pi^*$  to the triplet states<sup>37</sup> and accordingly, we would expect an ESCS induced by this state.

The  $\pi$  orbitals are less localised at the sulphur atom. Intuitively removal of an electron from a  $\pi$  orbital would not induce as strong an ESCS as the  $n$  removal, but it will still lead to some ESCS. These relative strengths of the ESCS can also be estimated by a simple charge analysis of the molecular wavefunctions, a method that can even be implemented with simple Hartree-Fock orbitals. We performed a Löwdin-population-analysis on the wavefunctions of the different electronic states at different geometries, which yields partial charges on the atoms of the molecule. In Fig. 4b, the calculated partial charge on the S atom is plotted against the calculated ESCS, which we will not use in the discussion yet as it is a much more complex entity to calculate. We clearly identify the strongest local positive charge on the sulphur atom with respect to the ground

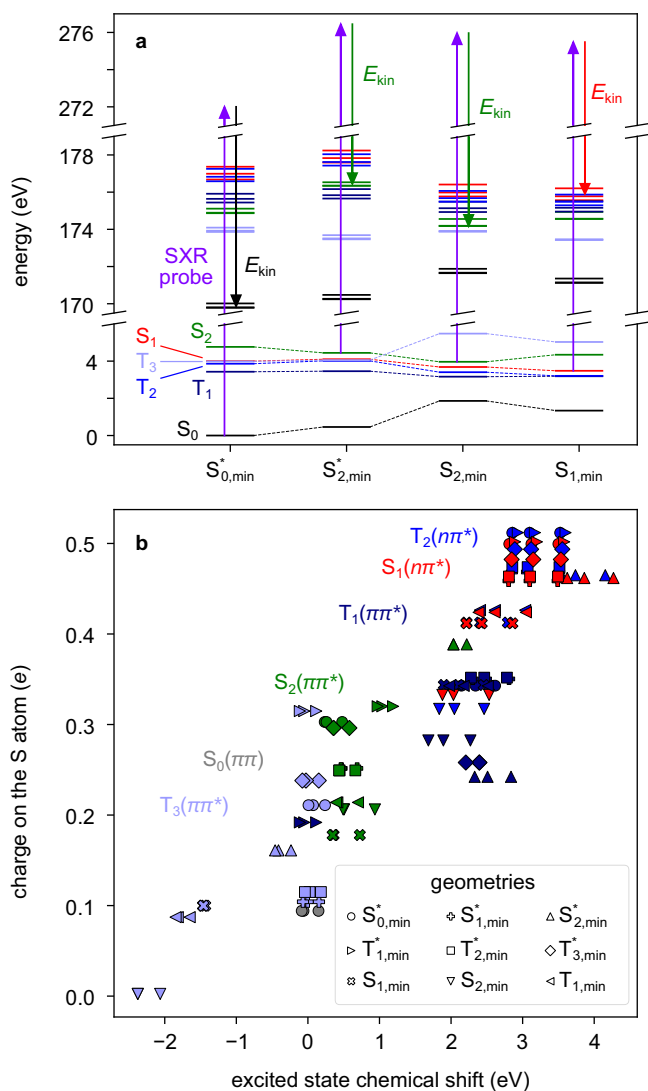


**Fig. 4** Soft x-ray photoelectron probing of the excited-state dynamics of 2-thiouracil in a multi-electron picture. **a** Calculated electronic energies of the valence excited states, in the range 0–6 eV, and the core ionised states, in the range of 170–179 eV, for four geometries relevant in the short time dynamics. The arrows illustrate the  $2p^{-1}$  ionisation process associated with the most intense transition. The core ionised states are grouped into sets of three states, which follow the colour coding of the valence states, meaning that their valence configuration is maintained with a  $2p_x$ ,  $2p_y$  or  $2p_z$  core hole. Accordingly, the electron kinetic energy  $E_{kin}$  refers to ionisations out of  $S_0$ ,  $S_1$  ( $n\pi^*$ ) and  $S_2$  ( $\pi\pi^*$ ), depending on the geometry. **b** Partial charges on the S atom are plotted against the excited state chemical shift of the  $2p$  electrons, calculated for the valence states at nine different geometries. For each geometry, the graph includes three markers for each excited state ( $S_1$ ,  $S_2$ ,  $T_1$ ,  $T_2$ ,  $T_3$ ); in addition, three dots are included for the ionisation from  $S_0$  at  $S_{0,min}^*$ , for a total of  $9 \times 3 \times 5 + 3 = 138$  markers. Asterisks denote restriction in the calculation of the states to planar geometries. Source Data are provided as a Source Data file.

states in the  $S_1$  ( $1n\pi^*$ ) and  $T_2$  ( $3\pi\pi^*$ ) states, confirming the intuitive arguments given above. The  $S_2$  ( $1\pi\pi^*$ ) state is characterised by a relatively low positive charge on the sulphur atom and the lowest  $T_1$  ( $3\pi\pi^*$ ) state in its minimum geometry, generally considered as the long-lasting state<sup>31,34</sup>, is lying in between the  $n\pi^*$  and  $S_2$  ( $1\pi\pi^*$ ) states. Thus, the permanent ESCS to lower kinetic energies (higher binding energies) is consistent with a relaxation cascade from the initially excited  $S_2$

( $1\pi\pi^*$ ) over the  $S_1$  ( $1n\pi^*$ ) and possibly also  $T_2$  ( $3\pi\pi^*$ ) states into the lowest  $T_1$  ( $3\pi\pi^*$ ) state.

Closer inspection of the short-time dynamics in Fig. 3a provides extraordinary experimental details on the molecular relaxation dynamics. In the spectral shift dynamics, the strongest ESCS to lower kinetic energies (higher binding energies) is found at 150 and 400 fs, interrupted with an interval and followed by delays of smaller ESCS. Intuition based on the lone-pair orbital localisation, as well as the simple local charge analysis at the sulphur atom mentioned above, indicate that this spectral shift reflects changes in the electronic state of the molecule with maximal  $n\pi^*$  contributions at 150 and 400 fs and consequently minimal  $n\pi^*$  contributions in between and after. We compare theoretical predictions of the  $S_1$  ( $1n\pi^*$ ) state population dynamics from the trajectory surface-hopping calculations of Mai et al.<sup>35,36</sup>, in Fig. 3b. The  $S_1$  populations calculated using CASPT2 and ADC(2) potentials show indeed dynamics that fit well to the experimentally observed shifts. The oscillation period depends on the theoretical approach, and the timing of the second  $S_1$  population maximum fits the experimental data better in the case of the ADC(2) approach. The simulations of Mai et al. predict a population transfer among the  $S_1$ ,  $S_2$  and triplet states in a coherent fashion and the details of states participating in the population dynamics depends on the applied electronic structure method. However, in both cases, the  $S_1$  state, having the highest IP of all states, carries the largest oscillation. This comparison strongly supports the experimental arguments for observing population dynamics entering and leaving the  $S_1$  state in a coherently modulated fashion.

Similar coherent modulations have been observed in the transient spectra for 4-tUra and 2-tUra and in liquid phase<sup>42,43</sup>. In case of 4-tUra, much faster, sub-100 fs, coherent modulations have been observed in fs transient absorption spectra and attributed to particular vibrational modes in the electronically excited state of 4-tUra<sup>43</sup>. For the case of 2-tUra, the same experimental methods exhibit oscillations with a period very similar to ours<sup>42</sup>, which are however not interpreted. We also checked the assignment to a purely vibrational coherence by performing a normal mode analysis at the calculated excited state minima. Only at the nonplanar minimum of the  $S_2$  ( $\pi\pi^*$ ) state we found a mode with a frequency of  $131\text{ cm}^{-1}$ , thus compatible with a 250 fs modulation. However, this would mean that the molecular population should be dominated by the  $S_2$  state for the 600 fs of our modulated time-interval, which is in contrast to all current literature suggestions. Also, for short times, we suggest that the molecule remains mostly planar on the  $S_2$  state, as will be shown below by comparison to calculated difference spectra. Remarkably, valence photoelectron spectra of 2-tUra in the gas phase do not show these modulations<sup>31</sup>, demonstrating that the ESCS in XPS is able to pick up molecular dynamics beyond reach for valence electron photoemission.

On top of the coherently modulated signal, we find an amplitude decay with a time-constant of 220–250 fs, being equal on the positive and negative lobe of the difference spectra within the error bars. Similar short decays have been observed in liquid and gas phase studies of 2-tUra. In valence photoelectron spectroscopy, a time constant of around 300 fs is observed for the excitation wavelength corresponding to the one used here<sup>31</sup>. Based on the calculated valence IPs of the different states<sup>44</sup>, the decay is attributed to relaxation from the  $S_1$  ( $1n\pi^*$ ) to the triplet state manifold. Liquid-phase transient absorption spectra of 2-tUra in the same work show similar time constants and the same interpretation is applied<sup>31</sup>. This is supported by a recent joint experimental-theoretical investigation that includes calculated transient absorption windows at some of the molecule's crucial excited state positions<sup>42</sup>. The observed vanishing contrast in our TR-XPS might need to be interpreted in a different way

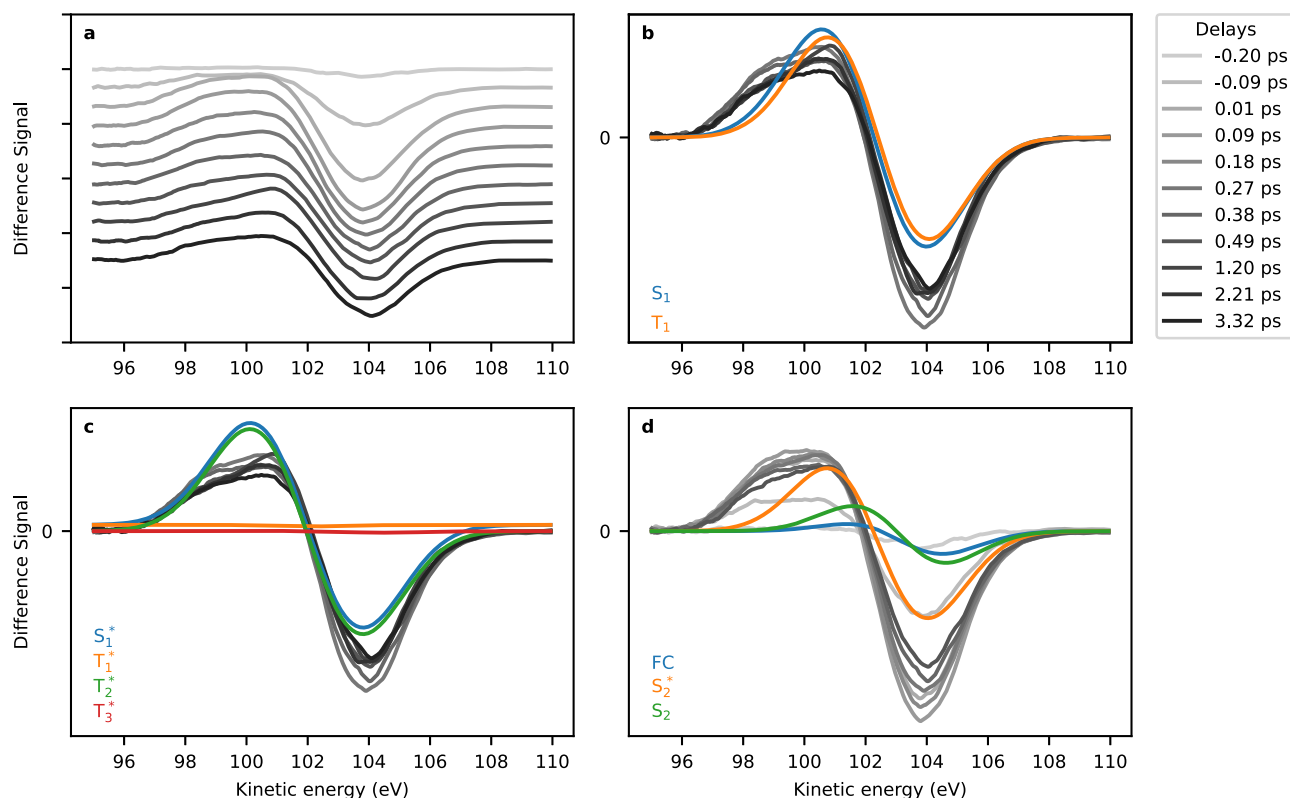


**Fig. 5 Comparison between experimental and theoretical difference spectra.** **a** Ridgeline plot of experimental difference spectra for different pump-probe delays between  $-0.2$  and  $3.32$  ps. **b–d** Comparison of experiment (greyscale lines) with theoretical (coloured lines) difference spectra computed at the coupled-cluster level of theory. All calculated difference spectra are shifted lower in kinetic energy by  $1.3$  eV. **b** and **c** Spectra with delays in the range  $0.27$ – $3.32$  ps, **(d)** spectra with delays  $-0.2$ – $0.49$  ps. The theoretical spectra use the energies at the minima ( $S_2$  is the nonplanar,  $S_2^*$  is the restricted geometry) and the Franck-Condon geometry. Asterisks denote restriction in the calculation of the states to planar geometries. Source Data are provided as a Source Data file.

than the  $S_1(1n\pi^*)$ —triplet state relaxation, as we would expect to still observe a ESCS leading to different features in the triplet manifold. The state diminishing the modulation contrast of the difference spectra would have to show a small ESCS with respect to the ground state, and thus be electronically similar—or identical—to the ground state. We thus suggest an ultrafast molecular decay of part of the population into the electronic ground state and check it further by comparison to ESCS simulations below.

We now discuss the calculated ESCS and its connection to the charge on the sulphur atom in the photoexcited states. We observe the remarkable linear relation between binding energy and charge, closely resembling the potential model introduced in static XPS<sup>6</sup>. While many effects such as final-state charge relaxation and core-hole screening<sup>13,45</sup> shape the calculated binding energy, the linear trend prevails. This provides a generalised concept for deducing local charge changes in electronically excited states from the ESCS. Further well-established corrections known from static XPS to this plot make the  $E_{\text{bind}}$ -charge connection even more obvious (Supplementary Discussion 6).

In addition, we can clearly distinguish drivers behind the charge and ESCS shifts. The colours in Fig. 4 indicate the electronic state while the different symbols indicate geometries, corresponding to minima or saddle points on different potential energy surfaces. We clearly observe clustering according to electronic state, although very widely differing geometries have been used. Thus, the main factor for local charge and therefore binding energy is the electronic state of the molecule. This in turn gives core-level photoelectron spectroscopy high electronic state sensitivity. The exceptions of one  $S_2$  and  $T_1$  geometry are explained

in the Supplementary Discussion 7. The data for the  $S_1$  and  $T_2$  states ( $n\pi^*$ ) are very well clustered in the upper right corner of Fig. 4b, with the highest ESCS. As explained above, these states have  $n\pi^*$  character and possess a high positive charge on the sulphur atom, which is also illustrated in Fig. 1.

In Fig. 5, we assess details of the TR-XPS spectra by comparison with the calculated spectra, extending our discussion of the purely experimental features. The onset of the experimental difference feature around time-zero is shown in more detail in the ridgeline plot of Fig. 5a. The difference signal gets stronger with delay indicating an increasing  $f$  over the time-resolution of 191 fs. We initially identify the development of the negative feature sitting stable at 104 eV and a comparatively broader positive feature at lower kinetic energies. The relative position of the positive and negative bands is very well captured by the simulation. Since similar Dyson norms were predicted for the different initial valence excited states, the calculated spectra essentially integrate to zero. According to model and intuition, the positive feature should be attributed to electronic states with higher positive charge on the sulphur atom.

We continue discussing the picosecond difference spectra, comparing them to calculated difference spectra in Fig. 5b and c. Among the states with highest local charge and thus highest  $E_{\text{bind}}$  are the  $S_1(n\pi^*)$ ,  $T_1(\pi\pi^*)$  and  $T_2(n\pi^*)$  states. The unstable, restricted planar minima/saddle points of  $S_1$  and  $T_2$  (Fig. 5c) could be responsible for parts of the difference spectra for a limited time until relaxation into a non-planar geometry. Among these non-planar geometries, both the  $S_1$  and  $T_1$  show agreement with the experimental difference spectra (Fig. 5b). The missing low-energy wing from 97 to 98.5 eV in the theoretical spectra can

likely be attributed to the fact that we neglect wave-packet and incoherent thermal distribution effects resulting in extended geometry coverage. The shake-up phenomena are also not modelled. However, we do not observe a change of the shake-up peaks and we would expect that the observation of UV-induced effects on the weaker satellite lines requires better signal-to-noise ratio. The theoretical simulations strengthen the arguments given in the context of Fig. 3, showing that a strong ESCS due to the  $S_1$  coherent dynamics is followed by a state with less ESCS. We note that simulations/experiments on the pyrimidine nucleobases call for the  $S_1$   $1n\pi^*$  state to be occupied first after  $S_2$  relaxation<sup>46</sup>. Only thereafter will the triplet states gain population. Based on the experimental features, we can exclude the planar geometries of the  $T_1$  and  $T_3$  states to play a major role in the relaxation process. A comparison to the ESCS in Fig. 4b implies that the charge at the sulphur atom has reached about half a positive value due to the molecular relaxation.

We now return to the initial 220–250 fs decay of the difference feature, which can be an indication of relaxation of the charge back to the ground state distribution, into states with negligible photoionisation cross section, or into states with an IP equal to the electronic ground state before photoexcitation. To obtain more insight, we compare the experimental XPS to simulations in Fig. 5b–d. Figure 5d shows the  $S_2$  ( $\pi\pi^*$ ) state difference spectra in three different molecular geometries. Figure 5c shows spectra with ‘unstable’ planar geometries. The most important is the  $S_1$  ( $n\pi^*$ ) state, others are expected to play a minor role in the dynamics for short times<sup>35,36</sup>. Figure 5b shows difference spectra for the  $S_1$  and  $T_1$  states at their respective potential energy minimum geometry. The unstable  $T_1^*$  and  $T_3^*$  spectra are indeed flat on our scale and could in principle explain the observed decay in difference amplitude. However, these geometries cannot be stable, and cannot explain the long-lasting reduction in amplitude with the 220–250 fs exponential decay. In addition, the remaining calculated non-flat difference spectra do not exhibit a large enough difference. We therefore attribute the observed decay to an ultrafast relaxation into the electronic ground state with net zero charge change with a 220–250 fs time-constant.

Ground-state (GS) relaxation has been discussed before in the solution as well as in the gas phase<sup>31,37,47</sup>. In earlier solution-phase work, a remark on an incomplete triplet yield could be interpreted in favour of an ultrafast ground state decay channel<sup>37</sup>. More recent work in the gas phase has attributed time-constants from 50 to 200 ps to ground state relaxation<sup>31</sup>. Our ground state channel is close to the 300 fs decay observed in Ref. 31, which was attributed to intersystem crossing previously.

We now compare early difference spectra to the calculated spectra of the directly photoexcited  $S_2$  ( $\pi\pi^*$ ) state in different geometries in Fig. 5d. The best representation is given by the  $S_2^*$  planar geometry. The Franck-Condon spectrum should be included in the difference spectra, however, the short lifetime of this point as compared to our time-resolution makes it a minor contributor. We can, however, exclude a relaxation with major contributions from the  $S_2$  out-of-plane minimum (green line), as this would mean a shift in the zero-crossing feature by about 1 eV to higher kinetic energies, which is not observed in the experiment. This observation agrees with the predictions of trajectory calculations when using a CASPT2 approach to electronic structure<sup>35</sup> but is in contrast to trajectory calculations with an ADC(2) electronic structure approach<sup>36</sup>. While in the first reference the  $S_2$  lifetime is below 100 fs and thus too short for the molecule to effectively reach out of plane geometries, the latter predicts an  $S_2$  lifetime of 250 fs which allows for out of plane geometries.

In a recent theoretical-experimental solution phase study, two  $1\pi\pi^*$  states with a slight energy gap are assumed to be populated

and while the upper one is predicted to relax via out-of-plane geometries, the lower one is suggested to relax via planar geometries<sup>42</sup>. We find that our calculated geometries are very similar to the ones from Ref. 42. (see the Supplementary Discussion 4 for a full comparison) and thus our analysis above would clearly advocate for initial planar geometries in the relaxation path. However, as our study is performed on isolated molecules instead of in solution phase it is not clear if we have any appreciable admixture of the higher lying  $1\pi\pi^*$  state.

We have introduced the concept of ESCS in TR-XPS and shown that this powerful concept can be applied to deduce charge distribution changes in excited molecules. We observe rich dynamics on a sub-ps timescale. Based on intuitive arguments, we can assign the spectral features to coherent population exchange of the  $n\pi^*$  state, inducing a strong ESCS, with other electronic states of less ESCS. In addition, we identify an ultrafast ground state relaxation path based on decaying amplitude in the differential signal. The calculated ESCS as a function of electronic state and geometry help in interpreting the geometric changes of the molecule after UV excitation in terms of a planar relaxation path on the photoexcited  $1\pi\pi^*$  state. The connection between charge change at the probe site and the exactly calculated ESCS can be well approximated by a potential model, as in ground state XPS. This will provide a methodological basis for an intuitive understanding of charge dynamics in photoexcited isolated molecules on the femto- and attosecond timescale but also for photocatalytic systems. In a next step, one can address more than one site of the molecule using TR-XPS and map the charge flow induced by photoexcitation over the whole molecule.

## Methods

**Time-resolved UV pump soft x-ray probe (photo-) electron spectroscopy.** The experiment was performed at the FL24 beamline of the FLASH2 facility at DESY using the newly built URSA-PQ apparatus. A detailed description of the apparatus and the experiment can be found elsewhere<sup>48,49</sup>. In short, the apparatus includes a magnetic bottle time-of-flight electron spectrometer (MBES), a capillary oven to evaporate the 2-thiouracil samples at 150 °C and a paddle with beam diagnostics on top of the oven. UV pump pulses of 269 nm centre wavelength, 80 fs duration and an energy around 1  $\mu$ J were focused to a 50  $\mu$ m focus to pre-excite the molecules into the  $\pi\pi^*$  state. Power scans on the time-dependent spectral features were performed to assure that the signal is not over-pumped by the UV pulses (Supplementary Discussion 8).

Tunable soft x-ray pump pulses were produced in form of SASE (self-amplified spontaneous emission) radiation. Every second x-ray pulse was delivered without UV excitation for obtaining a reference on the non-excited molecule. The mean x-ray photon energy was set to 272 eV with a bandwidth of 1–2% (including jitter). The x-ray probe was linearly polarised parallel to the axis of the magnetic bottle spectrometer and the UV polarisation. The focal size of the x-ray beam was slightly larger than the UV spot size. Systematic power scans were performed to exclude nonlinear effects in the x-ray induced electron spectra (see Supplementary Discussion 8). To increase energy resolution of the spectrometer, the speed of the ejected electrons was reduced by an  $-80$  V retardation voltage on an electrostatic lens in front of the 1.7 m long flight tube which was kept at a constant potential. The energy resolving power of the MBES ( $E/\Delta E$ ) has been determined with Kr MNN Auger lines to be 40 at 0 V retardation. Based on the sulphur 2p-photoelectron line, we estimate the resolution to be better than 30 with respect to the total kinetic energy. The time-dependent spectra were measured for a series of delays. In each scan, the delays were set randomly to avoid systematic effects. We measure the difference spectra of UV excited to non-excited shots. The data evaluation is described in Supplementary Discussion 9.

**Theoretical calculations.** The geometry optimisation of ground state 2-thiouracil was performed using coupled-cluster theory with singles and doubles (CCSD) with the 6-311++G\*\* basis set<sup>50,51</sup>. Valence excited state optimisations and energy calculations at specific geometries were performed using the equation-of-motion formalism (EOM-CCSD) with the same basis set. All calculations were performed using the package Q-Chem 4.4<sup>52</sup>. At all computed geometries the valence excited states' wavefunctions are dominated by a singly-excited configuration. For the states  $S_1$ ,  $T_2$  ( $n\pi^*$ ) and  $S_2$ ,  $T_1$  ( $\pi\pi^*$ ) the involved orbitals at the Franck-Condon point are shown in Fig. 1. The structural parameters of the optimised planar and non-planar geometries on the different electronic states are reported in the Supplementary Discussion 4.

The binding energy of the electrons in the  $2p$  orbitals of the sulphur atom were calculated using the equation-of-motion coupled-cluster method for IPs (EOM-IP-CCSD)<sup>53</sup> with the  $6-311++G^{**}$  basis set for the S atom and the  $6-31++G$  basis for all other atoms. Photoelectron intensities were approximated as the geometric mean of the norms of the left and right Dyson orbitals associated with the ionisation process<sup>10</sup>. The target core-excited states of the cation were identified as the eigenstates which have the largest overlap with initial guess states, obtained by applying the annihilation operator of the three  $2p$  electrons on reference CCSD wavefunctions, according to the procedure implemented in Q-Chem. To this end, reference CCSD wavefunctions for the different electronic states of the neutral molecule were calculated starting from unrestricted Hartree-Fock wavefunctions, which were optimised using the maximum overlap method, in order to mimic the (singly excited) orbital occupancy of the excited states. A similar strategy has been recently validated by Coriani et al. to model pump-probe x-ray absorption spectra of nucleobases at the coupled-cluster level<sup>54</sup>. Spin-orbit coupling, leading to a splitting of the core-ionised states of the order of 1 eV (not resolved due to spectral broadening) is not included in the calculations.

### Data availability

Source data are provided with this paper. The FEL raw data, several TB in size, that support the findings of this study are available from the corresponding authors upon request. The processed photoelectron spectra are provided in the Source Data File. The results of the theoretical calculations i.e. optimised geometries, ionisation potentials, state energies and partial charges, are provided in the Source Data File. Source data are provided with this paper.

### Code availability

The codes used to generate the computational results of this study are highly adapted to the hdf5 output of the FLASH free-electron laser. They are available from the corresponding authors upon request.

Received: 8 August 2021; Accepted: 20 December 2021;

Published online: 11 January 2022

### References

- Domcke, W., Yarkony, D. R. & Köppel, H. *Conical intersections: theory, computation and experiment*. Advanced Series in Physical Chemistry 17 (World Scientific, 2011).
- Levine, B. G. & Martínez, T. J. Isomerization Through Conical Intersections. *Ann. Rev. Phys. Chem.* **58**, 613–634 (2007).
- Weinberg, D. R. et al. Proton-Coupled Electron Transfer. *Chem. Rev.* **112**, 4016–4093 (2012).
- Tian, H., Boschloo, G. & Hagfeldt, A. *Molecular devices for solar energy conversion and storage*. (Springer Berlin Heidelberg, 2017).
- Siegbahn, K. *ESCA applied to free molecules*. (North-Holland Pub. Co, 1969).
- Gelius, U. Binding Energies and Chemical Shifts in ESCA. *Phys. Scr.* **9**, 133–147 (1974).
- Bennett, K., Kowalewski, M. & Mukamel, S. Nonadiabatic Dynamics May Be Probed through Electronic Coherence in Time-Resolved Photoelectron Spectroscopy. *J. Chem. Theory Comput.* **12**, 740–752 (2016).
- Neville, S. P., Chergui, M., Stolow, A. & Schuurman, M. S. Ultrafast X-Ray Spectroscopy of Conical Intersections. *Phys. Rev. Lett.* **120**, 243001 (2018).
- Inhester, L., Li, Z., Zhu, X., Medvedev, N. & Wolf, T. J. A. Spectroscopic Signature of Chemical Bond Dissociation Revealed by Calculated Core-Electron Spectra. *J. Phys. Chem. Lett.* **10**, 6536–6544 (2019).
- Vidal, M. L., Krylov, A. I. & Coriani, S. Dyson orbitals within the fc-CVS-EOM-CCSD framework: theory and application to X-ray photoelectron spectroscopy of ground and excited states. *Phys. Chem. Chem. Phys.* **22**, 2693–2703 (2020).
- Siefermann, K. R. et al. Atomic-Scale Perspective of Ultrafast Charge Transfer at a Dye-Semiconductor Interface. *J. Phys. Chem. Lett.* **5**, 2753–2759 (2014).
- Braufé, F. et al. Time-resolved inner-shell photoelectron spectroscopy: from a bound molecule to an isolated atom. *Phys. Rev. A* **97**, 043429 (2018).
- Leitner, T. et al. Time-resolved electron spectroscopy for chemical analysis of photodissociation: photoelectron spectra of  $\text{Fe}(\text{CO})_5$ ,  $\text{Fe}(\text{CO})_4$ , and  $\text{Fe}(\text{CO})_3$ . *J. Chem. Phys.* **149**, 44307 (2018).
- Bergmann, U., Yachandra, V. & Yano, J. *X-ray free electron lasers: applications in materials, chemistry and biology*. Energy and Environment Series (Royal Society of Chemistry, 2017).
- Young, L. et al. Roadmap of ultrafast x-ray atomic and molecular physics. *J. Phys. B: Mol. Opt. Phys.* **51**, 032003 (2018).
- Neville, S. P. et al. Beyond structure: Ultrafast X-ray absorption spectroscopy as a probe of non-adiabatic wavepacket dynamics. *Faraday Discuss.* **194**, 117–145 (2016).
- Neville, S. P. et al. Excited state X-ray absorption spectroscopy: Probing both electronic and structural dynamics. *J. Chem. Phys.* **145**, 144307 (2016).
- Segatta, F. et al. Exploring the capabilities of optical pump X-ray probe NEXAFS spectroscopy to track photo-induced dynamics mediated by conical intersections. *Faraday Discuss.* **221**, 245–264 (2020).
- Attar, A. R. et al. Femtosecond x-ray spectroscopy of an electrocyclic ring-opening reaction. *Science* **356**, 54–59 (2017).
- Pertot, Y. et al. Time-resolved x-ray absorption spectroscopy with a water window high-harmonic source. *Science* **355**, 264–267 (2017).
- Bhattacharjee, A. et al. Ultrafast Intersystem Crossing in Acetylacetone via Femtosecond X-ray Transient Absorption at the Carbon K-Edge. *J. Am. Chem. Soc.* **139**, 16576–16583 (2017).
- Loh, Z.-H. et al. Observation of the fastest chemical processes in the radiolysis of water. *Science* **367**, 179–182 (2020).
- Wolf, T. J. A. et al. Probing ultrafast  $\pi\pi^*/n\pi^*$  internal conversion in organic chromophores via K-edge resonant absorption. *Nat. Comm.* **8**, 29 (2017).
- Ehlert, C., Gühr, M. & Saalfrank, P. An efficient first principles method for molecular pump-probe NEXAFS spectra: Application to thymine and azobenzene. *J. Chem. Phys.* **149**, 144112 (2018).
- Bressler, C. & Chergui, M. Ultrafast X-ray Absorption Spectroscopy. *Chem. Rev.* **104**, 1781–1812 (2004).
- Zhang, W. et al. Tracking excited-state charge and spin dynamics in iron coordination complexes. *Nature* **509**, 345–348 (2014).
- Arslançan, S., Martínez-Fernández, L. & Corral, I. Photophysics and photochemistry of canonical nucleobases' thioanalogs: from quantum mechanical studies to time resolved experiments. *Molecules* **22**, 998 (2017).
- Ashwood, B., Pollum, M. & Crespo-Hernández, C. E. Photochemical and Photodynamical Properties of Sulfur-Substituted Nucleic Acid Bases. *Photochem. Photobiol.* **95**, 33–58 (2019).
- Zhang, X. et al. Novel DNA lesions generated by the interaction between therapeutic thiopurines and UVA light. *DNA Repair* **6**, 344–354 (2007).
- Brem, R., Daehn, I. & Karran, P. Efficient DNA interstrand crosslinking by 6-thioguanine and UVA radiation. *DNA Repair* **10**, 869–876 (2011).
- Sánchez-Rodríguez, J. A. et al. 2-Thiouracil intersystem crossing photodynamics studied by wavelength-dependent photoelectron and transient absorption spectroscopies. *Phys. Chem. Chem. Phys.* **19**, 19756–19766 (2017).
- Mohamadzade, A., Bai, S., Barbatti, M. & Ullrich, S. Intersystem crossing dynamics in singly substituted thiouracil studied by time-resolved photoelectron spectroscopy: Micro-environmental effects due to sulfur. *Chem. Phys.* **515**, 572–579 (2018).
- Mai, S., Mohamadzade, A., Marquetand, P., González, L. & Ullrich, S. Simulated and Experimental Time-Resolved Photoelectron Spectra of the Intersystem Crossing Dynamics in 2-Thiouracil. *Molecules* **23**, 2836 (2018).
- Mai, S., Marquetand, P. & González, L. A Static Picture of the Relaxation and Intersystem Crossing Mechanisms of Photoexcited 2-Thiouracil. *J. Phys. Chem. A* **119**, 9524–9533 (2015).
- Mai, S., Marquetand, P. & González, L. Intersystem Crossing Pathways in the Noncanonical Nucleobase 2-Thiouracil: a time-dependent picture. *J. Phys. Chem. Lett.* **7**, 1978–1983 (2016).
- Mai, S. et al. Surface hopping dynamics including intersystem crossing using the algebraic diagrammatic construction method. *J. Chem. Phys.* **147**, 184109 (2017).
- Pollum, M. & Crespo-Hernández, C. E. Communication: The dark singlet state as a doorway state in the ultrafast and efficient intersystem crossing dynamics in 2-thiothymine and 2-thiouracil. *J. Chem. Phys.* **140**, 071101 (2014).
- Faatz, B. et al. Simultaneous operation of two soft x-ray free-electron lasers driven by one linear accelerator. *N. J. Phys.* **18**, 062002 (2016).
- Giuliano, B. M. et al. Tautomerism in 4-Hydroxypyrimidine, S-Methyl-2-thiouracil, and 2-Thiouracil. *J. Phys. Chem. A* **114**, 12725–12730 (2010).
- Plekan, O. et al. Functionalisation and immobilisation of an Au(110) surface via uracil and 2-thiouracil anchored layer. *Phys. Chem. Chem. Phys.* **17**, 15181–15192 (2015).
- Föhlisch, A. et al. Direct observation of electron dynamics in the attosecond domain. *Nature* **436**, 373–376 (2005).
- Teles-Ferreira, D. C. et al. A Unified Experimental/Theoretical Description of the Ultrafast Photophysics of Single and Double Thionated Uracils. *Chem. - A Eur. J.* **26**, 336–343 (2020).
- Borrego-Varillas, R. et al. Observation of the Sub-100 Femtosecond Population of a Dark State in a Thiobase Mediating Intersystem Crossing. *J. Am. Chem. Soc.* **140**, 16087–16093 (2018).
- Ruckenbauer, M., Mai, S., Marquetand, P. & González, L. Photoelectron spectra of 2-thiouracil, 4-thiouracil, and 2,4-dithiouracil. *J. Chem. Phys.* **144**, 074303 (2016).
- Mårtensson, N. & Nilsson, A. On the origin of core-level binding energy shifts. *J. Electr. Spectr. Rel. Phen.* **75**, 209–223 (1995).

46. Improta, R., Santoro, F. & Blancafort, L. Quantum Mechanical Studies on the Photochemistry and the Photochemistry of Nucleic Acids and Nucleobases. *Chem. Rev.* **116**, 3540–3593 (2016).
47. Yu, H. et al. Internal conversion and intersystem crossing pathways in UV excited, isolated uracils and their implications in prebiotic chemistry. *Phys. Chem. Chem. Phys.* **18**, 20168–20176 (2016).
48. Metje, J. et al. URSA-PQ: A Mobile and Flexible Pump-Probe Instrument for Gas Phase Samples at the FLASH Free Electron Laser. *Appl. Sci.* **10**, 7882 (2020).
49. Lever, F. et al. Ultrafast dynamics of 2-thiouracil investigated by time-resolved Auger spectroscopy. *J. Phys. B. Mol. Opt. Phys.* **54**, 014002 (2020).
50. Shavitt, I. & Bartlett, R. J. *Many – Body Methods in Chemistry and Physics: MBPT and Coupled-Cluster Theory*. (Cambridge University Press, 2009).
51. Bartlett, R. J. & Musiał, M. Coupled-cluster theory in quantum chemistry. *Rev. Mod. Phys.* **79**, 291–352 (2007).
52. Shao, Y. et al. Advances in molecular quantum chemistry contained in the Q-Chem 4 program package. *Mol. Phys.* **113**, 184–215 (2015).
53. Krylov, A. I. Equation-of-Motion Coupled-Cluster Methods for Open-Shell and Electronically Excited Species: The Hitchhiker’s Guide to Fock Space. *Annu. Rev. Phys. Chem.* **59**, 433–462 (2008).
54. Tsuru, S. et al. An assessment of different electronic structure approaches for modeling time-resolved x-ray absorption spectroscopy. *Struct. Dyn.* **8**, 24101 (2021).

## Acknowledgements

We thank the Volkswagen foundation for funding via a Lichtenberg Professorship. We thank the BMBF for funding the URSA-PQ apparatus and for funding J.M. via Verbundforschungsproject 05K16IP1. We acknowledge DFG funding via Grants GU 1478/1-1 (M.G.) and SA 547/17-1 (P.S.). T.J.A.W. was supported by the US Department of Energy, Office of Science, Basic Energy Sciences, Chemical Sciences, Geosciences, and Biosciences Division. R.F. thanks the Swedish Research Council (VR) and the Knut and Alice Wallenberg Foundation, Sweden, for financial support. We acknowledge DESY (Hamburg, Germany), a member of the Helmholtz Association HGF, for the provision of experimental facilities. Part of this research was carried out at FLASH2. F.C. acknowledges support from the European Research Council under the ERC-2014-StG STAR-LIGHT (Grant Agreement No. 637756).

## Author contributions

J.M. and M.G. did the conceptual design for the experimental apparatus. J.M. designed and built the apparatus. The magnetic bottle spectrometer was designed by J.M. with help of R.F. and R.J.S. and M.G. J.M., D.M., F.L. and S.D. integrated the apparatus into the FLASH beamline. F.L. designed and executed the data interfacing between the experiment and the FLASH data infrastructure. D.M., F.L., J.M., S.A., F.C., S.D., R.F., M.N.,

B.M., M.K., T.M., M.S.R., R.J.S., A.T., M.W., T.J.A.W. and M.G. performed the experiment. D.M. and F.L. analysed the data. D.P. performed the calculations and discussed the theoretical methods with C.E. and P.S. D.M., F.L., D.P. and M.G. discussed the data and theory and prepared the paper. All authors contributed to the final version of the paper by discussions and/or edits. M.G. wrote the beamtime proposal for this experiment and serves as spokesperson for the collaboration.

## Funding

Open Access funding enabled and organized by Projekt DEAL.

## Competing interests

The authors declare no competing interests.

## Additional information

**Supplementary information** The online version contains supplementary material available at <https://doi.org/10.1038/s41467-021-27908-y>.

**Correspondence** and requests for materials should be addressed to D. Picconi or M. Gühr.

**Peer review information** *Nature Communications* thanks the anonymous reviewers for their contribution to the peer review of this work. Peer reviewer reports are available.

**Reprints and permission information** is available at <http://www.nature.com/reprints>

**Publisher’s note** Springer Nature remains neutral with regard to jurisdictional claims in published maps and institutional affiliations.



**Open Access** This article is licensed under a Creative Commons Attribution 4.0 International License, which permits use, sharing, adaptation, distribution and reproduction in any medium or format, as long as you give appropriate credit to the original author(s) and the source, provide a link to the Creative Commons license, and indicate if changes were made. The images or other third party material in this article are included in the article’s Creative Commons license, unless indicated otherwise in a credit line to the material. If material is not included in the article’s Creative Commons license and your intended use is not permitted by statutory regulation or exceeds the permitted use, you will need to obtain permission directly from the copyright holder. To view a copy of this license, visit <http://creativecommons.org/licenses/by/4.0/>.

© The Author(s) 2022, corrected publication 2022

# Ultrafast dynamics of 2-thiouracil investigated by time-resolved Auger spectroscopy

F Lever<sup>1,\*\*</sup> , D Mayer<sup>1,\*\*</sup> , D Picconi<sup>2,\*</sup> , J Metje<sup>1</sup>, S Alisauskas<sup>3</sup>,  
F Calegari<sup>3,4,5,6</sup>, S Düsterer<sup>3</sup>, C Ehlert<sup>7</sup>, R Feifel<sup>8</sup>, M Niebuhr<sup>1</sup>,  
B Manschwetus<sup>3</sup> , M Kuhlmann<sup>3</sup>, T Mazza<sup>9</sup>, M S Robinson<sup>1</sup>, R J Squibb<sup>8</sup>,  
A Trabattoni<sup>3,4</sup> , M Wallner<sup>8</sup>, P Saalfrank<sup>2</sup>, T J A Wolf<sup>10</sup>  and M Gühr<sup>1,\*</sup> 

<sup>1</sup> Institut für Physik und Astronomie, Universität Potsdam, 14476 Potsdam Germany

<sup>2</sup> Institut für Chemie, Universität Potsdam, 14476 Potsdam Germany

<sup>3</sup> Deutsches Elektronen Synchrotron (DESY), 22607 Hamburg, Germany

<sup>4</sup> Center for Free-Electron Laser Science (CFEL), DESY, 22607 Hamburg, Germany

<sup>5</sup> The Hamburg Centre for Ultrafast Imaging, Universität Hamburg, 22761 Hamburg, Germany

<sup>6</sup> Institut für Experimentalphysik, Universität Hamburg, 22761 Hamburg, Germany

<sup>7</sup> Heidelberg Institute for Theoretical Studies, HITS gGmbH, 69118 Heidelberg, Germany

<sup>8</sup> Department of Physics, Gothenburg University, SE-41296 Gothenburg, Sweden

<sup>9</sup> European XFEL GmbH, 22869 Schenefeld, Germany

<sup>10</sup> Stanford PULSE Institute, SLAC National Accelerator Laboratory, 94025 Menlo Park, United States of America

E-mail: [david.picconi@uni-potsdam.de](mailto:david.picconi@uni-potsdam.de) and [mguehr@uni-potsdam.de](mailto:mguehr@uni-potsdam.de)

Received 31 July 2020, revised 19 October 2020

Accepted for publication 12 November 2020

Published 17 December 2020



CrossMark

## Abstract

We present time-resolved ultraviolet-pump x-ray probe Auger spectra of 2-thiouracil. An ultraviolet induced shift towards higher kinetic energies is observed in the sulfur 2p Auger decay. The difference Auger spectra of pumped and unpumped molecules exhibit ultrafast dynamics in the shift amplitude, in which three phases can be recognized. In the first 100 fs, a shift towards higher kinetic energies is observed, followed by a 400 fs shift back to lower kinetic energies and a 1 ps shift again to higher kinetic energies. We use a simple Coulomb-model, aided by quantum chemical calculations of potential energy states, to deduce a C–S bond expansion within the first 100 fs. The bond elongation triggers internal conversion from the photoexcited  $S_2$  to the  $S_1$  state. Based on timescales, the subsequent dynamics can be interpreted in terms of  $S_1$  nuclear relaxation and  $S_1$ -triplet internal conversion.

Keywords: time-resolved x-ray spectroscopy, Auger spectroscopy, thionucleobases

(Some figures may appear in colour only in the online journal)

## 1. Introduction

Nucleobases are strong absorbers in the ultraviolet (UV) domain and show ultrafast processes after photoexcitation. Canonical nucleobases exhibit ultrafast relaxation to the singlet and triplet ground states after UV excitation through

internal conversion and intersystem crossing [1–4]. Electronic energy is efficiently transferred into vibrational excitation, a process that likely contributes to the remarkable stability of nucleic acids against UV-induced damage [1–3]. The processes underlying the ultrafast transitions violate the Born–Oppenheimer–Approximation (BOA), which allows for separate treatment of the electronic and nuclear degrees of freedom of a molecule, and is an important tool in

\*\*Contributed equally.

\*Author to whom any correspondence should be addressed.

modeling many molecular phenomena. In the case of close-lying potential energy surfaces such as avoided crossings or conical intersections, non-adiabatic coupling elements, which are neglected in the BOA, become large and lead to mixing of different Born–Oppenheimer electronic states. This redistributes the molecular population over initially unexcited potential energy surfaces [4, 5, 6]. The study of nucleobase dynamics, that cannot be described within the framework of the BOA, presents challenges both for theory as well as experiments that have been faced in the past by many systematic theoretical and experimental studies, reviewed for example in references [1–3, 7].

Thionucleobases are obtained by replacing one or two oxygen atoms by sulfur in canonical nucleobases, and exhibit two major differences compared to their canonical counterparts. The absorption spectrum is shifted from the UVC region into the UVA region [8, 9], which is much more abundant on the earth surface. In addition, photoexcitation produces long living triplet states in thionucleobases, leading to cross linking [10, 11] and the creation of reactive singlet oxygen via a reaction with the triplet oxygen molecules in the vicinity [12, 13]. These properties create on one hand a higher skin cancer risk for patients treated with thionucleobase medication for immunosuppression [14], on the other hand they might open the path for targeted photoinduced tumor therapy [15, 16].

The special case of thiouracil can be used for sketching the reaction pathway following UV excitation. The system is initially excited to the  $S_2$  state, with  $^1\pi\pi^*$  electronic character. In solution, intersystem crossing has been determined to be on a few hundred femtosecond timescale in 2-thiouracil and 4-thiouracil, as well as doubly thionated 2–4-thiouracil [9]. The  $S_1$   $^1n\pi^*$  state has been suggested to act as a doorway state to the lower lying triplet states in excited-state absorption studies in 2-thiouracil [13] as well as for 4-thiouracil. For the latter, the lifetime of the  $^1n\pi^*$  state has been indirectly determined to be 225 fs in solution [13, 17] by looking at the mismatch between the  $^1\pi\pi^*$  singlet decay and triplet rise times. In contrast, time-resolved photoelectron studies in the gas phase deduce an  $^1n\pi^*$  lifetime in 4-thiouracil of several picoseconds via fit of the photoelectron spectra [18]. This discrepancy is unlikely a solvent effect, as similar comparisons of gas and condensed phase techniques in 2-thiouracil give good agreements [19]. For 2-thiouracil, a joint theoretical-experimental investigation using Dyson orbitals in conjunction with gas-phase photoelectron spectroscopy [20] deduced a very fast time constant of 50 fs for  $^1\pi\pi^* \rightarrow ^1n\pi^*$  internal conversion and 500 fs for the  $^1n\pi^*$  lifetime; excited state absorption studies in condensed phase report on a similar  $^1n\pi^*$  lifetime [9].

We now concentrate on the case of 2-thiouracil (2-TU), on which we perform our studies. The mechanism for sub-100 fs decay out of the initially photoexcited  $S_2$  state as well as the ultrafast intersystem crossing from the  $S_1$   $^1n\pi^*$  state into triplet states are illuminated by theoretical investigations (see reference [21] for a concise review). Cui and Fang suggest electronic states as well as crucial geometries for three different pathways, one of which includes the  $^1n\pi^*$  state, while the other

paths involve transitions directly from the  $S_2$  to triplet states. Calculations by Mai, Marquetand and González predict two different pathways for  $S_2 \rightarrow S_1$  internal conversion, involving two different minima of the photoexcited state of 2-thiouracil [22]. One minimum is attributed to a  $^1\pi_s\pi_6^*$  electronic character possessing a nearly planar geometry, while the other minimum is attributed to a  $^1\pi_s\pi_2^*$  electronic character and it is reached via elongation and out-of-plane pyramidalization of the C–S bond. In nonadiabatic surface-hopping calculations at the CASPT2 level by the same group, both minima are predicted to be transiently populated, although the majority of the molecular photoexcited population is predicted to pass through the  $^1\pi_s\pi_6^*$  minimum within 60 fs to a conical intersection connecting it to the  $^1n\pi^*$  state, which then is populated for around 500 fs before decaying into triplet states [23]. A second dynamics paper from the same group on this topic using ADC(2) comes to very similar results but a longer 250 fs  $^1\pi\pi^* \rightarrow ^1n\pi^*$  transition time due to pyramidalization occurring in the  $^1\pi\pi^*$  state [24].

In this paper, we investigate the dynamics of 2-thiouracil using ultrashort x-ray probe pulses. Generally, time-resolved x-ray spectroscopy has been proven to be a useful tool for the study of structural changes in isolated molecules [25]. The x-rays interact with core electrons of the molecule, whose binding energies are strongly dependent on the element. Thus, x-rays offer the advantage of an element-selective spectroscopic view on molecular dynamics. In addition, due to the narrow spatial confinement of core-electronic wavefunctions, the transitions are highly site-specific. In the gas phase, these advantages have been used to follow for instance nucleobase internal conversion [26], fragmentation [27], ring-opening [28] as well as dissociation [29].

We use ultrafast x-ray induced Auger decay to investigate 2-thiouracil. This method has been applied before to investigate the internal conversion of thymine [30]. The key feature in this study was the change in molecular geometry on the photoexcited state. This can be deduced from the delay-dependent kinetic energy shift in the Auger spectrum. We used the fact that the kinetic energy of emitted Auger electrons depends strongly on the local bond distance of the molecule around the core hole created by the x-ray probe pulse. Auger electron spectroscopy is particularly suited for the use with free-electron lasers (FELs), since nonresonant Auger processes are insensitive to the energy of the probing photon, rendering the method immune against the energy fluctuation inherent in the self-amplified spontaneous emission (SASE) process. Moreover, for a given x-ray energy, several Auger decays of different elements can be addressed separately by analyzing different kinetic energy ranges, allowing the simultaneous study of the dynamics for different locations in the molecule.

We use ultrashort x-ray pulses to probe the sulfur 2p core electrons of UV-photoexcited 2-thiouracil. We measure a general shift of the 2p Auger spectrum towards higher kinetic energies. By comparison to simulations, we deduce that the molecule does not return to the molecular ground state for the maximal delay of our measurements of 2 ps. On the transient Auger signal, we identify three different dynamic features.



A first, sub-100 fs shift of the Auger band towards higher energies, followed by a 500 fs period with a slight shift towards lower energies and finally a picosecond modulation with a shift to higher kinetic energies. We show that the initial sub-100 fs modulation in the Auger spectrum can be clearly attributed to a C–S local bond elongation in the photoexcited  $S_2$  state as predicted in the theoretical literature [22–24]. The high-energy edge shifts to lower kinetic energies in this time interval and we show that an effective theoretical model can reproduce this trend. The later modulations in the Auger spectrum fit dynamics previously attributed to the  $S_1$  relaxation and  $S_1$ -triplet intersystem crossing.

## 2. Methods

The experiment was performed at the FLASH2 facility at DESY, where the newly built URSA-PQ (German: Ultraschnelle Röntgenspektroskopie zur Abfrage der Photoenergiekonversion in Quantensystemen, engl. Ultrafast x-ray spectroscopy for probing photoenergy conversion in quantum systems) experimental chamber [31] built by the Potsdam group was connected to the FEL beamline FL24 (see figure 1).

The sample was introduced via a capillary oven [32], heated to a temperature of 150 °C, creating a molecular gas jet that crosses the x-ray beam in the interaction region of the TOF spectrometer. We have not observed degradation of the sample in previous experiments with our capillary oven under the conditions used. The 150 °C for sample evaporation have also been used in other studies on 2-thiouracil [18, 33] as tautomerization can be neglected in this regime [33].

The molecule is preexcited with a 269 nm laser pulse at the maximum of its  $^1\pi\pi^*$  absorption band [18]. The pulse duration was about 80 fs as determined with an FROG (frequency resolved optical gating) setup. In the interaction region, the pulse was focused to a spot size of 50  $\mu\text{m}$  by means of a focusing mirror. Inside the beamline, the x-ray beam passed unperturbed through the center of a holey mirror, while the UV beam was directed onto the reflective section of the holey mirror (just off to the side from the hole) to produce near-collinear trajectories for the two beams, as seen in figure 1. The UV laser power was adjusted by means of a  $\lambda/2$  plate–polarizer combination. In the experiments, the UV laser pulse energy was set below 1  $\mu\text{J}$ . We performed systematic power scans on the time-dependent spectral features to make sure that the UV induced signal is not over-pumped.

The FEL produces frequency-tunable x-ray pulses via SASE radiation. We used a mean photon energy of 272 eV with a spectral bandwidth of 1%–2% (including jitter), as determined by the photoemission of rare gases in electron time-of-flight spectrometers (eTOF) integrated into the beamline [34]. The x-ray beam was linearly polarized parallel to the axis of our magnetic bottle spectrometer and parallel to the UV polarization. The x-ray pulses were focused by means of Kirkpatrick–Baez mirrors to a spot size slightly larger than the UV spot. We used systematic power scans to make sure that the x-ray induced electron spectra did not exhibit nonlinear phenomena.

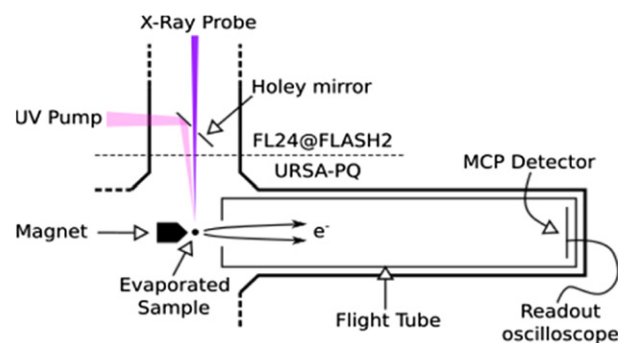


**Figure 1.** Experimental setup at the FL24 beamline of FLASH2. The UV pump and x-ray probe beams from FLASH2 are focused into the URSA-PQ chamber and hit the sample in the interaction region of the magnetic bottle spectrometer. The sample is evaporated using a capillary oven (located above the interaction region, out of the plane of the diagram) [31]. The photo- and Auger electrons generated by the x-ray interaction are guided into the flight tube by the magnetic bottle, detected using a multi-channel-plate (MCP) and their time of flight is measured by a fast analogue-digital converter (ADC).

The URSA-PQ setup contains a magnetic bottle electron spectrometer (MBES), providing high angular collection efficiency for electrons [35]. We used a permanent magnet and soft iron cone to reach a high magnetic field at the interaction region, which adiabatically transforms into a homogeneous magnetic field of a solenoid in a 1.7 m long flight tube. The magnet defines a small volume from which the electrons are guided into the flight tube. This volume is smaller than the optical beam overlap along the beam propagation axis. A retardation potential of 80 V was applied to the electrons using an electrostatic lens in front of the flight tube, diminishing their speed and increasing the time of flight and thus energy resolution.

The flight tube is kept at constant potential. At the very end, electrons are accelerated on the multi-channel-plate detector by a 300 V potential drop over 3 mm. The amplified electron signal trace is fully digitized using a 12 bit analog-to-digital converter (ADC) with 2 Gs  $\text{s}^{-1}$  sample rate. The amplified electron pulses have an FWHM of 10 ns, typical flight times are on the order of 250 ns for the fast valence electrons and 410 ns for the slower Auger electrons. We chose to integrate the ADC-traces to obtain our spectra, as individual electron hits could not be distinguished in TOF regions of high signal strength. The spectra were subsequently converted to a kinetic energy scale.

Tests on the Kr MNN Auger lines at 0 V retardation demonstrated an MBES resolution ( $E/\Delta E$ ) of 40. This is not yet the maximum achievable resolution, as some x-ray beam-halo problems at the beamline prevented us from positioning the magnet closer to the interaction region which would allow for a better optimised signal. We did not check the resolution at the retardation used further below (80 V). We estimate the resolution based on the sulfur 2p photoline with 3.5 eV width at 103.5 eV to be better than 30 with respect to the total kinetic energy or 7 relative to the retarded kinetic energy. The photoline itself is considerably broadened due to the FEL linewidth and therefore our estimate is really an upper limit.

Spatial overlap of the UV-pump and x-ray probe pulses was obtained by viewing a YAG screen inserted in the interaction region through a large work-distance microscope lens. Temporal overlap was established coarsely on a 50 ps scale using a fast photodiode and high-bandwidth (13 GHz) oscilloscope checking the rising flank of the UV and x-ray induced signals. Fine temporal overlap was found with the use of the sample itself, utilizing the time-dependent behavior of Auger and 2p-photoelectron lines. The width of the time-uncertainty function is 180 fs, time zero can be found with an accuracy of  $\pm 20$  fs.

The FLASH2 FEL delivers pulse-trains with a frequency of 10 Hz; we used 50 pulses at a 200 kHz repetition rate in each pulse-train [36]. An eTOF spectrum is recorded and saved for each FEL pulse. The UV laser is set to run at 100 kHz intra-burst rep-rate, such that every second x-ray shot is pumped by the optical laser, allowing the calculation of shot-by-shot difference spectra. This results in 500 x-ray pulses per second, with 250 pulses UV pumped. In the rest of the discussion, we will refer to UV pumped shots as UV-on, while x-ray only shots will be referred to as UV-off. FLASH2 instruments also provide a shot-by-shot measurement of the x-ray pulse power by means of a combined ion–electron detector. This data has been used to rescale each eTOF spectra, therefore correcting for fluctuations in the SASE pulse power.

A bunch arrival monitor (BAM) at the FEL measures the time of arrival of each electron bunch, giving information on the jitter of the x-ray arrival time [37, 38]. The width of the arrival time distribution has been measured to be 140 fs. The length of the x-ray pulse plus non-corrected jitter was estimated to be 160 fs. Pump-probe delays have been corrected with the BAM data and rebinned, exploiting the jitter and allowing finer delay binning than the time steps chosen during the measurement. The bin sizes are chosen by dividing the shot distribution in discrete parts, so that each bin is populated by the same number of shots. That is, the delay length of each bin is adjusted so that all bins have the same statistics. The delay points have been measured by random scans in repeated cycles over many hours. Thus any systematic drifts in the data-acquisition would average out.

To facilitate the interpretation of the experimental data, we make use of *ab initio* quantum chemical calculations to explore the potential energy surfaces (PESs) of the neutral (2-TU), core-ionized (2-TU+) and dicationic (2-TU++) molecule. The ground and excited states of 2-TU and 2-TU++ were computed using ground state coupled cluster theory with singles and doubles (CCSD) and the equation-of-motion formalism for the excitation energies (EOM-EE-CCSD) with the 6–311++G\*\* basis set [39]. In order to explore the high lying states of 2-TU++, potential energy cuts along the C–S bond distance were performed using time-dependent density functional theory (TDDFT) with the B3LYP functional and the 6–311++G\*\* basis set. Geometry optimizations for the ground and excited states of 2-TU were also performed at the (EOM-)CCSD/6–311++G\*\* level without geometrical constraints using Q-chem, and the stability was verified by frequency calculations with the smaller 6–31++G\*\* basis set. Stable minima were found for the states  $S_0$ ,  $S_1$ ,  $S_2$  and  $T_1$ .

The minimum of  $S_0$  has a nearly planar structure. Furthermore, optimizations where the molecule was constrained to be planar were also carried out and additional (unstable) stationary points could be located for the states  $S_0$ ,  $S_1$ ,  $S_2$ ,  $T_1$  and  $T_2$ . The core-ionized states were computed using the equation-of-motion ionization potential formalism (EOM-IP-CCSD) with the 6–311++G\*\* basis set for the S atom and the 6–31++G basis for all other atoms; in order to simulate the ionization from the excited states of 2-TU, the reference (neutral) CCSD wavefunction was obtained starting from an unrestricted Hartree–Fock wavefunction optimized using the maximum-overlap-method (MOM) [40]. All calculations were performed using the package Q-chem 4.4 [41]. Spin–orbit coupling, leading to a splitting of the core ionized states of about 1 eV is not included in the calculations, instead we model photoionization from the px, py, pz orbitals.

### 3. Results

The 272 eV photons used in the experiment allow for an element and site-specific investigation of the molecular dynamics from the perspective of the sulfur atom. An overview of the electron kinetic energy spectrum without UV pre-excitation is shown in figure 2. Various features are visible in the graph. A sharp line at 103 eV in kinetic energy, corresponding to a binding energy of 169 eV, is attributed to photoemission from the sulfur 2p ( $j = 3/2$  and  $1/2$ ) levels according to reference [33]. The  $\sim 1$  eV spin–orbit splitting [33, 42] cannot be resolved due to insufficient spectral resolution determined by the bandwidth of the SASE FEL and the MBES energy resolution. The neighboring feature, spanning the range 115–150 eV is attributed to the Auger emission caused by the 2p core vacancy. Scanning the photon energy does not change this feature, as it is typical for Auger decay. Furthermore, the energy levels with 2p core hole binding energies around 170 eV and ten to a few ten eV valence binding energies result in Auger features at this energy band. No detailed structure is visible, even at higher MBES resolution with higher retardations, due to many broad Auger decay channels overlapping. Coarsely, the atomic Auger spectrum should divide into three larger groups belonging to sulfur  $3p3p \rightarrow 2p$  (highest energy),  $3p3s \rightarrow 2p$  and  $3s3s \rightarrow 2p$  (lowest energy) type Auger decays. For molecules with mixed atomic orbitals resulting in molecular orbitals, these groups can still be identified in case of oxygen Auger decay [30], here it is less pronounced.

In figure 3(a), we show the pump-probe difference spectra in the energy range of the Auger features in false color-representation. The spectra are obtained by subtracting UV-off shots from the UV-on shots, accumulating data from  $\sim 16$  million FEL shots over all delays. A positive differential signal (rendered with red color in the figures) signifies that UV pumping leads to more emitted electrons for that specific kinetic energy, while negative values (rendered with blue color in the figures) stand for a UV-induced depletion of the electron signal. Time zero was determined by maximizing the cross-correlation between a step function and the differential signal intensity. The delay values should therefore be regarded as relative to the appearance time of this feature.

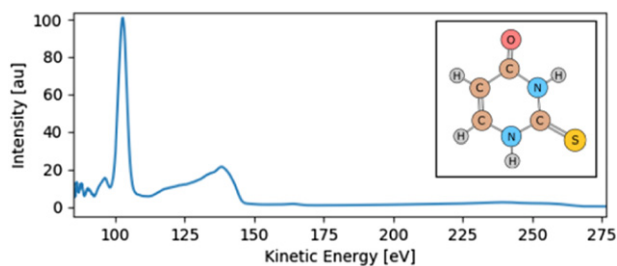


**Figure 2.** Overview of the photoemission spectrum of 2-thiouracil at 272 eV photon energy on an electron kinetic energy axis. Two main features are visible; the sulfur 2p photoline centered at 103 eV and the Auger band in the 115-150 eV range. Inset: structure of 2-thiouracil.

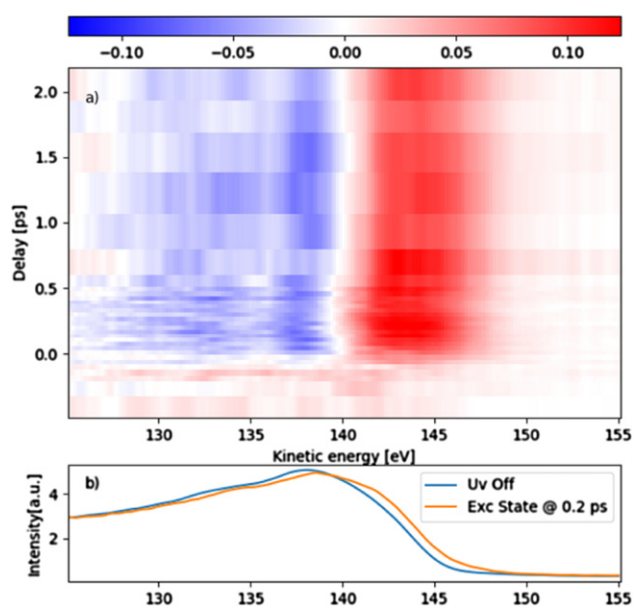


**Figure 3.** (a) False-color representation of time resolved differential Auger spectrum (UV-on–UV-off) for 2-thiouracil (red: positive signal, blue: negative signal). A differential feature appears at  $t \sim -60$  fs and remains visible for all recorded delays. The Auger emission shifts to higher kinetic energies with UV-illumination and ultrafast changes in the shape are visible around time zero. (b) Spectra without UV excitation (UV off, blue) and spectrum of the excited state at 0.2 ps delay (orange) recovered by the procedure described in the text.

For positive delays, a general shift of the Auger spectrum toward higher kinetic energies is visible. This coarse shift of intensity in the difference spectrum related to the UV excitation is about 4 eV, however, the shift undergoes dynamics on an eV scale, as we will show below. We first investigate the coarse shift closer. The UV-on spectrum is given as  $fES + (1 - f)GS$ , where ES and GS are the excited state and ground state Auger spectra respectively and  $f$  is the fraction of excited molecules. The UV-off spectrum is given as GS. The difference UV-on minus UV-off is thus  $f(ES - GS)$ . In the process of photoexcitation, the  $f$  changes.

An estimate of the excited state Auger spectrum is shown in figure 3(b). It has been obtained from the UV-on and UV-off data. We need to model  $f$  as a function of delay to obtain ES. Assuming that the fraction of excited molecules,  $f$  introduced

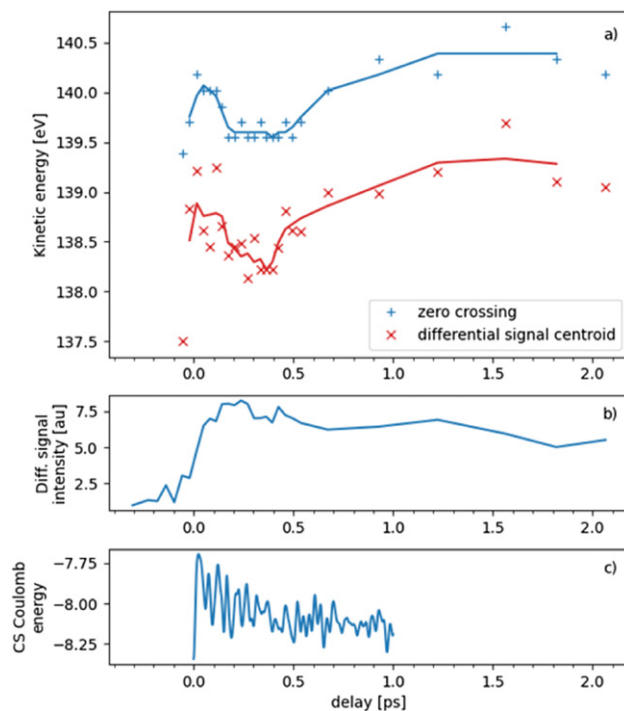


**Figure 4.** (a) Zero crossing and differential signal centroid positions vs delay. Ultrafast dynamics is visible after time zero, with changes occurring on timescales from 100 fs to 1 ps. Solid lines are 3 point moving averages. (b) Differential signal intensity, calculated from the cumulative sum of positive plus absolute of negative data points for each delay value. (c) Negative Coulomb energy constructed from the trajectory set of reference [24] using a simple Coulomb potential as a function of C–S distance.

above, in the ensemble rises as an error function from 0 to 0.22 we succeeded to reconstruct the ES spectrum. The final  $f$  of 0.22 was chosen as the minimum possible value that does not lead to negative amplitudes in the reconstructed excited spectrum ES. We identify that the shape of the Auger spectrum changes by comparing the UV-off spectrum with the reconstructed ES spectrum at 200 fs delay. The maximum in the UV-off spectra is located at 138 eV. For the excited state spectrum at 200 fs, the region around the maximum flattens up to about 142 eV, for higher energies the excited state spectrum drops. This leads to the observed gross shift in the difference spectra with a bleach at 138 eV and an increase from 140 eV on with its maximum at 142 eV. The edge itself shifts only by about 1 eV in the center of the edge and about 2 eV at the very high energy region. Assuming that the ES spectrum is completely static (no molecular dynamics after photoexcitation), the difference spectrum would not show any dynamics, apart from a changing scaling factor  $f$ . We however observe a fine shift visible in the zero line, thus indicating the presence of ultrafast processes in the relaxation pathway of the molecule.

In order to quantify the shift dynamics, the zero-crossing position of the differential signal (white line in between blue and red features) needs to be analyzed for each time delay. We estimated this parameter by maximizing the cross-correlation of the kinetic energy spectrum with a sign function. This method delivers the blue datapoints in figure 4(a). In addition,

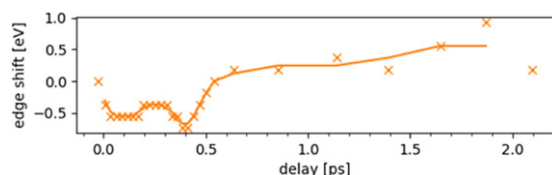


**Figure 5.** Auger edge shift as a function of pump-probe delay. Edge values are taken at the point where the signal rises over 20% of the peak intensity. Data points are shown for delays where the excited state population is above 1% of the final value. Solid line is a 3 point moving average.

we calculated the center of mass of the positive and negative contributions and averaged their value (red datapoints in figure 4(a)). The analysis of the centroid positions allows us to be sensitive to changes in the overall spectral distribution that might not affect the zero crossing point.

The aforementioned analysis technique does not give meaningful results when no differential features are present as it would be noise dominated. Therefore, we use the absolute intensity of the differential signal in figure 4(b)) (positive contribution + absolute of negative contribution) to select the delay regions that can be interpreted. The onset of the differential feature is found at delay  $\sim -60$  fs, and we clearly identify the typical lineshape in this time bin in the false color plot of figure 3(a).

The Auger dynamics shows three phases (see figure 4(a)). First, a fast shift towards higher kinetic energies on a  $\sim 100$  fs scale is visible, shifting the centroid difference as well as the zero crossing up by about 1 eV in kinetic energy. Since the time resolution of the experiment is in this regime, we cannot give more precise estimates of the dynamics. After this initial rise in the kinetic energy, a transient dip of  $\sim 0.5$  eV is visible, lasting for about 400 fs. This is followed by a 1 ps rise in centroid/zero crossing energy by 1 eV.

We now concentrate on the shift in the edge of the excited state Auger spectrum at high kinetic energies. We therefore analyze the time dependent ES spectra with the dynamic  $f$  described above. Figure 5 shows the edge-position, defined by the ES signal being above 20% of the peak signal for each delay bin. The shifts are evaluated relative to the ES spectrum at zero delay. Ultrafast dynamics on the same time scales as presented above can be discerned here, with some differences in the shift amplitudes.

The three phases mentioned above are discernible here again. The initial 100 fs dynamics is characterized by a shift of the edge position of  $-0.5$  eV (relative to the first datapoint), which is the opposite trend as shown in the zero position and centroid. This is followed by a plateau and a further dip at the 400 fs mark. After the dip, a fast 1 eV blue shift is observed, persisting for the remaining of the time evolution. The different signs of spectral shift in the edge and at zero crossing in the beginning actually indicate that the excited state Auger spectrum undergoes changes in its shape.

## 4. Discussion

First, we discuss the results of the calculations. Table 1 reports our calculated energies at different stationary points on the excited states surfaces, and the corresponding value for the C–S bond distance. Geometry optimizations have been carried out with and without the constraint of planarity. Local and global minima on the singlet and triplet potential energy surfaces of 2-TU have been located by Mai *et al* using multistate complete active space perturbation theory calculations and in the present study using EOM–CCSD theory [22]. The calculated energies as well as geometry parameters are close to those of Mai *et al* [21]. Surface-hopping trajectories calculated by Mai *et al* predict that in the first 50 fs the molecule retains a near-planar geometry, and so do many trajectories at subsequent times and after transitions from  $S_2$  to other states.

In order to investigate the initial behavior of the Auger signal at photoexcitation, we computed the energies of the valence-excited, core-ionized and dicationic states in the Franck–Condon region (see figure 6). We also calculated PESs along a reaction pathway which linearly interpolates between the unrestricted optimized minima of  $S_0$  (reaction coordinate = 0) and the initially photoexcited  $S_2$  (reaction coordinate = 1) states. This will help later in the interpretation of the high kinetic energy Auger edge.

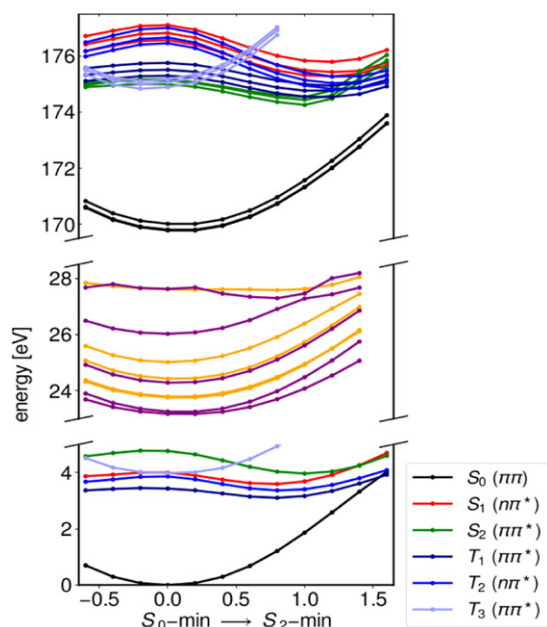
The data in the Franck–Condon region allows us to estimate the change in the kinetic energy of emitted Auger electrons, as Auger kinetic energy is equal to the difference between the core ionized state (one electron missing from the sulfur 2p shell) and the dicationic manifold (with two electrons missing in the valence orbitals). Auger emission from the non-UV excited molecule occurs from the ground core-excited state (black around 170 eV) to many different dicationic states, of which only the lowest ones are calculated. Auger emission from the UV excited molecule occurs from the core ionized  $S_2^{-1}\pi\pi^*$  state (green with an energy of 175 eV in the Franck–Condon region). Assuming that the rates for the Auger transitions do not change upon UV excitation, the model predicts a general shift towards higher kinetic energy of the Auger spectrum in the range of 5 eV.

Molecular dynamics on the core-ionized states can be neglected within the few fs-Auger decay timescale. All the states visited by the molecule after UV excitation show a gap with respect to the ground state. If efficient coupling to the ground state is absent on our measured timescales, as predicted by many previous papers [9, 20, 21], the measured Auger spectra must show a long lasting blue shift that begins at time zero and remains present for all probed delays. This is in general agreement with the spectral trend observed in our measurements, and thus serves as a confirmation of excited state lifetimes longer than a few picoseconds.

The assumption of no Auger rate changes upon UV excitation however is oversimplified. As the valence occupation of

**Table 1.** Calculated electronic energies and C–S bond distances at planar (\*) and non-planar minima of 2-thiouracil, optimized at the EOM–CCSD/6–311++G\*\* level.

Minimum	Planar geometries					Non-planar geometries		
	S <sub>0</sub> *	S <sub>1</sub> *	S <sub>2</sub> *	T <sub>1</sub> *	T <sub>2</sub> *	S <sub>1</sub>	S <sub>2</sub>	T <sub>1</sub>
Energy (eV)	0.00	3.78	4.44	3.17	3.65	3.48	3.96	3.00
C–S distance (Å)	1.65	1.74	1.76	1.67	1.73	1.77	1.90	1.77

**Figure 6.** Calculated energy values for different electronic levels and for various nuclear configurations interpolated between the S<sub>0</sub> and S<sub>2</sub> minima. The energy scale is divided in ground and valence excited states (lower portion), 10 lowest energy dicationic states (middle) and core ionized (2p<sup>-1</sup>) states (upper). The core excited states follow the color coding of the valence states, meaning that their valence configuration is maintained with a 2p core hole. The core ionized states of each valence state are divided into three states, according to px, py, pz ionization. SO coupling, leading to an observed core-ionized state splitting of 1 eV, is not included in our calculation. Singlet and triplet dicationic states are shown in orange and violet, respectively. Auger features with the highest observable kinetic energy can be calculated from the energy gap between core excited and dicationic states.

two of the highest valence orbitals changes, there will be rate changing effects. Similar to the resonant-Augur language, one can define spectator and participator channels here but the calculation of those rates is beyond the scope of this paper. We expect the valence reorganization effects induced by the UV excitation to be most effective at the high energy edge of the Auger spectrum, with participation from the highest orbitals. A comparison with the reconstructed ES spectrum (figure 3(b)) serves to support this point. The edge of the spectrum shows a UV induced shift of only 1–2 eV. In the region around the maximum, the redistribution of population is larger indicating shifts closer to those predicted by the gap between ground cationic state and excited cationic states, thus rate changes due to UV are less important in this region.

In order to interpret the initial ultrafast changes of the shift in the Auger spectrum, we include a model for the more energetic states of the dicationic manifold. The previously presented calculations on the lowest dicationic states will be used further below in a comparison to the edge features presented in figure 5. Upon sulfur 2p Auger decay, dicationic states with electrons missing in orbitals localized at the sulfur atom will be preferentially populated, as the decay matrix element is sensitive on the overlap of core and valence holes [30, 43]. Those orbitals promote the C–S bonding and thus the Auger decay kinetic energy will be sensitive to the C–S bond [30]. Since the missing valence electrons expose the nuclear charges, the Auger manifold will be dominated by Coulomb repulsion. The lowest energy dicationic states often show a binding character as seen in figure 6. We performed a Löwdin population analysis on the dicationic states of figure 6. Indeed, for most states the computed charge on the S atom is in the range 0.8–1.0 e. The electron hole on the S atom is present for all geometries, suggesting that Coulomb repulsion should be present, at least at longer C–S distances. From the kinetic energy difference between the maximum and the edge of the Auger band, the Coulomb repulsive states should be located 7–8 eV above the lowest (bound) states of 2-TU2+, therefore they are not covered by our EOM–CCSD calculations. Repulsive potential energy curves in this energy range are predicted by TDDFT scans we performed along the C–S bond distance (not shown here). Indeed, with higher potential energy, dicationic states are increasingly dominated by Coulomb repulsion [44]. All statements below are therefore valid for the majority of the Auger decay channels, apart from the highest kinetic energy ones. Figure 7 shows a sketch of the electrostatic energy  $e^2/R$  for a dicationic state as a function of C–S bond stretch  $R$ . Qualitatively speaking, this can be seen as the central energy of the final state in the Auger decay process. Therefore, the decrease of Coulomb energy with increasing C–S bond distance will lead to an increase in Auger kinetic energy, given that the core ionized starting state remains approximately constant in energy along the reaction coordinate as seen in figure 6.

The data on the zero-crossing as well as the centroid in figure 4 indicates an initial dynamic shift towards higher kinetic energies around time zero by less than 1 eV. Assuming that the ground and excited state spectra have similar shape, the overall spectral shift will be double the zero crossing shift, so between 1 and 2 eV. According to figure 7, the simple Coulomb-potential model predicts a bond expansion. At the Franck–Condon point, the molecule possesses a C–S bond distance of 1.65 Å (table 1). The experimentally observed shift

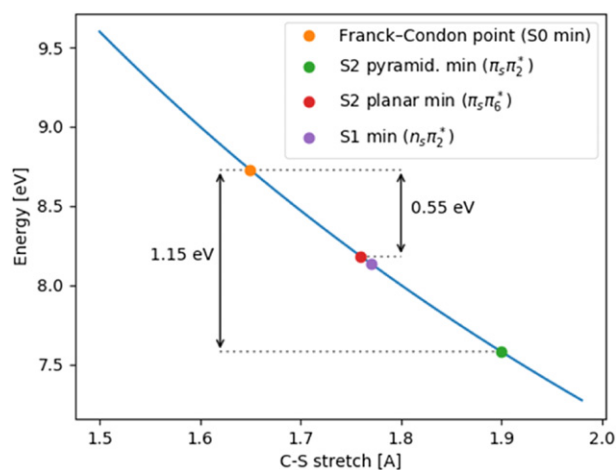


**Figure 7.** Electrostatic energy for a dicationic state for various bond lengths. Numerical values for the bond lengths as in table 1. In the suggested dynamics, the electrostatic contribution to the molecular energy follows the highlighted path, caused by an ultrafast stretch and subsequent contraction of the C–S bond.

would predict an expansion of the C–S bond by nuclear relaxation into an interval from 1.85 to over 2 Å within a delay range limited essentially by our temporal resolution. This interval does not include the calculated planar minimum at 1.76 Å. Our planar minimum has a structure similar to the (slightly non-planar)  $\pi_s\pi_6^*$  minimum found by Mai *et al* [23], and predicted to be the dominant pathway for nuclear relaxation out of the Franck–Condon region on the  $S_2$  surface at short times. The experimentally found interval includes the unrestricted minimum at 1.90 Å. This minimum has a structure similar to the  $\pi_s\pi_2^*$  minimum found by Mai *et al* [22]. It is predicted to be populated, however with much less amplitude compared to the other minimum. The ADC(2) calculations by the same group however predict the internal conversion mostly occurring through a pyramidal deformation [24].

Shortly after the maximum in spectral shift, there is a reverse shift in the zero crossing and centroid towards lower kinetic energies by about 0.5 eV, as observed in figure 4. The feature is then stable for about 400 fs. The ADC(2) based trajectory calculations indeed show a reverse trend. In order to compare the results to our data, Mai *et al* kindly sent us the C–S distance of their trajectories [24]. We used those to calculate the dicationic energies and show them in figure 4(c). We clearly identify the reverse trend indicating shrinking C–S bond length over 400 fs. In the framework of the ADC(2) calculations, this period is dominated by dynamics on the  $S_2$  state [24]. In comparison to these simulations, we seem to pick up the trends in the bond extension well. The rising kinetic energy after 400 fs does not find its counterpart in any of the calculated C–S bond data of [24]. Thus it would need to be attributed to electronic state effects. On this timescale the triplet  $T_1$  state is predicted to take over in referene [24].

The CASPT2 trajectory calculations of Mai *et al* [23], display a  $S_2$ – $S_1$  internal conversion on the order of 60 fs (below our time-resolution), with an  $S_1$  state lifetime of 400–500 fs [23]. This interpretation is also chosen in previous experiments [18, 19, 40]. Afterwards, the  $T_1$  and  $T_2$  states become popu-

lated via an intersystem crossing with the  $S_1$ . In this framework, the fitting time scales suggests that the pump-probe Auger signal in the interval between 50 fs and 400 fs is most likely due to the population in the  $S_1$  ( $^1n\pi^*$ ) state. According to the Coulomb-potential model, the decrease in kinetic energy should be associated with a slight contraction of the C–S bond. However, at the  $S_1$  minimum, optimized at the EOM–CCSD level, the C–S distance is 1.77 Å, i.e. very similar to the bond length at the  $S_2$  planar minimum. Therefore, the C–S bond contraction could be explained by allowing that a relevant fraction of molecules on the  $S_2$  surface either evolve towards the  $^1\pi_s\pi_2^*$  minimum (a barrierless pathway as shown in figure 6, but less relevant according to the simulations of reference [23]) or undergo a large C–S elongation while retaining planarity, before undergoing the internal conversion. On the other hand, many of the nonadiabatic dynamics trajectories of reference [23] evolve along planar configurations also on the  $S_1$  surface. Optimizing the  $S_1$  state with the constraint of planarity we obtained a stationary point with a shorter C–S distance (1.74 Å), which might also explain the observed decrease in kinetic energy. This model of course neglects all changes in the Auger spectra induced by electronic transitions. While our assumptions are justified on the initially photoexcited state, a transition from  $S_2$  to  $S_1$  can equally alter the Auger kinetic energies on the eV level. In order to make more precise statements about the competition of electronic vs nuclear relaxation in shaping the Auger spectrum, further simulations need to be accomplished, which are beyond the scope of this work.

As stated above, we assumed that only nuclear geometry is able to influence the Auger kinetic energy. This is certainly justified for the initial relaxation of the molecular vibrational wave packet out of the Franck–Condon window. At later times, there might be an increasing influence of the electronic state changes on the Auger spectrum, and the argument will become more intertwined. However, we note that for Auger decay of the lighter oxygen, we have observed this strong electronic state dependence before as a massive redshift of the Auger band [30]. This is obviously lacking in our current experiment. We thus speculate, that the Auger decay of the much heavier sulfur, due to its increased density of states on the dicationic manifold will be less susceptible to those electronic state effects.

Regarding the dynamics of the high energy Auger edge, we can compare the excited state spectrum inferred from the experimental data to a synthetically constructed spectrum from the calculated potential energy curves of figure 6. It is important to note, that the computational results do not give us any information on the relative strengths of the various transitions; therefore, the constructed spectrum should be regarded as a qualitative guideline, and not as a predictive tool. Assuming a linear relaxation along the  $S_2$  potential surface on a time scale of 60 fs, a time dependent excited state spectrum from the data in figure 6 can be constructed. The energy difference between the core excited  $S_2$  state and each of the calculated dicationic states is taken as a function of time, and all the contributions are broadened and summed together to generate the time dependent spectrum. Convoluting the result with an error function in order to model the non-simultaneous excitation of

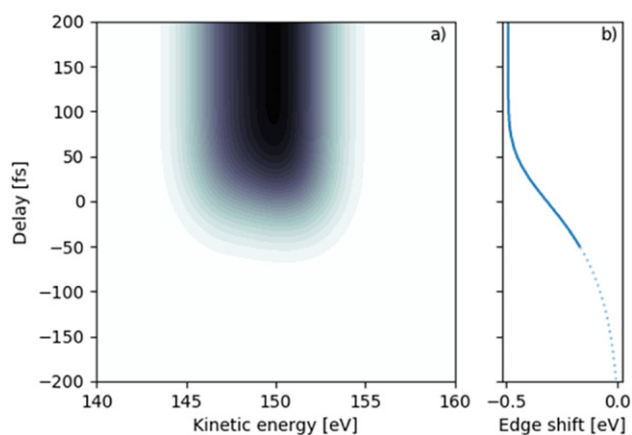


**Figure 8.** (a) Reconstructed high kinetic energy band of the Auger spectrum for the calculated energy levels, convoluted with an error function to account for non-simultaneous excitation of the molecular ensemble. (b) Auger edge shift in the reconstructed spectrum as a function of pump-probe delay. Dashed line shows values where the excited fraction is below 1% (compare to figure 4(b)).

the ensemble, we obtain an estimate for the dynamics of the Auger edge.

The calculated spectrum is shown in figure 8(a). Analyzing the edge shift in the same way as in figure 5, we deduce a redshift of the edge position (figure 8(b)) in agreement with the experimental result in figure 5. The calculated value is 0.3 eV, while the experimental shift in the edge is 0.5 eV with a discrete bin interval of 0.2 eV. According to the simulation, the energies of the lowest dicationic states and of the core-ionized states accessed from  $S_2$  increase and decrease respectively, along the reaction pathway of figure 6. This is associated with a highest kinetic energy of the Auger electrons. Therefore, the short-time observed redshift of the Auger band edge provides further evidence for an ultrafast nuclear relaxation of the molecule out of the Franck–Condon region on a sub 100 fs timescale.

On a longer time scale, for delays in the range 0.4 to 1.5 ps, the shift to higher kinetic energies observed on both the zero crossing and the edge position points to further ultrafast processes in the molecular dynamics (figures 4 and 5). The detailed interpretation of those features however requires a deeper understanding of the Auger processes in the molecule, due to the aforementioned electronic state effects.

## 5. Summary

In this work, we have used Auger spectroscopy to investigate the ultrafast dynamics of 2-thiouracil after UV excitation, using a UV pump—x-ray probe setup. The experiment has been carried out at beamline FL24 at the FLASH2 free electron laser. We observe a shift in the overall Auger emission pattern, as well as ultrafast dynamics in the shift amplitude, providing evidence for ultrafast processes in the molecule. The dynamics of the zero-crossing/centroid of figure 4 in conjunction with our quantum chemical calculations and the trajectory simulations by Mai *et al* [23, 24] strongly suggests that the

time-resolved Auger signal is capable of capturing the main relaxation pathway of 2-thiouracil, which involves three steps: (i) an ultrafast, <100 fs, process likely associated with an overstretching of the C–S bond, which leads to the  $S_2$ – $S_1$  internal conversion; (ii) an intermediate evolution on the  $S_1$  surfaces, for approximately 400 fs [23] or alternatively a shrinking C–S bond dominated by  $S_2$  dynamics [24]; (iii) the final intersystem crossing and subsequent relaxation in the triplet manifold. The C–S bond elongation in step (i) can be deduced from the observed zero line/centroid Auger shift towards higher kinetic energies using a simple Coulomb-model for dicationic states. Additional support for this behavior is delivered by an observed edge shift towards lower kinetic energies, which is predicted by our model using the lowest dicationic states. Experimental evidence for (ii) and (iii) comes from an agreement of timescales in the zero line/centroid Auger shift, the details of the shift required additional Auger spectrum modeling involving electronic and nuclear dynamics, which is beyond the scope of this work.

## Acknowledgments

We thank S Mai (González group, Theoretical Chemistry, University of Vienna) for generously sending us trajectory data from reference [24] used in figure 4(c). We thank the Volkswagen foundation for funding via a Lichtenberg Professorship. We thank the BMBF for funding the URSA-PQ apparatus and for funding JM via Verbundforschungsprojekt 05K16IP1. We acknowledge DFG funding via Grants GU 1478/1-1 (MG) and SA 547/17-1 (PS). TJAW was supported by the US Department of Energy, Office of Science, Basic Energy Sciences, Chemical Sciences, Geosciences, and Biosciences Division. We acknowledge DESY (Hamburg, Germany), a member of the Helmholtz Association HGF, for the provision of experimental facilities. Part of this research was carried out at FLASH2. FC acknowledges support from the European Research Council under the ERC-2014-StG STARLIGHT (Grant Agreement No. 637756).

## ORCID iDs

F Lever <https://orcid.org/0000-0002-8448-7594>  
 D Mayer <https://orcid.org/0000-0002-1858-6818>  
 D Picconi <https://orcid.org/0000-0001-6468-1595>  
 B Manschwetus <https://orcid.org/0000-0001-6165-9560>  
 A Trabattoni <https://orcid.org/0000-0002-0187-9075>  
 T J A Wolf <https://orcid.org/0000-0002-0641-1279>  
 M Gühr <https://orcid.org/0000-0002-9111-8981>

## References

- [1] Barbatti M, Borin A C and Ullrich S (ed) 2015 *Nucleobases in the Gas Phase and in Solvents* (Berlin: Springer)
- [2] Middleton C T, de La Harpe K, Su C, Law Y K, Crespo-Hernández C E and Kohler B 2009 *Annu. Rev. Phys. Chem.* **60** 217

- [3] Crespo-Hernández C E, Cohen B, Hare P M and Kohler B 2004 *Chem. Rev.* **104** 1977
- [4] Wolf T J A, Parrish R M, Myhre R H, Martínez T J, Koch H and Gühr M 2019 *J. Phys. Chem. A* **123** 6897
- [5] Levine B G and Martínez T J 2007 *Annu. Rev. Phys. Chem.* **58** 613
- [6] Yarkony D R 1996 *Rev. Mod. Phys.* **68** 985
- [7] Improta R, Santoro F and Blancafort L 2016 *Chem. Rev.* **116** 3540
- [8] Ashwood B, Pollum M and Crespo-Hernández C E 2019 *Photochem. Photobiol.* **95** 33
- [9] Pollum M, Jockusch S and Crespo-Hernández C E 2015 *Phys. Chem. Chem. Phys.* **17** 27851
- [10] Brem R, Daehn I and Karran P 2011 *DNA Repair* **10** 869
- [11] Zhang X, Jeffs G, Ren X, O'Donovan P, Montaner B, Perrett C M, Karran P and Xu Y-Z 2007 *DNA Repair* **6** 344
- [12] Kuramochi H, Kobayashi T, Suzuki T and Ichimura T 2010 *J. Phys. Chem. B* **114** 8782
- [13] Pollum M, Martínez-Fernández L and Crespo-Hernández C E 2014 *Photoinduced Phenom: Nucleic Acids I* ed M Barbatti, A C Borin and S Ullrich (Berlin: Springer) pp 245–327
- [14] Euvrard S, Kanitakis J and Claudy A 2003 *N. Engl. J. Med.* **348** 1681
- [15] Massey A, Xu Y-Z and Karran P 2001 *Curr. Biol.* **11** 1142
- [16] Reelfs O, Karran P and Young A R 2012 *Photochem. Photobiol. Sci.* **11** 148
- [17] Borrego-Varillas R, Teles-Ferreira D C, Nenov A, Conti I, Ganzer L, Manzoni C, Garavelli M, Maria de Paula A and Cerullo G 2018 *J. Am. Chem. Soc.* **140** 16087
- [18] Mohamadzade A, Bai S, Barbatti M and Ullrich S 2018 *Chem. Phys.* **515** 572
- [19] Sánchez-Rodríguez J A, Mohamadzade A, Mai S, Ashwood B, Pollum M, Marquetand P, González L, Crespo-Hernández C E and Ullrich S 2017 *Phys. Chem. Chem. Phys.* **19** 19756
- [20] Mai S, Mohamadzade A, Marquetand P, González L and Ullrich S 2018 *Molecules* **23** 2836
- [21] Arslançan S, Martínez-Fernández L and Corral I et al 2017 *Molecules* **22** 998
- [22] Mai S, Marquetand P and González L 2015 *J. Phys. Chem. A* **119** 9524
- [23] Mai S, Marquetand P and González L 2016 *J. Phys. Chem. Lett.* **7** 1978
- [24] Mai S, Plasser F, Pabst M, Neese F, Köhn A and González L 2017 *J. Chem. Phys.* **147** 184109
- [25] Young L et al 2018 *J. Phys. B: At. Mol. Opt. Phys.* **51** 032003
- [26] Wolf T J A et al 2017 *Nat. Commun.* **8** 29
- [27] Pertot Y et al 2017 *Science* **355** 264
- [28] Attar A R, Bhattacharjee A, Pemmaraju C D, Schnorr K, Closser K D, Prendergast D and Leone S R 2017 *Science* **356** 54
- [29] Brauße F et al 2018 *Phys. Rev. A* **97** 043429
- [30] McFarland B K et al 2014 *Nat. Commun.* **5** 4235
- [31] Metje J 2020 *Applied Sci.* **10** 7882
- [32] McFarland B K et al 2014 *J. Phys.: Conf. Ser.* **488** 012015
- [33] Giuliano B M, Feyer V, Prince K C, Coreno M, Evangelisti L, Melandri S and Caminati W 2010 *J. Phys. Chem. A* **114** 12725
- [34] Braune M, Buck J, Kuhlmann M, Grunewald S, Düsterer S, Viefhaus J and Tiedtke K 2018 *J. Synchrotron Radiat.* **25** 3
- [35] Kruit P and Read F H 1983 *J. Phys. E: Sci. Instrum.* **16** 313
- [36] Faatz B et al 2016 *New J. Phys.* **18** 062002
- [37] Schulz S et al 2015 *Nat. Commun.* **6** 5938
- [38] Savelyev E et al 2017 *New J. Phys.* **19** 043009
- [39] Krylov A I 2008 *Annu. Rev. Phys. Chem.* **59** 433
- [40] Besley N A, Gilbert A T B and Gill P M W 2009 *J. Chem. Phys.* **130** 124308
- [41] Shao Y et al 2015 *Mol. Phys.* **113** 184
- [42] Thompson A C and Vaughan D 2009 *X-RAY Data Booklet* (Washington DC: GPO - United States Government Publishing Office)
- [43] Siegbahn H, Asplund L and Kelfve P 1975 *Chem. Phys. Lett.* **35** 330
- [44] Cryan J P et al 2012 *J. Phys. B: At. Mol. Opt. Phys.* **45** 055601



# Appendix A

## Experimental Control and Online Data Analysis

To aid in the operation of the URSA-PQ chamber, I developed a set of complementary tools and software applications. They interface with the DESY infrastructure through the DOOCS (Distributed Object Oriented Control System) system. Section A.1 focuses on the tools developed for the control of the experimental hardware, while section A.2 presents the online data analysis and display utilities.

The entire codebase is open source and is made available, together with its documentation, at [158].

### A.1 Safety, monitoring and control system

Low-level control of the experimental hardware is taken care of by a combination of a PLC (Programmable Logic Computer) and a Unix server. The PLC is responsible for all real-time sensitive tasks, such as vacuum and high voltage interlocks; the Unix server acts as an interface to the DESY network and handles data processing. A schematic overview of the system architecture is shown in Fig. A.1.

Safety routines are constantly running, the PLC monitors the pressure in the chamber via a combination of a Pirani and cold cathode gauges, and controls high voltage and beamline vacuum interlocks to ensure safe operation. A set of vacuum valves are used to separate the main chamber from the pre-vacuum pumps. In case of a pre-vacuum failure, the valves lock to protect the main chamber. Moreover, the PLC controls the actuators for the in-vacuum manipulator stages.

The sample oven is controlled by three independent PID (Proportional Integral Derivative) filters, one for each heater section. The temperature is read by the PLC via vacuum-compatible thermocouples; the Unix server controls the power supplied to the heating elements in order to maintain the temperature at a user-defined setpoint.

The readout of the MCP detector is done through the 2 GHz ADC (Analog to Digital Converter) provided by DESY, and the data is automatically recorded by the DESY DAQ (Data Acquisition) system. This data is acquired by the Unix Server through DESY

DOOCS for online analysis. Moreover, all experimental parameters and status variables are pushed to the DOOCS system, so that they can be recorded and correlated with experiment data and other FEL parameters.

A python API (Application Program Interface) allows programmatic monitoring and control of all experimental hardware, as well as access to pre-processed and filtered experimental data for online evaluation and analysis. The API is built around a client-server architecture, enabling concurrent connections of many clients. A Graphical User Interface (GUI) for experiment control, as well as online data display utilities and measurement control scripts are built on top of this API.

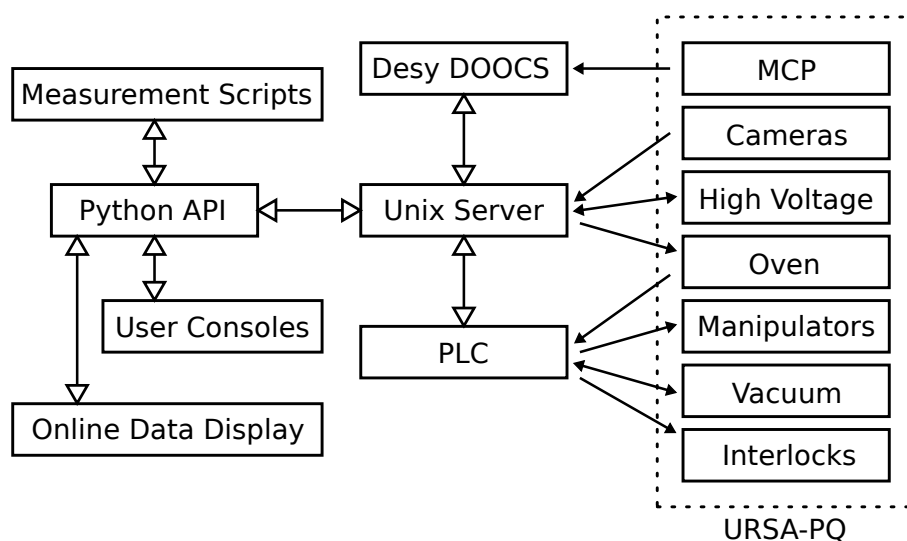


**Figure A.1:** Architecture of the control and monitoring system. Arrows represent data flow. The Unix server acts as a coordinator between the various components. It connects to the Desy DOOCS (Distributed Object Oriented Control System), interfacing the URSA-PQ apparatus with the Desy control and data acquisition system. A network-based python API can be used to monitor and control all experimental parameters programmatically or via a purpose-built GUI (Graphical User Interface) remotely. The API allows simultaneous connection from multiple clients, so that all experimental parameters can be monitored from multiple stations. The MCP output signal is read out directly by beamline ADCs and recorded by DOOCS.

The User Interface can be simultaneously used from multiple experimental stations, and can be operated in both read-only (monitor) and write (control) mode (preventing accidental changes to the hardware from monitoring stations). It provides an overview window (Fig. A.2) on the system status, as well as subpanels for the control of each subsystem (Fig. A.3).



**Figure A.2:** Control Console main window. Each one of the four subsystems has a dedicated panel, showing its status with an update frequency of 2 Hz. The ‘config’ buttons give access to the subsystems control windows (Fig. A.3).

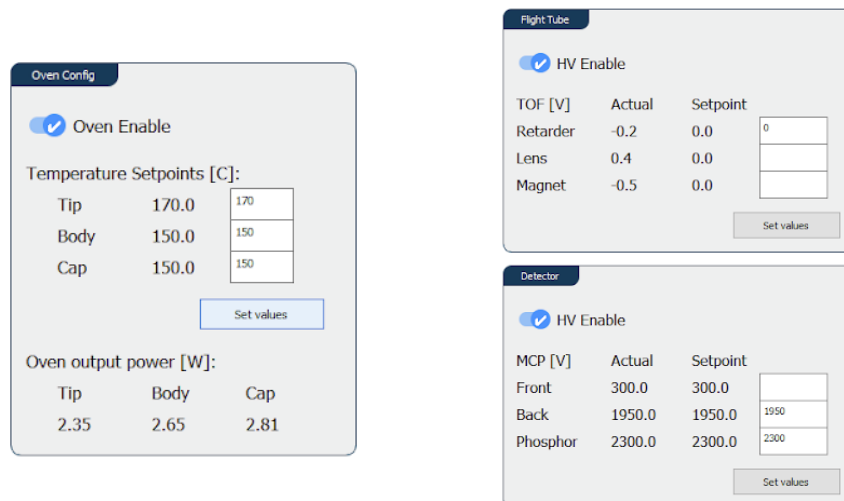


**Figure A.3:** Example of the sample oven (left) and high voltage (right) control panels.

## A.2 Measurement and Online Data Analysis

On top of hardware control, the system described in section A.1 provides tools to aid in the execution of many experiment-related tasks, such as measurement automation and online data analysis.

The MCP readout is constantly retrieved from the DOOCS system and processed. A full TOF trace is recorded every 100 *ms*, one for each pulse train, and consists of 50 concatenated time of flight signals. Even ordered shots are UV-pumped, odd shots are x-ray only; a difference signal can be constructed by subtracting odd shots from their even counterpart.

The incoming data is passed through a Lorentzian low pass filter (with a user-controllable time constant), and can be displayed through a data visualization utility (Fig. A.4 left). The filtered trace is then split into its single-shot components, and even and odd shots are averaged to create UV-on, UV-off and difference signals (Fig. A.4 right). The time-of-flight axis is converted to a kinetic energy axis using the calibration function presented in subsection 2.2.3 in combination with a real-time readout of the retardation voltage.

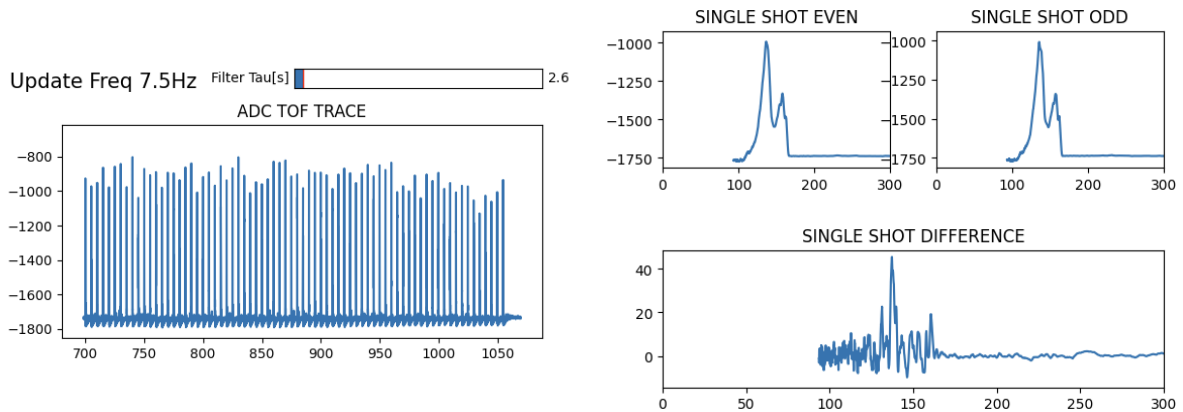


**Figure A.4:** Example panels from the online data display utility. Left: full MCP trace from DESY ADC, low pass filtered, x-axis in  $\mu s$ . The panel contains a control slider for the filter time constant, and a real-time display of the frequency at which data is being received from DOOCS. Right: visualization of single shot data. UV-on (even), UV-off (odd) and difference signals are plotted as a function of the electrons kinetic energy in *eV*

A collection of measurement scripts can be used to automate data acquisition. Such scripts use the python API to set parameters such as UV intensity or retardation voltage, programmatically scan the pump-probe delay or x-ray photon energy, and display a real-time view of the acquired data. Figure A.5 shows such a measurement preview.

To minimize systematic errors, the order in which data is acquired is randomized. That is, the scanned parameters are not swiped sequentially, but are acquired using a

different (random) order for each measurement run.

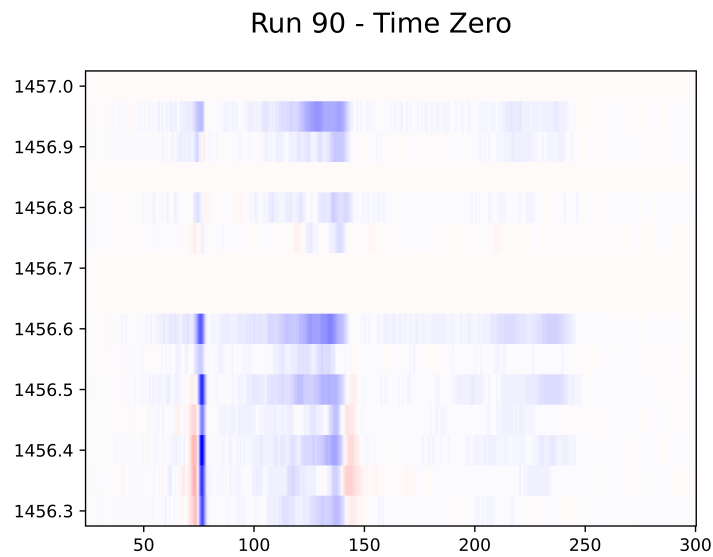


**Figure A.5:** Real time view of measured data in a time zero scan. The differential signal (UV-on - UV-off) is displayed as a function of both pump-probe delay (y-axis,  $ps$ ) and electron kinetic energy (x-axis,  $eV$ ). The various delay bins are populated as they are measured, the missing data (white horizontal lines) corresponds to values not yet scanned.



# Appendix B

## Data analysis

In order to interpret the raw data collected during the experiment, I developed and implemented data preprocessing and analysis tools. This chapter presents some of the steps taken in this regard, with a focus on the techniques used to improve the quality and ease of use of the data.

### B.1 Data preprocessing and data fusion

The data is recorded for storage by the Data Acquisition (DAQ) system at DESY, where a selected subset of all the DOOCS parameters can be flagged for long term storage. The data is subsequently composed in HDF5 files and made available to users.

For each FEL pulse train, consisting of 50 shots, a continuous signal from the MCP detector is recorded, together with data from FLASH sensors, such as shot-by-shot beam intensity data from Gas-Monitor Detectors (GMD) or electron bunch arrival time from the Beam Arrival Monitor (BAM). Other parameters are available once per pulse train, such as laser delay stage or undulator setting.

The HDF5 files are preprocessed, to simplify the subsequent analysis process. Each MCP trace is split into 50 slices, one for each shot, and the sliced data is indexed by a pulse train ID and a shot number going from 0 to 49. The same indexing scheme is used for other shot-by-shot parameters, while ‘slow’ variables are indexed by their pulse train ID only. The processed data is then saved as pandas dataframes for further analysis.

This indexing scheme enables efficient filtering of the data, so that binning and averaging of the eTOF traces can be done independently from the actual measurement runs in which the data was collected. This reduces the effect of systematic errors by averaging the data over longer time frames and across different scans.

To improve the quality of the analysis, data fusion techniques are employed. That is, data from several instruments is used in combination.

The shot-by-shot data from the Gas-Monitor Detector (GMD) is used to renormalize the eTOF data from the MCP. Moreover, the pump-probe delay resolution has been augmented by combining the nominal UV delay stage position with the shot-by-shot data

from the BAM, reducing the negative effects of FEL timing jitter on delay resolution.

Figure B.1 compares the rising edge of the 2TU sulfur photoline with and without BAM correction.

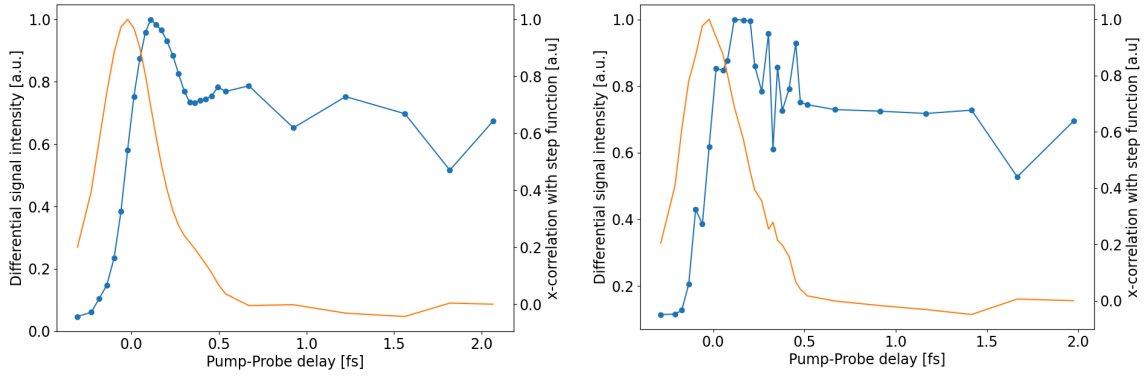


**Figure B.1:** Comparison of pump-probe delay resolution with (right) and without (left) BAM correction. Blue line is the integrated differential intensity, the orange line is the cross-correlation of the signal with a step function. The correction is applied by subtracting the timing shift measured by the BAM from the nominal delay position for each x-ray shot. The data is then rebinned on the corrected delay values.

The photon energy data has been corrected using the information from the OPIS (On-line PhotoIonization Spectrometer) whenever possible, instead of relying on the calibrated values provided from the variable gap undulator.

## B.2 GPU accelerated computing

GPGPU computing (General Purpose computing on Graphics Processing Units) is a computational paradigm that uses hardware designed to process computer graphics for general purpose computations [159]. This technique became popular in the early 2000, and exploits the highly parallelized processing pipelines of GPUs.

Commercial CPUs (Central Processing Unit), consists of a control unit driving a few (2 to 8) general purpose processing cores. Each core is capable of performing a wide range of operations, and all available cores can be used independently and work on a different set of instructions. In contrast, GPUs are built with hundreds or thousands of highly specialized cores divided in groups, with each group controlled collectively by a single control unit.



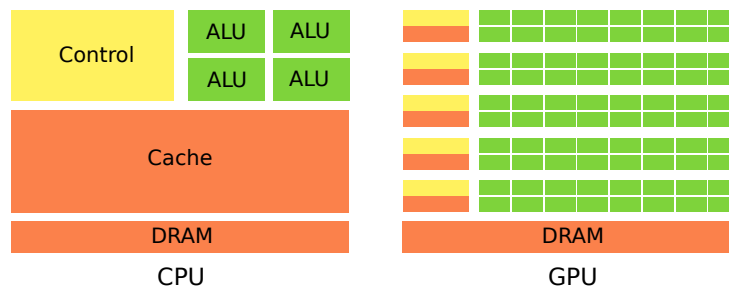


**Figure B.2:** Comparison of GPU vs CPU architecture. In a CPU (left), a few general purpose ALUs (Arithmetic and Logic Unit) are independently controlled and are able to carry out a wide set of instructions. GPUs (right) are made of thousands of highly specialized ALUs, controlled in groups by a few control units.

In the case of highly parallel applications, where the same calculation sequence is carried out on different data, this processing architecture (shown in Fig. B.2) allows for a very efficient use of the available silicon. This allows to greatly reduce the amount of time taken for a given computation, by simultaneously executing different parts of the calculation on different ALUs. Figure B.3 shows how an array integration task can be carried out with  $O(\ln(N))$  time steps, as opposed to the linear  $O(N)$  scaling for normal CPUs.

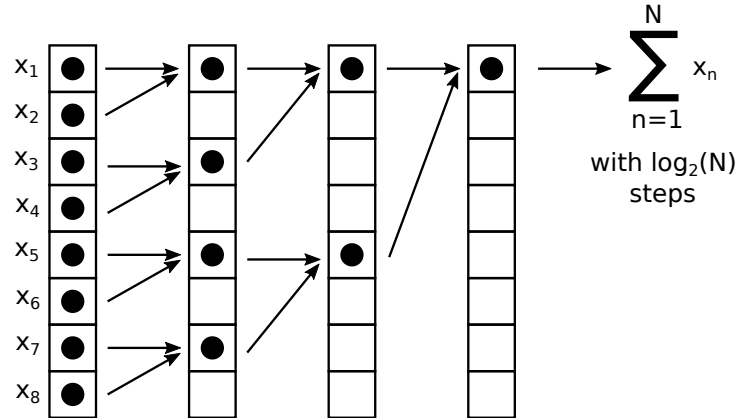


**Figure B.3:** Scheme of a GPU-parallelized array integral. By executing multiple additions concurrently, a GPU can perform an array integration with logarithmic scaling  $O(\ln(N))$ .

In the context of our research, GPU parallelization was used whenever practical, enhancing the speed of data analysis. This in turn allowed for greater ease for data exploration and manipulation, making tasks that would otherwise require days complete in a matter of hours. Figure B.4 shows a comparison of time taken and corresponding computational speed for a practical analysis task, showing improvements of up to one order of magnitude.

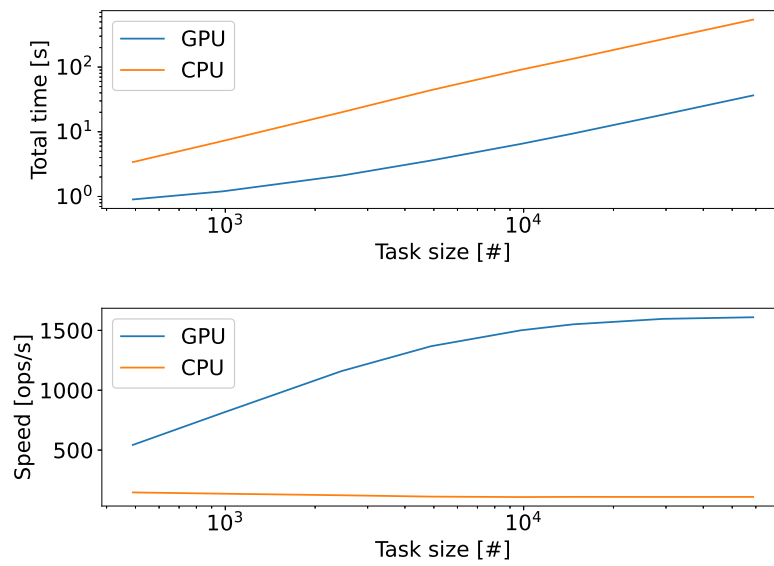


**Figure B.4:** Comparison between CPU and GPU computing, showing total time and corresponding speed *vs* task size. Test system consists of a 4-core Intel® Core™ i7-7700K CPU @ 4.20GHz, an NVIDIA Quadro RTX 4000 GPU with 2304 cuda cores, running Ubuntu 18.04.2 LTS with Linux version 4.15.0-118-generic kernel.

# Bibliography

- [1] A. D. Hershey and Martha Chase. INDEPENDENT FUNCTIONS OF VIRAL PROTEIN AND NUCLEIC ACID IN GROWTH OF BACTERIOPHAGE. *Journal of General Physiology*, 36(1):39–56, 1952, doi:10.1085/jgp.36.1.39.
- [2] J. D. Watson and F. H. C. Crick. Molecular Structure of Nucleic Acids: A Structure for Deoxyribose Nucleic Acid. *Nature*, 171(4356):737–738, 1953, doi:10.1038/171737a0.
- [3] James D. Watson, editor. *Molecular Biology of the Gene*. Pearson/Benjamin Cummings ; Cold Spring Harbor Laboratory Press, San Francisco : Cold Spring Harbor, N.Y, 6th ed edition, 2008.
- [4] Simone Reuter, Subash C. Gupta, Madan M. Chaturvedi, and Bharat B. Aggarwal. Oxidative stress, inflammation, and cancer: How are they linked? *Free Radical Biology and Medicine*, 49(11):1603–1616, 2010, doi:10.1016/j.freeradbiomed.2010.09.006.
- [5] Gerd P. Pfeifer, Young-Hyun You, and Ahmad Besaratinia. Mutations induced by ultraviolet light. *Mutation Research/Fundamental and Molecular Mechanisms of Mutagenesis*, 571(1-2):19–31, 2005, doi:10.1016/j.mrfmmm.2004.06.057.
- [6] Wolfgang J. Schreier, Peter Gilch, and Wolfgang Zinth. Early Events of DNA Photodamage. *Annual Review of Physical Chemistry*, 66(1):497–519, 2015, doi:10.1146/annurev-physchem-040214-121821.
- [7] Arie A Vink and Len Roza. Biological consequences of cyclobutane pyrimidine dimers. *Journal of Photochemistry and Photobiology B: Biology*, 65(2-3):101–104, 2001, doi:10.1016/S1011-1344(01)00245-7.
- [8] Andrea Christa Kneuttinger, Gengo Kashiwazaki, Stefan Prill, Korbinian Heil, Markus Müller, and Thomas Carell. Formation and Direct Repair of UV-induced Dimeric DNA Pyrimidine Lesions. *Photochemistry and Photobiology*, 90(1):1–14, 2014, doi:10.1111/php.12197.
- [9] R. B. Setlow. Cyclobutane-Type Pyrimidine Dimers in Polynucleotides. *Science*, 153(3734):379–386, 1966, doi:10.1126/science.153.3734.379.

- [10] S. Mouret, C. Baudouin, M. Charveron, A. Favier, J. Cadet, and T. Douki. Cyclobutane pyrimidine dimers are predominant DNA lesions in whole human skin exposed to UVA radiation. *Proceedings of the National Academy of Sciences*, 103(37):13765–13770, 2006, doi:10.1073/pnas.0604213103.
- [11] David S. Goodsell. The Molecular Perspective: Ultraviolet Light and Pyrimidine Dimers. *The Oncologist*, 6(3):298–299, 2001, doi:10.1634/theoncologist.6-3-298.
- [12] M. Daniels and W. Hauswirth. Fluorescence of the Purine and Pyrimidine Bases of the Nucleic Acids in Neutral Aqueous Solution at 300 K. *Science*, 171(3972):675–677, 1971, doi:10.1126/science.171.3972.675.
- [13] Carlos E. Crespo-Hernández, Boiko Cohen, Patrick M. Hare, and Bern Kohler. Ultrafast Excited-State Dynamics in Nucleic Acids. *Chemical Reviews*, 104(4):1977–2020, 2004, doi:10.1021/cr0206770.
- [14] Chris T. Middleton, Kimberly de La Harpe, Charlene Su, Yu Kay Law, Carlos E. Crespo-Hernández, and Bern Kohler. DNA Excited-State Dynamics: From Single Bases to the Double Helix. *Annual Review of Physical Chemistry*, 60(1):217–239, 2009, doi:10.1146/annurev.physchem.59.032607.093719.
- [15] Thomas Gustavsson, Roberto Improta, and Dimitra Markovitsi. DNA/RNA: Building Blocks of Life Under UV Irradiation. *The Journal of Physical Chemistry Letters*, 1(13):2025–2030, 2010, doi:10.1021/jz1004973.
- [16] Mario Barbatti, Antonio Carlos Borin, and Susanne Ullrich, editors. *Nucleobases in the Gas Phase and in Solvents*. Number Mario Barbatti; Antonio Carlos Borin; Susanne Ullrich, editors ; 1 in Photoinduced Phenomena in Nucleic Acids. Springer, Cham, 2015.
- [17] Angelo Giussani and Graham A. Worth. On the Intrinsically Low Quantum Yields of Pyrimidine DNA Photodamages: Evaluating the Reactivity of the Corresponding Minimum Energy Crossing Points. *The Journal of Physical Chemistry Letters*, 11(13):4984–4989, 2020, doi:10.1021/acs.jpcclett.0c01264.
- [18] Jean-Marc L. Pecourt, Jorge Peon, and Bern Kohler. DNA Excited-State Dynamics: Ultrafast Internal Conversion and Vibrational Cooling in a Series of Nucleosides. *Journal of the American Chemical Society*, 123(42):10370–10378, 2001, doi:10.1021/ja0161453.
- [19] W. J. Schreier, T. E. Schrader, F. O. Koller, P. Gilch, C. E. Crespo-Hernandez, V. N. Swaminathan, T. Carell, W. Zinth, and B. Kohler. Thymine Dimerization in DNA Is an Ultrafast Photoreaction. *Science*, 315(5812):625–629, 2007, doi:10.1126/science.1135428.
- [20] Thomas Carell, Caterina Brandmayr, Antje Hienzsch, Markus Müller, David Pearson, Veronika Reiter, Ines Thoma, Peter Thumbs, and Mirko Wagner. Structure and

- Function of Noncanonical Nucleobases. *Angewandte Chemie International Edition*, 51(29):7110–7131, 2012, doi:10.1002/anie.201201193.
- [21] Reto Brem, Ilse Daehn, and Peter Karran. Efficient DNA interstrand crosslinking by 6-thioguanine and UVA radiation. *DNA Repair*, 10(8):869–876, 2011, doi:10.1016/j.dnarep.2011.05.010.
- [22] Xiaohong Zhang, Graham Jeffs, Xiaolin Ren, Peter O’Donovan, Beatriz Montaner, Conal M. Perrett, Peter Karran, and Yao-Zhong Xu. Novel DNA lesions generated by the interaction between therapeutic thiopurines and UVA light. *DNA Repair*, 6(3):344–354, 2007, doi:10.1016/j.dnarep.2006.11.003.
- [23] Alain Favre, Carole Saintomé, Jean-Louis Fourrey, Pascale Clivio, and Philippe Laugâa. Thionucleobases as intrinsic photoaffinity probes of nucleic acid structure and nucleic acid-protein interactions. *Journal of Photochemistry and Photobiology B: Biology*, 42(2):109–124, 1998, doi:10.1016/S1011-1344(97)00116-4.
- [24] S. Zhang, J. C. Blain, D. Zielinska, S. M. Gryaznov, and J. W. Szostak. Fast and accurate nonenzymatic copying of an RNA-like synthetic genetic polymer. *Proceedings of the National Academy of Sciences*, 110(44):17732–17737, 2013, doi:10.1073/pnas.1312329110.
- [25] Jack W Szostak. The eightfold path to non-enzymatic RNA replication. *Journal of Systems Chemistry*, 3(1):2, 2012, doi:10.1186/1759-2208-3-2.
- [26] P. F. Swann, T. R. Waters, D. C. Moulton, Y.-Z. Xu, Q. Zheng, M. Edwards, and R. Mace. Role of Postreplicative DNA Mismatch Repair in the Cytotoxic Action of Thioguanine. *Science*, 273(5278):1109–1111, 1996, doi:10.1126/science.273.5278.1109.
- [27] Katharina Kramer, Timo Sachsenberg, Benedikt M Beckmann, Saadia Qamar, Kum-Loong Boon, Matthias W Hentze, Oliver Kohlbacher, and Henning Urlaub. Photo-cross-linking and high-resolution mass spectrometry for assignment of RNA-binding sites in RNA-binding proteins. *Nature Methods*, 11(10):1064–1070, 2014, doi:10.1038/nmeth.3092.
- [28] Serra Arslançan, Lara Martínez-Fernández, and Inés Corral. Photophysics and Photochemistry of Canonical Nucleobases’ Thioanalogs: From Quantum Mechanical Studies to Time Resolved Experiments. *Molecules*, 22(6):998, 2017, doi:10.3390/molecules22060998.
- [29] Brennan Ashwood, Marvin Pollum, and Carlos E. Crespo-Hernández. Photochemical and Photodynamical Properties of Sulfur-Substituted Nucleic Acid Bases,. *Photochemistry and Photobiology*, 95(1):33–58, 2019, doi:10.1111/php.12975.
- [30] M. Pollum, S. Jockusch, and C. E. Crespo-Hernández. Increase in the photoreactivity of uracil derivatives by doubling thionation. *Phys. Chem. Chem. Phys.*, 17(41):27851–27861, 2015, doi:10.1039/C5CP04822B.

- [31] Marvin Pollum, Lara Martínez-Fernández, and Carlos E. Crespo-Hernández. Photochemistry of Nucleic Acid Bases and Their Thio- and Aza-Analogues in Solution. In Mario Barbatti, Antonio Carlos Borin, and Susanne Ullrich, editors, *Photoinduced Phenomena in Nucleic Acids I*, vol. 355, pages 245–327. Springer International Publishing, Cham, 2014.
- [32] Hikaru Kuramochi, Takashi Kobayashi, Tadashi Suzuki, and Teijiro Ichimura. Excited-State Dynamics of 6-Aza-2-thiothymine and 2-Thiothymine: Highly Efficient Intersystem Crossing and Singlet Oxygen Photosensitization. *The Journal of Physical Chemistry B*, 114(26):8782–8789, 2010, doi:10.1021/jp102067t.
- [33] Sylvie Euvrard, Jean Kanitakis, and Alain Claudy. Skin Cancers after Organ Transplantation. *New England Journal of Medicine*, 348(17):1681–1691, 2003, doi:10.1056/NEJMra022137.
- [34] Andrew Massey, Yao-Zhong Xu, and Peter Karran. Photoactivation of DNA thiobases as a potential novel therapeutic option. *Current Biology*, 11(14):1142–1146, 2001, doi:10.1016/S0960-9822(01)00272-X.
- [35] Olivier Reelfs, Peter Karran, and Antony R. Young. 4-thiothymidine sensitization of DNA to UVA offers potential for a novel photochemotherapy. *Photochem. Photobiol. Sci.*, 11(1):148–154, 2012, doi:10.1039/C1PP05188A.
- [36] M. Born and R. Oppenheimer. Zur Quantentheorie der Molekeln. *Annalen der Physik*, 389(20):457–484, 1927, doi:10.1002/andp.19273892002.
- [37] David R. Yarkony. Diabolical conical intersections. *Reviews of Modern Physics*, 68(4):985–1013, 1996, doi:10.1103/RevModPhys.68.985.
- [38] Wolfgang Domcke, David R Yarkony, and Horst Köppel. *Conical Intersections: Electronic Structure, Dynamics and Spectroscopy*, vol. 15 of Advanced Series in Physical Chemistry. WORLD SCIENTIFIC, 2004.
- [39] Roberto Improta, Fabrizio Santoro, and Lluís Blancafort. Quantum Mechanical Studies on the Photophysics and the Photochemistry of Nucleic Acids and Nucleobases. *Chemical Reviews*, 116(6):3540–3593, 2016, doi:10.1021/acs.chemrev.5b00444.
- [40] Barbara M. Giuliano, Vitaliy Feyrer, Kevin C. Prince, Marcello Coreno, Luca Evangelisti, Sonia Melandri, and Walther Caminati. Tautomerism in 4-Hydroxypyrimidine, *S*-Methyl-2-thiouracil, and 2-Thiouracil. *The Journal of Physical Chemistry A*, 114(48):12725–12730, 2010, doi:10.1021/jp106883s.
- [41] Hui Yu, Jose A. Sanchez-Rodriguez, Marvin Pollum, Carlos E. Crespo-Hernández, Sebastian Mai, Philipp Marquetand, Leticia González, and Susanne Ullrich. Internal conversion and intersystem crossing pathways in UV excited, isolated uracils and their implications in prebiotic chemistry. *Physical Chemistry Chemical Physics*, 18(30):20168–20176, 2016, doi:10.1039/C6CP01790H.

- [42] José A. Sánchez-Rodríguez, Abed Mohamadzade, Sebastian Mai, Brennan Ashwood, Marvin Pollum, Philipp Marquetand, Leticia González, Carlos E. Crespo-Hernández, and Susanne Ullrich. 2-Thiouracil intersystem crossing photodynamics studied by wavelength-dependent photoelectron and transient absorption spectroscopies. *Physical Chemistry Chemical Physics*, 19(30):19756–19766, 2017, doi:10.1039/C7CP02258A.
- [43] Sebastian Mai, Abed Mohamadzade, Philipp Marquetand, Leticia González, and Susanne Ullrich. Simulated and Experimental Time-Resolved Photoelectron Spectra of the Intersystem Crossing Dynamics in 2-Thiouracil. *Molecules*, 23(11):2836, 2018, doi:10.3390/molecules23112836.
- [44] Sebastian Mai, Philipp Marquetand, and Leticia González. A Static Picture of the Relaxation and Intersystem Crossing Mechanisms of Photoexcited 2-Thiouracil. *The Journal of Physical Chemistry A*, 119(36):9524–9533, 2015, doi:10.1021/acs.jpca.5b06639.
- [45] Sebastian Mai, Philipp Marquetand, and Leticia González. Intersystem Crossing Pathways in the Noncanonical Nucleobase 2-Thiouracil: A Time-Dependent Picture. *The Journal of Physical Chemistry Letters*, 7(11):1978–1983, 2016, doi:10.1021/acs.jpcllett.6b00616.
- [46] Shuming Bai and Mario Barbatti. On the decay of the triplet state of thionucleobases. *Physical Chemistry Chemical Physics*, 19(20):12674–12682, 2017, doi:10.1039/C7CP02050C.
- [47] Ahmed Zewail. *Femtochemistry: Atomic-Scale Dynamics of the Chemical Bond Using Ultrafast Lasers*, 1999.
- [48] T Jahnke, A Czasch, M Schöffler, S Schössler, M Kász, J Titze, K Kreidi, R E Grisenti, A Staudte, O Jagutzki, L Ph H Schmidt, S K Semenov, N A Cherepkov, H Schmidt-Böcking, and R Dörner. Photoelectron and ICD electron angular distributions from fixed-in-space neon dimers. *Journal of Physics B: Atomic, Molecular and Optical Physics*, 40(13):2597–2606, 2007, doi:10.1088/0953-4075/40/13/006.
- [49] Kai M. Siegbahn. *Electron Spectroscopy for Atoms, Molecules and Condensed Matter (Nobel Lecture)*. [www.nobelprize.org/prizes/physics/1981/siegbahn/lecture](http://www.nobelprize.org/prizes/physics/1981/siegbahn/lecture), 1981.
- [50] Christian Bressler and Majed Chergui. Ultrafast X-ray Absorption Spectroscopy. *Chemical Reviews*, 104(4):1781–1812, 2004, doi:10.1021/cr0206667.
- [51] Wenkai Zhang, Roberto Alonso-Mori, Uwe Bergmann, Christian Bressler, Matthieu Chollet, Andreas Galler, Wojciech Gawelda, Ryan G. Hadt, Robert W. Hartsock, Thomas Kroll, Kasper S. Kjær, Katharina Kubiček, Henrik T. Lemke, Huiyang W. Liang, Drew A. Meyer, Martin M. Nielsen, Carola Purser, Joseph S. Robinson, Edward I. Solomon, Zheng Sun, Dimosthenis Sokaras, Tim B. van Driel, György

- Vankó, Tsu-Chien Weng, Diling Zhu, and Kelly J. Gaffney. Tracking excited-state charge and spin dynamics in iron coordination complexes. *Nature*, 509(7500):345–348, 2014, doi:10.1038/nature13252.
- [52] Megan L. Shelby, Patrick J. Lestrangle, Nicholas E. Jackson, Kristoffer Haldrup, Michael W. Mara, Andrew B. Stickrath, Diling Zhu, Henrik T. Lemke, Matthieu Chollet, Brian M. Hoffman, Xiaosong Li, and Lin X. Chen. Ultrafast Excited State Relaxation of a Metalloporphyrin Revealed by Femtosecond X-ray Absorption Spectroscopy. *Journal of the American Chemical Society*, 138(28):8752–8764, 2016, doi:10.1021/jacs.6b02176.
- [53] Nils Huse, Hana Cho, Kiryong Hong, Lindsey Jamula, Frank M. F. de Groot, Tae Kyu Kim, James K. McCusker, and Robert W. Schoenlein. Femtosecond Soft X-ray Spectroscopy of Solvated Transition-Metal Complexes: Deciphering the Interplay of Electronic and Structural Dynamics. *The Journal of Physical Chemistry Letters*, 2(8):880–884, 2011, doi:10.1021/jz200168m.
- [54] Benjamin E. Van Kuiken, Hana Cho, Kiryong Hong, Munira Khalil, Robert W. Schoenlein, Tae Kyu Kim, and Nils Huse. Time-Resolved X-ray Spectroscopy in the Water Window: Elucidating Transient Valence Charge Distributions in an Aqueous Fe(II) Complex. *The Journal of Physical Chemistry Letters*, 7(3):465–470, 2016, doi:10.1021/acs.jpcclett.5b02509.
- [55] Andrew R. Attar, Aditi Bhattacharjee, C. D. Pemmaraju, Kirsten Schnorr, Kristina D. Closser, David Prendergast, and Stephen R. Leone. Femtosecond x-ray spectroscopy of an electrocyclic ring-opening reaction. *Science*, 356(6333):54–59, 2017, doi:10.1126/science.aaj2198.
- [56] Yoann Pertot, Cédric Schmidt, Mary Matthews, Adrien Chauvet, Martin Huppert, Vit Svoboda, Aaron von Conta, Andres Tehlar, Denitsa Baykusheva, Jean-Pierre Wolf, and Hans Jakob Wörner. Time-resolved x-ray absorption spectroscopy with a water window high-harmonic source. *Science*, 355(6322):264–267, 2017, doi:10.1126/science.aah6114.
- [57] Markus Gühr. Probing Molecular Photoexcited Dynamics by Soft X-Rays. In Markus Kitzler and Stefanie Gräfe, editors, *Ultrafast Dynamics Driven by Intense Light Pulses*, vol. 86, pages 341–371. Springer International Publishing, Cham, 2016.
- [58] T. J. A. Wolf, R. H. Myhre, J. P. Cryan, S. Coriani, R. J. Squibb, A. Battistoni, N. Berrah, C. Bostedt, P. Bucksbaum, G. Coslovich, R. Feifel, K. J. Gaffney, J. Grilj, T. J. Martinez, S. Miyabe, S. P. Moeller, M. Mucke, A. Natan, R. Obaid, T. Osipov, O. Plekan, S. Wang, H. Koch, and M. Gühr. Probing ultrafast  $\Pi\pi^*/n\pi^*$  internal conversion in organic chromophores via K-edge resonant absorption. *Nature Communications*, 8(1):29, 2017, doi:10.1038/s41467-017-00069-7.
- [59] B. K. McFarland, J. P. Farrell, S. Miyabe, F. Tarantelli, A. Aguilar, N. Berrah, C. Bostedt, J. D. Bozek, P. H. Bucksbaum, J. C. Castagna, R. N. Coffee, J. P.



- Cryan, L. Fang, R. Feifel, K. J. Gaffney, J. M. Glowina, T. J. Martinez, M. Mucke, B. Murphy, A. Natan, T. Osipov, V. S. Petrović, S. Schorb, Th. Schultz, L. S. Spector, M. Swiggers, I. Tenney, S. Wang, J. L. White, W. White, and M. Gühr. Ultrafast X-ray Auger probing of photoexcited molecular dynamics. *Nature Communications*, 5:4235, 2014, doi:10.1038/ncomms5235.
- [60] T. Leitner, I. Josefsson, T. Mazza, P. S. Miedema, H. Schröder, M. Beye, K. Kunus, S. Schreck, S. Düsterer, A. Föhlisch, M. Meyer, M. Odelius, and Ph. Werner. Time-resolved electron spectroscopy for chemical analysis of photodissociation: Photoelectron spectra of  $\text{Fe}(\text{CO})_5$ ,  $\text{Fe}(\text{CO})_4$ , and  $\text{Fe}(\text{CO})_3$ . *The Journal of Chemical Physics*, 149(4):044307, 2018, doi:10.1063/1.5035149.
- [61] Frank Jensen. *Introduction to Computational Chemistry*. Wiley, Chichester ; New York, 1999.
- [62] S.I. Vetchinkin, A.S. Vetchinkin, V.V. Eryomin, and I.M. Umanskii. Gaussian wavepacket dynamics in an anharmonic system. *Chemical Physics Letters*, 215(1-3):11–16, 1993, doi:10.1016/0009-2614(93)89255-G.
- [63] J. von Neumann and E. P. Wigner. über merkwürdige diskrete Eigenwerte. In Arthur S. Wightman, editor, *The Collected Works of Eugene Paul Wigner*, pages 291–293. Springer Berlin Heidelberg, Berlin, Heidelberg, 1993.
- [64] M. Baer. *Beyond Born-Oppenheimer: Conical Intersections and Electronic Non-Adiabatic Coupling Terms*. Wiley, Hoboken, N.J, 2006.
- [65] Lev Davidovič Landau, Evgenij M. Lifšic, and Lev Davidovič Landau. *Quantum Mechanics: Non-Relativistic Theory*. Number by L. D. Landau and E. M. Lifshitz ; Vol. 3 in Course of Theoretical Physics. Elsevier [u.a.], Singapore, 3. ed., rev. and enl., authorized engl. reprint ed edition, 2007.
- [66] Claude Cohen-Tannoudji, Bernard Diu, and Franck Laloë. *Quantum mechanics*. Wiley, New York, 1977.
- [67] Albert Einstein. Strahlungs-emission und Absorption nach der quantentheorie. *Deutsche Physikalische Gesellschaft*, 18:318–323, 1916.
- [68] Robert C. Hilborn. Einstein coefficients, cross sections,  $f$  values, dipole moments, and all that. *American Journal of Physics*, 50(11):982–986, 1982, doi:10.1119/1.12937.
- [69] A A Ischenko, P M Weber, and R J Dwayne Miller. Transient structures and chemical reaction dynamics. *Russian Chemical Reviews*, 86(12):1173–1253, 2017, doi:10.1070/RCR4754.
- [70] Gregory J. Atchity, Sotirios S. Xantheas, and Klaus Ruedenberg. Potential energy surfaces near intersections. *The Journal of Chemical Physics*, 95(3):1862–1876, 1991, doi:10.1063/1.461036.

- [71] Non-adiabatic crossing of energy levels. *Proceedings of the Royal Society of London*, 137(833):696–702, 1932, doi:10.1098/rspa.1932.0165.
- [72] Amar C Vutha. A simple approach to the Landau–Zener formula. *European Journal of Physics*, 31(2):389–392, 2010, doi:10.1088/0143-0807/31/2/016.
- [73] Michael S. Schuurman and Albert Stolow. Dynamics at Conical Intersections. *Annual Review of Physical Chemistry*, 69(1):427–450, 2018, doi:10.1146/annurev-physchem-052516-050721.
- [74] Jaroslaw J. Szymczak, Mario Barbatti, Jason T. Soo Hoo, Jaclyn A. Adkins, Theresa L. Windus, Dana Nachtigallová, and Hans Lischka. Photodynamics Simulations of Thymine: Relaxation into the First Excited Singlet State. *The Journal of Physical Chemistry A*, 113(45):12686–12693, 2009, doi:10.1021/jp905085x.
- [75] Christel M. Marian. Spin-orbit coupling and intersystem crossing in molecules: Spin-orbit coupling. *Wiley Interdisciplinary Reviews: Computational Molecular Science*, 2(2):187–203, 2012, doi:10.1002/wcms.83.
- [76] Thomas J. Penfold, Etienne Gindensperger, Chantal Daniel, and Christel M. Marian. Spin-Vibronic Mechanism for Intersystem Crossing. *Chemical Reviews*, 118(15):6975–7025, 2018, doi:10.1021/acs.chemrev.7b00617.
- [77] David W. Oxtoby, H. P. Gillis, and Alan Champion. *Principles of Modern Chemistry*. Thomson Brooks/Cole, Belmont, CA, 6th ed edition, 2007.
- [78] Sebastian Mai, Martin Richter, Philipp Marquetand, and Leticia González’s. Ultrafast Intersystem Crossing in SO<sub>2</sub> and Nucleobases. In Kaoru Yamanouchi, Steven Cundiff, Regina de Vivie-Riedle, Makoto Kuwata-Gonokami, and Louis DiMauro, editors, *Ultrafast Phenomena XIX*, vol. 162, pages 509–513. Springer International Publishing, Cham, 2015.
- [79] R. S. Minns, D. S. N. Parker, T. J. Penfold, G. A. Worth, and H. H. Fielding. Competing ultrafast intersystem crossing and internal conversion in the “channel 3” region of benzene. *Physical Chemistry Chemical Physics*, 12(48):15607, 2010, doi:10.1039/c001671c.
- [80] Rosalind E. Franklin and R. G. Gosling. Molecular Configuration in Sodium Thymonucleate. *Nature*, 171(4356):740–741, 1953, doi:10.1038/171740a0.
- [81] Bruce Alberts, editor. *Molecular Biology of the Cell*. Garland Science, New York, 5th ed edition, 2008.
- [82] P. Yakovchuk. Base-stacking and base-pairing contributions into thermal stability of the DNA double helix. *Nucleic Acids Research*, 34(2):564–574, 2006, doi:10.1093/nar/gkj454.
- [83] Michael Ströck. Ausschnitt von 20 Basenpaaren aus der DNA-Doppelhelix - Creative Commons BY SA 3.0 (creativecommons.org/licenses/by-sa/3.0/), 2006.

- [84] Madeleine Price Ball. Chemical structure of DNA - Creative Commons BY SA 3.0 (creativecommons.org/licenses/by-sa/3.0/) - Modified from original -, 2020.
- [85] Jeremy Mark Berg, John L Tymoczko, Lubert Stryer, Lubert Stryer, and National Center for Biotechnology Information (U.S.). *Biochemistry*. W.H. Freeman ; NCBI, New York; [Bethesda, MD, 2002.
- [86] Mitchell Guttman and John L. Rinn. Modular regulatory principles of large non-coding RNAs. *Nature*, 482(7385):339–346, 2012, doi:10.1038/nature10887.
- [87] Ricki Lewis. *Human Genetics*. McGraw-Hill, New York; London, 2005.
- [88] James F. Crow. How much do we know about spontaneous human mutation rates? *Environmental and Molecular Mutagenesis*, 21(2):122–129, 1993, doi:10.1002/em.2850210205.
- [89] Séverine Boillée, Christine Vande Velde, and Don W. Cleveland. ALS: A Disease of Motor Neurons and Their Nonneuronal Neighbors. *Neuron*, 52(1):39–59, 2006, doi:10.1016/j.neuron.2006.09.018.
- [90] J C Chang and Y W Kan. Beta 0 thalassemia, a nonsense mutation in man. *Proceedings of the National Academy of Sciences*, 76(6):2886–2889, 1979, doi:10.1073/pnas.76.6.2886.
- [91] Thomas Carell, Matthias Q. Kurz, Markus Müller, Martin Rossa, and Fabio Spada. Non-canonical Bases in the Genome: The Regulatory Information Layer in DNA. *Angewandte Chemie International Edition*, 57(16):4296–4312, 2018, doi:10.1002/anie.201708228.
- [92] Mitchell Guttman, Julie Donaghey, Bryce W. Carey, Manuel Garber, Jennifer K. Grenier, Glen Munson, Geneva Young, Anne Bergstrom Lucas, Robert Ach, Laurakay Bruhn, Xiaoping Yang, Ido Amit, Alexander Meissner, Aviv Regev, John L. Rinn, David E. Root, and Eric S. Lander. lincRNAs act in the circuitry controlling pluripotency and differentiation. *Nature*, 477(7364):295–300, 2011, doi:10.1038/nature10398.
- [93] M. E. Dinger, P. P. Amaral, T. R. Mercer, K. C. Pang, S. J. Bruce, B. B. Gardiner, M. E. Askarian-Amiri, K. Ru, G. Solda, C. Simons, S. M. Sunkin, M. L. Crowe, S. M. Grimmond, A. C. Perkins, and J. S. Mattick. Long noncoding RNAs in mouse embryonic stem cell pluripotency and differentiation. *Genome Research*, 18(9):1433–1445, 2008, doi:10.1101/gr.078378.108.
- [94] Treat B. Johnson and Robert D. Coghill. RESEARCHES ON PYRIMIDINES. C111. THE DISCOVERY OF 5-METHYL-CYTOSINE IN TUBERCULINIC ACID, THE NUCLEIC ACID OF THE TUBERCLE BACILLUS <sup>1</sup>. *Journal of the American Chemical Society*, 47(11):2838–2844, 1925, doi:10.1021/ja01688a030.

- [95] Ganglong Cui and Wei-hai Fang. State-specific heavy-atom effect on intersystem crossing processes in 2-thiothymine: A potential photodynamic therapy photosensitizer. *The Journal of Chemical Physics*, 138(4):044315, 2013, doi:10.1063/1.4776261.
- [96] Rocío Borrego-Varillas, Danielle C. Teles-Ferreira, Artur Nenov, Irene Conti, Lucia Ganzer, Cristian Manzoni, Marco Garavelli, Ana Maria de Paula, and Giulio Cerullo. Observation of the Sub-100 Femtosecond Population of a Dark State in a Thiobase Mediating Intersystem Crossing. *Journal of the American Chemical Society*, 140(47):16087–16093, 2018, doi:10.1021/jacs.8b07057.
- [97] Abed Mohamadzade, Shuming Bai, Mario Barbatti, and Susanne Ullrich. Intersystem crossing dynamics in singly substituted thiouracil studied by time-resolved photoelectron spectroscopy: Micro-environmental effects due to sulfur position. *Chemical Physics*, 515:572–579, 2018, doi:10.1016/j.chemphys.2018.08.011.
- [98] Artem Khvorostov, Leszek Lapinski, Hanna Rostkowska, and Maciej J. Nowak. UV-Induced Generation of Rare Tautomers of 2-Thiouracils: A Matrix Isolation Study. *The Journal of Physical Chemistry A*, 109(34):7700–7707, 2005, doi:10.1021/jp051940e.
- [99] Nobuko Igarashi-Yamamoto, Akio Tajiri, Masahiro Hatano, Susumu Shibuya, and Tohru Ueda. Ultraviolet absorption, circular dichroism and magnetic circular dichroism studies of sulfur-containing nucleic acid bases and their nucleosides. *Biochimica et Biophysica Acta (BBA) - Nucleic Acids and Protein Synthesis*, 656(1):1–15, 1981, doi:10.1016/0005-2787(81)90020-4.
- [100] João Paulo Gobbo and Antonio Carlos Borin. 2-Thiouracil deactivation pathways and triplet states population. *Computational and Theoretical Chemistry*, 1040–1041:195–201, 2014, doi:10.1016/j.comptc.2014.03.021.
- [101] Marvin Pollum and Carlos E. Crespo-Hernández. Communication: The dark singlet state as a doorway state in the ultrafast and efficient intersystem crossing dynamics in 2-thiothymine and 2-thiouracil. *The Journal of Chemical Physics*, 140(7):071101, 2014, doi:10.1063/1.4866447.
- [102] Rodney Loudon. *The Quantum Theory of Light*. Oxford Science Publications. Oxford University Press, Oxford ; New York, 3rd ed edition, 2000.
- [103] M Babiker and R Loudon. Derivation of the Power-Zienau-Woolley Hamiltonian in quantum electrodynamics by gauge transformation. *Proceedings of the Royal Society of London. A. Mathematical and Physical Sciences*, 385(1789):439–460, 1983, doi:10.1098/rspa.1983.0022.
- [104] Robin Santra. Concepts in x-ray physics. *Journal of Physics B: Atomic, Molecular and Optical Physics*, 42(2):023001, 2009, doi:10.1088/0953-4075/42/2/023001.

- [105] U. Ankerhold, B. Esser, and F. von Busch. Ionization and fragmentation of OCS and CS<sub>2</sub> after photoexcitation around the sulfur 2p edge. *Chemical Physics*, 220(3):393–407, 1997, doi:10.1016/S0301-0104(97)00111-0.
- [106] K. Siegbahn and Kungl. Vetenskaps-societeten i Uppsala. *ESCA; Atomic, Molecular and Solid State Structure Studied by Means of Electron Spectroscopy*. Acta Universitatis Upsaliensis: Nova Acta Regiae Societatis Scientiarum Upsaliensis. Almqvist & Wiksells, 1967.
- [107] Oksana Travnikova, Knut J. Borve, Minna Patanen, Johan Söderström, Catalin Miron, Leif J. Saethre, Nils Martensson, and Svante Svensson. The ESCA molecule—Historical remarks and new results. *Journal of Electron Spectroscopy and Related Phenomena*, 185(8-9):191–197, 2012, doi:10.1016/j.elspec.2012.05.009.
- [108] Manfred O. Krause, Thomas A. Carlson, and R. D. Dismukes. Double Electron Ejection in the Photoabsorption Process. *Physical Review*, 170(1):37–47, 1968, doi:10.1103/PhysRev.170.37.
- [109] R. L. Martin and D. A. Shirley. Theory of the neon 1 s correlation-peak intensities. *Physical Review A*, 13(4):1475–1483, 1976, doi:10.1103/PhysRevA.13.1475.
- [110] R. L. Martin and D. A. Shirley. Theory of core-level photoemission correlation state spectra. *The Journal of Chemical Physics*, 64(9):3685–3689, 1976, doi:10.1063/1.432679.
- [111] T. A. Carlson, M. O. Krause, and W. E. Moddeman. EXCITATION ACCOMPANYING PHOTOIONIZATION IN ATOMS AND MOLECULES AND ITS RELATIONSHIP TO ELECTRON CORRELATION. *Le Journal de Physique Colloques*, 32(C4):C4–76–C4–84, 1971, doi:10.1051/jphyscol:1971416.
- [112] J. V. Ortiz. Dyson-orbital concepts for description of electrons in molecules. *The Journal of Chemical Physics*, 153(7):070902, 2020, doi:10.1063/5.0016472.
- [113] Pierre Auger. Sur les rayons beta; secondaires produits dans un gaz par des rayons X. 177:169–171, 1923.
- [114] Lise Meitner. Über die Entstehung der Beta-Strahl-Spektren radioaktiver Substanzen. *Zeitschrift fuer Physik*, 9(1):131–144, 1922, doi:10.1007/BF01326962.
- [115] Olivier Hardouin Duparc. Pierre Auger – Lise Meitner: Comparative contributions to the Auger effect. *International Journal of Materials Research*, 100(9):1162–1166, 2009, doi:10.3139/146.110163.
- [116] D. Coster and R. De L. Kronig. New type of auger effect and its influence on the x-ray spectrum. *Physica*, 2(1-12):13–24, 1935, doi:10.1016/S0031-8914(35)90060-X.
- [117] H. Siegbahn, L. Asplund, and P. Kelfve. The Auger electron spectrum of water vapour. *Chemical Physics Letters*, 35(3):330–335, 1975, doi:10.1016/0009-2614(75)85615-6.

- [118] K. Zähringer, H.-D. Meyer, and L. S. Cederbaum. Molecular scattering wave functions for Auger decay rates: The Auger spectrum of hydrogen fluoride. *Physical Review A*, 45(1):318–328, 1992, doi:10.1103/PhysRevA.45.318.
- [119] Thomas Wolf, Fabian Holzmeier, Isabella Wagner, Nora Berrah, Christoph Bostedt, John Bozek, Phil Bucksbaum, Ryan Coffee, James Cryan, Joe Farrell, Raimund Feifel, Todd Martinez, Brian McFarland, Melanie Mucke, Saikat Nandi, Francesco Tarantelli, Ingo Fischer, and Markus Gühr. Observing Femtosecond Fragmentation Using Ultrafast X-ray-Induced Auger Spectra. *Applied Sciences*, 7(7):681, 2017, doi:10.3390/app7070681.
- [120] Marcos Dantus, Mark J. Rosker, and Ahmed H. Zewail. Real-time femtosecond probing of “transition states” in chemical reactions. *The Journal of Chemical Physics*, 87(4):2395–2397, 1987, doi:10.1063/1.453122.
- [121] Mark J. Rosker, Marcos Dantus, and Ahmed H. Zewail. Femtosecond real-time probing of reactions. I. The technique. *The Journal of Chemical Physics*, 89(10):6113–6127, 1988, doi:10.1063/1.455427.
- [122] Marcos Dantus, Mark J. Rosker, and Ahmed H. Zewail. Femtosecond real-time probing of reactions. II. The dissociation reaction of ICN. *The Journal of Chemical Physics*, 89(10):6128–6140, 1988, doi:10.1063/1.455428.
- [123] Richard B. Bernstein and Ahmed H. Zewail. Femtosecond real-time probing of reactions. III. Inversion to the potential from femtosecond transition-state spectroscopy experiments. *The Journal of Chemical Physics*, 90(2):829–842, 1989, doi:10.1063/1.456108.
- [124] P. Cong, A. Mokhtari, and A.H. Zewail. Femtosecond probing of persistent wave packet motion in dissociative reactions: Up to 40 ps. *Chemical Physics Letters*, 172(2):109–113, 1990, doi:10.1016/0009-2614(90)87281-U.
- [125] Todd S. Rose, Mark J. Rosker, and Ahmed H. Zewail. Femtosecond real-time probing of reactions. IV. The reactions of alkali halides. *The Journal of Chemical Physics*, 91(12):7415–7436, 1989, doi:10.1063/1.457266.
- [126] A. Mokhtari, P. Cong, J. L. Herek, and A. H. Zewail. Direct femtosecond mapping of trajectories in a chemical reaction. *Nature*, 348(6298):225–227, 1990, doi:10.1038/348225a0.
- [127] M. Gruebele, G. Roberts, M. Dantus, R.M. Bowman, and A.H. Zewail. Femtosecond temporal spectroscopy and direct inversion to the potential: Application to iodine. *Chemical Physics Letters*, 166(5-6):459–469, 1990, doi:10.1016/0009-2614(90)87134-D.
- [128] Albert Stolow, Arthur E. Bragg, and Daniel M. Neumark. Femtosecond Time-Resolved Photoelectron Spectroscopy. *Chemical Reviews*, 104(4):1719–1758, 2004, doi:10.1021/cr020683w.

- [129] Simon P. Neville, Majed Chergui, Albert Stolow, and Michael S. Schuurman. Ultrafast X-ray spectroscopy of conical intersections. *Physical Review Letters*, 120(24):243001, 2018, doi:10.1103/PhysRevLett.120.243001.
- [130] Felix Brauße, Gildas Goldsztejn, Kasra Amini, Rebecca Boll, Sadia Bari, Cédric Bomme, Mark Brouard, Michael Burt, Barbara Cunha de Miranda, Stefan Düsterer, Benjamin Erk, Marie Géléoc, Romain Geneaux, Alexander S. Gentleman, Renaud Guillemin, Iyas Ismail, Per Johnsson, Loïc Journal, Thomas Kierspel, Hansjochen Köckert, Jochen Küpper, Pascal Lablanquie, Jan Lahl, Jason W. L. Lee, Stuart R. Mackenzie, Sylvain Maclot, Bastian Manschwetus, Andrey S. Mereshchenko, Terence Mullins, Pavel K. Olshin, Jérôme Palaudoux, Serguei Patchkovskii, Francis Penent, Maria Novella Piancastelli, Dimitrios Rompotis, Thierry Ruchon, Artem Rudenko, Evgeny Savelyev, Nora Schirmel, Simone Techert, Oksana Travnikova, Sebastian Trippel, Jonathan G. Underwood, Claire Vallance, Joss Wiese, Marc Simon, David M. P. Holland, Tatiana Marchenko, Arnaud Rouzée, and Daniel Rolles. Time-resolved inner-shell photoelectron spectroscopy: From a bound molecule to an isolated atom. *Physical Review A*, 97(4):043429, 2018, doi:10.1103/PhysRevA.97.043429.
- [131] Sébastien Boutet, Petra Fromme, and Mark S. Hunter, editors. *X-Ray Free Electron Lasers: A Revolution in Structural Biology*. Springer International Publishing, Cham, 2018.
- [132] C. Pellegrini. The history of X-ray free-electron lasers. *The European Physical Journal H*, 37(5):659–708, 2012, doi:10.1140/epjh/e2012-20064-5.
- [133] C. Pellegrini, A. Marinelli, and S. Reiche. The physics of x-ray free-electron lasers. *Reviews of Modern Physics*, 88(1):015006, 2016, doi:10.1103/RevModPhys.88.015006.
- [134] R. Bonifacio, C. Pellegrini, and L.M. Narducci. Collective instabilities and high-gain regime in a free electron laser. *Optics Communications*, 50(6):373–378, 1984, doi:10.1016/0030-4018(84)90105-6.
- [135] Christoph Bostedt, Sébastien Boutet, David M. Fritz, Zhirong Huang, Hae Ja Lee, Henrik T. Lemke, Aymeric Robert, William F. Schlotter, Joshua J. Turner, and Garth J. Williams. Linac Coherent Light Source: The first five years. *Reviews of Modern Physics*, 88(1):015007, 2016, doi:10.1103/RevModPhys.88.015007.
- [136] C. Pellegrini. Progress toward a soft X-ray FEL. *Nuclear Instruments and Methods in Physics Research Section A: Accelerators, Spectrometers, Detectors and Associated Equipment*, 272(1-2):364–367, 1988, doi:10.1016/0168-9002(88)90252-5.
- [137] K Tiedtke, A Azima, N von Bargen, L Bittner, S Bonfigt, S Düsterer, B Faatz, U Frühling, M Gensch, Ch Gerth, N Guerassimova, U Hahn, T Hans, M Hesse, K Honkavaar, U Jastrow, P Juranic, S Kapitzki, B Keitel, T Kracht, M Kuhlmann,

- W B Li, M Martins, T Núñez, E Plönjes, H Redlin, E L Saldin, E A Schneidmiller, J R Schneider, S Schreiber, N Stojanovic, F Tavella, S Toleikis, R Treusch, H Weigelt, M Wellhöfer, H Wabnitz, M V Yurkov, and J Feldhaus. The soft x-ray free-electron laser FLASH at DESY: Beamlines, diagnostics and end-stations. *New Journal of Physics*, 11(2):023029, 2009, doi:10.1088/1367-2630/11/2/023029.
- [138] W. Ackermann, G. Asova, V. Ayvazyan, A. Azima, N. Baboi, J. Bähr, V. Balandin, B. Beutner, A. Brandt, A. Bolzmann, R. Brinkmann, O. I. Brovko, M. Castellano, P. Castro, L. Catani, E. Chiadroni, S. Choroba, A. Cianchi, J. T. Costello, D. Cubaynes, J. Dardis, W. Decking, H. Delsim-Hashemi, A. Delsérieys, G. Di Pirro, M. Dohlus, S. Düsterer, A. Eckhardt, H. T. Edwards, B. Faatz, J. Feldhaus, K. Flöttmann, J. Frisch, L. Fröhlich, T. Garvey, U. Gensch, Ch. Gerth, M. Görler, N. Golubeva, H.-J. Grabosch, M. Grecki, O. Grimm, K. Hacker, U. Hahn, J. H. Han, K. Honkavaara, T. Hott, M. Hüning, Y. Ivanisenko, E. Jaeschke, W. Jalmuzna, T. Jezynski, R. Kammering, V. Katalev, K. Kavanagh, E. T. Kennedy, S. Khodyachykh, K. Klose, V. Kocharyan, M. Körfer, M. Kollowe, W. Koprek, S. Korepanov, D. Kostin, M. Krassilnikov, G. Kube, M. Kuhlmann, C. L. S. Lewis, L. Lilje, T. Limberg, D. Lipka, F. Löhler, H. Luna, M. Luong, M. Martins, M. Meyer, P. Michelato, V. Miltchev, W. D. Möller, L. Monaco, W. F. O. Müller, O. Napieralski, O. Napoly, P. Nicolosi, D. Nölle, T. Nuñez, A. Oppelt, C. Pagani, R. Paparella, N. Pchalek, J. Pedregosa-Gutierrez, B. Petersen, B. Petrosyan, G. Petrosyan, L. Petrosyan, J. Pflüger, E. Plönjes, L. Poletto, K. Pozniak, E. Prat, D. Proch, P. Pucyk, P. Radcliffe, H. Redlin, K. Rehlich, M. Richter, M. Roehrs, J. Roensch, R. Romaniuk, M. Ross, J. Rossbach, V. Rybnikov, M. Sachwitz, E. L. Saldin, W. Sandner, H. Schlarb, B. Schmidt, M. Schmitz, P. Schmüser, J. R. Schneider, E. A. Schneidmiller, S. Schnepp, S. Schreiber, M. Seidel, D. Sertore, A. V. Shabunov, C. Simon, S. Simrock, E. Sombrowski, A. A. Sorokin, P. Spanknebel, R. Spesyvtsev, L. Staykov, B. Steffen, F. Stephan, F. Stulle, H. Thom, K. Tiedtke, M. Tischer, S. Toleikis, R. Treusch, D. Trines, I. Tsakov, E. Vogel, T. Weiland, H. Weise, M. Wellhöfer, M. Wendt, I. Will, A. Winter, K. Wittenburg, W. Wurth, P. Yeates, M. V. Yurkov, I. Zagorodnov, and K. Zapfe. Operation of a free-electron laser from the extreme ultraviolet to the water window. *Nature Photonics*, 1(6):336–342, 2007, doi:10.1038/nphoton.2007.76.
- [139] B Faatz, E Plönjes, S Ackermann, A Agababyan, V Asgekar, V Ayvazyan, S Baark, N Baboi, V Balandin, N von Bargen, Y Bican, O Bilani, J Bödewadt, M Böhnert, R Böspflug, S Bonfigt, H Bolz, F Borges, O Borkenhagen, M Brachmanski, M Braune, A Brinkmann, O Brovko, T Bruns, P Castro, J Chen, M K Czwalinna, H Damker, W Decking, M Degenhardt, A Delfs, T Delfs, H Deng, M Dressel, H-T Duhme, S Düsterer, H Eckoldt, A Eislage, M Felber, J Feldhaus, P Gessler, M Gibau, N Golubeva, T Golz, J Gonschior, A Grebentsov, M Grecki, C Grün, S Grunewald, K Hacker, L Hänisch, A Hage, T Hans, E Hass, A Hauberg, O Hensler, M Hesse, K Heuck, A Hidvegi, M Holz, K Honkavaara, H Höppner, A Ignatenko, J Jäger, U Jastrow, R Kammering, S Karstensen, A Kaukher, H Kay, B Keil, K Klose, V Kocharyan, M Köpke, M Körfer, W Kook, B Krause, O Krebs, S Kreis,



- F Krivan, J Kuhlmann, M Kuhlmann, G Kube, T Laarmann, C Lechner, S Lederer, A Leuschner, D Liebertz, J Liebing, A Liedtke, L Lilje, T Limberg, D Lipka, B Liu, B Lorbeer, K Ludwig, H Mahn, G Marinkovic, C Martens, F Marutzky, M Maslocv, D Meissner, N Mildner, V Miltchev, S Molnar, D Mross, F Müller, R Neumann, P Neumann, D Nölle, F Obier, M Pelzer, H-B Peters, K Petersen, A Petrosyan, G Petrosyan, L Petrosyan, V Petrosyan, A Petrov, S Pfeiffer, A Piotrowski, Z Pisarov, T Plath, P Pototzki, M J Prandolini, J Prenting, G Priebe, B Racky, T Ramm, K Rehlich, R Riedel, M Roggli, M Röhling, J Rönsch-Schulenburg, J Rossbach, V Rybnikov, J Schäfer, J Schaffran, H Schlarb, G Schlesselmann, M Schlösser, P Schmid, C Schmidt, F Schmidt-Föhre, M Schmitz, E Schneidmiller, A Schöps, M Scholz, S Schreiber, K Schütt, U Schütz, H Schulte-Schrepping, M Schulz, A Shabunov, P Smirnov, E Sombrowski, A Sorokin, B Sparr, J Spengler, M Staack, M Stadler, C Stechmann, B Steffen, N Stojanovic, V Sychev, E Syresin, T Tanikawa, F Tavella, N Tesch, K Tiedtke, M Tischer, R Treusch, S Tripathi, P Vagin, P Vetrov, S Vilcins, M Vogt, A de Zubiaurre Wagner, T Wamsat, H Weddig, G Weichert, H Weigelt, N Wentowski, C Wiebers, T Wilksen, A Willner, K Wittenburg, T Wohlenberg, J Wortmann, W Wurth, M Yurkov, I Zagorodnov, and J Zemella. Simultaneous operation of two soft x-ray free-electron lasers driven by one linear accelerator. *New Journal of Physics*, 18(6):062002, 2016, doi:10.1088/1367-2630/18/6/062002.
- [140] Elke Plönjes, Bart Faatz, Marion Kuhlmann, and Rolf Treusch. FLASH2: Operation, beamlines, and photon diagnostics. *AIP Conference Proceedings*, 1741:20008, 2016, doi:10.1063/1.4952787.
- [141] Daniel Meissner, Maciej Brachmanski, Mathias Hesse, Ulf Jastrow, Marion Kuhlmann, Helmut Mahn, Frank Marutzky, Elke Plönjes-Palm, Maike Röhling, Horst Schulte-Schrepping, Kai Tiedtke, and Rolf Treusch. Designing the Flash II Photon Diagnostic Beamline and Components. *Proceedings of the 9th Edition of the Mechanical Engineering Design of Synchrotron Radiation Equipment and Instrumentation Conference*, 2017, doi:10.18429/JACOW-MEDSI2016-MOPE40.
- [142] Markus Braune, Günter Brenner, Siarhei Dziarzhytski, Pavle Juranić, Andrey Sorokin, and Kai Tiedtke. A non-invasive online photoionization spectrometer for FLASH2. *Journal of Synchrotron Radiation*, 23(1):10–20, 2016, doi:10.1107/S1600577515022675.
- [143] Markus Braune, Jens Buck, Marion Kuhlmann, Sören Grunewald, Stefan Düsterer, Jens Viefhaus, and Kai Tiedtke. Non-invasive online wavelength measurements at FLASH2 and present benchmark. *Journal of Synchrotron Radiation*, 25(1):3–15, 2018, doi:10.1107/S1600577517013893.
- [144] F Loehl, K E Hacker, F Ludwig, H Schlarb, and B Schmidt. A Sub 100 fs Electron Bunch Arrival-time Monitor System for FLASH. *Proceedings of EPAC*, 2006.
- [145] Michele Viti, M. K. Czwalińska, H. Dinter, C. Gerth, Konrad Przygoda, R. Rybaniec, and H. Schlarb. The Bunch Arrival Time Monitor at FLASH and European XFEL.

- The 16th International Conference on Accelerator and Large Experimental Control Systems*, 2017, doi:10.3204/PUBDB-2017-12190.
- [146] Paul Kirkpatrick and A. V. Baez. Formation of Optical Images by X-Rays. *Journal of the Optical Society of America*, 38(9):766, 1948, doi:10.1364/JOSA.38.000766.
- [147] L. Raimondi, C. Svetina, N. Mahne, D. Cocco, F. Capotondi, E. Pedersoli, M. Manfreda, M. Kiskinova, B. Keitel, G. Brenner, E. Plönjes, T. Mey, K. Mann, and M. Zangrando. Status of the K-B bendable optics at FERMI@Elettra FEL. In Stephen L. O'Dell and Ali M. Khounsary, editors, *SPIE Optical Engineering + Applications*, page 920804, San Diego, California, United States, 2014.
- [148] T. Lang, S. Schulz, A. Swiderski, J. Zheng, I. Hartl, S. Alisauskas, U. Grosse-Wortmann, T. Hulsenbusch, B. Manschwetus, C. Mohr, J. Muller, F. Peters, and N. Schirmel. Versatile OPCPA Pump-Probe Laser System for the FLASH2 XUV FEL Beamline at DESY. In *2019 Conference on Lasers and Electro-Optics Europe & European Quantum Electronics Conference (CLEO/Europe-EQEC)*, pages 1–1, Munich, Germany, 2019. IEEE.
- [149] Lorenzo Raimondi, Michele Manfreda, Nicola Mahne, Daniele Cocco, Flavio Capotondi, Emanuele Pedersoli, Maya Kiskinova, and Marco Zangrando. Kirkpatrick–Baez active optics system at FERMI: System performance analysis. *Journal of Synchrotron Radiation*, 26(5):1462–1472, 2019, doi:10.1107/S1600577519007938.
- [150] Marion Kuhlmann. Status of FL24 (focused): Report on current commissioning results., 2017.
- [151] J Müller, C Sydlo, M Schäfer, M Felber, F Zummack, M K Czwalinna, S Schulz, H Schlarb, and B Schmidt. ALL-OPTICAL SYNCHRONIZATION OF PULSED LASER SYSTEMS AT FLASH AND XFEL. page 3.
- [152] B K McFarland, N Berrah, C Bostedt, J Bozek, P H Bucksbaum, J C Castagna, R N Coffee, J P Cryan, L Fang, J P Farrell, R Feifel, K J Gaffney, J M Glowia, T J Martinez, S Miyabe, M Mucke, B Murphy, A Natan, T Osipov, V S Petrovic, S Schorb, Th Schultz, L S Spector, M Swiggers, F Tarantelli, I Tenney, S Wang, J L White, W White, and M Gühr. Experimental strategies for optical pump – soft x-ray probe experiments at the LCLS. *Journal of Physics: Conference Series*, 488(1):012015, 2014, doi:10.1088/1742-6596/488/1/012015.
- [153] P Kruit and F H Read. Magnetic field paralleliser for  $2\pi$  electron-spectrometer and electron-image magnifier. *Journal of Physics E: Scientific Instruments*, 16(4):313–324, 1983, doi:10.1088/0022-3735/16/4/016.
- [154] Manuel A.V. Ribeiro da Silva, Luísa M.P.F. Amaral, and Piotr Szterner. Experimental study on the thermochemistry of 2-thiouracil, 5-methyl-2-thiouracil and 6-methyl-2-thiouracil. *The Journal of Chemical Thermodynamics*, 57:380–386, 2013, doi:10.1016/j.jct.2012.08.004.

- [155] Daniel R. Stull. Vapor Pressure of Pure Substances. Organic and Inorganic Compounds. *Industrial & Engineering Chemistry*, 39(4):517–540, 1947, doi:10.1021/ie50448a022.
- [156] D. Ferro, L. Bencivenni, R. Teghil, and R. Mastromarino. Vapour pressures and sublimation enthalpies of thymine and cytosine. *Thermochimica Acta*, 42(1):75–83, 1980, doi:10.1016/0040-6031(80)87117-6.
- [157] Joseph Ladislav Wiza. Microchannel plate detectors. *Nuclear Instruments and Methods*, 162(1-3):587–601, 1979, doi:10.1016/0029-554X(79)90734-1.
- [158] Fabiano Lever. UrsaPQ-Manager Codebase. <https://github.com/pnjun/UrsaPQ-Manager>.
- [159] J. Fung and S. Mann. Using multiple graphics cards as a general purpose parallel computer: Applications to computer vision. In *Proceedings of the 17th International Conference on Pattern Recognition, 2004. ICPR 2004.*, pages 805–808 Vol.1, Cambridge, UK, 2004. IEEE.